

NORTHWESTERN UNIVERSITY

The Low Mach Number Approximation for  
Multidimensional Hydrodynamical Modeling of  
Type I X-Ray Bursts

A DISSERTATION

SUBMITTED TO THE GRADUATE SCHOOL  
IN PARTIAL FULFILLMENT OF THE REQUIREMENTS

for the degree

DOCTOR OF PHILOSOPHY

Field of Physics and Astronomy

By

David J. Lin

EVANSTON, ILLINOIS

June 2006

© Copyright by David J. Lin 2006

All Rights Reserved

## ABSTRACT

### The Low Mach Number Approximation for Multidimensional Hydrodynamical Modeling of Type I X-Ray Bursts

**David J. Lin**

The Low Mach Number Approximation (LMNA) is applied to 1D and 2D hydrodynamical modeling of Type I X-ray bursts on the surface of non-rotating neutron stars. Because many astrophysical phenomena involve subsonic flows (maximum Mach number  $M_{max} < 0.1$ ), the time-step increase offered by the LMNA makes feasible routine simulations of astrophysical deflagrations where strong gravity produces significant stratification.

The LMNA is implemented as a split, explicit, finite-difference scheme on a uniform grid, forward-Euler in time. Input physics include thermal diffusion, realistic equation of state, and  $3\alpha$  nuclear burning. Closing the fluid equations requires solving an elliptic equation, in which one term involves a density-integral function  $K(z)$ . This function enhances computational stability by minimizing computational inaccuracies involving the imbalance between pressure gradient forces and gravitational acceleration ( $g = 2 \times 10^{14}$  cm s $^{-2}$ ).

A neutron star's outer envelope is first constructed in hydrostatic and thermal equilibrium and evolved through several burst cycles with a diffusional-thermal code to create pre-burst peak initial conditions for the hydrodynamic simulations. The heating, peak, and cooling stages of the burst are modeled and analyzed. In 2D, convective cells dynamically develop in a vertically expanding layer. The layer boundaries propagate upward at 10<sup>4</sup> cm s $^{-1}$ , while downward at only 10<sup>2</sup> cm s $^{-1}$ . During the deflagration, the maximum convective flow speed is 10<sup>7</sup> cm s $^{-1}$  ( $M_{max} < 0.1$ ).

On average, the convective layer is superadiabatic by the Schwarzschild criteria, but significant local fluctuations occur on sub-convective timescales. A temperature gradient more consistent with the Ledoux criteria is sustained at the convective boundaries due to

less efficient mixing there. A tracer particle analysis reveals particle penetration through the convective boundaries is temporary and limited in extent. A modal analysis reveals convective-modes are a necessary but not sufficient condition for penetration.

Potentially, the method can be extended into 3D and applied to model deflagrations in other important astrophysical phenomena, such as classical nova on white dwarf stars, pre-supernova events in the cores of evolved stars, nuclear burning in the cores of main sequence stars, and wherever nuclear burning and hydrodynamics occur in a significantly stratified environment.

## Acknowledgments

I sincerely appreciate my thesis advisers, Alvin Bayliss and Ronald Taam, to which this method belongs. They graciously gave me the opportunity to build a set of wings for their idea. Moreover, they routinely, freely, and enthusiastically carved out significant blocks of time and energy from their already busy schedules to guide me through this detail-ridden endeavor. Their insights, suggestions, and encouragements along the way proved invaluable in surmounting the almost-daily obstacles which threatened to doom our efforts.

I greatly appreciate Professor Edward A. Spiegel and Professor Mordecai-Mark Mac Low of Columbia University, whose insights and suggestions proved very helpful in interpreting the results of the model. I also thank Mike Zingale and Paul Ricker for introducing me to FLASH during the initial stages of this project. While the final version of the LMNA model is completely independent of FLASH, I learned much about computational astrophysics from being acquainted with FLASH. I also appreciate the great technical consulting team at NCSA, who always immediately responded to any problems I encountered while using their supercomputers during the initial development phases of this project. I offer many thanks to Jesse Becker, who managed Northwestern's Applied Math department's new Linux cluster, Hydra, on which the development of the LMNA model was completed and the final calculations performed. Thanks, also, to Doug Roberts for his helpful advice regarding 3D visualization programs.

Finally, I thank Mom, Dad, and Sis for their constant support, stimulating conversations and correspondence, and unending challenges which have always motivated me in the life-long quest for what is good and true. Their example of selfless ministry is something I always admire, and their ability to see beyond the ordinary, something to which I will always aspire.



## Contents

List of Tables	11
List of Figures	13
Chapter 1. Introduction	20
1.1. Thermonuclear Flash Model for Type I X-ray Bursts	21
1.2. More Recent Observations	25
1.3. Earlier Theoretical-Computational Investigations	27
1.4. Road Map For the Reader	34
Chapter 2. The Low Mach Number Approximation	36
2.1. Limitations of Fully Explicit Hydrodynamics	36
2.2. Limitations of Other Simplifying Approximations	38
2.3. Summary of the LMNA Advantages	40
2.4. Motivation of the LMNA Model	41
2.5. Outline of LMNA Procedure	45
2.6. Computational Methods	48
Chapter 3. 1D	54
3.1. Initial Model	54
3.2. 1D Hydrodynamical Models	66
3.3. 1D Summary	86
Chapter 4. 2D	87
4.1. Introduction	87
4.2. Summary of 2D results	89

4.3. Initial Model	90
4.4. 2D Domains and Boundary Conditions	91
4.5. Overview of Burst Sequence	98
4.6. Time Evolution of Thermodynamic and Dynamic Quantities	101
4.7. Flow Fields	114
4.8. Thermodynamical Fluctuations	119
4.9. Velocity Correlations and Thermodynamic Gradients	179
4.10. Tracer Particle Analyses	184
4.11. Modal Analysis	207
4.12. Mixing-Length Theory	217
 Chapter 5. 2D Validation Studies	219
5.1. 2D Domains	219
5.2. Grid Refinement Study	220
5.3. Time Resolution Study	234
5.4. Extended Vertical Boundary Study	243
5.5. Other tests	247
5.6. Summary	247
 Chapter 6. Discussion	248
6.1. Contribution of Carbon Reactions in Helium Burning	249
6.2. 1D vs. 2D Flux Comparisons	253
6.3. Schwarzschild vs. Ledoux Criteria	266
6.4. Summary of Main Results	267
6.5. Future Development and Applications	269
 Bibliography	279
 Appendix A. List of Symbols, Abbreviations, and Physical Constants	289
A.1. Definition of Symbols	289

A.2. Abbreviations	291
A.3. Physical Constants	292
Appendix B. The Numerical Procedure for the Low Mach Number Approximation	293
B.1. Composition $X_{(i,j,k)}^{(n+1)}$ and Total Reaction Rate $R_{(i,j,k)}^{(n+1)}$	293
B.2. Temperature $T_{(i,j,k)}^{(n+1)}$	296
B.3. Density $\rho_{(i,j,k)}^{(n+1)}$	297
B.4. Elliptic Equation	299
B.5. Velocity $\vec{v}_{(i,j,k)}^{(n+1)}$	304
B.6. Pressure Perturbation $P_{(i,j,k)}^{(n+1)}$	305
B.7. Check Criteria of Validity	305
B.8. Time-Step Complete	305
B.9. Final Comment	305
Appendix C. The $K$ Function	307
C.1. $K_{bottom-up}$	307
C.2. $K_{top-down}$	309
C.3. Taylor's Rule	310
C.4. Boundary Conditions on $\phi$	311
Appendix D. The Analytical Determination of $\frac{\partial \rho}{\partial t}$	313
Appendix E. Methods of Discretizing Differentials	316
E.1. Temporal Derivatives	316
E.2. Spatial Derivatives	316
Appendix F. The Low Mach Number Approximation vs. the Anelastic Approximation	322
F.1. Preliminary Definitions	322
F.2. The Anelastic Approximation	323
F.3. The Low Mach Number Approximation	323

F.4. Summary	324
Appendix G. Computing Environment Specifications	325

## List of Tables

4.1	2D Boundary Conditions	95
4.2	Summary of Dynamical Parameters at Four EGR levels.	118
4.3	General Guidelines of 5-shade Scheme	120
4.4	$d(T)$ Figures	120
4.5	$d(Y)$ Figures	121
4.6	SAd Figures	121
4.7	SLed Figures	121
4.8	5-shade Scheme for $d(T)$ at log EGR 16	124
4.9	5-shade Scheme for $d(T)$ at log EGR 17	128
4.10	5-shade Scheme for $d(T)$ at log EGR 18	131
4.11	5-shade Scheme for $d(T)$ at log EGR 19	134
4.12	5-shade Scheme for $d(Y)$ at log EGR 16	139
4.13	5-shade Scheme for $d(Y)$ at log EGR 17	142
4.14	5-shade Scheme for $d(Y)$ at log EGR 18	145
4.15	5-shade Scheme for $d(Y)$ at log EGR 19	148
4.16	5-shade Scheme for SAd at all EGR levels	152
4.17	5-shade Scheme for SLed at all EGR levels	165
4.18	Extent of Under- and Over-Penetration	189
4.19	Initial Vertical Positions of Tracer Particles.	197

5.1	2D Domain Sizes in Grid Refinement Study	221
6.1	1D, 2D $F_{nuc}$ Rise and Fall Times	255
6.2	1D, 2D $F$ Rise, Fall, Decay Times	265
F.1	LMNA vs AA	324
G.1	<i>Hydra</i> Hardware Specifications	325
G.2	<i>Hydra</i> Software Specifications	325

## List of Figures

1.1	2D Contour Plot of log Total Velocity at $t = 50 \mu s$	30
1.2	2D Contour Plot of log Total Velocity at $t = 700 \mu s$	30
2.1	A Computational Zone at $i, j, k$	49
3.1	Raw Initial Conditions: Log Density vs. Depth	56
3.2	Raw Initial Conditions: Log Pressure vs. Depth	56
3.3	Raw Initial Conditions: Temperature vs. Depth	57
3.4	Raw Initial Conditions: Log Energy Generation Rate vs. Depth	57
3.5	Raw Initial Conditions: Log ${}^4_2He$ vs. Depth	58
3.6	Twelve Bursts: Log Peak Energy Generation Rate vs. Time	60
3.7	Twelve Bursts: Peak Temperature vs. Time	60
3.8	Twelve Bursts: Log Nuclear Flux vs. Time	61
3.9	Twelve Bursts: Total ${}^4_2He$ vs. Time	61
3.10	Second Burst: Log Peak Energy Generation Rate vs. Time	62
3.11	Second Burst: Peak Temperature vs. Time	62
3.12	Second Burst: Log Nuclear Flux vs. Time	63
3.13	Second Burst: Total ${}^4_2He$ vs. Time	63
3.14	Second Burst: Log Energy Generation Rate vs Depth	64
3.15	Second Burst: Temperature vs Depth	64
3.16	Second Burst: ${}^4_2He$ vs Depth	65

3.17	1D Hydrodynamics: Log Peak Energy Generation Rate vs. Time	67
3.18	1D Hydrodynamics: Peak Temperature vs. Time	68
3.19	1D Hydrodynamics: Log Nuclear Flux vs. Time	68
3.20	1D Hydrodynamics: Total $\frac{4}{2}He$ vs. Time	69
3.21	1D Hydrodynamics: Vertical Velocity vs. Time	69
3.22	1D Hydrodynamics: Log Energy Generation Rate vs Depth	70
3.23	1D Hydrodynamics: Temperature vs Depth	70
3.24	1D Hydrodynamics: $\frac{4}{2}He$ vs Depth	71
3.25	1D Hydrodynamics: Vertical Velocity vs Depth	71
3.26	1D Hydrodynamics: $gK$ vs Depth	73
3.27	1D Hydrodynamics: $P'$ vs Depth	73
3.28	1D $No - K$ : Log Peak Energy Generation Rate vs. Time	75
3.29	1D $No - K$ : Peak Temperature vs. Time	75
3.30	1D $No - K$ : Log Nuclear Flux vs. Time	76
3.31	1D $No - K$ : Total $\frac{4}{2}He$ vs. Time	76
3.32	1D $No - K$ : Vertical Velocity vs. Time	77
3.33	1D $No - K$ : Log Energy Generation Rate vs Depth	77
3.34	1D $No - K$ : Temperature vs Depth	78
3.35	1D $No - K$ : $\frac{4}{2}He$ vs Depth	78
3.36	1D $No - K$ : Vertical Velocity vs Depth	79
3.37	1D $K$ vs. $No - K$ : $P'$ vs Depth	81
3.38	1D $K$ vs. $No - K$ : Force vs Depth	82
3.39	1D $K$ vs. $No - K$ : $\frac{\partial P'}{\partial z}$ vs Depth	83
3.40	1D $K$ vs. $No - K$ : $\rho'g$ vs Depth	84

		15
3.41	1D $K$ vs. $No - K$ : Vertical Velocity vs Depth	85
4.1	Initial Vertical Profiles of Thermodynamic Quantities	92
4.2	Burst Sequence Snapshots A	96
4.3	Burst Sequence Snapshots B	97
4.4	Global Thermodynamic Quantities vs. Time	103
4.5	Thermodynamical Quantities vs. z, Pre-Burst Peak	105
4.6	Thermodynamical Quantities vs. z, Post-Burst Peak	106
4.7	Global Velocity Quantities vs. Time	108
4.8	He4 Front Position and Speed	109
4.9	EGR vs. z, Post-Burst Peak	110
4.10	Convective Quantities vs. Time	112
4.11	Velocity Flow Fields, log EGR 16, 17	115
4.12	Velocity Flow Fields, log EGR 18, 19	116
4.13	Contours of $d(T)$ and Flow Field at log EGR = 16 A	125
4.14	Contours of $d(T)$ and Flow Field at log EGR = 16 B	126
4.15	Contours of $d(T)$ and Flow Field at log EGR = 17 A	129
4.16	Contours of $d(T)$ and Flow Field at log EGR = 17 B	130
4.17	Contours of $d(T)$ and Flow Field at log EGR = 18 A	132
4.18	Contours of $d(T)$ and Flow Field at log EGR = 18 B	133
4.19	Contours of $d(T)$ and Flow Field at log EGR = 19 A	135
4.20	Contours of $d(T)$ and Flow Field at log EGR = 19 B	136
4.21	Contours of $d(Y)$ and Flow Field at log EGR = 16 A	140
4.22	Contours of $d(Y)$ and Flow Field at log EGR = 16 B	141
4.23	Contours of $d(Y)$ and Flow Field at log EGR = 17 A	143

4.24	Contours of $d(Y)$ and Flow Field at log EGR = 17 B	144
4.25	Contours of $d(Y)$ and Flow Field at log EGR = 18 A	146
4.26	Contours of $d(Y)$ and Flow Field at log EGR = 18 B	147
4.27	Contours of $d(Y)$ and Flow Field at log EGR = 19 A	149
4.28	Contours of $d(Y)$ and Flow Field at log EGR = 19 B	150
4.29	Contours of SAd and Flow Field at log EGR = 16 A	154
4.30	Contours of SAd and Flow Field at log EGR = 16 B	155
4.31	Contours of SAd and Flow Field at log EGR = 17 A	157
4.32	Contours of SAd and Flow Field at log EGR = 17 B	158
4.33	Contours of SAd and Flow Field at log EGR = 18 A	160
4.34	Contours of SAd and Flow Field at log EGR = 18 B	161
4.35	Contours of SAd and Flow Field at log EGR = 19 A	163
4.36	Contours of SAd and Flow Field at log EGR = 19 B	164
4.37	Contours of SLed and Flow Field at log EGR = 16 A	168
4.38	Contours of SLed and Flow Field at log EGR = 16 B	169
4.39	Contours of SLed and Flow Field at log EGR = 17 A	171
4.40	Contours of SLed and Flow Field at log EGR = 17 B	172
4.41	Contours of SLed and Flow Field at log EGR = 18 A	174
4.42	Contours of SLed and Flow Field at log EGR = 18 B	175
4.43	Contours of SLed and Flow Field at log EGR = 19 A	177
4.44	Contours of SLed and Flow Field at log EGR = 19 B	178
4.45	Vertical Velocity Correlation $W$ and $\nabla$ 's	181
4.46	Vertical Velocity Correlation $W$	182
4.47	Lateral Velocity Correlation $V$	183

4.48	Ten Particle Trajectories, log EGR = 16 and 17	187
4.49	Ten Particle Trajectories, log EGR = 18 and 19	188
4.50	Particle Trajectory Limits (inside-out), log EGR = 16, 17	191
4.51	Particle Trajectory Limits (inside-out), log EGR = 18, 18.5	192
4.52	Particle Trajectory Limits (inside-out), log EGR = 18.5, 19	193
4.53	Penetration at log EGR = 16 and 17	194
4.54	Penetration at log EGR = 18 and 18.5	195
4.55	Penetration at log EGR = 19	196
4.56	Particle Trajectory Limits (outside-in), log EGR = 17	199
4.57	Particle Trajectory Limits (outside-in), log EGR = 18.5	200
4.58	Particle Trajectory Limits (extended domain), log EGR = 17	202
4.59	Particle Trajectory Limits (extended domain), log EGR = 18.5	203
4.60	Average Vertical Velocity at Major EGR Levels	205
4.61	Brunt-Väisälä Frequency vs. Vertical Position	209
4.62	$k - w$ Diagrams, Lower Convective Boundary, log EGR = 17	213
4.63	$k - w$ Diagrams, Upper Convective Boundary, log EGR = 17	214
4.64	$k - w$ Diagrams, Lower Convective Boundary, log EGR = 18.5	215
4.65	$k - w$ Diagrams, Upper Convective Boundary, log EGR = 18.5	216
5.1	Grid Refinement: log EGR = 16	222
5.2	Grid Refinement: log EGR = 17	223
5.3	Grid Refinement: log EGR = 18	224
5.4	Grid Refinement: log EGR = 19	225
5.5	Grid Refinement: $W$ vs $\nabla$ 's, log EGR = 16	227
5.6	Grid Refinement: $W$ vs $\nabla$ 's, log EGR = 17	228

5.7	Grid Refinement: $W$ vs $\nabla$ 's, log EGR = 18	229
5.8	Grid Refinement: $W$ vs $\nabla$ 's, log EGR = 19	230
5.9	Grid Refinement: Global Thermodynamic Quantities vs. Time	231
5.10	Grid Refinement: Global Velocity Quantities vs. Time	232
5.11	Grid Refinement: He4 Front Position and Speed	233
5.12	Time-Step Refinement A	235
5.13	Time-Step Refinement B	236
5.14	Time-Step Refinement, log EGR = 16	237
5.15	Time-Step Refinement, log EGR = 17	238
5.16	Time-Step Refinement, log EGR = 18	239
5.17	Time-Step Refinement, log EGR = 19	240
5.18	Time-Step Refinement: Global Thermodynamic Quantities vs. Time	241
5.19	Time-Step Refinement: Global Velocity Quantities vs. Time	242
5.20	Extended Vertical Boundary: Flow Fields	244
5.21	Extended Vertical Boundary: $W$ vs $\nabla$ 's	245
5.22	Extended Vertical Boundary: $W$ Comparison	246
6.1	EGR Ratios vs. z, Pre- and Post-Burst Peak	251
6.2	$F_{3\alpha}/(F_{3\alpha} + F_{12,\alpha})$ vs. Time	252
6.3	1D, 2D Nuclear Flux Ratio vs. Time	255
6.4	1D, 2D Thermodynamic Quantities vs. z	256
6.5	1D $F_{rad}$ vs. z for Several Times	259
6.6	2D $F_{rad}$ and $F_{adv}$ vs. z for Several Times	260
6.7	1D, 2D $F$ vs. Time	261
6.8	2D $F_{adv} + F_{rad}$ vs. Time	262

6.9	1D Simulated Light Curve	264
6.10	Log Degeneracy Ratio vs. z	270

## CHAPTER 1

### **Introduction**

Ever since the 1970's with the advent of space telescopes designed to study X-ray emission from astronomical sources, evidence of the existence of compact objects, such as neutron stars and black holes, has been accumulating. Observed phenomena from these objects reveal interesting physics which might occur under their extreme environments. For example, a certain kind of X-ray burst has been interpreted as being caused by explosive thermonuclear reactions occurring on the surface of neutron stars. Theoretical explanations have successfully described some features of these bursts, but other aspects have yet to be elucidated, for instance, how fast does such an explosion actually travel across the neutron star, does it propagate supersonically (a detonation) or rather does it propagate subsonically (a deflagration), how does convection and turbulence affect the dynamics, what determines the time intervals between bursts, and what causes quasi-periodic fluctuations in the signals, to name a few. As the phenomenological picture improves, consistent physical explanations are needed to advance our understanding of what might be happening on these exotic objects.

Part of the effort requires multidimensional modeling of the dynamic gas motions which may arise during a burst, but as of yet, such computations have been prohibitively expensive. One reason for the computational expense is due to a time-step limitation required for the numerical stability of a calculation, the well-known Courant-Friedrichs-Lowy (CFL) condition which restricts the time-step to be inversely proportional to the largest wave speeds present. A fully explicit hydrodynamical treatment evolves acoustic pressure waves as well as the material flow of gas. However, if the maximum flow speeds are very subsonic (as would be true during a deflagration), and if the acoustic waves are not expected to play an

important role in the gas dynamics (a fair assumption for very subsonic flows), then excluding the acoustic waves from the problem allows a significant increase in time-step. This is essentially what the Low Mach Number Approximation (LMNA) achieves. By substantially increasing the time-step and thus shortening the computational time necessary to evolve to the necessary physical time-scales of the problem, the LMNA makes feasible routine multidimensional modeling of the hydrodynamics of phenomena such as X-ray bursts on the surface of neutron stars.

This project has many major goals. The LMNA will be formulated, developed, and implemented as a stable, multidimensional model which includes the relevant physics necessary to study deflagrations where strong gravity results in significant stratification, such as on the surface of neutron stars. The input physics includes thermonuclear burning, thermal diffusion, and an equation of state applicable to semi-degenerate matter. The LMNA model will then be validated with rigorous refinements in spatial and temporal resolution, and varying domain sizes. The model will then be applied to a set of hydrostatic, initial conditions representing the surface layer of a neutron star, and 1D and 2D calculations will be performed through the peak of a helium-ignition, Type I X-ray burst. The resulting gas dynamics will be qualitatively described and quantitatively analyzed. The analyses will involve studying the key dynamic and thermodynamic behavior of the flow fields which develop during the burst, tracer particle penetration through convective boundaries, and dominant modes of motion near convective boundaries. Comparison of the numerical results with predictions of mixing length theory will also be attempted.

### **1.1. Thermonuclear Flash Model for Type I X-ray Bursts**

Observationally, only neutron stars in low mass X-ray binaries (LMXBs) exhibit X-ray bursts. LMXBs consist of a pair of stars in orbit around their common center of mass, where one object is a compact object, either a neutron star or a black hole (called the accretor), while the other is a main-sequence star with relatively low mass (called the donor).

As the donor expands during its natural evolution, or if the binary orbit shrinks due to angular momentum loss, the donor's outer envelope may eventually overspill its Roche lobe, a mathematically determined volume around a star in a binary system, inside of which material is gravitationally bound to that star. This gas then spills over and may become gravitationally bound to the accretor. Furthermore, over time, orbital angular momentum loss causes the binary orbit to shrink, promoting mass transfer from the donor to the accretor. Conserving angular momentum, this flow of gas may form a hot, inspiralling accretion disk around the accretor. The relatively low level, persistent X-ray flux detected from these systems is thought to originate from both the accretion disk, which is hot enough to emit X-rays, or if the accretor is a neutron star, the neutron star's surface, when the accreted gas impacts onto it, releasing gravitational energy as heat and radiation. In addition to the persistent X-ray emission, some of these systems also exhibit sudden and substantial increases in X-ray flux above persistent levels, known as X-ray bursts. Estimates of radii based on the assumption that the emitting object is a black-body indicate bright bursts must involve the entire neutron star surface.

X-ray bursts can be classified into two major types, Type I and Type II. This thesis focuses on simulating Type I X-ray bursts. For completeness, however, a brief description of the key features of Type II X-ray bursts is warranted. Type II X-ray bursts are believed to be due to sudden increases in the accretion rate of gas from the donor, caused by such factors as changes in the viscous properties of the accretion disk or the influence of the neutron star's magnetic field. While Type II burst profiles vary greatly, they share general characteristics, which include rapid successions of bursts a few minutes apart, sudden drops in flux without a gradual decay from peak values, no spectral softening during decay, and sustained peak values of flux in longer bursts. Notably, Type II bursts have been observed in only two sources: 1) MXB 1730-335 (the Rapid Burster) and, 2) GRO J1744-28 (the Bursting Pulsar) Lewin et al. (1993, 1995).

By far, most X-ray bursts are Type I. Henceforth, reference to X-ray bursts and bursters will mean the Type I variety. Type I burst profiles vary greatly, but characteristic features include a sudden, rapid (1 to 10 seconds) increase in X-ray flux, reaching 5 to 20 times quiescent values, followed by a more extended period of decay (10 seconds to several minutes), during which the energy of the X-rays diminishes from peak values. The thermonuclear flash model Taam (1980, 1985); Lewin et al. (1995) successfully explains these general features as resulting from explosive nuclear ignition on the surface of neutron stars. In short, after gas from the accretion disk reaches the surface of the neutron star, it spreads out evenly over it and proceeds to burn in the extremely high pressure environment. At a critical point, degenerate hydrogen and/or helium burning ignites explosively, suddenly heating up the entire surface to around  $3 \times 10^7$  K, enough to emit strong X-rays. This flash is observed as the start of an X-ray burst. After the explosion, the surface cools, a process observed as the decay of the burst profile. Moreover, as more nuclear fuel continues to accrete onto the surface, the process may repeat. Thus, the model accounts for the general observational features of burst properties such as the energies involved ( $\sim 10^{38}$  to  $10^{39}$  ergs), their rise time (seconds), duration ( $\sim 10$  to 100 seconds), spectral softening, and recurrence intervals (several hours).

The flash model enjoys widespread consensus. However, some observations are difficult to interpret in its framework. For instance, the bursting behavior of 1735-444 (van Paradijs et al., 1988) can range from intervals of less than an hour, where observations are consistent with explosive helium ignition, to very long intervals of no bursts, during which the hydrogen and helium burning appears to be stable. This raises questions concerning what kinds of conditions favor one type of burning over another, and what causes the sudden change between the two.

Another example is the relationship between the time interval between two bursts and the total burst energy of the later burst. According to the flash model, a longer time interval allows more fuel to accrete, which should make the subsequent burst more powerful. While

extensive EXOSAT observations of several bursters such as 1735-444 (Lewin et al., 1980) support this prediction, others do not. For instance, sources as 0748-673 (Gottwald et al., 1986) and 0836-429 (Aoki et al., 1992) have very short burst intervals, around 10 minutes. This is not enough time to accrete enough nuclear fuel to power a second burst. One possible explanation is that a significant amount of fuel may be left over from one burst to be involved in a subsequent one (Hanawa and Fujimoto, 1984).

Yet another difficulty is trying to correlate the bursting interval with the persistent X-ray flux. No clear relationships are evident. For instance, in 1820-303, the persistent flux increased five-fold as the burst intervals decreased by half, eventually stopping altogether (Clark et al., 1977). Cessation of bursting when the persistent flux increased was similarly found in other systems such as 1658-298 (Hoffman et al., 1978) and GX3+1 (Makishima et al., 1983). However, other systems exhibit bursting when the persistent flux is very high. Examples include Cyg X-2 (Smale, 1998), GX17+1 (Tawara et al., 1984), and MXB 1730-335 (the Rapid Burster) in its strong persistent emission phase (Guerriero et al., 1999). Interestingly, bright sources such as these sometimes also exhibit very irregular bursting intervals, where the time between bursts vary greatly. Very bright neutron stars have high accretion rates approaching Eddington values. Eddington luminosity and accretion rates represent natural limits, above which the gradient of the radiation pressure exceeds the attractive gravitational force per unit volume of the material ( $\nabla P_{radiation} > -\rho g$ ), thereby minimizing further accretion. Under these conditions and in a hydrogen deficient environment, helium may not burn over the neutron star symmetrically, but in slowly moving fronts. Instead of the entire surface of the neutron star contributing to a large scale burst, the bursting occurs in limited regions, producing smaller luminosity fluctuations of minute-long duration. Bildsten suggests this may account for the very low frequency noise detected from very bright sources (Bildsten, 1993, 1995). However, this does not explain very bright bursts.

Assuming the flash model validly describes the underlying physical cause of bursts, examples such as these suggest other significant factors exist which affect the nuclear burning.

For instance, the current thermal state of the star, which in turn depends on its history of previous bursts, was found to affect nuclear burning (Taam, 1980). A star's compositional state also depends on its history and may influence burning (Woosley and Weaver, 1985). A model which takes into account the thermal and compositional histories of a burster may give results very different from a model which does not.

## 1.2. More Recent Observations

Recent observations from more advanced instruments such as RXTE and BeppoSAX have provided new details which both support and challenge the flash model.

**1.2.1. The Bursting Pulsar.** For example, RXTE observed bursts from a 2.5 ms pulsar, XTE J1808-3658 (SAX J1808.4-3658), and thus convincingly showed that a neutron star can be a burst source (Marshall et al., 1998; Wijnands and van der Klis, 1998). Previously, Type I bursts had never been observed from pulsars, suggesting that bursters had low magnetic fields. (A Type II burst had been previously observed from a pulsar, GRO J1744-28, but these kinds of bursts are believed to arise from changes in the properties of the accretion disk.) The discovery of a pulsing Type I burster not only confirms a neutron star can exhibit bursting behavior but also yields an important physical parameter, the magnetic field, previously indeterminable from bursters. The magnetic field of XTE J1808-3658 is estimated to be around  $10^8$  to  $10^9$  Gauss (Psaltis and Chakrabarty, 1999). Though the magnetic field is low, positively identifying a burster with a magnetic field helps support the hypothesis that magnetic fields may be responsible for channeling matter onto localized regions on the star, such as the magnetic poles, thus forming hotter regions there.

**1.2.2. Quasi-Periodic Oscillations.** Recent observations have also revealed rapid fluctuations in both persistent and burst spectra of several X-ray sources. In the persistent flux, these quasi-periodic oscillations (QPOs) usually occur in pairs 250-350 Hz part, with the higher frequency around 1000 Hz and the lower one, around 700 Hz. While the actual frequencies may drift, the difference between the two frequencies is nearly constant. Numerous

models have been advocated to explain their origin, though none are completely satisfactory. For instance, the sonic-point model (Miller et al., 1998) suggests the higher frequency  $\nu_h$  is caused by a spinning clump of matter at a point (the sonic point) where its radial velocity becomes supersonic. Influenced by the magnetic field, the matter may then plunge down onto the surface of the neutron star, forming a slightly hotter patch than its surroundings. An observer watching this spot spinning with the star would see brightness fluctuations with a frequency  $\nu_r$  roughly equal to the rotational frequency of the star. The lower frequency  $\nu_l$  is interpreted as the beat frequency between  $\nu_h$  and  $\nu_r$ , that is,  $\nu_l = \nu_h - \nu_r$ . Thus, the difference between the observed QPO frequencies may provide a way to measure, or at least constrain, the rotational frequency of the neutron star ( $\Delta\nu = \nu_r = \nu_h - \nu_l$ ).

QPOs have also been observed in bursts (Strohmayer, 2001; Strohmayer et al., 1997). For instance, QPOs were found in 17 bursts from 4U 1728-34, five from 4U 1636-536, and three from X 1743-29 (Strohmayer et al., 1998). This supports the idea they originate from some surface phenomenon. In one interpretation, the magnetic field of the star funnels gas from the accretion disk onto the magnetic poles, pooling more fuel there. Energy generation due to nuclear burning would naturally be higher in this patch, increasing the temperature above its surroundings. As the burning patches grow in size to cover the rest of the star when a burst develops, this might be observed as strong QPOs at the start of the X-ray burst signal. Since burst QPOs typically have frequencies  $\sim 300$  Hz and 600 Hz, a simple explanation may be that the smaller frequency is caused by the modulation of luminosity due to one hot spot rotating with the neutron star, and the larger frequency due to two (possibly bi-polar) spots. A rotation frequency of the star of  $\sim 300$  Hz is also consistent with the sonic point model's predictions, since the difference between the higher and lower frequencies of the persistent QPOs is generally  $\sim 300$  Hz. There are exceptions, however. Bursts of several sources have frequencies twice the star's rotational frequency predicted by the sonic point model, for instance, 4U 1608-52, where the only observed burst frequency is 619 Hz, while  $\Delta\nu \sim 225\text{-}325$  Hz (Strohmayer, 2001).

Other observational details complicate the picture. For instance, oscillations often occur in the tail of the burst, after the nuclear fuel should have been entirely burned. Moreover, the oscillation frequency in some sources changes from 1 to 3 Hz throughout the duration of the burst. The most extreme case is X 1656-298, which showed an increase in QPO frequencies of 5 Hz in the burst tail compared to burst onset (Wijnands et al., 2000). Another puzzle is why QPOs are not always observed during bursts. In fact, bursts from a given burster, such as 4U 1728-34 (Strohmayer et al., 1997), sometimes exhibit QPOs and other times not, while many bursters do not exhibit QPOs at all.

While phenomenology such as these need to be explained satisfactorily, the existence of QPOs can be interpreted as strengthening the possibility that bursts initiate in a small number of limited regions on the neutron star. Clearly, additional observational and theoretical work are needed to understand both old and new aspects of X-ray bursts such as these in the framework of the flash model. In terms of computational modeling, particularly lacking are multidimensional simulations involving hydrodynamics which take into account thermal and compositional histories of the star. If hot spots due to spatially-limited combustion patches form on the surface of a neutron star, their behavior in a convective and turbulent environment need elucidating. Only recently have computational resources and methodology improved to make these complex calculations feasible.

### 1.3. Earlier Theoretical-Computational Investigations

**1.3.1. Burning Front Propagation.** Earlier theoretical work investigated the ignition of a thermonuclear flash starting in a limited patch and how quickly the burning front would propagate around the star. Fryxell and Woosley examined four possible mechanisms of flame propagation: i) pure diffusion via conduction or radiation; ii) convection assuming symmetrical convection cells; iii) convection with weak turbulence; and, iv) convection with strong turbulence (Fryxell and Woosley, 1982).

With convection, they estimate the velocity at which the burning front moves is  $\sim 5 \times 10^5$  cm s $^{-1}$ . Thus, a deflagration wave would require  $\sim 10$  s to travel around the entire star, roughly agreeing with the observed burst rise-times. However, their calculations involved many assumptions regarding the size of the convection cells and convective velocities, so their results can only be taken as reasonable estimates.

Nozakura, Ikeuchi, and Fujimoto (1984) proceeded to numerically calculate in 2D the lateral propagation of a thermal wave which would result from a He shell flash on the surface of an accreting neutron star. While they examined both a purely conductive case as well as a convective case, their simulation did not involve hydrodynamics. Rather, they calculated the convective velocity based on mixing length theory. Their results showed that depending on the temperature of the hydrogen burning zone, the travel time across most of the star was found to be  $\sim 0.1$  to  $10$  s, again, roughly agreeing with observations.

Flames may also propagate more slowly, as reported by Bildsten (1995), who identified a new regime of time dependent helium burning for neutron stars with very high accretion rates. In this regime, convection never occurs during the thermal instability, and the burning front travels relatively slowly via conduction at  $\sim 300$  cm s $^{-1}$ . Thus, distinct, burning patches on the star's surface may exist for a significant amount of time ( $\sim 10$  to  $10^4$  s). Such a limited burning may account for the very low-frequency noise (VLFN) observed in the persistent flux of some very bright sources such as GX5-1 (van der Klis et al., 1987).

**1.3.2. Quasi-Periodic Oscillations.** Recent efforts to computationally evolve a neutron star atmosphere using a rotating, one-dimensional, hydrostatic model support the theory that QPOs are due to rotating hot spots on the star surface and suggest possible explanations for other QPO phenomenology (Cumming and Bildsten, 2000). For instance, angular momentum conservation as a burning shell expands and relaxes during bursts may account for the 1 to 2 Hz QPO frequency change in burst tails. Moreover, the rotational behavior was found to strongly depend upon the composition of the burning layers. This would be consistent with studies which correlate burst duration with QPO occurrence. Bursts of long

duration (indicative of hydrogen burning) in GS 1826-24 do not exhibit QPOs (Kong et al., 2000), while those of short duration (indicative of pure helium burning) in KS 1731-26 do exhibit QPOs (Muno et al., 2000). However, additional observational studies are needed to strengthen the case.

Assuming X-ray bursts to be thermonuclear in origin, the observed energy in a typical burst suggests the entire star is involved in the event, and it is unlikely that the whole star, which has a radius of  $\sim 10^6$  cm, explodes simultaneously. Prime candidates for locations where bursts may ignite include: i) magnetic poles, where accretion onto the star might be channeled (Lamb, 2000); or, ii) the equatorial region, where the force of gravity may be lessened due to centripetal effects (Spitkovsky et al., 2002), allowing fuel to reach a greater column depth faster than other places on the star's surface, and hence ignite sooner.

**1.3.3. Irregular Bursting Behavior.** Proceeding with the idea that localized patches of burning may occur on the surface of a neutron star, a recent investigation by Taam, Bayliss, and Sandquist (2000) offer insights into a possible reason why bursting intervals can be irregular in some bright LMXBs. In this study, a localized temperature perturbation was introduced in the initial conditions to simulate a region on the neutron star's surface which is hotter than its immediate surroundings. The thermal evolution was followed, and the temperature perturbation was found to be quickly smoothed out by thermal diffusion. As additional mass accreted near Eddington values onto the surface, a burst finally resulted. However, the time it took for the burst to occur was much longer than in the control case in which no temperature perturbation was introduced. (The control case produced regular bursting intervals.) Thus it was demonstrated that localized temperature disturbances due to localized accretion of fuel can significantly affect X-ray burst duration. Irregularities in burst duration, then, may be due to varying degrees of such localization.

**1.3.4. Preliminary Studies Using FLASH.** If fuel is localized as portrayed in the above scenario, it must be able to spread over the entire neutron star in a relatively short amount of time, since in order to form a bright burst with a rapid increase in luminosity, the

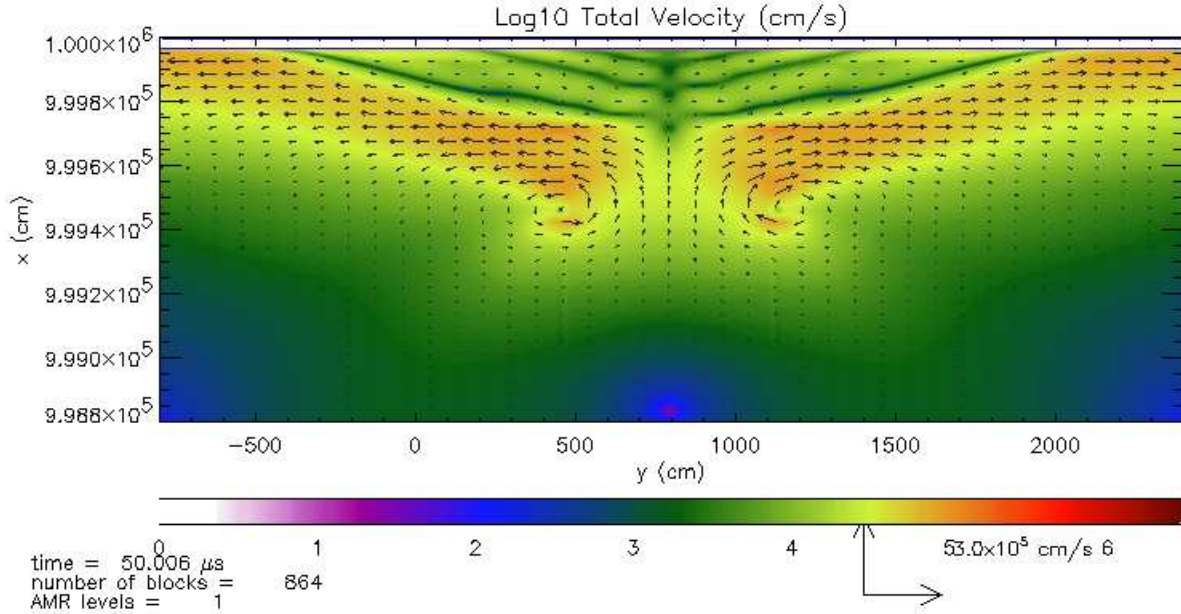


FIGURE 1.1. 2D Contour Plot of log Total Velocity at  $t = 50 \mu\text{s}$   
 Energy is added at a rate of  $10^{17} \text{ erg g}^{-1} \text{ s}^{-1}$  in a region  $667 \text{ cm} \times 350 \text{ cm}$  at the center of  
 the domain. At first, hydrodynamical circulation patterns are present.

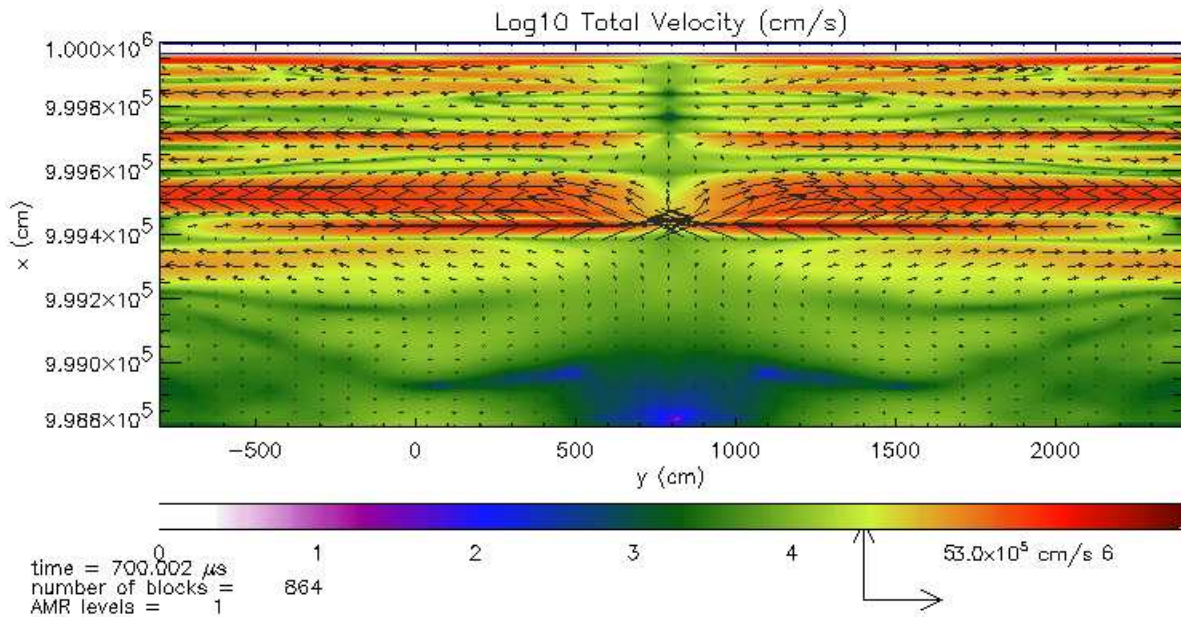


FIGURE 1.2. 2D Contour Plot of log Total Velocity at  $t = 700 \mu\text{s}$   
 Energy is added at a rate of  $10^{17} \text{ erg g}^{-1} \text{ s}^{-1}$  in a region  $667 \text{ cm} \times 350 \text{ cm}$  at the center of  
 the domain. By this time, large outflowing behavior becomes evident.

explosion must involve most of the neutron star nearly simultaneously. Given that the radius of a neutron star is about  $10^6$  cm, matter would need to move relatively quickly (greater than  $10^5$  to  $10^6$  cm s $^{-1}$ ) to account for the observed burst properties. To discover what might cause such motion, a preliminary investigation was initiated by the author in 2000. The preliminary results strongly suggested that hydrodynamical mechanisms exist which may move matter and energy rapidly away from a localized region where energy generation occurs at a higher rate than its immediate surroundings.

Using FLASH (Fryxell et al., 2000), an explicit code based on the Piecewise Parabolic Method (PPM) (Colella and Woodward, 1984), developed by the DOE-supported ASCI/Alliance Center for Astrophysical Thermonuclear Flashes at the University of Chicago, the author constructed and evolved one and two-dimensional, non-rotating models of the outer surface of a neutron star (Lin, 2000). First, 1D calculations were performed to see whether significant hydrodynamical waves would develop as a result of introducing energy at a constant rate in a limited region of the domain. Both a vertical model and a lateral model were constructed, which represent simple cross-sectional slices of a neutron star surface. Energy generation was simulated by adding a constant energy generation rate of  $10^{17}$  erg g $^{-1}$ s $^{-1}$  to a small region on the domain. Sound waves developed from the region, but the velocities induced were insignificant ( $\sim 50$  cm s $^{-1}$ ), far too small to carry matter and energy very far in the timescale of interest. However, in both vertical and lateral models, the site where energy was added did exhibit small, persistent differences in pressure and density from its surroundings, of the order of  $10^{-4}$  in terms of fractional difference. Moreover, after the initial wave passes, the regions in the wake of the wave showed a fractional difference in pressure and density of  $10^{-7}$ . Since differences of these magnitudes suggested the possibility that hydrodynamic circulation may develop in a 2D domain, the results encouraged the author to proceed to a 2D model.

The 2D calculations yielded a much more dynamic picture. Starting with pre-burst-peak, hydrostatic initial conditions, nuclear reactions were simulated by constantly inputting a

fixed energy generation rate of  $10^{17}$  erg g $^{-1}$  s $^{-1}$  in a spatially-limited patch, the size of which was a parameter. As the simulation begins, a circulation pattern develops around the energy input region (Figure 1.1). Later, much larger velocity outflows develop (Figure 1.2), set up by an initial pressure wave that propagates through the computational domain at the sound speed ( $\sim 10^8$  cm s $^{-1}$ ). The magnitude of the velocity outflows was found to be related to the size of the energy generation region. For example, in the case when the region is 667 cm long, the magnitude of the outflowing velocities are on the order of 10 $^5$  cm s $^{-1}$ . If the magnitudes of these velocity fields persist on the timescale of enhanced nuclear energy generation (around 10 seconds), they will propel fuel around the star in time to involve most of it in a large-scale burst.

Together with the earlier finding that bursts are delayed due to such perturbations, this mechanism may be one explanation why some bright X-ray sources burst irregularly. That is, a localized region of greater burning of nuclear fuel due to greater accretion on a certain part of the star not only significantly delays the time required to develop a burst due to thermal effects, but also establishes flows due to hydrodynamical effects sufficient to carry the fuel to the rest of the star in time for the entire star to be involved in a burst.

While promising, these results were preliminary. A more complete investigation would involve careful parameter studies of how changing different variables affects the dynamic evolution of the system. One parameter which was rather arbitrary were the dimensions of the energy generation region. Previous calculations suggest enhanced nuclear reactions will occur between densities of  $2 \times 10^5$  and  $2 \times 10^6$  g cm $^{-3}$ , helping to constrain the vertical limits. However, the lateral extent of the region is a parameter which could be explored. In reality, the magnetic polar cap is likely to be on the order of a kilometer or longer. While computational limitations may prohibit studies of such extent, it may be possible to adequately scale the velocities which develop from smaller regions of different sizes, to the limits of computational feasibility. One would expect that larger flows would develop from larger regions of energy generation, since more energy is being introduced. In fact, an

investigation using the current model supports this physically intuitive idea: the velocity of the developing flows scales roughly linearly with the lateral extent of the energy generating region.

Another improvement to the calculation would be the inclusion of a nuclear reaction network, which may lead to unexpected dynamics. Energy generation from nuclear reactions were introduced into the system by simply adding a constant term to the total energy in the hydrodynamical equations. While the energy generation rate used was consistent with independent calculations involving a nuclear reaction network, it may change when hydrodynamics is included. Moreover the preliminary simulation suggested inflow of matter from deeper in the star into the energy generation region may occur, thereby enriching the nuclear fuel with heavier elements. Another possibility is the formation of other burning regions in other parts of the domain, due to dynamic flows which develop. More complete modeling is necessary to carefully examine the consequences of these potentially important mechanisms.

Yet another avenue of questions involve how lateral differences in the initial conditions affect how the system evolves. Steep thermodynamic gradients in latitude may result in baroclinic instabilities, resulting in substantial horizontal fluid motion. For example, terrestrial baroclinic instability arises when the temperature differences between the equatorial tropics and the polar caps becomes excessive, resulting in significant winds which help to equalize the energy difference. Astrophysically, baroclinic instability has been studied for its possible role in transporting angular momentum in the interiors of stars (Spruit and Knobloch, 1984) and in accreting compact objects (Fujimoto, 1988, 1993). Baroclinic instability may likely occur in systems with strong differential rotation or high accretion rates. Such motion may enhance turbulence and mixing of fuel to deeper parts of the star. Fujimoto proposed that flashes which originate in the deeper layers due to such fuel enrichment may explain bursters with very short intervals, too short for surface accretion to explain (Fujimoto, 1988) . However, Cumming and Bildsten found that mixing between burning and ash layers by baroclinic

instability does not occur in strongly stratified systems, but that baroclinic instability may operate within a differentially rotating burning layer (Cumming and Bildsten, 2000). Fujimoto also proposed that varying degrees of turbulent mixing may explain irregular bursting behavior, although a study has yet to explore the possibility (Fujimoto, 1993). The initial model was based on a uniformly lateral distribution of matter. Inhomogeneities in pressure and density as initial conditions could be introduced to examine how the developing hydrodynamic flows depend on varying degrees of the instability.

#### 1.4. Road Map For the Reader

While this thesis project begins to develop the tools to answer some of the open questions regarding Type I X-ray bursts, it is but a small step forward and far from complete. As of this writing, a good part of a decade has been poured into this effort, and the following chapters summarize only a fraction of the most essential mathematical techniques and computational analyses which have been developed and performed during this time.

In Chapter 2, the motivation for the LMNA is presented, along with an overview of the computational methodology unique to the present implementation of the method. Detailed elucidation of the actual numerical procedure is reserved for Appendix B and the methods used to difference the differential equations are presented in Appendix E.

Next, the LMNA is applied to a 1D model in Chapter 3 to establish important reference values. Moreover, the importance of a novel mathematical device, termed the  $K$  function, is first revealed in the 1D calculations. Full details about the  $K$  function is offered in Appendix C.

Subsequently, 2D calculations in Chapter 4 reveal for the first time dynamically evolving convective patterns, interesting thermodynamic behavior (such as the nature of the temperature gradient in comparison to the Schwarzschild and Ledoux criteria), convective layer boundary and burning front propagation speeds, tracer particle penetration behavior, and dominant modes of motion during a complete Type I X-ray burst. Since the maximum

instantaneous flow speed never exceeds Mach 0.10 throughout the burst sequence, the results presented in this chapter computationally demonstrate that a Type I X-ray burst may progress as a deflagration. Also, the predictions of local mixing-length theory are not relevant to the results.

As importantly, 2D validation studies are presented in Chapter 5, where several refinements in spatial and temporal resolution, as well as differences in domain sizes are tested to rigorously establish the current LMNA model's integrity.

Finally, because only the  $3\alpha$  reaction ( $3_{\frac{1}{2}}^4He \rightarrow {}_6^{12}C$ ) is the only nuclear burning process currently considered, Chapter 6 examines the contribution of the energy generation rate due to the subsequent burning of carbon ( ${}_{\frac{1}{2}}^{12}C + {}_{\frac{1}{2}}^4He \rightarrow {}_{\frac{1}{8}}^{16}O + \gamma$ ), which becomes significant after the peak of the burst. Also in this chapter, nuclear, radiative, and advective fluxes of the 1D and 2D models are compared, and differences are attributed to the extra mode of energy transfer which convection provides. Finally, the main results of the project are summarized and numerous directions to further develop and apply the LMNA model are proposed.

Due to space limitations, only the most representative results from a small fraction of the total number of calculations and analyses performed are presented in this dissertation. A more complete record of the effort, including full-color animations, can be found at the project's web-site: <http://www.astro.northwestern.edu/~lin/>

## CHAPTER 2

### The Low Mach Number Approximation

Due to its inherent complexity, the study of nonlinear phenomena in astrophysics requires significant computational resources. Improvements in computational speed and methodology have recently allowed more realistic, multi-dimensional modeling of long standing, fundamental problems; for instance, convective mixing in stellar atmospheres, hydrodynamical flows on the surface of compact objects, and dynamics of deflagration and detonation in explosive events such as novae and supernovae, to name a few. Nevertheless, some of these problems still cannot be effectively studied with current methodologies, one reason being that calculating to observationally significant time-scales would simply require too much computational time. To remedy this limitation and make computationally feasible an entire class of otherwise intractable calculations, this project implements a novel application of the Low Mach Number Approximation (LMNA) for astrophysical conditions.

#### 2.1. Limitations of Fully Explicit Hydrodynamics

**2.1.1. The CFL Condition on Time-step.** The time-step ( $dt$ ) in explicit hydrodynamical calculations is limited by the CFL condition. In each zone, the time-step is determined from the relation:

$$(2.1) \quad dt_{CFL} = \frac{\lambda dx}{(v_s + v)}$$

where  $\lambda$  is the Courant factor (usually less than 0.8 and smaller for higher dimensions),  $dx$  is the computational zone size,  $v_s$  is the local sound speed in the zone, and  $v$  is the local

propagation speed of matter. Limiting the time-step in this way guarantees that matter will move a distance less than the size of the computational zone in one computational step.

In practice, the global value of  $dt_{CFL}$  used for all zones per time-step is the smallest local value of  $dt_{CFL}$  in the domain. If  $v_s \gg v$ , then  $dt_{CFL}$  effectively depends on the greatest acoustic wave speed in the domain. Thus, for calculations of dynamics involving very subsonic flows, the time-step as limited by the CFL condition is unnecessarily small.

By keeping the pressure of the environment temporarily constant and thus preventing acoustic waves from developing, the LMNA allows  $dt_{CFL}$  to be limited by the greatest flow speed, rather than the sound speed. This immediately translates into a substantial increase in time-step for flows where  $M \ll 0.1$ , where the energy carried by acoustic waves is small. This significant practical advantage may help make routinely possible the study of problems which would otherwise require too much computational and real time.

**2.1.2. Subsonic Boundary Problems.** The wave equation has three families of solutions, or characteristics (Laney, 1998). One characteristic propagates at the local flow speed  $v$ , and it is the physically relevant solution. However, two other characteristics travel at the flow speed plus-and-minus the local sound speed ( $v \pm v_s$ ), and are called acoustic waves. All three characteristics propagate in the computational domain. The behavior of acoustic waves at domain boundaries can be problematic. For instance, acoustic waves generated inside the domain may reflect back into the domain when they reach the boundary. Or, the boundary itself may generate acoustic waves which propagate into the domain. These artifacts may potentially affect dynamical evolution and compromise the integrity of the results. The problem of subsonic boundary conditions is an active area of research in computational fluid dynamics.

Despite these problems, fully explicit hydrodynamical methods are used extensively in astrophysical computations, including studies on solar convection (Chan and Sofia, 1986; Abbott et al., 1997; D.H. and Woodward, 2000), He-shell flashes in asymptotic giant branch stars (Herwig et al., 2006), accreting neutron stars (Urpin, 2005), and modeling Type I X-ray

bursts as a detonation (Zingale et al., 2001), to name just a few topics appropriate to the present thesis.

Since the LMNA excludes acoustic waves from the calculation, the problem of subsonic boundary artifacts due to acoustic reflections is automatically eliminated. The method helps remove a potential source of error in the computations, offering another significant practical advantage over methods which evolve acoustic waves.

## 2.2. Limitations of Other Simplifying Approximations

In the same spirit of the LMNA, other approximations have been developed to allow sufficiently long calculations to be completed in a reasonable amount of time. These include the Boussinesq Approximation, the Anelastic Approximation, and implicit methods of solving the Euler equations.

**2.2.1. The Boussinesq Approximation.** In the Boussinesq Approximation (BA), the continuity equation is simplified to the vanishing of the divergence of the velocity field ( $\nabla \cdot \mathbf{v} = 0$ ) (Spiegel and Veronis, 1959). In effect, Lagrangian density variations are neglected in the inertial term but not the buoyancy term. Thus, the fluid is treated as essentially incompressible.

The BA is also used in astrophysical research, for example, to study convective instabilities in proto-neutron stars (Miralles et al., 2000) and to determine criteria for surface convective instabilities on neutron stars in the presence of strong magnetic fields (Miralles et al., 1997).

Compressibility effects in the velocity field are expected to be important in the astrophysical problems of interest, and thus the BA is too restrictive for this project.

**2.2.2. The Anelastic Approximation.** The Anelastic Approximation (AA) (Ogura and Phillips, 1962; Bannon, 1996) is somewhat similar to the Boussinesq Approximation. The continuity equation is reduced to the vanishing of the divergence of the product of density and the velocity field. ( $\nabla \cdot \rho \mathbf{v} = 0$ ). The fluid is assumed to be essentially incompressible,

although temporal variations in density are allowed on a convective timescale. This method effectively eliminates sound waves, and can be used when  $M \ll 1$ . For very subsonic flows, the AA equilibrates pressure perturbations on acoustic time-scales, but allows for changes in pressure and density on convective time-scales. In this formalism, all physical quantities are expanded as a dominant term, which is a zonal average, plus a small perturbation assumed to be of order  $M^2$ . Then, by setting  $\frac{\partial \rho}{\partial t} = 0$  in the continuity equation, sound waves are filtered out of the computation. (See Appendix F for more details.)

The AA has been extensively used to model terrestrial processes which do not involve combustion, for example geophysical flows (Bannon, 1996). Fundamentally, the reason why the AA is not appropriate for combustive processes is because it assumes all perturbed quantities and gradients (besides velocity, which is by definition of order  $M$ ) are of order  $M^2$ . Since the AA does not allow for large gradients of density and/or temperature, such as those which might occur between burning and non-burning regions, for example, a flame front, the AA is not appropriate for studying deflagrations. On the other hand, the LMNA allows for significant density and temperature gradients and it has been successfully applied to studying problems in terrestrial combustion (McGrattan et al., 2004).

Astrophysical studies using the AA were pioneered by Glatzmaier (1984) to study stellar convection. The AA has evolved to a level of sophistication where convection can be followed in 3D for hundreds of convective turnover times in the cores of massive stars (Kuhlen et al., 2002, 2003). Recently, the AA has been used to model carbon ignition in Type Ia supernovae in 3D to investigate the effects of rotation on the nature of turbulent flows prior to the explosive event (Kuhlen et al., 2005).

For a more detailed comparison between the LMNA and AA, see Appendix F.

**2.2.3. Implicit Schemes.** The implicit scheme is a standard hydrodynamical method which use information from the present as well as previous time-steps to evolve the Euler equations (Laney, 1998). These methods are computationally more expensive, but allow for larger time-steps. However, acoustic waves are included in the method and may not be

accurately calculated, possibly negatively affecting the solutions. Moreover, the same kind of subsonic boundary problems which plague explicit methods apply to implicit schemes, as described in Sub-Section 2.1.2. An example of an astrophysical application of the fully-implicit method is the work by Deupree (2000) in studying hydrogen-burning convective cores in zero-age-main-sequence stellar models.

### 2.3. Summary of the LMNA Advantages

Hence, the LMNA will provide unique advantages which other methods of approximating the Euler equations do not offer. It effectively filters out the acoustic waves from the domain (thereby significantly increasing the time-step for very subsonic flows), allows for large lateral variations in thermodynamic variables, includes fully compressible fields, and eliminates subsonic boundary issues. While the LMNA has been extensively used to study terrestrial problems such as fire-dynamics (Bayliss et al., 1992; McGrattan et al., 2004), it has just begun to be applied to astrophysical problems.

For example, certain aspects of Type Ia supernovae, which are thought to be detonations within white dwarf stars, are currently being computationally explored using a different astrophysical formulation of the low Mach number approximation by Bell et al. (2004a) and Almgren et al. (2006a). Thus far, these efforts have involved detailed comparisons of test problems between the LMNA, Anelastic Approximation, and traditional hydrodynamic methods in a regime for which all are valid (Almgren et al., 2006a). Rayleigh-Taylor unstable flames have also been simulated in 2D and 3D (to a limited extent), and the turbulence which naturally arises shows a Kolmogorov-like power spectrum (Bell et al., 2004c; Zingale et al., 2005). Likewise, 2D Landau-Darrieus planar flame instabilities have been investigated during the late stages of a supernovae explosion, but their effects were found to insignificantly contribute to the energetics of the supernova (Bell et al., 2004b).

As formulated in this thesis, the present LMNA model is able to address questions involving deflagrations where strong gravity results in significant vertical stratification, a distinct

advantage over the LMNA method by Bell et al. (2004a). Potentially, our LMNA model will be an important new tool for studying astrophysical deflagrations where large density and temperature gradients exist.

What is sacrificed to gain the benefits of the LMNA, of course, is that the results are by definition incomplete, since the method completely excludes any evolution of acoustic waves. However, since very little energy is carried by acoustic waves in very low Mach number flows, the physical effects of acoustic waves on the dynamics of the system are reasonably negligible, and their exclusion should be inconsequential.

## 2.4. Motivation of the LMNA Model

The fully compressible, hydrodynamical (Euler) equations are:

Equation of Continuity:

$$(2.2) \quad \frac{\partial \rho}{\partial t} + \nabla \cdot \rho \vec{v} = 0$$

Equation of Momentum:

$$(2.3) \quad \rho \frac{D \vec{v}}{Dt} + \nabla P = \rho \vec{g}$$

Equation of Energy:

$$(2.4) \quad \rho c_p \frac{DT}{Dt} - \delta \frac{DP}{Dt} = Q + \nabla \cdot \kappa \nabla T$$

Equation of State:

$$(2.5) \quad \rho = F(T, P, X_l)$$

Equation of Species:

$$(2.6) \quad \frac{DX_l}{Dt} = R_l$$

where all symbols are defined in Appendix A.

For terrestrial models without strong vertical stratification, it is instructive to non-dimensionalize the Euler equations, that is, to introduce the terms  $A_N = A_D/A_o$ , where  $A_D$  is each of the dimensional, thermodynamic quantities  $(\rho, \vec{v}, T, P, X_l)$ , and  $A_o$  is a characteristic value of each quantity. For example, for the case of velocity, the characteristic value may be the adiabatic flame speed. Doing so, the non-dimensionalized gradient of the pressure can be expressed in terms of the Mach number:

$$(2.7) \quad \nabla P = -M^2 \left( \rho \frac{D\vec{v}}{Dt} + F_r^{-1} \rho \hat{g} \right)$$

Here,  $P$ ,  $\rho$ ,  $t$ ,  $\nabla$  and  $\vec{v}$  are non-dimensionalized quantities;  $M$  is the Mach Number ( $M = v_o/v_s$ ,  $v_o$ = the local flame speed,  $v_s$ = the local sound speed); and  $F_r$  is the Froude Number, a measure of the inertial versus gravitational influence ( $F_r = \frac{v_o^2/L_o}{g}$ ,  $L_o$ = a characteristic length scale).

Thus, it is evident that  $\nabla P \sim 0$  for very subsonic flows ( $M \ll 1$ ). Then, the pressure can be expressed as a term to 1st order possibly having dependence on time but not space, and another term to order  $M^2$ , which may have both time and spatial dependence. That is,

$$(2.8) \quad P = P_1(t) + M^2 P_2(\vec{r}, t)$$

Here, the second term of order  $M^2$  can be considered a perturbation, which can be neglected for small values of  $M$ .

Non-dimensionalizing the equations for an astrophysical model may not be helpful, since the large stratification in the vertical direction due to gravity makes it difficult to determine characteristic values for the physical quantities. Nevertheless, the above analysis may still be instructive. For instance, when gravitational effects dominate,  $F_r$  is very small, potentially making the second term in Equation 2.7 significant. This admits the existence of a strong pressure gradient, but only in the vertical ( $k$ ) direction. Applying the results of the previous analysis to the astrophysical model, it is thus reasonable to perturbatively expand the physical quantities about a time-independent, hydrostatic base state with large vertical gradients:

$$(2.9) \quad A(\vec{r}, t) = A_h(z) + A'(\vec{r}, t)$$

where  $A_h(z)$  is a physical quantity  $(\rho_h(z), \vec{v}_h(z), T_h(z), P_h(z), X_{l,h}(z))$  of a hydrostatic base state, assumed to be independent of time, and,  $A'(\vec{r}, t)$  is a perturbation to the base state. Only the perturbation in pressure  $P'$  is assumed to be small compared to  $P_h(z)$ , while no assumptions regarding the relative amplitudes of the perturbations in the other quantities compared to their respective base states are made. Since  $\vec{v}_h(z) = 0$ , the symbol  $\vec{v}(z)$  will be used in subsequent expressions to represent the perturbative velocity,  $\vec{v}'(z)$ .

As presently formulated, the LMNA model assumes a time-independent base pressure state, since the level of electron degeneracy is relatively high for gas on the surface of a neutron star. Time-dependency of the base pressure to account for expansion effects may be readily incorporated into the model as an improvement, and this possibility is discussed in Section 6.5.1 of Chapter 6.

In the Low Mach Number Approximation, the pressure perturbation  $P'(\vec{r}, t)$  is neglected in the equations of energy and state, the mathematical essence of this approximation. The LMNA can be interpreted physically as stating that pressure disturbances due to acoustic energy are virtually instantaneously smoothed out, and thus can be left out of the equations

of energy and state. In effect, the speed of sound is considered to be infinite, and all acoustic effects pass through the domain instantly. In this way, sound waves are filtered out of the domain.

The governing equations of the Low Mach Number Approximation are obtained by substituting the perturbative expansion of the physical quantities in the form given in Equation 2.9 into the Euler equations, taking the LMNA by omitting  $P'(\vec{r}, t)$  in the equations of energy and state, and using the hydrostatic equilibrium condition  $\frac{dP_h}{dz} = -\rho_h g$ :

LMNA Equation of Continuity:

$$(2.10) \quad \frac{\partial \rho}{\partial t} + \nabla \cdot \rho \vec{v} = 0$$

LMNA Equation of Momentum:

$$(2.11) \quad \rho \frac{D\vec{v}}{Dt} + \nabla P' = \rho' \vec{g}$$

LMNA Equation of Energy:

$$(2.12) \quad \rho c_p \frac{DT}{Dt} - \delta \frac{DP_h}{Dt} = Q + \nabla \cdot \kappa \nabla T$$

LMNA Equation of State:

$$(2.13) \quad \rho = F(T, P_h, X_l)$$

LMNA Equation of Species:

$$(2.14) \quad \frac{DX_l}{Dt} = R_l$$

In this formulation of the LMNA model, the continuity equation is used to further expand the momentum equation, but is not explicitly solved. Further discussion explaining this strategy is given in Sub-section 2.5.3 below.

## 2.5. Outline of LMNA Procedure

In this section, the general outline of the numerical procedure for the LMNA as implemented in the present algorithm is presented. To prevent the reader from becoming lost in details, only a brief description of each principle evolution step is offered here, but in Appendix B, the procedure, its motivation, and derivation of all equations are exhaustively detailed. The definitions of all symbols are given in the List of Symbols, Abbreviations, and Physical Constants (Appendix A). It is important to note that the continuity equation, while used in deriving the elliptic equation, is not explicitly solved.

The following are the principal evolution equations:

$$(2.15) \quad \frac{\partial X_l}{\partial t} = -\vec{v} \cdot \nabla X_l + R_l$$

$$(2.16) \quad \frac{\partial T}{\partial t} = -\vec{v} \cdot \nabla T + \frac{1}{c_p} \left( \dot{s} - \frac{\delta}{\rho} w \rho_h g + \frac{1}{\rho} \nabla \cdot \kappa \nabla T \right)$$

$$(2.17) \quad \begin{aligned} \rho &\Leftarrow EOS(T, P_h, X_l) \\ e &\Leftarrow EOS(T, P_h, X_l) \end{aligned}$$

$$(2.18) \quad \nabla^2 P' = \frac{\partial^2 \rho}{\partial t^2} - \nabla \cdot \{ \nabla \cdot (\rho \vec{v} \vec{v}) \} + \nabla \cdot (\rho' \vec{g})$$

$$(2.19) \quad \frac{\partial(\rho\vec{v})}{\partial t} = -\nabla \cdot (\rho\vec{v}\vec{v}) - \nabla P' + \rho'\vec{g}$$

As presented above, the elliptic (Equation 2.18) and momentum (Equation 2.19) equations constitute the most straightforward expressions involving the gravitational acceleration, a formalism which is termed *No-K*. To enhance vertical stability during the calculation, a mathematical device called the *K* function is introduced, and is fully motivated in Appendix B (The LMNA Numerical Procedure) and Appendix C (The *K* Function). Re-expressed with the *K* function in a potential-like term,  $\phi \equiv P' \pm gK$ , the elliptic and momentum equations become:

$$(2.20) \quad \nabla^2\phi = \frac{\partial^2\rho}{\partial t^2} - \nabla \cdot \{\nabla \cdot (\rho\vec{v}\vec{v})\} \pm \left\{ \frac{\partial^2(gK)}{\partial x^2} + \frac{\partial^2(gK)}{\partial y^2} \right\}$$

$$(2.21) \quad \frac{\partial(\rho\vec{v})}{\partial t} = -\nabla \cdot (\rho\vec{v}\vec{v}) - \nabla\phi \pm \left\{ \frac{\partial(gK)}{\partial x}\hat{i} + \frac{\partial(gK)}{\partial y}\hat{j} \right\}$$

In these expressions, which sign (+ or -) is used depends on how *K* is calculated, as fully explained in Appendix C.

**2.5.1. Composition *X*.** Equation 2.15 describes the equation for composition evolution. Updating composition is operator split into two stages: i) composition advection via upwinding, and ii) composition change due to combustion. In the present model, the combustive process considered is the  $3\alpha$  reaction ( $3\frac{4}{2}He \rightarrow \frac{12}{6}C$ ), where two species are considered,  $\frac{4}{2}He$  and  $\frac{12}{6}C$ . The energy generation rate is obtained from the S-matrix calculations of Fushiki and Lamb (1987). Subsequent reactions involving  $\frac{12}{6}C$  and  $\frac{16}{8}O$  are neglected, since

the energy generation rates of these reactions before the peak of the burst are negligible compared to that of the  $3\alpha$  reaction at the densities and temperatures of the present problem. (This is quantitatively demonstrated in Section 6.1 of Chapter 6.)

**2.5.2. Temperature  $T$ .** Equation 2.16 describes the equation for temperature evolution, which is the energy equation in this algorithm. As with composition, updating temperature is operator split into separate stages. Upwinding is used to advect temperature, while central differencing is used to diffuse it.  $\kappa(\rho, T, X_l)$ , the radiative thermal conductivity, is found using the conductivity routine from FLASH (Fryxell et al., 2000). (See Section B.2 in Appendix B for the definition of  $\kappa$ .) By the LMNA approximation, the pressure at a given point is fixed for all time, and since the initial structure is in hydrostatic equilibrium,  $P = P_h$  for all time for every zone. Thus, in this equation, the key approximation of the LMNA is made:  $\frac{\partial P}{\partial t} = 0$ , where  $P$  at a given point is fixed for all time. In this way, acoustic waves are naturally suppressed during the evolution. The term involving  $g$  originates from the hydrostatic condition,  $\nabla P_h = -\rho_h g$ .

**2.5.3. Density  $\rho$  and Internal Energy  $e$ .** Having updated composition and temperature, and assuming pressure is fixed at hydrostatic values, a consistent density and internal energy can be obtained from the equation of state (EOS). A Newton-Raphson convergence is required, because the direct inputs of the Helmholtz EOS are density and pressure (Timmes and Swesty, 2000).

In principle, an alternative and apparently equivalent procedure would be to evolve the density using the continuity equation and use the EOS to obtain a consistent temperature and internal energy. In fact, this was attempted during the earlier development phase of the LMNA procedure. However, because the conditions on the surface of a neutron star are semi-degenerate, computational experiments quickly revealed that small errors in density, which naturally arose due to truncation and other numerical errors, were translated into large errors in temperature, ultimately leading to unrealistic and unstable results. Consequently, the current procedure of using the energy equation to solve for temperature, and then the

EOS to determine the consistent density, was implemented and found to be computationally stable and more accurate. Thus, the degenerate conditions of the system being studied requires the direct evolution of temperature and the indirect determination of a consistent density, not the other way around.

**2.5.4. Elliptic Equation for  $\phi$ .** Equation 2.20 gives the elliptic equation for  $\phi \equiv P' \pm gK$ , a potential-like term, which involves the special  $K \equiv \int^z \rho'(x, y, z') dz'$  density function. The  $K$  density function is introduced as an important mathematical device which allows two large numbers,  $\frac{\partial P'}{\partial z}$  and  $\rho'g$  to be absorbed into one term,  $\phi$ . Doing so replaces differences in the vertical direction to the lateral direction, but since  $K$  is a vertically summed quantity, lateral differences may not be as severe as vertical ones. In practice, using the  $K$  density function greatly enhances the numerical stability of the code. Appendix C is devoted to describing the numerical methods, sign conventions, and other details of the  $K$  density function.

In the temperature equation, the other terms on the right-hand-side are the time derivative of  $\frac{\partial \rho}{\partial t}$  and the convective term,  $\nabla \cdot \{\nabla \cdot (\rho \vec{v} \vec{v})\}$ .

**2.5.5. Momentum Equation for  $\rho \vec{v}$ .** Equation 2.21 gives the momentum equation for the conserved quantity,  $\rho \vec{v}$ . Velocities are stored at zone edges, while other variables such as density are stored at zone centers. Thus, appropriate care is required to properly evaluate terms in the momentum equation.

## 2.6. Computational Methods

**2.6.1. Code Environment.** The programming language used is FORTRAN 90. The FORTRAN compiler used on Northwestern University's Applied Math Department's Linux cluster, *Hydra*, is by Intel. The code was also compiled and run at NCSA's IBM-based cluster, *Copper*, where the operating system is AIX (version 8.1), and the compiler is XL FORTRAN. Both on *Hydra* and *Copper*, the Message-Passing Interface (MPI) standard

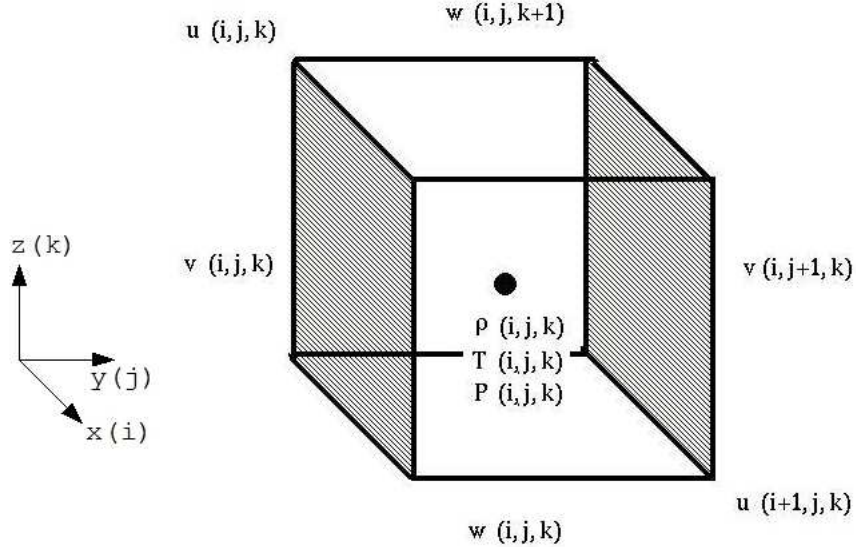


FIGURE 2.1. A Computational Zone at  $i, j, k$   
Zone centers store thermodynamic and related variables. Zone edges store velocity components: top/bottom for  $w$ , left/right for  $v$ , and front/back for  $u$ .

(2006) is employed for parallelizing the code. Appendix G on page 325 summarizes the key hardware and software configurations of *Hydra*.

**2.6.2. Computational Domain.** The domain is a Cartesian grid of uniformly sized zones (or cells). The two lateral dimensions are labeled  $x$  and  $y$  (or  $i$  and  $j$ , respectively, in discretized expressions), while the vertical dimension (which is the direction in which gravity acts) is  $z$  (or  $k$ ). In this dissertation, the entire grid is also called the *computational domain*.

The computational domain utilizes a staggered-grid system. That is, thermodynamic variables ( $\rho, P, T, e, X_l$ ) and other related quantities (such as  $\dot{s}, \phi, K$ , and  $\frac{\partial \rho}{\partial t}$ ) are stored in the zone centers, while the components of velocity ( $u, v$ , and  $w$ ) are stored at zone edges (one-half the distance between adjacent zone centers). See Figure 2.1 for a schematic of a computational zone.

Two extra zones, called boundary zones (or guard cells or ghost zones, etc.), are added to each row of a dimension of the total computational domain, one at each limit of the row.

At the extreme outer edges of the domain, these zones are needed to properly implement boundary conditions. In the parallelized version of the code, the boundary zones are added to the sub-domains of each processor, providing a depository of information between processors to ensure domain coherence and continuity.

With regards to the zone sizing, numerous different values from 10 cm zone<sup>-1</sup> to 1 cm zone<sup>-1</sup> were tested. The general rule of thumb is to use roughly ten zones for each scale height of pressure ( $\sim 200$  cm). In practice, 10 cm zone<sup>-1</sup> resolution sufficiently resolves much of hydrodynamic details which develop in the simulations. On the other hand, 1 cm zone<sup>-1</sup> requires an impractically long time to evolve. The zone size used to evolve the results presented in this dissertation is 5 cm zone<sup>-1</sup>. In Chapter 5, validation studies involving models with 5, 7.5 and 10 cm zone<sup>-1</sup> resolutions demonstrate satisfactory convergence of results.

**2.6.3. Differencing Methods.** Spatial derivatives are treated using upwind and central differencing. Appendix E explains in detail how specific terms in the LMNA differential equations are numerically differenced.

**2.6.4. Elliptic Solver.** The elliptic equation for  $\phi$  in Equation 2.20 is solved using FISHPAK, a package of FORTRAN subprograms for the solution of separable, elliptic partial differential equations (Adams et al., 1988). Alternatively, another partial differential equations solver in PETSc, Portable, Extensible Toolkit for Scientific Computation (Balay et al., 1997, 2001, 2004), was extensively used for much of the earlier testing and development of the code.

**2.6.5. Time-step Restriction.** At each computational step, the local CFL, thermal diffusion, and burning time-steps of every zone in the domain is calculated. These time-steps are defined as follows:

$$(2.22) \quad dt_{CFL} = \lambda_{CFL} \frac{dz}{v}$$

$$(2.23) \quad dt_{thermdiff} = \lambda_{thermdiff} \frac{(dz)^2}{\kappa(T, \rho)}$$

$$(2.24) \quad dt_{burn} = \lambda_{burn} \frac{e(T, \rho)}{c_p(T, \rho)}$$

Here,  $\lambda_{CFL} = \lambda_{thermdiff} = \lambda_{burn} = 0.8$  for 1D, and 0.5 for 2D. Also,  $dz$  is the uniform zone size;  $v$  is the local flow speed;  $e(T, \rho)$  is the specific internal energy; and,  $\kappa(T, \rho) = \frac{4}{3} \frac{acT^3}{\kappa_o \rho}$ , the radiative thermal conductivity.

Of the three time-steps calculated, the smallest one in the entire domain is compared to a fixed, maximum time-step (a parameter, chosen to be on the order of  $1 \times 10^{-6}$  s), and the smaller of the two becomes the time-step for the next computational step. This maximum time-step is found to be experimentally necessary for numerical stability and may be related to the gravitational acceleration.

Also, to avoid sudden, significant increases in time-step, the maximum allowed percentage increase in time-step is 10% above the previous value of the time-step.

**2.6.6. Boundary Conditions.** Detailed description of the multidimensional boundary conditions is given in Chapter 4 on the 2D results. In general, at the lateral ( $y$ ) boundary, periodic conditions are used for all variables and the elliptic equation. At the upper and lower boundaries, Dirichlet and Neumann conditions are used in the elliptic equation, while various other conditions are imposed for the thermodynamic and velocity variables. (Table 4.1 on page 95 summarizes the boundary conditions for all variables used in the 2D model. The 1D model uses only the vertical boundary conditions listed.)

Briefly, the boundary conditions on the elliptic equation are justified below, and further description will be offered in Chapter 4.

At the upper boundary ( $z_{top}$ ), the Dirichlet condition  $\phi = P' - gK_{top-down} = 0$  is used. (Consult Appendix C for the motivation and elucidation of the  $K$  function.) Both  $P' = 0$

and  $gK_{top-down} = 0$  at the upper boundary. The former is justified, because  $P'$  acts as a potential term and its value can be arbitrarily set as a constant. (Only  $\nabla P'$  is physically important in the evolution.) The latter is justified, because  $K$  is defined as an integral of perturbed densities as a function of height, and the value of  $K$  for the first zone being calculated is identically zero. Thus, at the upper boundary (for the *top-down* formalism)  $K$  is identically zero. Hence, the Dirichlet condition that  $\phi = 0$  is fully justified.

At the lower boundary ( $z_{bottom}$ ), the Neumann condition  $\frac{\partial\phi}{\partial z} = 0$  is used. This is equivalent to hydrostatic boundary conditions, because  $\frac{\partial\phi}{\partial z} = \frac{\partial(P' - gK_{top-down})}{\partial z} = \frac{\partial P'}{\partial z} + \rho'g = 0$ . To justify hydrostatic boundary conditions at this boundary, the bottom of the domain is positioned sufficiently deep compared to where significant motions arise.

For the lateral boundaries, periodic conditions were chosen to effectively extend the domain in the  $x$  and  $y$  directions indefinitely. Alternatively, reflecting conditions were also tested at the lateral boundaries, but as a result, vertical flows due to the extinguishing of lateral components of velocities grew unreasonably large at the lateral boundaries, causing numerical instabilities. On the other hand, periodic conditions resulted in well-behaved dynamics at the lateral boundaries. Because of this condition, the calculation may in principle be sensitive to the lateral extent of the domain. At a minimum, the lateral extent should allow several convective cells to comfortably fit inside the domain. More discussion about the lateral width requirements of a successful computation are given in Chapters 4 and 5 on the 2D results.

**2.6.7. Parallelism.** The Message-Passing Interface (MPI) standard (2006) is employed for parallelizing the code. Currently, the domain can be decomposed only into uniform units. For example, the minimum number of processors needed for a 3D calculation is 8 ( $2 \times 2 \times 2$ ), and each processor works on a sub-set of the entire domain which is identical in size to a sub-set which every other processor is calculating. The next smallest number of processors which can be used for a 3D calculation would be, for example, 12 ( $2 \times 2 \times 3$ ). Again, all processors would be allocated identically sized sub-domains. Thus, being able to evenly

divide the number of zones (minus 2 for the boundary zones) in one direction of the total domain by the number of processors intended for that direction is necessary. For example, a legitimate domain for the  $2 \times 2 \times 3$  processor decomposition would be  $102 \times 102 \times 302$  zones, where each processor would have  $52 \times 52 \times 102$  zones. (Note the extra 2 zones in each direction are boundary zones.)

When using multiple processors, information from the edges of each processor's sub-domain must be shared with adjacent processors in each dimension whenever a variable is updated. This transfer of information occurs via the boundary zones of each sub-domain. The cost for inter-processor communications becomes significant for an algorithm which is heavily operator split (like the current code). Currently, roughly 25% of the computational time is used for MPI inter-processor communications.

**2.6.8. Output File Format.** The outputted checkpoint file is structured in the Hierarchical Data Format (HDF) (2006), which is in a binary format. The HDF format is a particularly time- and memory-efficient way of storing data. Each checkpoint file contains complete information about the domain and can be used to restart the code from the time the checkpoint file was output. Alternatively, smaller plot files (either HDF or regular ASCII text) can be generated, which provides data to produce plots of desired variables, but plot files cannot be used to re-start a calculation from the time it was output. Checkpoint and plot files can be generated at any interval of time-step during the evolution.

## CHAPTER 3

### 1D

One-dimensional models are constructed and thoroughly tested as part of the code development process. The dimension represented in the 1D models is the vertical direction ( $z$ ), which is the defined direction of gravitational acceleration  $g$ . While limited, these models proved very useful in debugging and demonstrating the importance of the  $K$  function.

#### 3.1. Initial Model

The steady-state, initial conditions for the initial model are created by separate stellar structure and diffusional-thermal codes to eliminate the need to generate initial conditions every time the full code with hydrodynamics is run. Once created, the initial model can be re-used for as many hydrodynamic simulations as desired without having to regenerate these conditions, which can be a time-consuming procedure.

Creating the initial model involves two major phases: i) raw initial conditions from a stellar structure code; and, ii) pre-burst initial conditions from a diffusional-thermal code.

**3.1.1. Phase 1: Raw Initial Conditions.** The first phase of generating initial conditions involves a stellar structure code, programmed also in FORTRAN 90 by the author. The algorithm involves the standard steady-state equations and computational methods in stellar structure modeling. The principle equations of hydrostatic and thermal equilibrium with burning are:

$$(3.1) \quad \frac{\partial P}{\partial r} = -\rho g$$

$$(3.2) \quad \frac{\partial F}{\partial r} = \rho \dot{s}_{3\alpha}$$

$$(3.3) \quad \frac{\partial T}{\partial r} = -\frac{3\kappa_o \rho F}{16\sigma T^3}$$

$$(3.4) \quad \frac{\partial X}{\partial r} = -\frac{12m_p \dot{s}_{3\alpha}}{Q_{3\alpha} \dot{m}}$$

Local mass accretion is assumed to occur at a rate of  $\dot{m} = \frac{5 \times 10^{-9}}{4\pi R_{NS}^2} M_\odot \text{yr}^{-1} \text{cm}^{-2}$ . Canonical neutron star parameters are chosen:  $M_{NS} = 1.4M_\odot$ ,  $R_{NS} = 1.0 \times 10^6 \text{ cm}$ ,  $g = \frac{GM_{NS}}{R_{NS}^2} = 2 \times 10^{14} \text{ cm s}^{-2}$ . To find a surface flux consistent with a chosen base flux, which is a parameter chosen to be  $1.48 \times 10^{22} \text{ erg g}^{-1} \text{s}^{-1}$ , the shooting-method (Press et al., 1992) is utilized. Also included is the energy generation rate  $\dot{s}_{3\alpha}$  due to burning via the  $3\alpha$  reaction ( $3\text{He} \rightarrow {}^{12}\text{C}$ ) (Fushiki and Lamb, 1987). The opacity  $\kappa_o$  is determined from the opacity routine in FLASH (Fryxell et al., 2000). (Sub-section B.1.2 and Section B.2 in Appendix B explain the  $3\alpha$  reaction and  $\kappa_o$  in more detail.)

A 1 cm spatial interval is used to construct the raw initial conditions. Because the pressure scale-height is small ( $\sim 200 \text{ cm}$ ) compared to the neutron star radius, the plane-parallel approximation is invoked, effectively converting all radial derivatives into vertical ones. General relativistic effects are neglected. The fourth-order Runge-Kutta method (Press et al., 1992) is used to calculate derivatives.

Plots of the raw initial conditions of density (Figure 3.1), pressure (Figure 3.2), temperature (Figure 3.3), energy generation rate (Figure 3.4), and mass fraction of  ${}^4\text{He}$  (Figure 3.5) as a function of depth are presented.

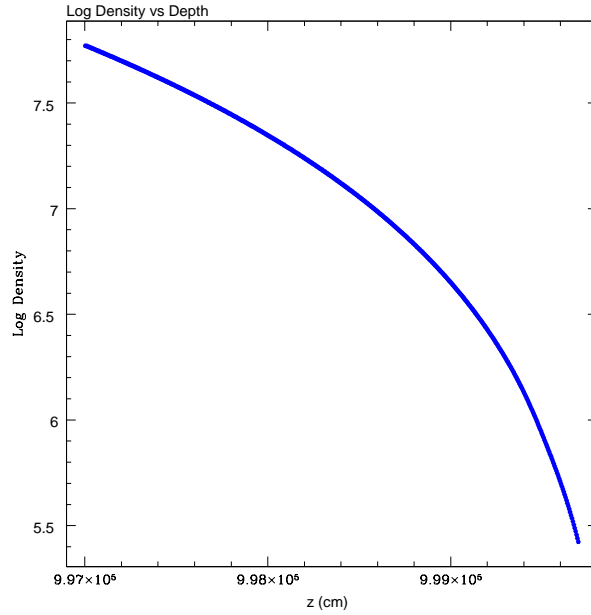


FIGURE 3.1. Raw Initial Conditions: Log Density vs. Depth  
The entire 2700 cm domain is plotted.

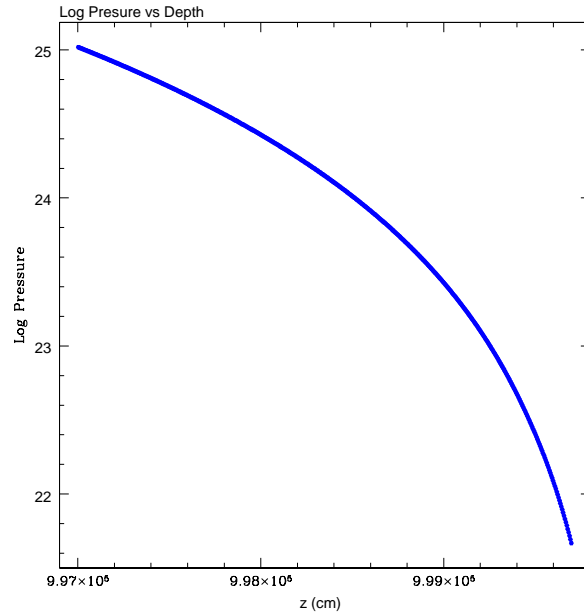


FIGURE 3.2. Raw Initial Conditions: Log Pressure vs. Depth  
The entire 2700 cm domain is plotted.

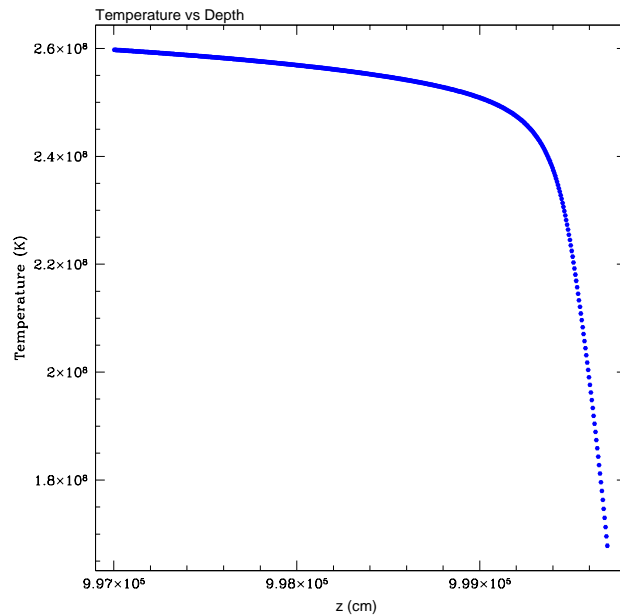


FIGURE 3.3. Raw Initial Conditions: Temperature vs. Depth  
The entire 2700 cm domain is plotted.

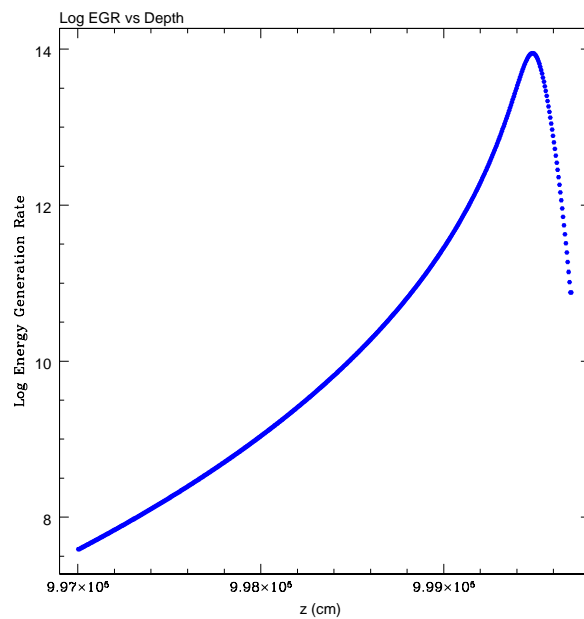


FIGURE 3.4. Raw Initial Conditions: Log Energy Generation Rate vs. Depth  
The entire 2700 cm domain is plotted.

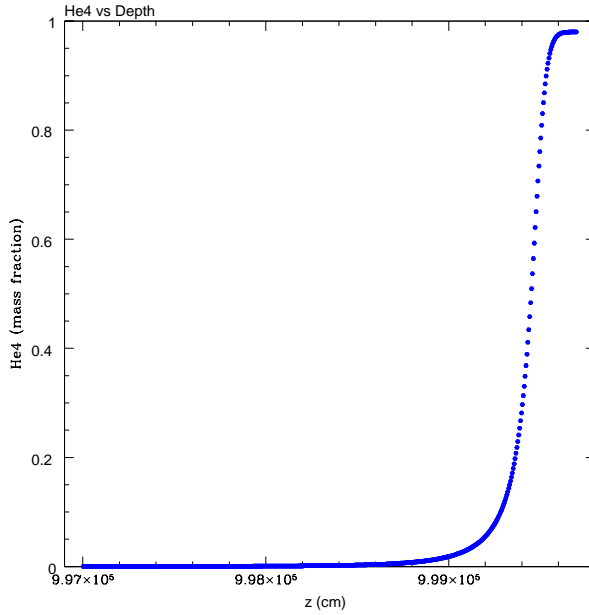


FIGURE 3.5. Raw Initial Conditions:  $\log \frac{4}{2}He$  vs. Depth  
The entire 2700 cm domain is plotted.

**3.1.2. Phase 2: Pre-Burst Initial Conditions.** After the vertical structure of the neutron star is generated in hydrostatic and thermal equilibrium from the stellar structure code, the raw initial conditions are inputted as starting data into a diffusional-thermal code. This code is identical to the full hydrodynamics code, but the hydrodynamic routines (and all supporting routines) are disabled. That is, the diffusional-thermal code includes only combustion ( $3\alpha$  reaction), thermal diffusion, and advection due to mass accretion, evolving Equations 2.16, 2.15, and 2.17. Since only one dimension is necessary, the diffusional-thermal code is 1D in the vertical direction. Hydrostatic equilibrium is re-calculated after every time-step. The boundary conditions are the same as those used in the full hydrodynamics code to maximize fidelity when the final data will be eventually transferred to and evolved by the full code. Also, the zone size is chosen to be the same as that of the intended hydrodynamical calculation which will use the initial conditions generated. While several different zone sizes were tested, the zone size found to be most practical in terms of calculation speed without compromising resolution is 5 cm zone<sup>-1</sup>.

The diffusional-thermal code is evolved through several complete burst events. At any stage during the evolution, data may be outputted to become the initial conditions for full hydrodynamical modeling. Depicted are the temporal evolution of the peak energy generation rate (Figure 3.6), temperature (Figure 3.7), nuclear flux (Figure 3.8), and total  $^4He$  (Figure 3.9) through twelve complete bursts.

Focusing on the second burst, see plots of the temporal evolution of the peak energy generation rate (Figure 3.10), temperature (Figure 3.11), nuclear flux (Figure 3.12), and total  $^4He$  (Figure 3.13). Also, the spatial distribution of energy generation rate (Figure 3.14), temperature (Figure 3.15), and  $^4He$  (Figure 3.16) at various times during the second burst are also plotted. Each burst exhibits the same qualitative behavior for peak energy generation rate and temperature, for instance, a peak energy generation rate of  $\sim 10^{18}$  erg g $^{-1}$ s $^{-1}$ , peak temperatures of  $\sim 10^9$  K, and the energy generation rate peaks a few tenths of a second before the temperature peaks. Moreover, the total amount of  $^4He$  oscillates as a function of time as expected, rising as fresh fuel is accreted, falling as it is consumed during each burst event. The flame front spreads out in both directions with slightly different propagation speeds. In the downward direction toward higher densities, it travels at roughly  $3 \times 10^2$  cm s $^{-1}$ , while upward toward the surface, it is about  $5 \times 10^2$  cm s $^{-1}$ .

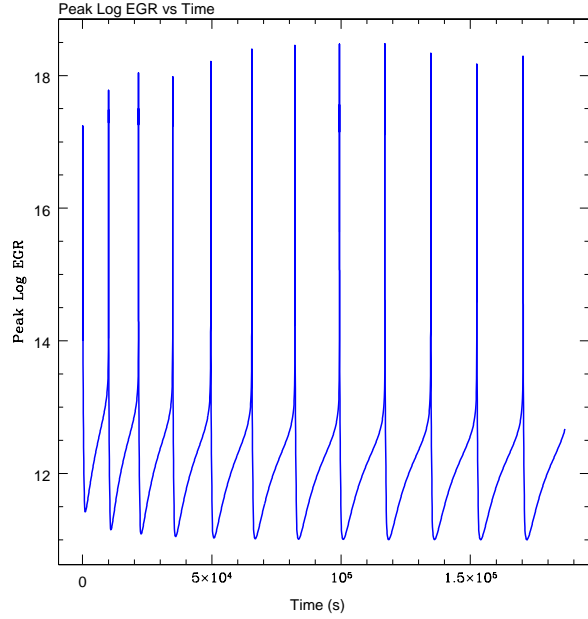


FIGURE 3.6. Twelve Bursts: Log Peak Energy Generation Rate vs. Time  
The diffusional-thermal code evolves through 12 bursts. The peak value of energy generation in the entire domain is plotted as a function of time.

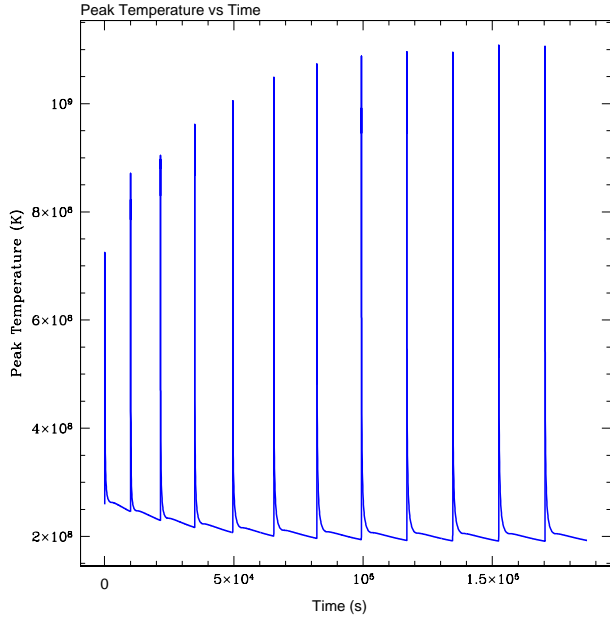


FIGURE 3.7. Twelve Bursts: Peak Temperature vs. Time  
The diffusional-thermal code evolves through 12 bursts. The peak value of temperature in the entire domain is plotted as a function of time.

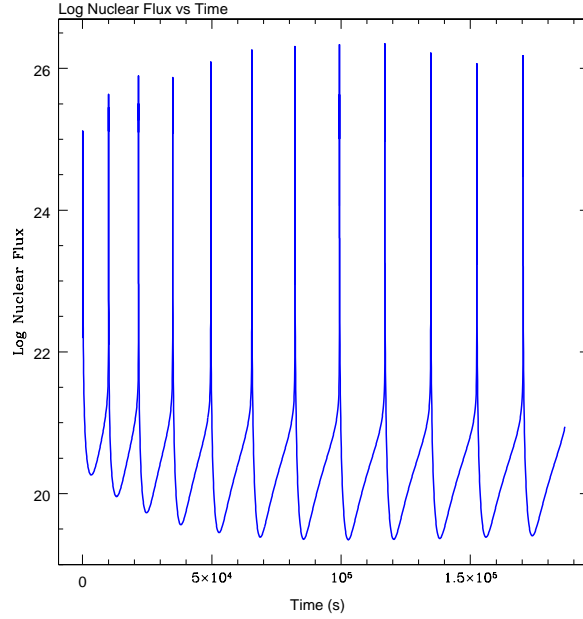


FIGURE 3.8. Twelve Bursts: Log Nuclear Flux vs. Time

The diffusional-thermal code evolves through 12 bursts. The value of nuclear flux in the entire domain is plotted as a function of time.

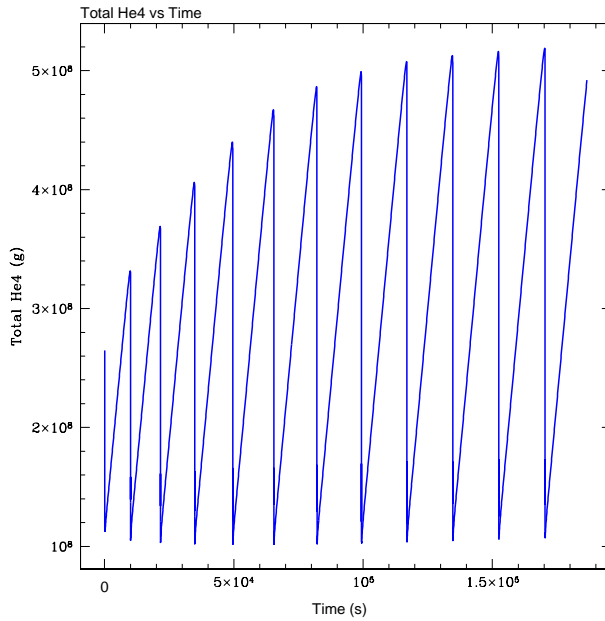


FIGURE 3.9. Twelve Bursts: Total  $^{4}_2He$  vs. Time

The diffusional-thermal code evolves through 12 bursts. The total value of  $^{4}_2He$  mass in the entire domain is plotted as a function of time.

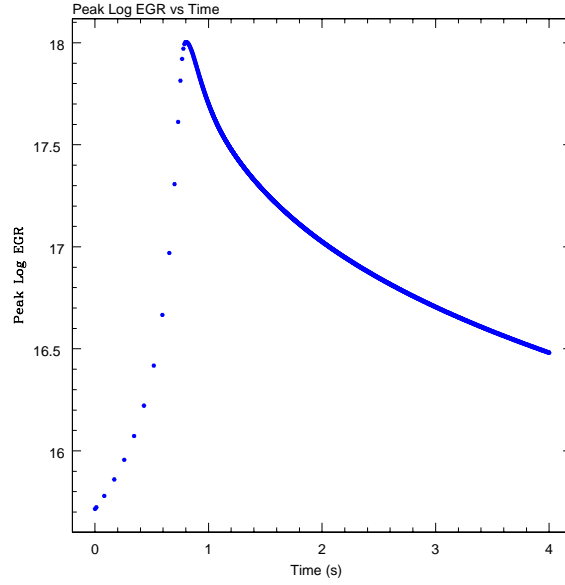


FIGURE 3.10. Second Burst: Log Peak Energy Generation Rate vs. Time  
The diffusional-thermal code evolves the second burst. The peak value of energy generation rate in the entire domain is plotted as a function of time.

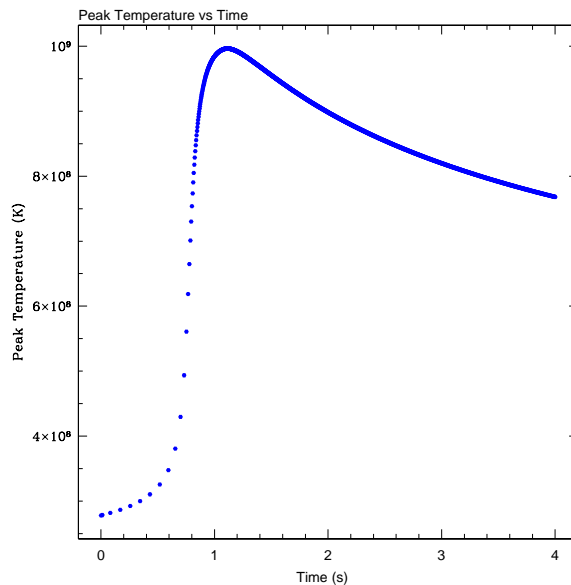


FIGURE 3.11. Second Burst: Peak Temperature vs. Time  
The diffusional-thermal code evolves the second burst. The peak value of temperature in the entire domain is plotted as a function of time.

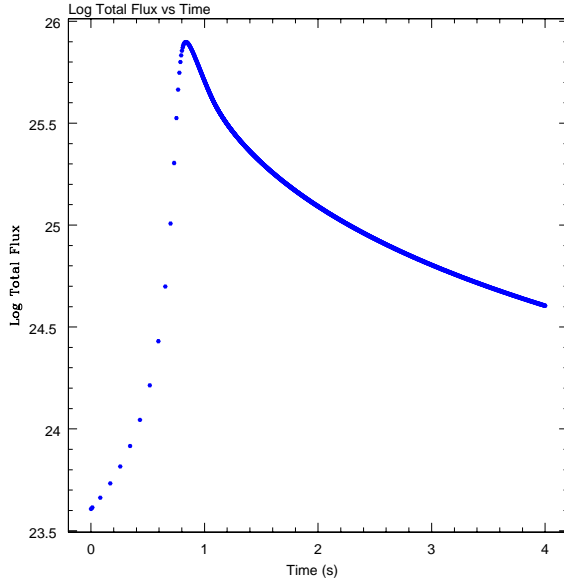


FIGURE 3.12. Second Burst: Log Nuclear Flux vs. Time  
The diffusional-thermal code evolves the second burst. The value of nuclear flux in the entire domain is plotted as a function of time.

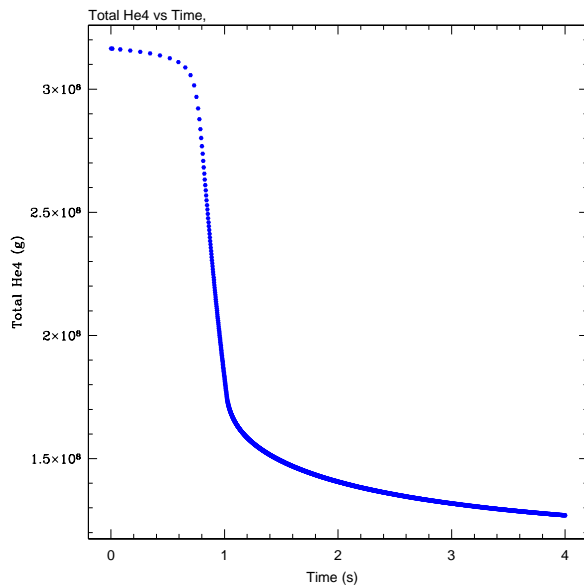


FIGURE 3.13. Second Burst: Total  $^{4}_2He$  vs. Time  
The diffusional-thermal code evolves the second burst. The total value of  $^{4}_2He$  mass in the entire domain is plotted as a function of time.

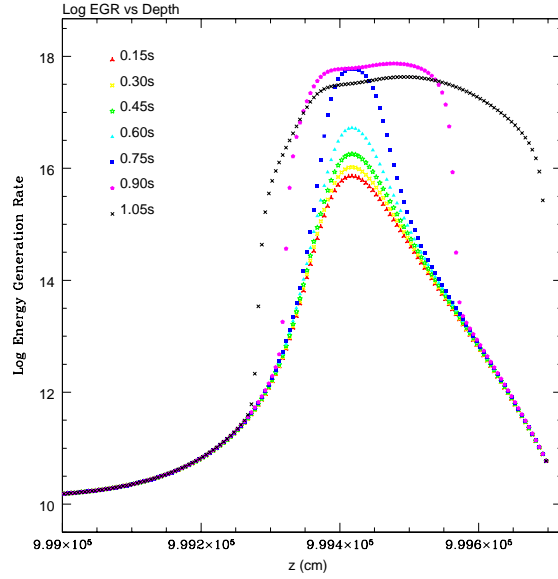


FIGURE 3.14. Second Burst: Log Energy Generation Rate vs Depth

For the second burst, the energy generation rate is plotted as a function of depth ( $t=10,340$ s plus values in legend). Only the upper 700 cm of the domain is plotted.

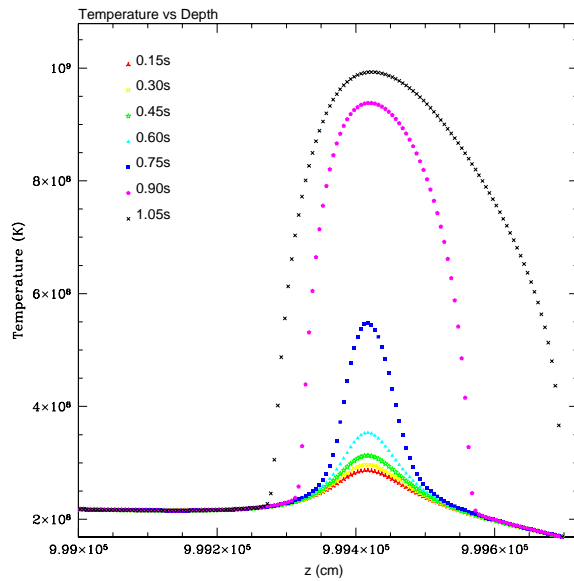


FIGURE 3.15. Second Burst: Temperature vs Depth

For the second burst, the temperature is plotted as a function of depth ( $t=10,340$ s plus values in legend). Only the upper 700 cm of the domain is plotted.

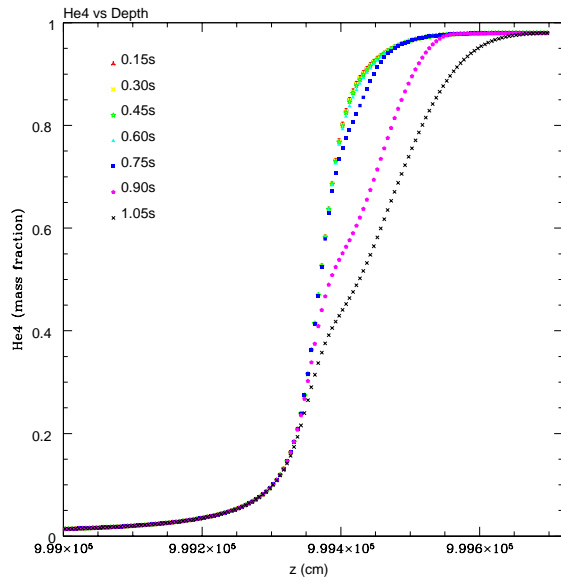


FIGURE 3.16. Second Burst:  ${}^4_2He$  vs Depth

For the second burst, the  ${}^4_2He$  mass fraction is plotted as a function of depth ( $t=10,340s$  plus values in legend). Only the upper 700 cm of the domain is plotted.

### 3.2. 1D Hydrodynamical Models

In 1D, the hydrodynamical equations simplify to be:

$$(3.5) \quad \frac{\partial X_l}{\partial t} = -w \frac{\partial X_l}{\partial z} + R_l$$

$$(3.6) \quad \frac{\partial T}{\partial t} = -w \frac{\partial T}{\partial z} + \frac{1}{c_p} \left\{ \dot{s} - \frac{\delta}{\rho} w \rho_h g + \frac{1}{\rho} \frac{\partial}{\partial z} \left( \kappa \frac{\partial T}{\partial z} \right) \right\}$$

$$(3.7) \quad \begin{aligned} \rho &\Leftarrow EOS(T, P_h, X_l) \\ e &\Leftarrow EOS(T, P_h, X_l) \end{aligned}$$

$$(3.8) \quad \frac{\partial^2 \phi}{\partial z^2} = \frac{\partial^2 \rho}{\partial t^2} - \frac{\partial^2 (\rho w w)}{\partial z^2}$$

$$(3.9) \quad \frac{\partial(\rho w)}{\partial t} = -\frac{\partial(\rho w w)}{\partial z} - \frac{\partial \phi}{\partial z}$$

where  $\phi \equiv P' \pm gK$ , as before. Notice that besides its inclusion in the function  $\phi$ , the special density function  $K$  plays no role in the 1D model, since the lateral dimensions do not exist. Thus, the advantage of using the  $K$  function becomes immediately apparent in 1D, as it helps to completely eliminate operations dealing with otherwise large-valued terms in the elliptic and momentum equations. As will be demonstrated, this advantage results in significantly more stable results as compared to a model which does not utilize the  $K$  density function.

**3.2.1. 1D Hydrodynamics with the K Formalism.** With pre-second burst initial conditions from the diffusional-thermal code, 1D hydrodynamical calculations are performed.

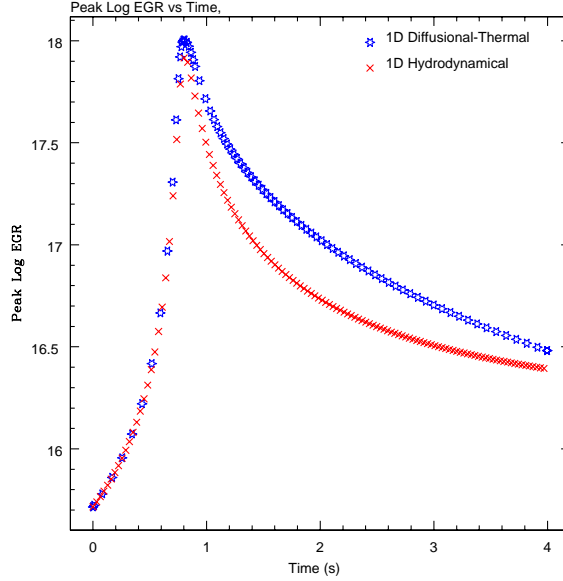


FIGURE 3.17. 1D Hydrodynamics: Log Peak Energy Generation Rate vs. Time  
The 1D hydrodynamics and the non-hydro results are compared. The peak value of energy generation rate in the entire domain is plotted as a function of time.

The total depth of the domain is 2700 cm (540 zones of 5 cm each). A fixed time-step of  $dt_{max} = 1 \times 10^{-6}$ s (which is always smaller than  $dt_{CFL}$ ,  $dt_{therm\,diff}$ , and  $dt_{burn}$ ) is used to facilitate regular intervals of data output. Standard boundary conditions are implemented: Dirichlet ( $\phi \equiv 0$ ) at the top boundary, and Neumann ( $\frac{\partial \phi}{\partial z} = 0$ , or HSE) at the bottom. The calculation is evolved for four seconds, completely through the second burst.

The following figures show the temporal evolution of the peak energy generation rate (Figure 3.17), temperature (Figure 3.18), nuclear flux (Figure 3.19), total  $^4_2He$  (Figure 3.20), and peak vertical velocity (Figure 3.21), where the diffusional-thermal results are also plotted for reference. The spatial distribution of energy generation rate (Figure 3.22), temperature (Figure 3.23),  $^4_2He$  (Figure 3.24), and vertical velocity (Figure 3.25) at various times during the second burst are also plotted, and the time intervals between different models correspond with those plotted for the diffusional-thermal plots previously presented in this chapter.

The peak vertical velocity is several times  $10^2$  to  $2 \times 10^3$  cm s $^{-1}$ , well below the sound speed ( $5 \times 10^8$  cm s $^{-1}$ ). The flow field is everywhere positive, flowing upward toward the

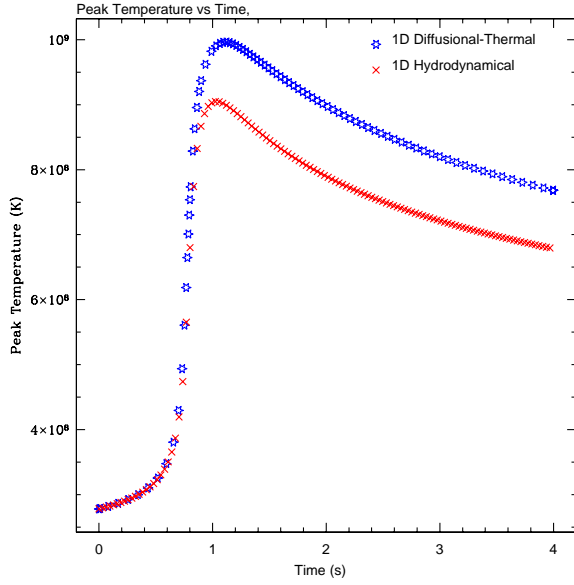


FIGURE 3.18. 1D Hydrodynamics: Peak Temperature vs. Time  
The 1D hydrodynamics and the non-hydro results are compared. The peak value of temperature in the entire domain is plotted as a function of time.

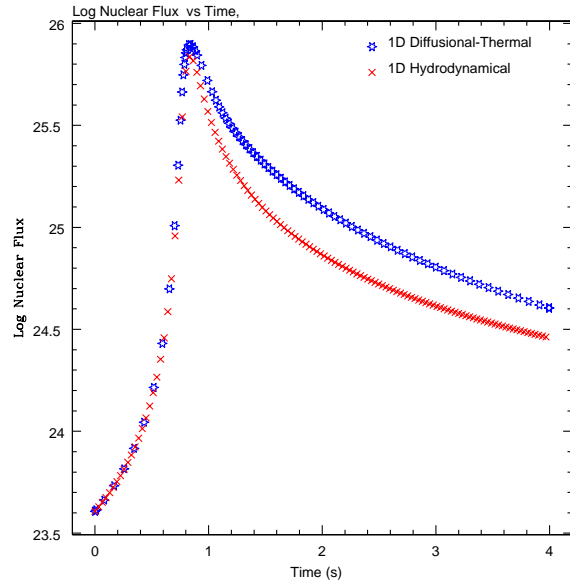


FIGURE 3.19. 1D Hydrodynamics: Log Nuclear Flux vs. Time  
The 1D hydrodynamics and the non-hydro results are compared. The nuclear flux in the entire domain is plotted as a function of time.

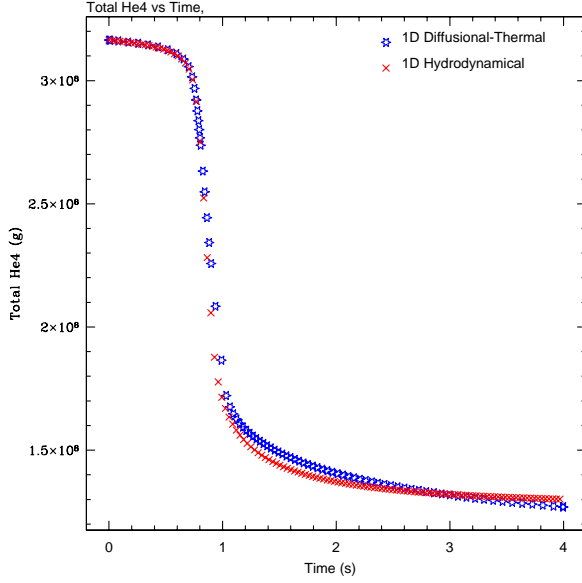


FIGURE 3.20. 1D Hydrodynamics: Total  $^{4}_2He$  vs. Time

The 1D hydrodynamics and the non-hydro results are compared. The total amount of  $^{4}_2He$  in the entire domain is plotted as a function of time.

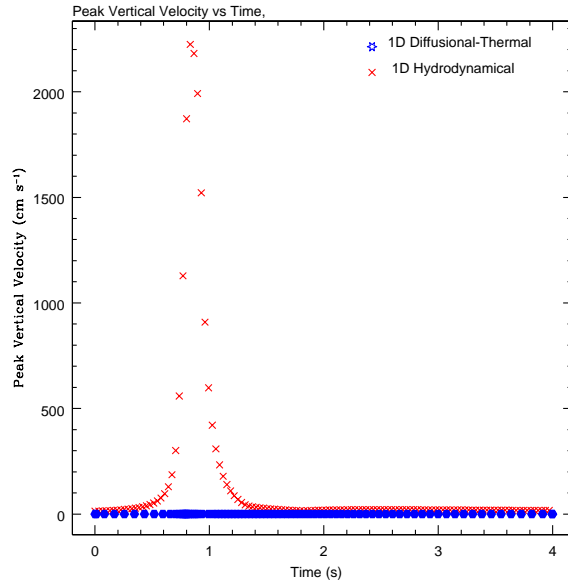


FIGURE 3.21. 1D Hydrodynamics: Vertical Velocity vs. Time

The 1D hydrodynamics and the non-hydro results are compared. The peak vertical velocity in the entire domain is plotted as a function of time.

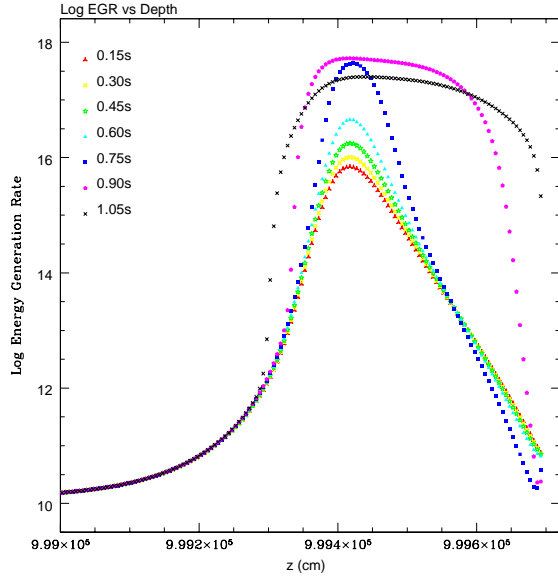


FIGURE 3.22. 1D Hydrodynamics: Log Energy Generation Rate vs Depth  
For the second burst, the energy generation rate is plotted as a function of depth for nine representative times. Only the upper 700 cm of the domain is plotted.

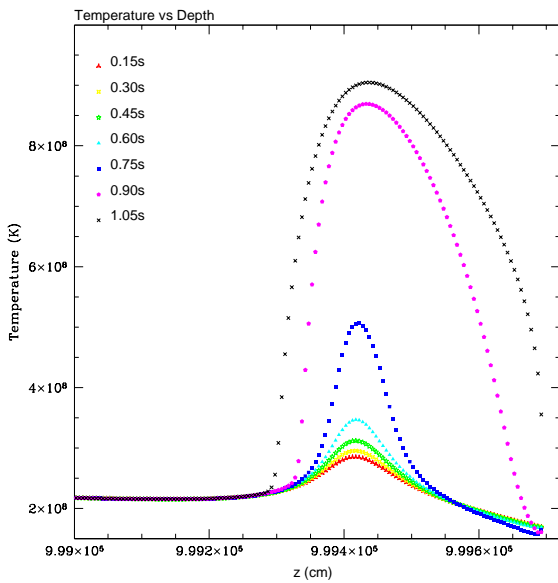


FIGURE 3.23. 1D Hydrodynamics: Temperature vs Depth  
For the second burst, the temperature is plotted as a function of depth for nine representative times. Only the upper 700 cm of the domain is plotted.

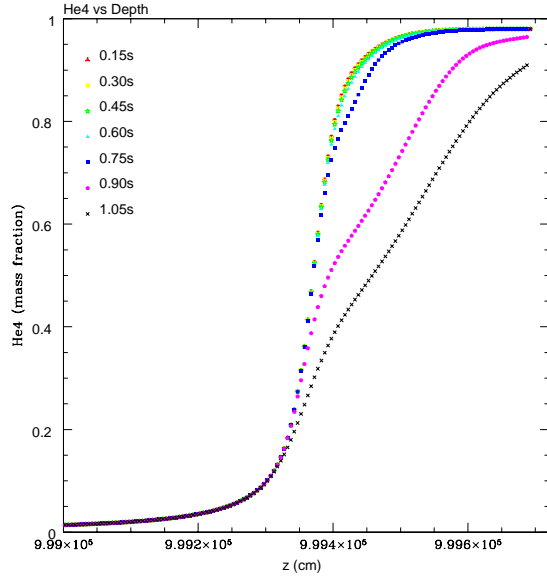


FIGURE 3.24. 1D Hydrodynamics:  ${}^4_2He$  vs Depth

For the second burst, the  ${}^4_2He$  mass fraction is plotted as a function of depth for nine representative times. Only the upper 700 cm of the domain is plotted.

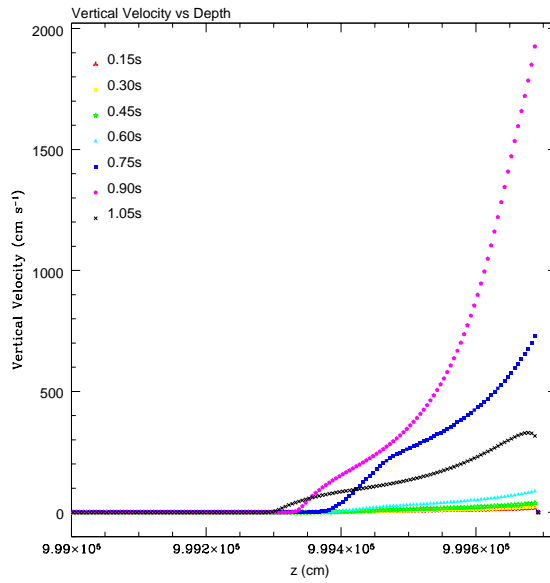


FIGURE 3.25. 1D Hydrodynamics: Vertical Velocity vs Depth

For the second burst, the vertical velocity is plotted as a function of depth for nine representative times. Only the upper 700 cm of the domain is plotted.

surface of the star. The advection caused by the flow introduces an additional cooling term, and consequently, the peak energy generation rate, temperature, and nuclear flux are less at a given time during the burst than they are in the diffusional-thermal model. The flame front moves at about  $3 \times 10^2$  cm s $^{-1}$  downward and  $1 \times 10^3$  cm s $^{-1}$  upward, showing that the flame front experiences a significant upward push by the hydrodynamical flows. Once the front reaches the upper boundary, the velocity there grows unreasonably large, perhaps due to unsatisfactory boundary conditions on the velocity. In the momentum equation, the updated velocity is inversely proportional to the density. As the high temperature flame front reaches the upper boundary and depresses the density in order to keep the pressure fixed, the velocity may become artificially augmented as a result. (See Section B.5 in Appendix B for details regarding how the momentum equation is evolved.) However, after the front moves through the upper boundary, the velocities moderate, and the calculation proceeds.

While not used for the calculation,  $gK$  (Figure 3.26) and  $P'$  (Figure 3.27) are plotted as a function of depth for nine time steps. In this calculation, the  $K_{top-down}$  formalism is used (See Appendix C), and thus the value of  $K$  at the upper boundary is identically equal to zero.  $P'$  is also defined to be zero at the upper boundary.

In summary, the hydrodynamical 1D results using the  $K$  formalism are well-behaved, noise-free, and physically reasonable, with the exception of a temporary, somewhat artificial increase in velocity at the upper boundary when the flame front passes through it. In contrast, exactly the same initial conditions are next evolved without using the  $K$  function, and the results will be noticeably worse in some respects.

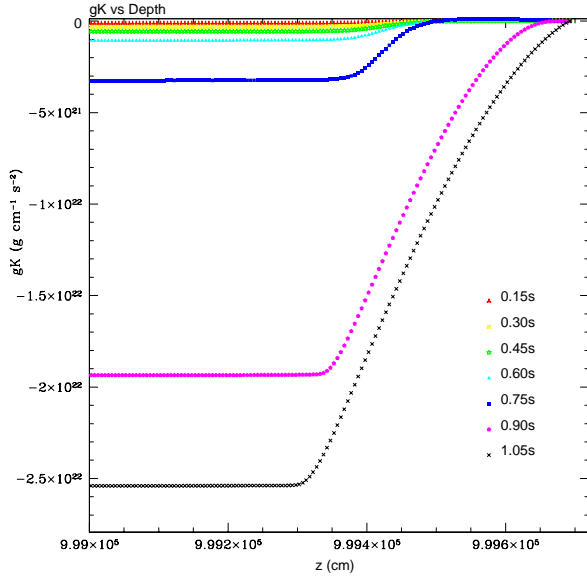


FIGURE 3.26. 1D Hydrodynamics:  $gK$  vs Depth

For the second burst, the quantity  $gK$  is plotted as a function of depth for nine representative times. Only the upper 700 cm of the domain is plotted.

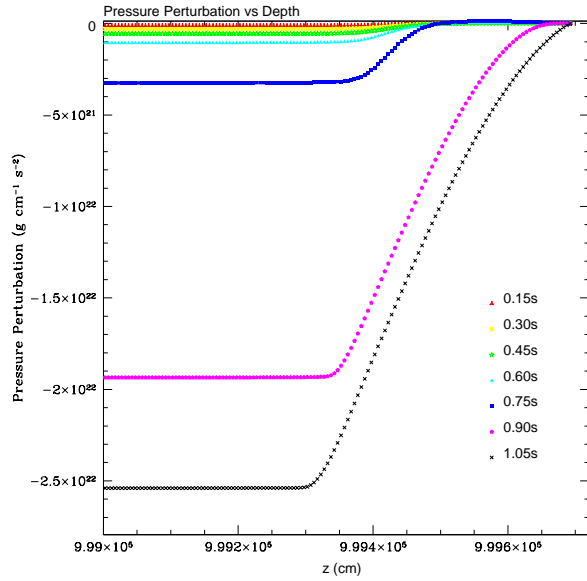


FIGURE 3.27. 1D Hydrodynamics:  $P'$  vs Depth

For the second burst,  $P'$  is plotted as a function of depth for nine representative times. Only the upper 700 cm of the domain is plotted.

**3.2.2. 1D Hydrodynamics without the K Formalism.** Without the  $K$  formalism (hereafter referred to as the “ $No - K$ ” formalism or model), the elliptic and momentum equations are:

$$(3.10) \quad \frac{\partial^2 P'}{\partial z^2} = \frac{\partial^2 \rho}{\partial t^2} - \frac{\partial^2(\rho w w)}{\partial z^2} - \frac{\partial(\rho' g)}{\partial z}$$

$$(3.11) \quad \frac{\partial(\rho w)}{\partial t} = -\frac{\partial(\rho w w)}{\partial z} - \frac{\partial P'}{\partial z} - \rho' g$$

Also, the boundary conditions must be consistently adjusted to suit these expressions. The Dirichlet condition is still used at the upper boundary, where  $P' \equiv 0$ , and the Neumann condition at the bottom boundary is hydrostatic equilibrium ( $\frac{\partial P'}{\partial z} + \rho' g = 0$ ). Everything else in the code is identical to those of the previous calculation using the  $K$  formalism.

The following results of the  $No - K$  calculation show the temporal evolution of the peak energy generation rate (Figure 3.28), temperature (Figure 3.29), nuclear flux (Figure 3.30), total  ${}^4_2He$  (Figure 3.31) in the domain, and peak vertical velocity (Figure 3.32), where the  $K$  formalism results are also plotted for reference. (The  $No - K$  results appear noisy and wildly oscillating after burst peak.) Also, the spatial distribution of energy generation rate (Figure 3.33), temperature (Figure 3.34),  ${}^4_2He$  (Figure 3.35), and vertical velocity (Figure 3.36) at various times during the second burst are also plotted, and the time intervals between different models correspond with those of the results from the  $K$ -formalism calculation.

The results indicate that while the qualitative features (such as the energetics) of the burst as evolved by the  $No - K$  model are qualitatively similar to those obtained from the  $K$  model, notable differences in the details are quite apparent. For instance, the velocity profile is very noisy and of much greater magnitude with the  $No - K$  model. The velocity is indeed where deficiencies of the  $No - K$  formalism would become most obvious, because it is in the momentum equation (Equation 3.11) where the summation of two large terms ( $\frac{\partial P'}{\partial z}$

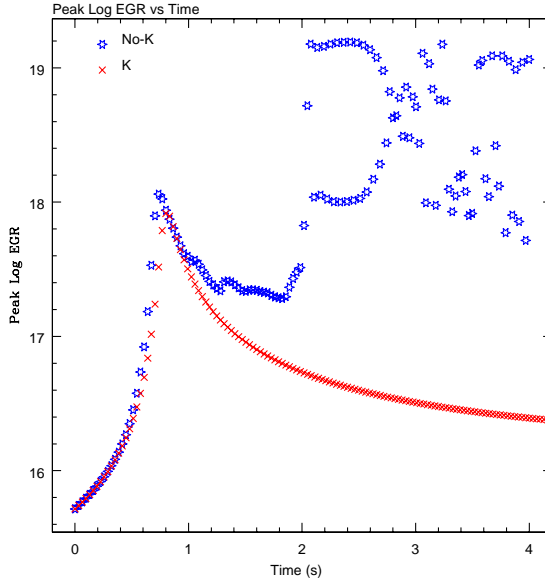


FIGURE 3.28. 1D  $No - K$ : Log Peak Energy Generation Rate vs. Time  
The 1D  $No - K$  and  $K$  results are compared. The peak value of energy generation rate in the entire domain is plotted as a function of time.

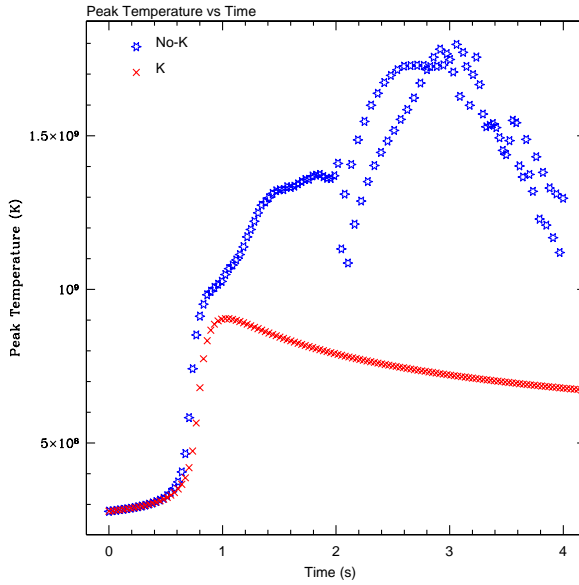


FIGURE 3.29. 1D  $No - K$ : Peak Temperature vs. Time  
The 1D  $No - K$  and  $K$  results are compared. The peak value of temperature in the entire domain is plotted as a function of time.

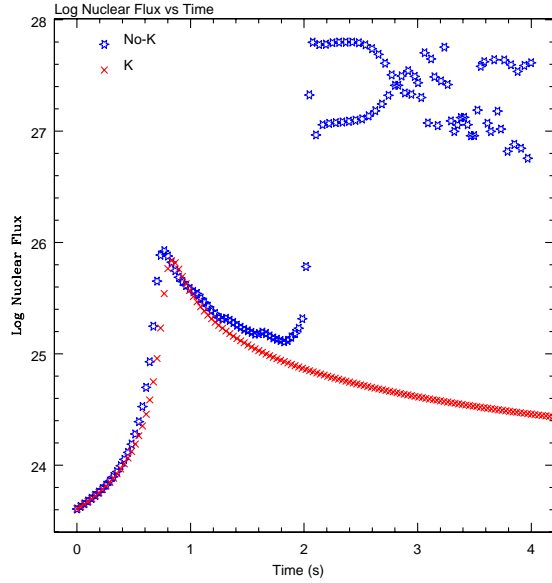


FIGURE 3.30. 1D  $No - K$ : Log Nuclear Flux vs. Time

The 1D  $No - K$  and  $K$  results are compared. The nuclear flux in the entire domain is plotted as a function of time.

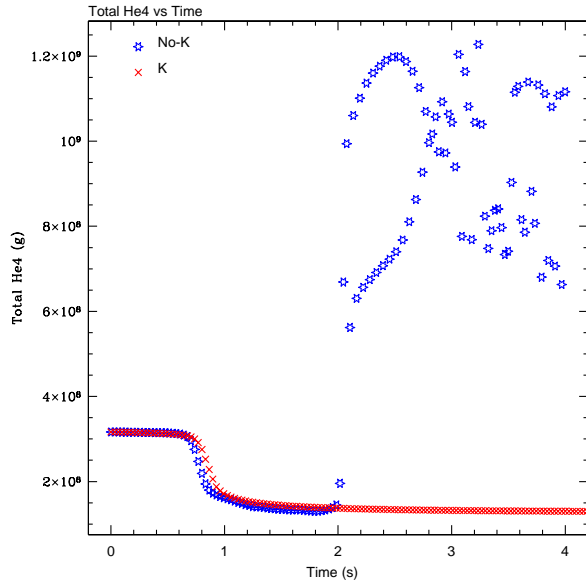


FIGURE 3.31. 1D  $No - K$ : Total  ${}_2^4He$  vs. Time

The 1D  $No - K$  and  $K$  results are compared. The total amount of  ${}_2^4He$  in the entire domain is plotted as a function of time.

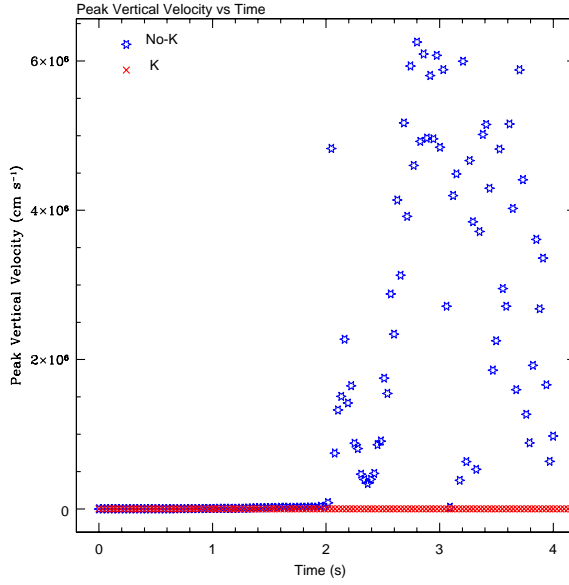


FIGURE 3.32. 1D *No – K*: Vertical Velocity vs. Time

The 1D *No – K* and *K* results are compared. The peak vertical velocity in the entire domain is plotted as a function of time. Note the magnitude of the velocities for the *K* model are insignificant on the scale of the this plot.

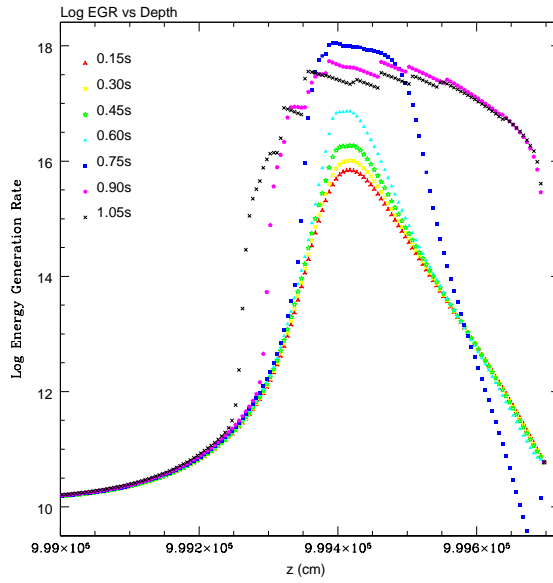
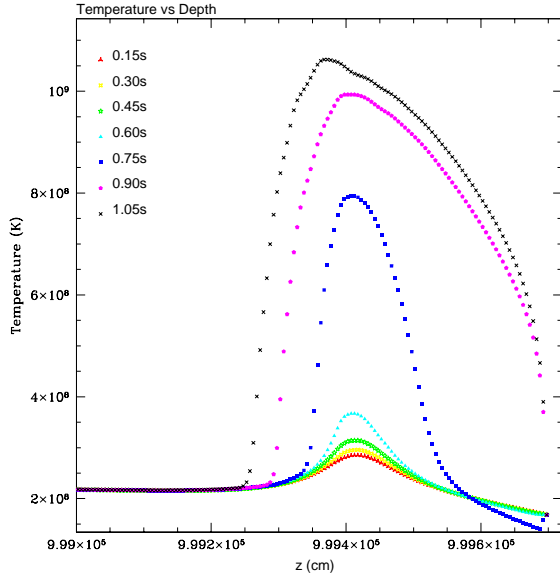
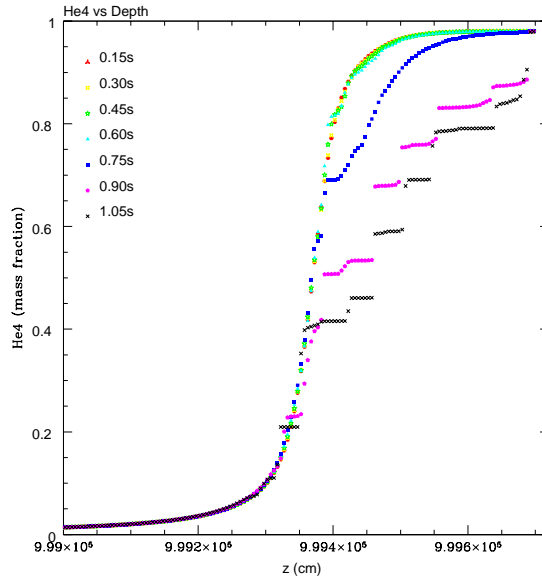


FIGURE 3.33. 1D *No – K*: Log Energy Generation Rate vs Depth

For the second burst, the energy generation rate is plotted as a function of depth for nine representative times. Only the upper 700 cm of the domain is plotted.

FIGURE 3.34. 1D  $No - K$ : Temperature vs Depth

For the second burst, the temperature is plotted as a function of depth for nine representative times. Only the upper 700 cm of the domain is plotted.

FIGURE 3.35. 1D  $No - K$ :  ${}^4_2He$  vs Depth

For the second burst, the  ${}^4_2He$  mass fraction is plotted as a function of depth for nine representative times. Only the upper 700 cm of the domain is plotted.

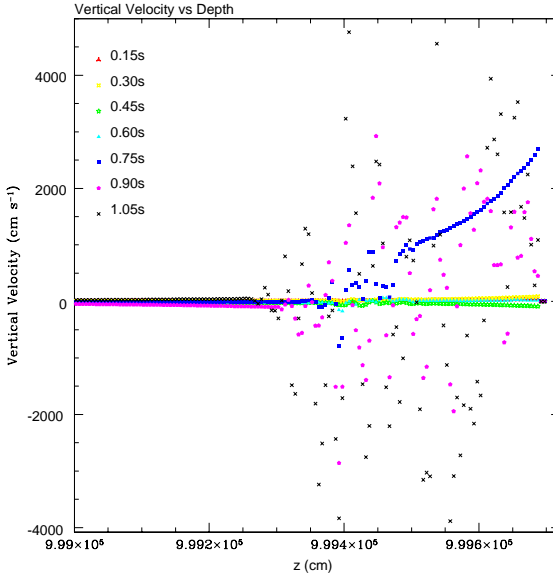


FIGURE 3.36. 1D  $No - K$ : Vertical Velocity vs Depth

For the second burst, the vertical velocity is plotted as a function of depth for nine representative times. Only the upper 700 cm of the domain is plotted.

and  $\rho'g$ ) occurs. These two terms are subsumed into a single term  $\phi$  in the  $K$  formalism, eliminating the need for such summations, and hence, sources of error.

To illustrate, five key quantities are compared at different times ( $1 \mu\text{s}$ ,  $5 \mu\text{s}$ ,  $15 \mu\text{s}$ , and  $0.15 \text{ s}$ ) for the two methods:  $P'$  (Figure 3.37), the force (Figure 3.38),  $\frac{\partial P'}{\partial z}$  (Figure 3.39),  $\rho'g$  (Figure 3.40), and the vertical velocity (Figure 3.41). First, consider  $P'$ . Because the two methods are solving the same fundamental problem,  $P'$  for both models should be identical at very early times. While  $P'$  is immediately available in the  $No - K$  model, it must be reconstructed in the  $K$  model from the definition  $\phi \equiv P' - gK_{top-down}$ . Indeed, as Figure 3.37 shows,  $P'$  for both models are in excellent agreement for all times. The agreement becomes noticeably worse by  $0.15 \text{ s}$ , due to diverging evolution at later times.

Next, consider the force. In the  $No - K$  model, the force is the sum  $\frac{\partial P'}{\partial z} + \rho'g$ , while in the  $K$  model, it is simply  $\frac{\partial \phi}{\partial z}$ . At the first time step, the force is identical for both models. However, even by the fifth step, noticeable departures become evident, worsening as the calculation proceeds. By  $0.15 \text{ s}$ , the difference in force is non-trivial, and its effects on the

vertical velocity are unmistakable. Examining the two terms  $\frac{\partial P'}{\partial z}$  and  $\rho'g$  which make up the force reveals that both have magnitudes on the order of  $10^{12}$  to  $10^{13}$  at early times, rising up to  $10^{18}$  by 0.15 s. The differences between these terms are on the order of  $10^{-6}$  to  $10^{-7}$  of the parent magnitudes, reflected in the value of the force. By 0.15 s, whereas the force remains on the order  $10^8$  in the  $K$  method, it is over three orders of magnitudes greater in the  $No - K$  method. This suggests that the limit of accuracy for the summation of these large quantities never exceeds one part in  $10^6$  or  $10^7$ . Note that  $\frac{\partial P'}{\partial z}$  and  $\rho'g$  show considerable agreement for both methods at all times ( $\frac{\partial P'}{\partial z}$  for the  $K$  model is numerically calculated from the reconstituted  $P'$  profile), so the apparent divergence in force must be due to a numerical error originating from the imperfect summation of  $\frac{\partial P'}{\partial z}$  and  $\rho'g$  in the  $No - K$  model. Moreover, considerable noise develops in the force in the  $No - K$  model, which directly affects the smoothness of the the velocities. Altogether, these effects undermine the stability of the  $No - K$  calculation, and the advantage of utilizing the  $K$  formalism for solving the 1D hydrodynamical equations becomes evident.

Despite the the significant differences in force and velocity on the small scale, the time evolution of the peak energy generation rate, peak temperature, nuclear flux and  ${}^4_2He$  show fair agreement between the two models during the rise of the burst. Shortly after the burst peak (at about 2 s in Figures 3.28 to 3.32), the  $No - K$  model exhibits highly non-linear behavior in the time evolution of these quantities, producing oscillatory patterns which are bounded below and above by floors and ceilings which vary over a much longer timescale. Even though the plot is made of single-valued data, it somewhat resembles multi-valued bifurcation diagrams in chaotic systems. For now, this result is merely noted as a curiosity.

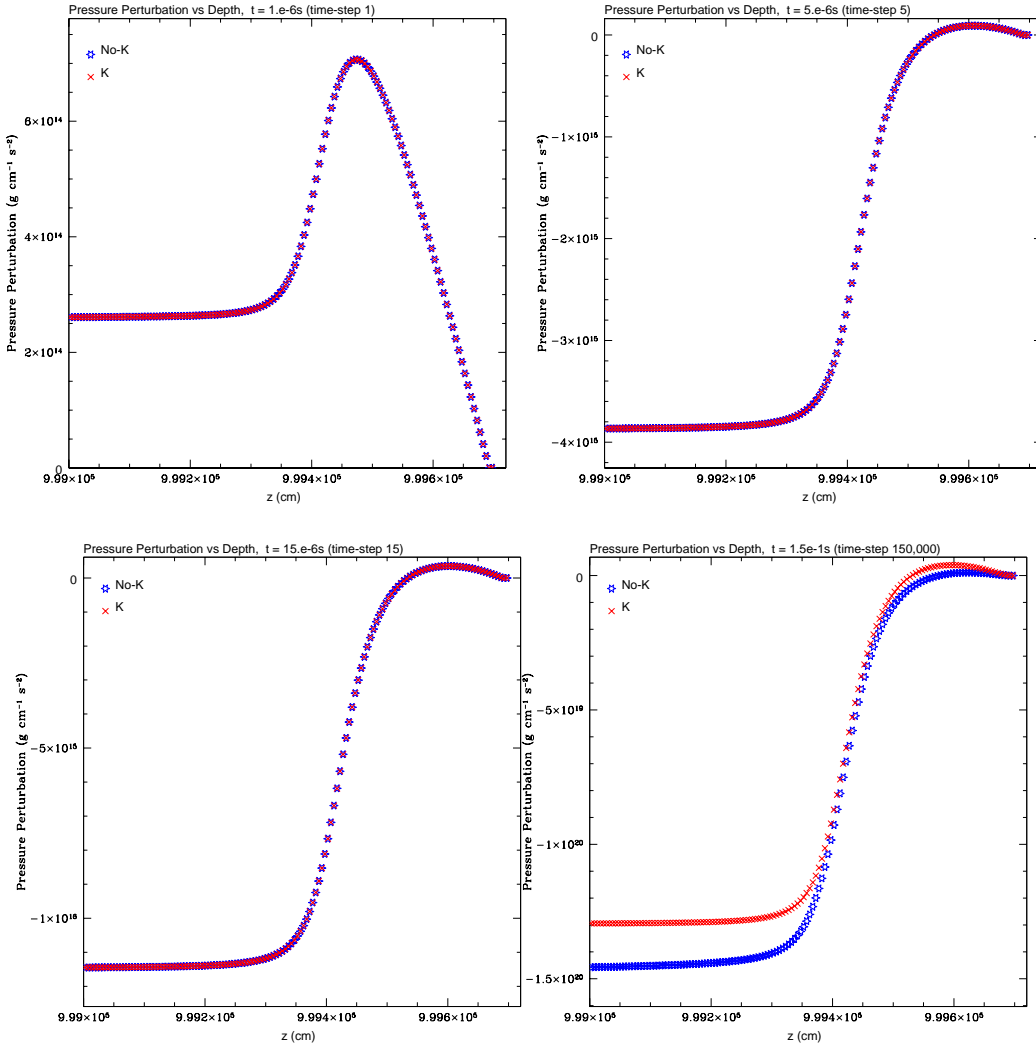


FIGURE 3.37. 1D  $K$  vs.  $No - K$ :  $P'$  vs Depth  
 $P'$  is compared for  $K$  and  $No - K$  at  $1 \mu\text{s}$ ,  $5 \mu\text{s}$ ,  $15 \mu\text{s}$ , and  $0.15$  s.

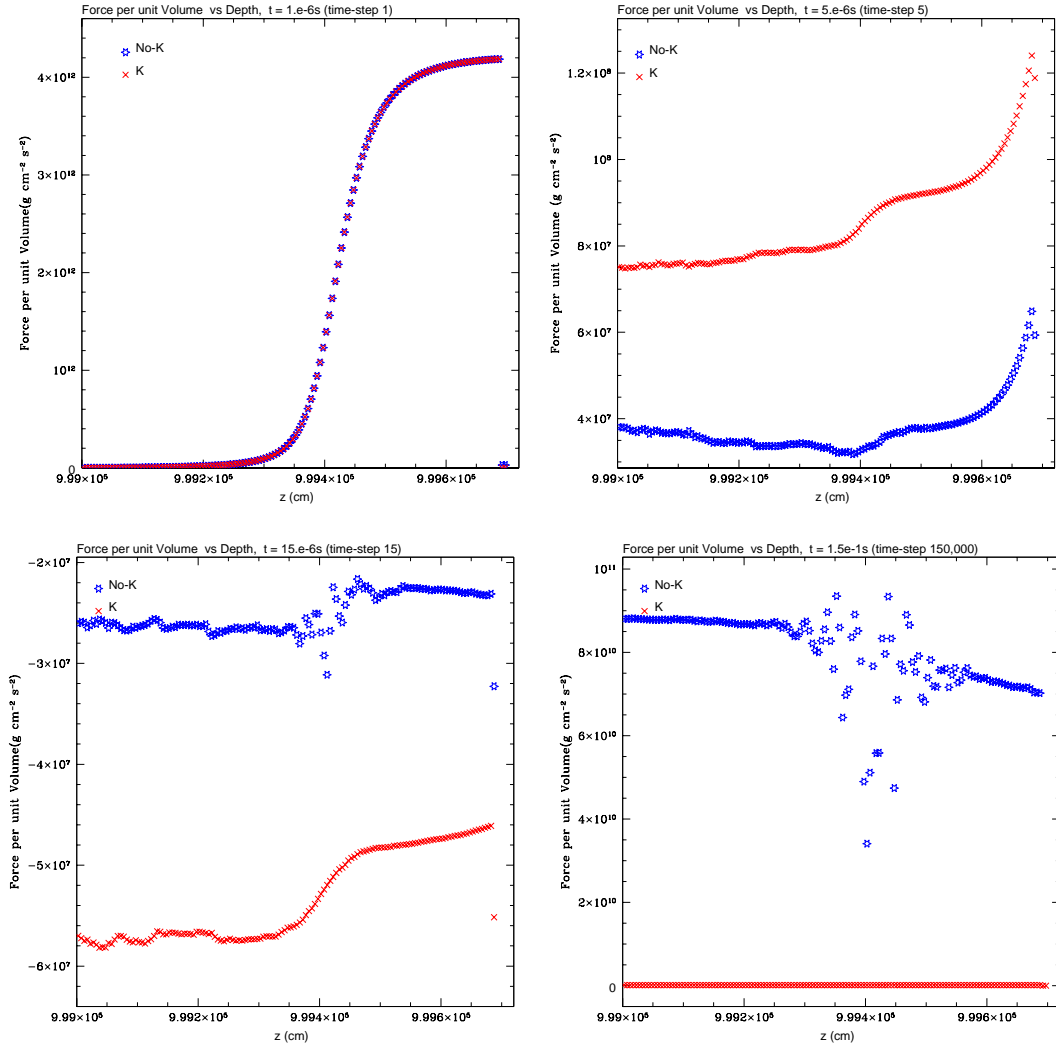


FIGURE 3.38. 1D *K* vs. *No-K*: Force vs Depth  
The force is compared for *K* and *No-K* at  $1 \mu\text{s}$ , and  $5 \mu\text{s}$ ,  $15 \mu\text{s}$ , and  $0.15 \text{s}$ .

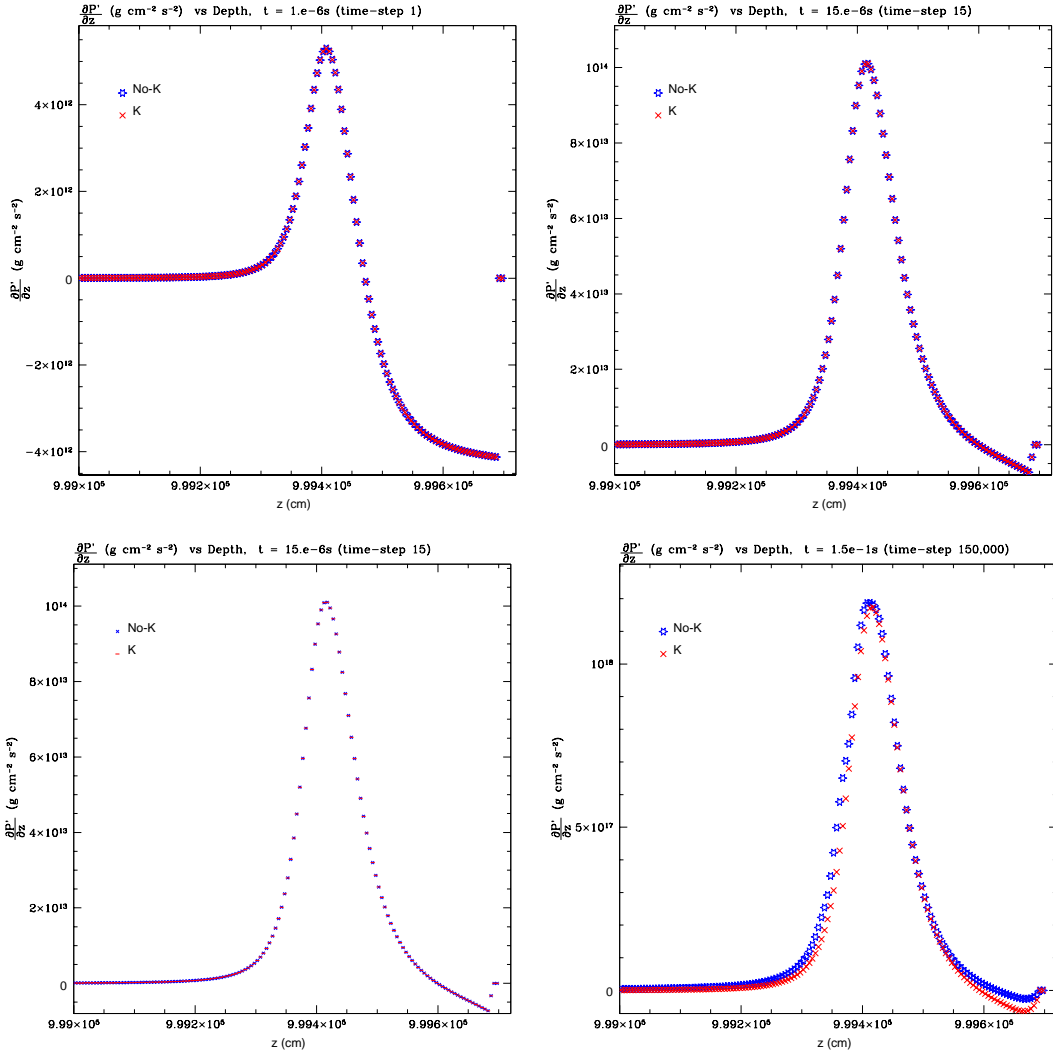


FIGURE 3.39. 1D  $K$  vs.  $No - K$ :  $\frac{\partial P'}{\partial z}$  vs Depth  
 $\frac{\partial P'}{\partial z}$  is compared for  $K$  and  $No - K$  at  $1 \mu s$ , and  $5 \mu s$ ,  $15 \mu s$ , and  $0.15$  s.

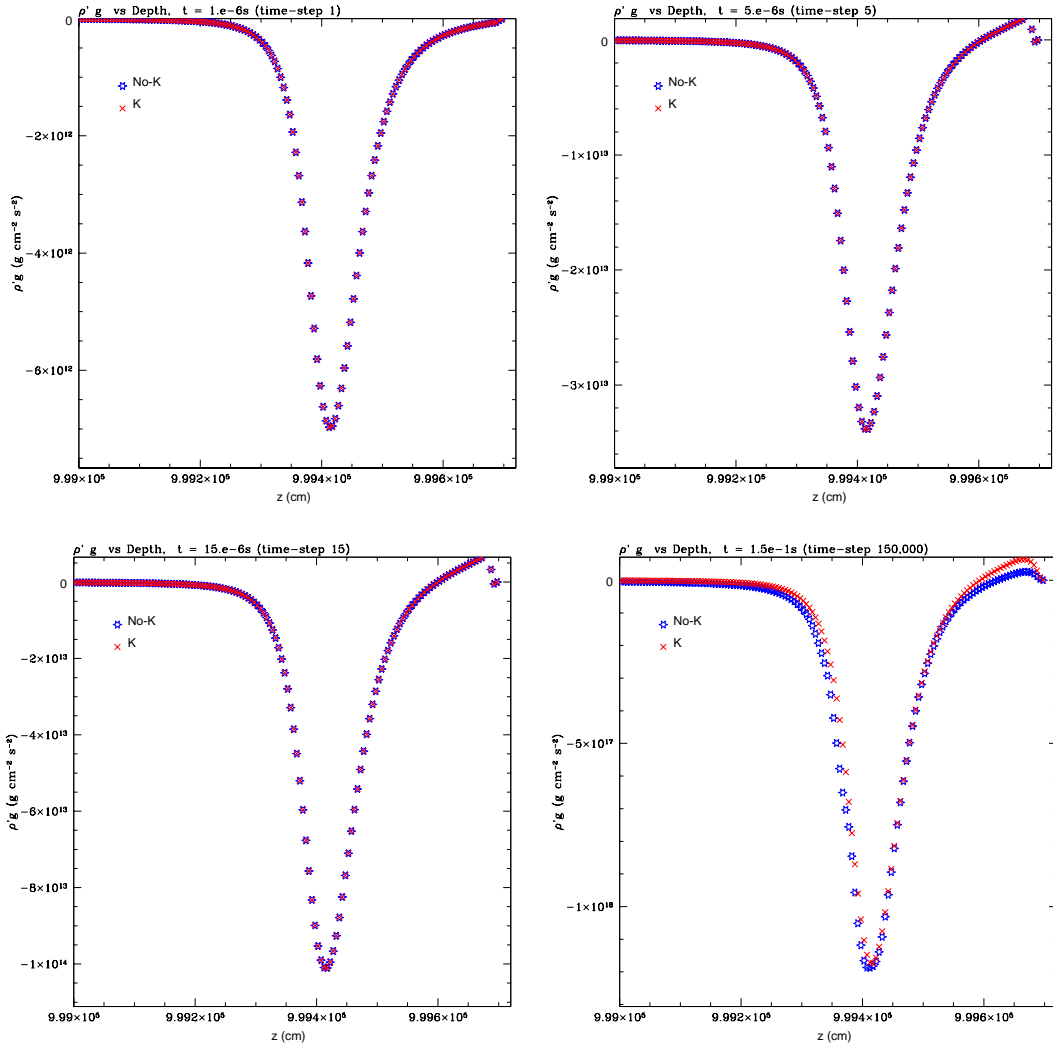


FIGURE 3.40. 1D  $K$  vs.  $No - K$ :  $\rho'g$  vs Depth  
 $\rho'g$  is compared for  $K$  and  $No - K$  at  $1 \mu\text{s}$ , and  $5 \mu\text{s}$ ,  $15 \mu\text{s}$ , and  $0.15 \text{ s}$ .

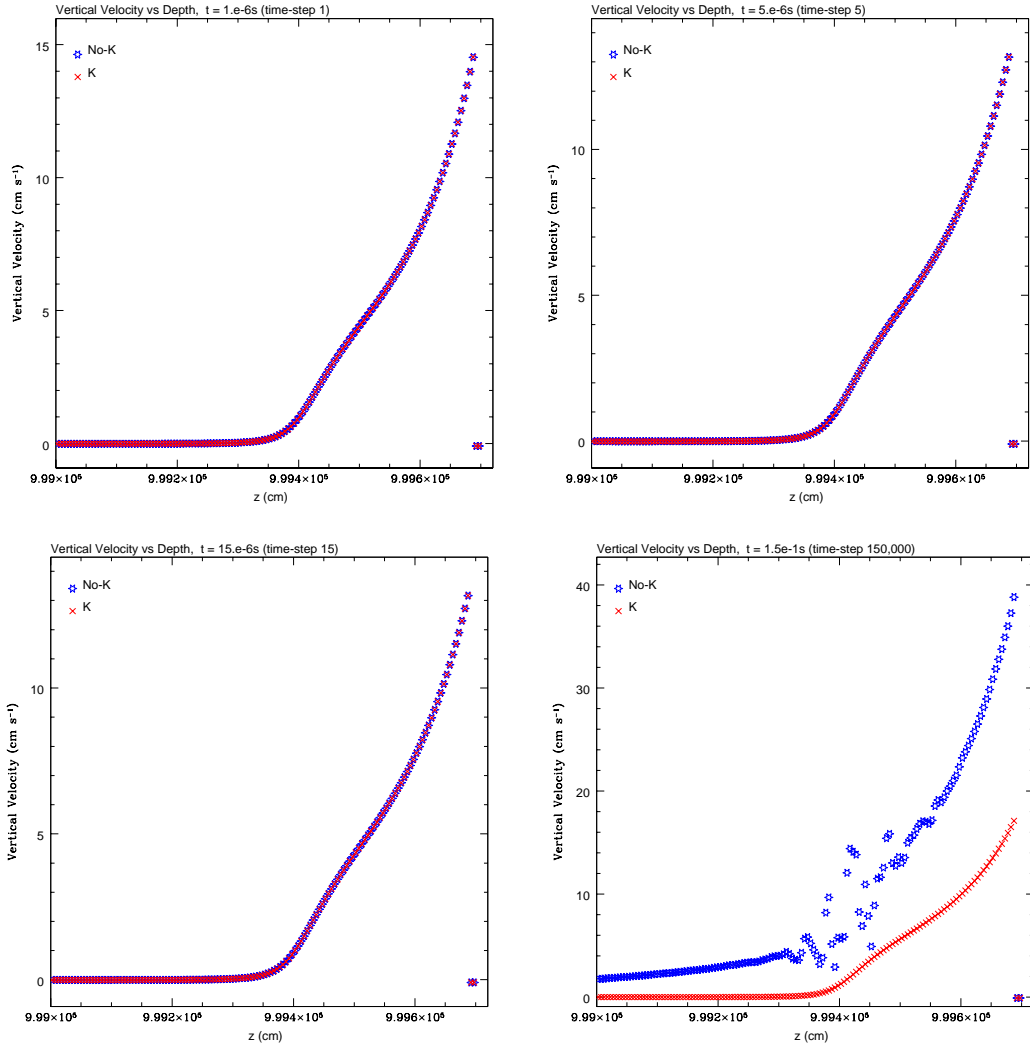


FIGURE 3.41. 1D  $K$  vs.  $No - K$ : Vertical Velocity vs Depth  
Vertical Velocity is compared for  $K$  and  $No - K$  at 1  $\mu$ s, and 5  $\mu$ s, 15  $\mu$ s, and 0.15 s.

### 3.3. 1D Summary

In 1D, initial models of the surface of neutron stars are constructed from stellar structure and diffusional-thermal codes. The completed initial models are used as initial conditions for 1D (and later, multidimensional) hydrodynamical calculations.

For the hydrodynamical models, both the straightforward  $No - K$  and special  $K$  formalisms are used. Without hydrodynamics, the burning front of a burst moves at about  $3 \times 10^2 \text{ cm}^{-1}$  downward toward the center of the star and  $5 \times 10^2 \text{ cm}^{-1}$  upward toward the surface. With hydrodynamics, the flow velocity is everywhere positive on the order of  $10^2$  to  $10^3 \text{ cm s}^{-1}$ , and it appears to help increase the upward moving part of the burning front to  $1 \times 10^3 \text{ cm s}^{-2}$ .

The  $No - K$  and  $K$  models are directly compared. While up to the burst peak, the two models yield qualitatively similar results, significant differences emerge post-burst. The differences are directly related to numerical inaccuracies in determining the force in the  $No - K$  model. This deficiency is eliminated by the  $K$  formalism, which yields considerably more stable results.

## CHAPTER 4

### 2D

#### 4.1. Introduction

The main results of this project are derived from the two-dimensional calculations performed with the LMNA model. Using a 5 cm zone<sup>-1</sup> model, the calculation covers 1.74 seconds of physical-time, beginning from a pre-convective stage, when the EGR is less than  $1 \times 10^{15}$  erg s<sup>-1</sup>g<sup>-1</sup>, through the onset of convection as the EGR steadily rises to a burst peak level of  $2 \times 10^{19}$  erg s<sup>-1</sup>g<sup>-1</sup>, and concluding a few tenths of a second past burst peak. To be presented in this chapter are the main qualitative and quantitative analyses of the calculation, including: an overview of the key features of the burst sequence; the time evolution of several important thermodynamic and velocity-related quantities; instantaneous snap-shots of velocity flow fields at representative EGR levels; velocity correlations and key thermodynamic gradients at these EGR levels; panels of figures showing dynamical and thermodynamical fluctuations covering a span of several convective crossing-times at each EGR level; evidence from tracer particle studies for convective over- and under-penetration during the later stages of the burst sequence; and evidence from modal analysis that convective-modes are necessary but not sufficient for elemental mixing at the borderline of the convective region.

To quantify the convective nature of the flow, adiabaticity is determined using key thermodynamic gradients (Kippenhahn and Weigert, 1990; Canuto, 2000): 1) the actual gradient,  $\nabla \equiv (\frac{d \ln T}{d \ln P})_{actual}$ ; 2) the adiabatic gradient,  $\nabla_{ad} \equiv (\frac{d \ln T}{d \ln P})_s$ ; and, 3) the Ledoux gradient,  $\nabla_L \equiv \nabla_{ad} + \frac{c_1}{c_2} \nabla_\mu$ , where  $\nabla_\mu \equiv (\frac{d \ln \mu}{d \ln P})$ , and  $c_1 \equiv \left(\frac{\partial \ln \rho}{\partial \ln \mu}\right)_{P,T}$ ,  $c_2 \equiv -\left(\frac{\partial \ln \rho}{\partial \ln T}\right)_{P,\mu}$ . The

Schwarzschild criteria for a convectively unstable region is  $\nabla > \nabla_{ad}$ , and regions characterized by this condition are considered to be superadiabatic, while convectively stable, subadiabatic regions occur where  $\nabla < \nabla_{ad}$ . For models involving weak composition gradients, the Schwarzschild criteria suffices to characterize a region's convective stability. However, the Ledoux criteria (where  $\nabla_L$  is replaced by  $\nabla_{ad}$  in the above definitions for superadiabaticity) becomes important where composition gradients are significant, as in certain regions of the present 2D domain.

Because convection is a multi-dimensional dynamic process, a minimum of two spatial dimensions are required to adequately demonstrate laminar convective cells, also known as Benard cells (Koschmieder, 1993). Even more complicated dynamics such as chaotic, turbulent convection requires three dimensions to be properly modeled, which is unfortunately beyond the scope of the present investigation, but extending the LMNA model into 3D is a straightforward extension of this project. Because the Reynolds number of a neutron star surface is expected to be well in the turbulent regime, convection most likely has a very turbulent nature there. As will be described in this chapter, the main qualitative features of the dynamical flow fields of the present 2D results are relatively large-scale, mostly symmetric, laminar flows resembling Benard cells. These results are expected, since the LMNA method solves the Euler equations, involving no explicit viscosity or turbulence model, and so in its present form, can not simulate truly turbulent processes. While numerical viscosity might be able to generate a pseudo-turbulent energy cascade, 2D calculations are inherently incomplete because the cascade of energy goes from small to large scales, exactly opposite what occurs in more realistic 3D turbulence (Khokhlov, 1994).

No claim is made that the results presented in this chapter suggest the flows on an actual neutron star surface are laminar in nature; indeed, they almost certainly are not. The focus of the qualitative studies is the large scale structures of the flow, not the small scales. On the other hand, the 2D results of the present calculations do show that the temperature gradient is always to a very high degree adiabatic and satisfying the Schwarzschild criteria

in the middle of the convectively unstable region, and the Ledoux criteria throughout, more obviously at the boundaries of the convectively unstable region. The quantitative aspects of convective energy transport may be more trustworthy than the qualitative features of the velocity flow fields. Code validation by zonal refinements is documented in Chapter 5.

## 4.2. Summary of 2D results

Detailed in this chapter are the main findings from the 2D calculations:

- heating due to energy generation during the X-ray burst generates convective dynamics in a vertically expanding, uniform layer across the entire width of the domain;
- during rise to burst peak, the latitude corresponding to the hottest burning layer remains the same ( $\sim 500$  cm) above the base of the domain;
- after  $\log \text{EGR} > 17$ , the upper boundary of the convective layer travels toward the surface of the star at roughly  $10^4 \text{ cm s}^{-1}$ , while the lower boundary moves downward at only  $10^2 \text{ cm s}^{-1}$ ;
- convective motions naturally develop in the bursting layer, and the maximum convective flow speeds throughout the entire burst sequence is on the order of  $10^7 \text{ cm s}^{-1}$ , so that  $M_{max} < 0.1$  always;
- on average, the convective layer is superadiabatic by a small margin (+0.01 before burst peak, +0.001 post burst peak) by the Schwarzschild criteria, while locally, both sub- and superadiabatic regions are present in the convectively unstable layer;
- significant local fluctuations in the temperature gradient and fractional differences in the thermodynamic variables occur on timescales less than the convective timescale;
- a temperature gradient more consistent with the Ledoux criteria is sustained at both of the convective boundaries due to less efficient mixing in these regions;
- extensive tracer particle analysis reveals penetration through the convective boundaries is temporary and limited in extent, with a tendency to favor the downward direction;

- modal analysis reveals the gradual transition from gravity- to convective modes near the convective boundaries where penetration occurs, and that convective-modes are a necessary but not sufficient condition for penetration; and,
- the predictions of mixing-length theory do not adequately describe the results.

Also, an examination and comparison of the behaviors of the 1D and 2D models' nuclear, radiative, and advective fluxes are presented in Section 6.2 of Chapter 6, which lead to important implications regarding how convective dynamics may affect the calculated light curves of X-ray bursts.

### 4.3. Initial Model

As with the 1D calculations described in the previous chapter, the initial model for the 2D calculations is prepared in two phases. First, raw initial conditions in hydrostatic and thermal equilibrium are generated from a stellar structure code to model the outer envelope of a neutron star. The mass accretion rate is  $\dot{m} = \frac{5 \times 10^{-9}}{4\pi R_{NS}^2} M_\odot \text{ yr}^{-1} \text{ cm}^{-2}$ , and the flux at the base of the model is a parameter chosen to be  $5 \times 10^{20} \text{ erg g}^{-1} \text{ s}^{-1}$ . This raw initial model is then evolved with a 1D diffusional-thermal code through several burst cycles. From this calculation, a set of pre-burst peak conditions is chosen to become the starting conditions of the 2D model. This 1D structure is reproduced across the width of the computational domain to create a laterally uniform 2D domain at  $t = 0$ . The reference base state ( $P_h$ ,  $T_h$ ,  $\rho_h$ ) for the 2D calculations is the raw, initial state which is in hydrostatic and thermal equilibrium.

Figure 4.1 shows the initial vertical profiles of  $Y$ ,  $\log \rho$ ,  $\log P$ ,  $T$ , and  $\log \text{EGR}$  for the 2D model. The vertical dimension consists of 200 zones and each zone is 5 cm in length. Thus, the domain represents a 1000 cm layer of the upper neutron star envelope, where the upper boundary of the computational domain is 500 cm from the actual surface of the neutron star. A temperature inversion and a very steep gradient in  $Y$  exists between  $z = 400$  and 600 cm, corresponding to where the central region of burst ignition is located. The domain extends

over one order of magnitude in  $\rho$  and nearly two orders of magnitude in  $P$  (4.5 pressure scale heights). At the start of the calculation, the peak value of  $T$  is  $2 \times 10^8$  K and the peak EGR is  $7 \times 10^{14}$  erg g<sup>-1</sup>s<sup>-1</sup>. During testing, velocity fields of various magnitudes were initially imposed as starting conditions on the flow, but subsequent dynamics were found to be insensitive to these initial conditions on the velocity; thus, the velocity field for the present calculation is initially zero.

To provide lateral inhomogeneity, a small, Gaussian perturbation in density is applied to the domain, such that the center of the perturbation is vertically positioned where the EGR is greatest, and which is laterally centered in the domain. The magnitude of the perturbation is Gaussian in nature, with a full-width-half-max of 50 cm in both lateral and vertical directions. The maximum value of the perturbation for the computations described in this chapter is a fractional difference of  $-1 \times 10^{-6}$  in density, which translates into a relative perturbation of  $+2 \times 10^{-5}$  in temperature. In other test-models, perturbations applied directly to composition and temperature were also tested, but all yielded essentially the same results after the magnitudes of the perturbations were appropriately scaled. Several magnitudes of perturbations were tested, and the overall features of the results were found to be generally independent of them, provided the perturbations were not so large (greater than a fractional difference of negative  $1 \times 10^{-2}$  in density or more) as to induce an unreasonably large change in the initial conditions. When no perturbation is applied to provide lateral inhomogeneity to the domain, the burst proceeds in a 1D mode, and the resulting dynamics exhibit a laterally uniform flow pattern devoid of 2D structure, such as convective cells. Thus, the purpose of the initial perturbation is merely to break the lateral symmetry of the starting conditions, allowing 2D dynamical motions to naturally develop.

#### 4.4. 2D Domains and Boundary Conditions

In the following chapter (Chapter 5), numerous validation tests are performed with various spatial and temporal resolutions, as well as different domain dimensions. These tests

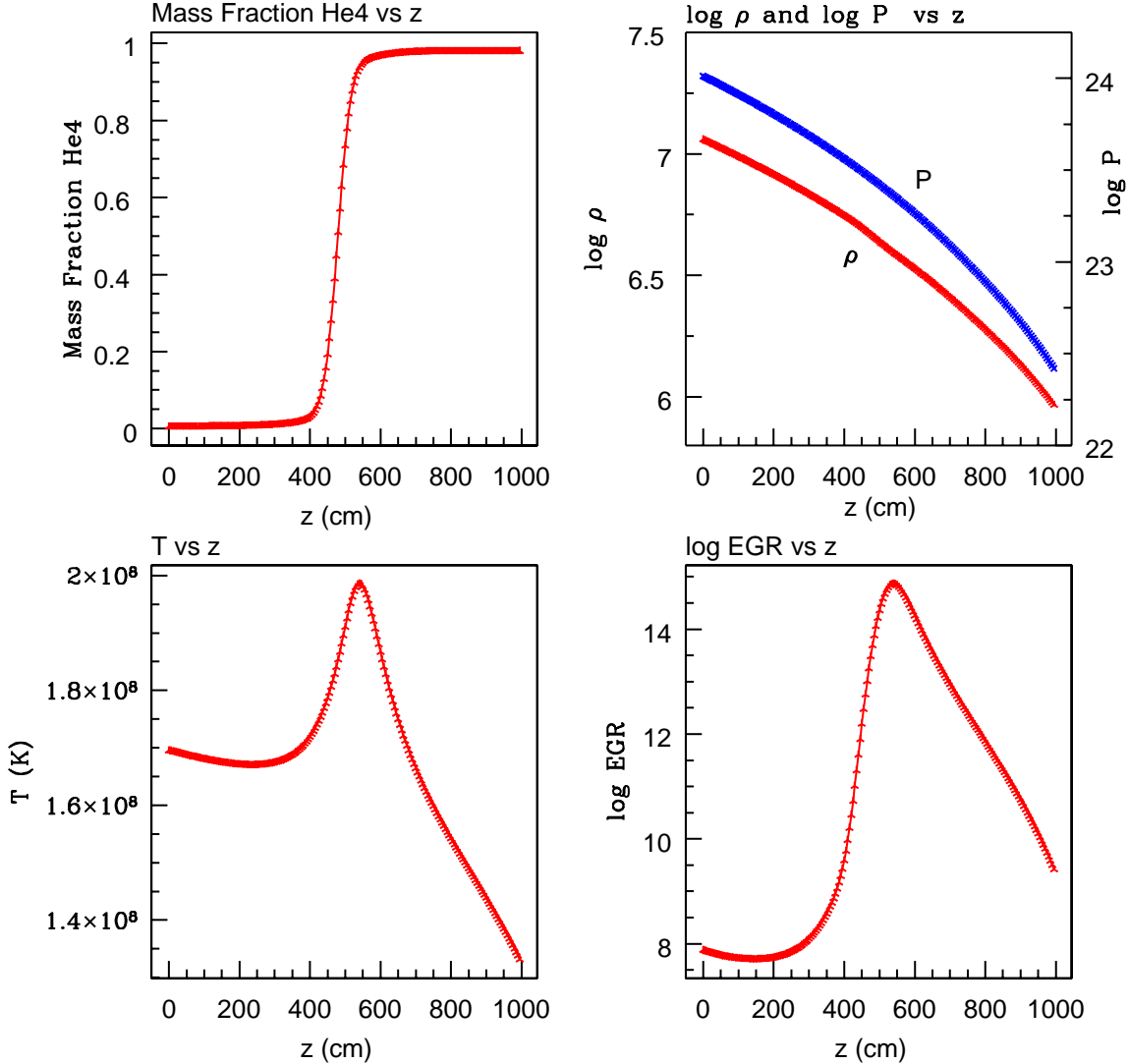


FIGURE 4.1. Initial Vertical Profiles of Thermodynamic Quantities  
 Initial values of mass fraction of  $He4$  (upper left),  $\log \rho$  and  $\log P$  (upper right),  $T$  (lower left), and  $\log EGR$  (lower right) as functions of height.  $5\text{ cm zone}^{-1}$  resolution.

demonstrate convergence and consistency of the results of the different models. Hence, the standard model used to generate the results in this chapter has a zone size of 5 cm, the smallest, practical zone size possible, given the available computational resources. For the 5 cm zone $^{-1}$  model, the 2D domain consists of a  $386 \times 200$  Cartesian grid of uniformly-sized zones, where the first value refers to the number of zones in the lateral ( $j$  or  $y$ ) direction,

and the second number, in the vertical ( $k$  or  $z$ ) direction. Being uniformly sized, each zone has an aspect ratio of 1:1 at all times. The main computational domain consists of a regularly spaced system of zones organized on a Cartesian coordinate system ( $j, k$ ), consisting of all the zones between the coordinates  $j, k = 2$ , and  $j = 385$  and  $k = 199$ . The rows and columns corresponding to  $j, k = 1$ , and  $j = 386, k = 200$  consist of guardcells which bound the main computational domain on all sides (upper, lower, left, right). The purpose of the guardcells is to facilitate the application of boundary conditions. (When the main domain is decomposed into sub-domains to be distributed among individual processors during parallel processing, intermediate guardcell layers also bound the sub-domains to provide continuity of communication of information between sub-domains. No boundary conditions are applied to these intermediate guardcell layers, but only to the guardcells at the most extreme edges of the main domain.)

The boundary conditions imposed on the main domain are as follows:

For the two lateral edges of the domain, the boundary conditions are straightforwardly periodic. All thermodynamic ( $\rho, T, X_l, \phi, K$ ) and velocity (lateral  $v$  and vertical  $w$  components, convective terms) quantities from the left-most, computational column ( $j = 2$ ) of the domain are copied to the guardcell column at the right edge ( $j = 386$ ), and from the right-most, computational column ( $j = 385$ ) to the guardcell column at the left edge ( $j = 1$ ). As will be discussed in more detail in the next chapter (Chapter 5), the domain needs to be sufficiently wide to accommodate the natural size of convective cells which develop. A domain width of 386 zones at a resolution of 5 cm zone<sup>-1</sup> is sufficient to contain numerous convective cells which form at all times throughout the burst sequence, and thus is considered sufficiently wide to prevent lateral boundary effects from influencing the results. The results of calculations using domains with different lateral sizes qualitatively agree.

For the vertical edges of the domain, the boundary conditions are more complicated. At the lower boundary ( $k = 1$ ), zero-gradient conditions are imposed on all thermodynamic quantities and the lateral component of velocity, while the vertical component of velocity and

all convective terms are set to zero for all times. For  $\phi \equiv P' - gK$ , the Neumann condition ( $\frac{\delta\phi}{\delta z} = 0$ ) is used in the elliptic solver. Note that this implementation of the Neumann condition is equivalent to imposing hydrostatic equilibrium at the lower boundary, implying no net force exists there. Thus, it is consistent to set the vertical component of velocity to be zero at the lower boundary, since the initial value there is zero.

The domain's lower edge is set sufficiently deep such that the regions near the lower boundary are always relatively calm ( $|\mathbf{v}| < 10^2 \text{ cm s}^{-1}$ ) compared to regions of the domain which are expected to be convectively unstable ( $|\mathbf{v}| > 10^6 \text{ cm s}^{-1}$ ). Also, extensive testing demonstrates that in order for the model to successfully evolve through a complete burst peak, the domain needs to have a certain minimum depth. Otherwise, a net upward flow evolves in the domain, effectively quenching the burst due to advection of nuclear fuel away from the regions having the highest temperatures. As long as the domain is deep enough, no net upward flow forms, and the burst proceeds to its peak. A domain depth of 200 zones at a resolution of  $5 \text{ cm zone}^{-1}$  is sufficient to avoid this complication. A sufficiently deep domain is consistent with imposing hydrostatic equilibrium at the lower boundary, since the farther the lower boundary is away from the convective region, the smaller the magnitudes of the motions which develop near the lower boundary.

At the upper boundary ( $k = 200$ ), zero-gradient conditions are imposed on all thermodynamic quantities, except for  $T$  and  $\rho$ . A temperature flux condition  $\frac{\partial T}{\partial z} = -\frac{\rho T}{4N_{top}}$  is used to update  $T$ , where  $N_{top}$  is the column density at the upper boundary ( $N_{top} = \frac{P_{top}}{g}$ ), and a consistent  $\rho$  is then found via the equation of state. The temperature flux condition is derived from equating the radiative flux  $F = -\frac{4ac}{3\kappa\rho}T^3\frac{dT}{dz}$  with the surface flux  $F = \sigma T_{eff}^4$ , where  $T^4 = \frac{3}{4}T_{eff}^4(\tau + \frac{2}{3})$  and  $\tau = \int \kappa\rho dz = \frac{\kappa P}{g}$ . Here,  $T_{eff}$  is the effective temperature at the neutron star's surface.

For both components of velocities, zero-gradient conditions are used, while all convective terms are set to zero for all times. For  $\phi$ , the Dirichlet condition ( $\phi = 0$ ) is imposed in the elliptic solver. In the *top – down* implementation of the  $K$  function,  $K \equiv 0$  at the upper

Computational Quantity	Right, Left	Upper	Lower
$T$	periodic	$\frac{\partial T}{\partial z} = -\frac{\rho T}{4N_{top}}$	zero-gradient
$\rho$	periodic	EOS consistent with $T$	zero-gradient
$X_l$	periodic	zero-gradient	zero-gradient
$v$	periodic	zero-gradient	zero-gradient
$w$	periodic	zero-gradient	zero
convective terms	periodic	zero	zero
$\phi$	periodic	Dirichlet ( $\phi = 0$ )	Neumann ( $\frac{\partial \phi}{\partial z} = 0$ )
$K$	periodic	zero	zero-gradient

TABLE 4.1. 2D Boundary Conditions

boundary, so the Dirichlet condition is effectively a condition that  $P' = 0$  at the top. The 2D model used in this chapter utilizes the  $K$  function in the *top – down* manner. (Consult Appendix C for details about the  $K$  function.)

The upper edge of the domain is set high enough to provide sufficient computational space to accommodate whatever dynamics develop throughout the entire burst sequence, but low enough to avoid very-low density regions, which would excessively limit the time-step as constrained by the diffusional-thermal term, which is proportional to density. In practice, the upper boundary is 500 cm from the actual surface of the neutron star.

Table 4.1 summarizes the 2D boundary conditions.

The CFL factor  $\lambda_{CFL}$  is set at 0.50 throughout the calculation. (Refer to Equations 2.22, 2.23, and 2.24 in Chapter 2 for timestep expressions.) The time-step  $dt$  at any time is not allowed to exceed  $dt_{max} = 5 \times 10^{-6}$  s, a constraint found to be necessary for computational stability. This  $dt_{max}$  dominates during the initial part of the calculation, but by the time the EGR level reaches  $1 \times 10^{16}$  erg g $^{-1}$  s $^{-1}$ , the magnitude of the flow speeds become large enough such that the time-step is thereafter limited by the CFL condition. Several CFL factors were tested to demonstrate temporal convergence of the results, as will be detailed in Chapter 5. Finally,  $dt$  is not allowed to increase by more than 10% per computational step.

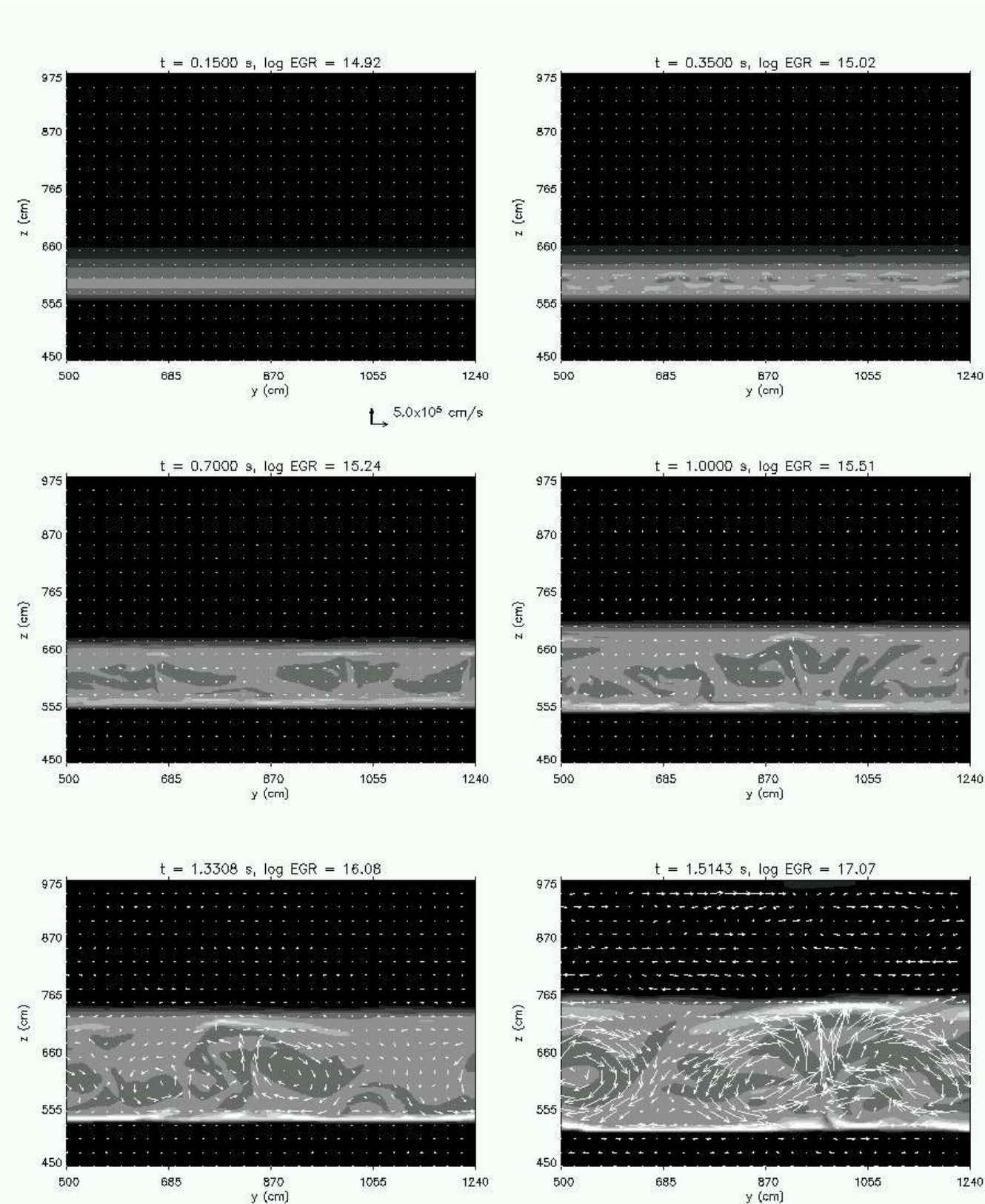


FIGURE 4.2. Burst Sequence Snapshots A  
Velocity flow fields against SAd contours. See Table 4.16 for the legend.

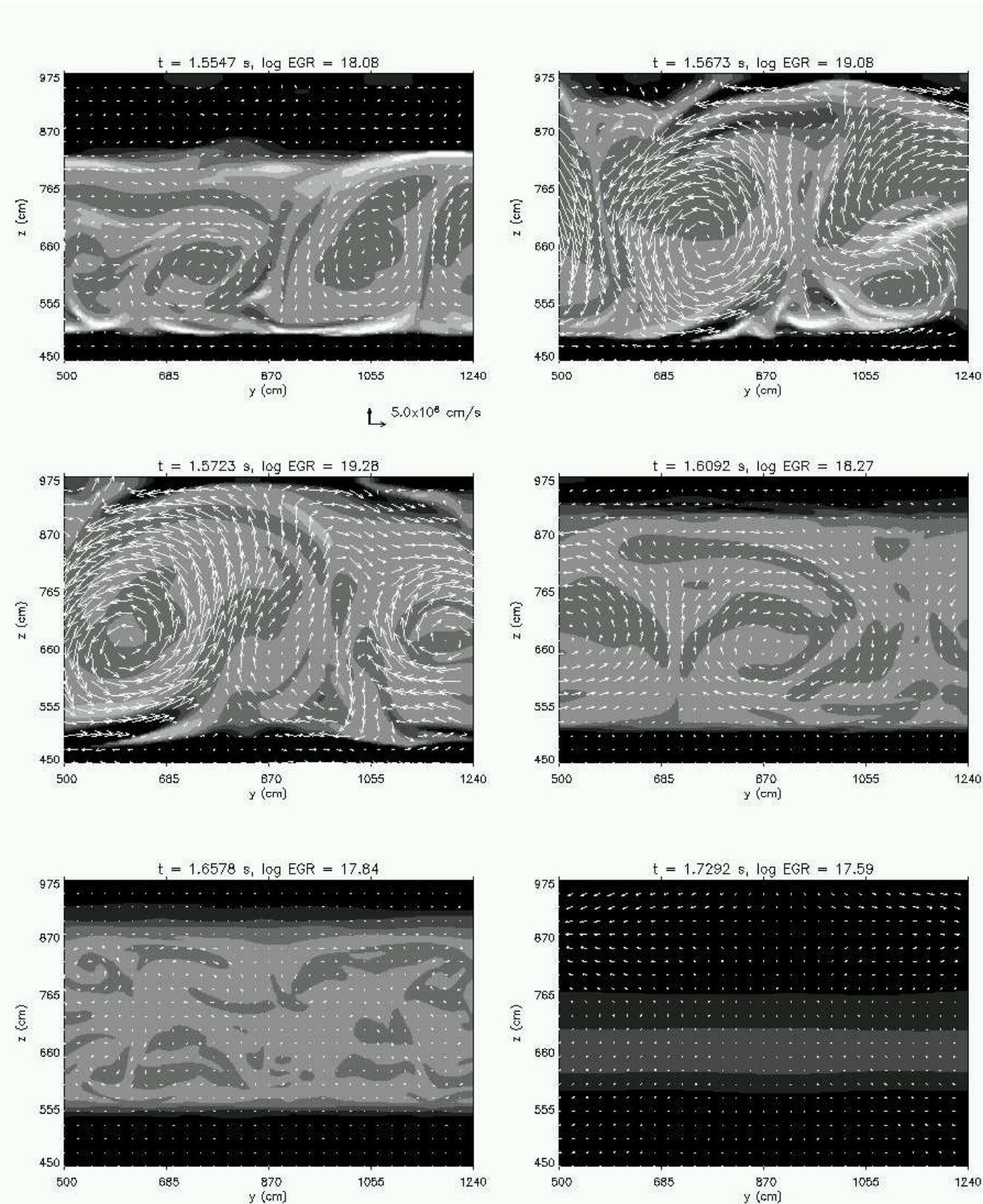


FIGURE 4.3. Burst Sequence Snapshots B  
Velocity flow fields against SAd contours. See Table 4.16 for the legend.

## 4.5. Overview of Burst Sequence

To better appreciate the overall evolution of the flow fields throughout the burst sequence, numerous animations of the  $5 \text{ cm zone}^{-1}$  ( $386 \times 200$  zones) model were generated. These animations show the overall evolution of the flow field from the beginning ( $t = 0.00 \text{ s}$ ) to the end ( $t = 1.74 \text{ s}$ ) of the calculation, as well as at a finer time-resolution at four representative EGR levels at  $\log \text{EGR} = 16, 17, 18,$  and  $19$  (pre-burst peak), each one lasting many dozens of convective-crossing times. Against the dynamic flow field background, evolving contours of many different quantities are overlayed, including the fractional differences of the temperature and He4 from the lateral mean, the sub- and superadiabaticity as determined by both the Schwarzschild and Ledoux criteria, and the peak EGR levels. The same data used to generate these animations also form the basis of all the contour plots, flow fields, and quantitative analyses presented in this chapter.

First, a very broad outline of key features during the entire burst sequence is presented to help establish a framework on which more detailed analyses may be based. Figures 4.2 and 4.3 present velocity flow fields plotted against contours of superadiabaticity at twelve representative times throughout the burst sequence. (A careful study of the time evolution of fluctuations in SAd will be presented in Sub-section 4.8.3.) A brief narrative of the events follow in the next few paragraphs.

Initially, everything is quiet. The temperature gradient is everywhere sub-adiabatic. Lateral inhomogeneities introduced by the initial perturbation cause small-scale, localized eddies to develop everywhere in the domain. The magnitude of the average velocity of these eddies is on the order of  $10^2 \text{ cm s}^{-1}$ . The patterns in the flows field dynamically change, but the magnitude of the average velocity stays fairly constant.

At  $t = 0.15 \text{ s}$  ( $\max \text{EGR} = 8.3 \times 10^{14} \text{ erg g}^{-1} \text{s}^{-1}$ ), a thin layer becomes slightly superadiabatic (maximum value = 0.1205), and by  $t = 0.35 \text{ s}$  ( $\max \text{EGR} = 1.05 \times 10^{15} \text{ erg g}^{-1} \text{s}^{-1}$ ), convective motions become evident in this layer. While there are minor inhomogeneities within it, the convective layer initially forms not as a localized pocket within the domain,

but as a long, straight band spanning the domain's entire width. When convective motions begin, the band is approximately 50 cm in vertical extent, and pockets of sub-adiabaticity are immediately observed within it. The maximum EGR layer is located approximately 50 cm beneath the convective region. The average magnitude of the velocities in the convective region is  $1 \times 10^4$  cm s $^{-1}$  and is steadily increasing. The flow field initially lacks apparent structure.

By  $t = 0.70$  s (max EGR =  $1.73 \times 10^{15}$  erg g $^{-1}$  s $^{-1}$ ), the convective layer has a vertical extent of about 150 cm, and the flow field self-organizes into distinct Benard cells, each characterized by a central upflow and two downflows. The shapes and sizes of the cells are dynamically evolving on sub-convective timescales, which varies from  $150\ \mu s$  to  $1000\ \mu s$ , depending on the stage of the burst (see Table 4.2). Upflows are always associated with columns which are locally slightly warmer than their surroundings. Conversely, downflows are always slightly cooler. The fractional difference in temperature  $d(T)$  and He4  $d(Y)$  from lateral means are nearly perfectly complementary at all times. Where one is positive, the other is negative. Thus, upflows are characterized by positive  $d(T)$  and negative  $d(Y)$  compared to their immediate surroundings. The opposite is true for downflows. As the EGR increases, the magnitude of  $d(T)$  and  $d(Y)$  increases, as does the rate at which fluctuations develop.

As the burst proceeds and the EGR rises, the superadiabatic layer and the convective region expands vertically. By the time the EGR is  $1 \times 10^{17}$  erg g $^{-1}$ s $^{-1}$ , the vertical extent of the convective region is roughly one pressure scale height, and by burst peak when the EGR reaches its maximum value of  $2 \times 10^{19}$  erg g $^{-1}$ s $^{-1}$ , it has expanded to about two pressure scale heights. Initially, the convective layer's boundaries (defined to be where the slopes of the He4 profile are steepest, fully discussed in Sub-section 4.6.3) propagates upward and downward at roughly the same speed, on the order of  $10^2$  cm s $^{-1}$ . After the EGR exceeds  $1 \times 10^{17}$  erg g $^{-1}$  s $^{-1}$ , the boundary accelerates upward significantly faster ( $\sim 10^4$  cm s $^{-1}$ ) than it does downward ( $\sim 10^2$  cm s $^{-1}$ ).

Throughout the burst sequence, both sub- and superadiabatic pockets persist in the convective region. Very superadiabatic regions appear to form near the bottom of the convective region as elongated "fronts" which appear to be pushed up by the strongest currents to the top of the convective region. Laterally averaged over time, however, the adiabaticity of the convective region is convectively unstable by the Schwarzschild criteria, as expected.

In the same way as the convective region spans the entire lateral width of the computational domain, contours of equivalent values of the EGR span the entire width of the domain and are not localized. That is, as the burst proceeds, the EGR increases uniformly across the domain's lateral extent. In terms of the behavior of the EGR, the burst appears to occur as if it were simply multiple 1D domains stacked side-by-side, each one bursting in step with its neighbors. What distinguishes the 2D evolution from a simple 1D burst are the dynamic convection patterns which develop and the time evolution of the burst due to the additional mode of energy transport by convection, as will be described in Sub-section 4.6.1. Nevertheless, in terms of the nature of the ignition, the burst begins and proceeds roughly uniformly across the entire width of the domain, not from any localized regions, such as a spot, within the domain. Said another way, while the initial perturbation is localized, the burning layer which ensues is roughly uniform in the lateral direction.

At any given time, the maximum EGR throughout the domain can be found in a layer at the same depth, about 475 cm below the upper boundary. The layer which exhibits the peak value that the EGR attains throughout the entire sequence ( $\sim 2 \times 10^{19} \text{ erg g}^{-1} \text{ s}^{-1}$ ) appears limited to this depth; that is, it does not travel outward from this latitude very far. The peak temperature also occurs at this depth, however the temperature lags the EGR as the burst progresses, since heating dominates over cooling factors during this time. The temperature reaches its maximum value slightly over a tenth of a second after the EGR reaches its peak value.

A roughly uniform layer reaches a peak EGR value of  $2 \times 10^{19} \text{ erg g}^{-1} \text{ s}^{-1}$  simultaneously at  $t = 1.572 \text{ s}$ . At this time, the greatest magnitude of velocity in the domain also peaks at

a value of  $3 \times 10^7 \text{ cm s}^{-1}$  ( $M_{peak} = 0.085$ ). Since the peak Mach number is always less than 0.10 throughout the entire burst sequence, simulating Type I X-ray bursts with a low Mach number model is justified.

Post-burst peak, the region becomes increasingly sub-adiabatic. Convective motions gradually diminish, and the Mach number falls. By the conclusion of the calculation ( $t = 1.74 \text{ s}$ ), the domain has become completely sub-adiabatic again, and all convective motions cease. Residual motion occurs at the upper boundary, but these velocities are relatively insignificant ( $M < 0.02$ ).

## 4.6. Time Evolution of Thermodynamic and Dynamic Quantities

**4.6.1. Thermodynamical Quantities .** Starting from an EGR of  $7 \times 10^{14} \text{ erg g}^{-1} \text{ s}^{-1}$  at  $t = 0 \text{ s}$ , the calculation evolves through the entire burst sequence and ends at  $t = 1.74 \text{ s}$ . Figure 4.4 shows a panel of four plots of global values of certain thermodynamic indicators as a function of time ( $t = 1.00$  to  $1.74 \text{ s}$ ). The upper left figure displays the log of the peak EGR. Over 1.6 s, the EGR rises more than four orders of magnitude to peak at  $t = 1.572 \text{ s}$ , reaching a burst peak EGR value of nearly  $2 \times 10^{19} \text{ erg g}^{-1} \text{ s}^{-1}$ . Immediately after reaching burst peak, the EGR diminishes rapidly, decaying by almost two orders of magnitude during 0.10 s post-burst peak. In the upper right panel, the log of the ratio of the instantaneous nuclear flux (the vertically integrated value of the laterally averaged  $\rho \dot{s} \Delta z$  over the entire domain) to the Eddington value of the flux ( $F_{Edd} = 2.5 \times 10^{25} \text{ erg s}^{-1} \text{ cm}^{-2}$  for a  $1.4 M_\odot$  neutron star of radius  $10^6 \text{ cm}$ ) is plotted, showing a burst peak value nearing  $F_{nuc, peak} = 400 F_{Edd}$ . Peak temperatures (lower left figure) reach and level off at  $1.7 \times 10^9 \text{ K}$ . (Note that the peak value of a given thermodynamic value such as  $T$  or the EGR over the entire domain may be associated with different zones at different times. As mentioned already, however, the layer which exhibits the greatest temperature and EGR remains always at roughly the same depth.)

Finally, the lower right plot in Figure 4.4 shows the time evolution of the ratio of the total amount of He4 by mass (the integrated value of  $\rho Y \Delta V$  over the entire domain, where  $Y$  is the mass fraction of He4) to the total initial value. Most of the fuel is consumed during the 0.05 s preceding the burst peak, dropping nearly 65% from the initial value during that brief time. Also, barely visible on the scale of the plot, the ratio actually increases very slightly from the beginning of the calculation until  $t = 1.55$  s ( $\log \text{EGR} = 18$ ). This increase can be attributed to a net downward flow which occurs in the domain and is documented quantitatively in Figure 4.60 and discussed in Section 4.10 below. The downward flow advects composition down deeper in the domain where density is greater, thus effectively increasing the total amount of He4.

In Figures 4.5 and 4.6, laterally averaged values of  $T$ ,  $\log \text{EGR}$ ,  $\rho$ , and  $Y$  are plotted as a function of vertical position at 14 different times throughout the burst sequence, 7 times pre-burst peak (Figure 4.5,  $t = 1.000$  s - 1.572 s), and 7 time post-burst peak (Figure 4.6,  $t = 1.572$  s - 1.738 s). During the pre-burst peak stage, Figure 4.5 shows a steady rise in temperature and EGR. As more of the domain ignites, the He4 profile indicates the progress of the upper and lower edges of the convective layer boundaries. A more quantitative analysis of the speeds at which the boundaries travel is presented in Sub-section 4.6.3. Notably, the flat plateau regions in the He4 profiles at all times indicate the efficient, homogenizing action of convective motions. Evidence that He4 is advected deeper down into the domain is also apparent. This is not an artifact due to numerical diffusion, as the same results are found when the grid is refined. Also, the temperature profile in the upper part of the domain maintains a nearly adiabatic profile throughout the rise to burst peak, as will be quantitatively demonstrated in Sub-section 4.6.5.

Defining the burst peak as the time when the EGR reaches its maximum value, burst peak occurs at  $t = 1.572$  s, and the EGR attains a peak value of nearly  $2 \times 10^{19}$  erg g $^{-1}$  s $^{-1}$ . At burst peak, the temperature is less than  $9 \times 10^8$  K and is still steadily rising. The concentration of He4 in the upper half of the domain has been completely homogenized and

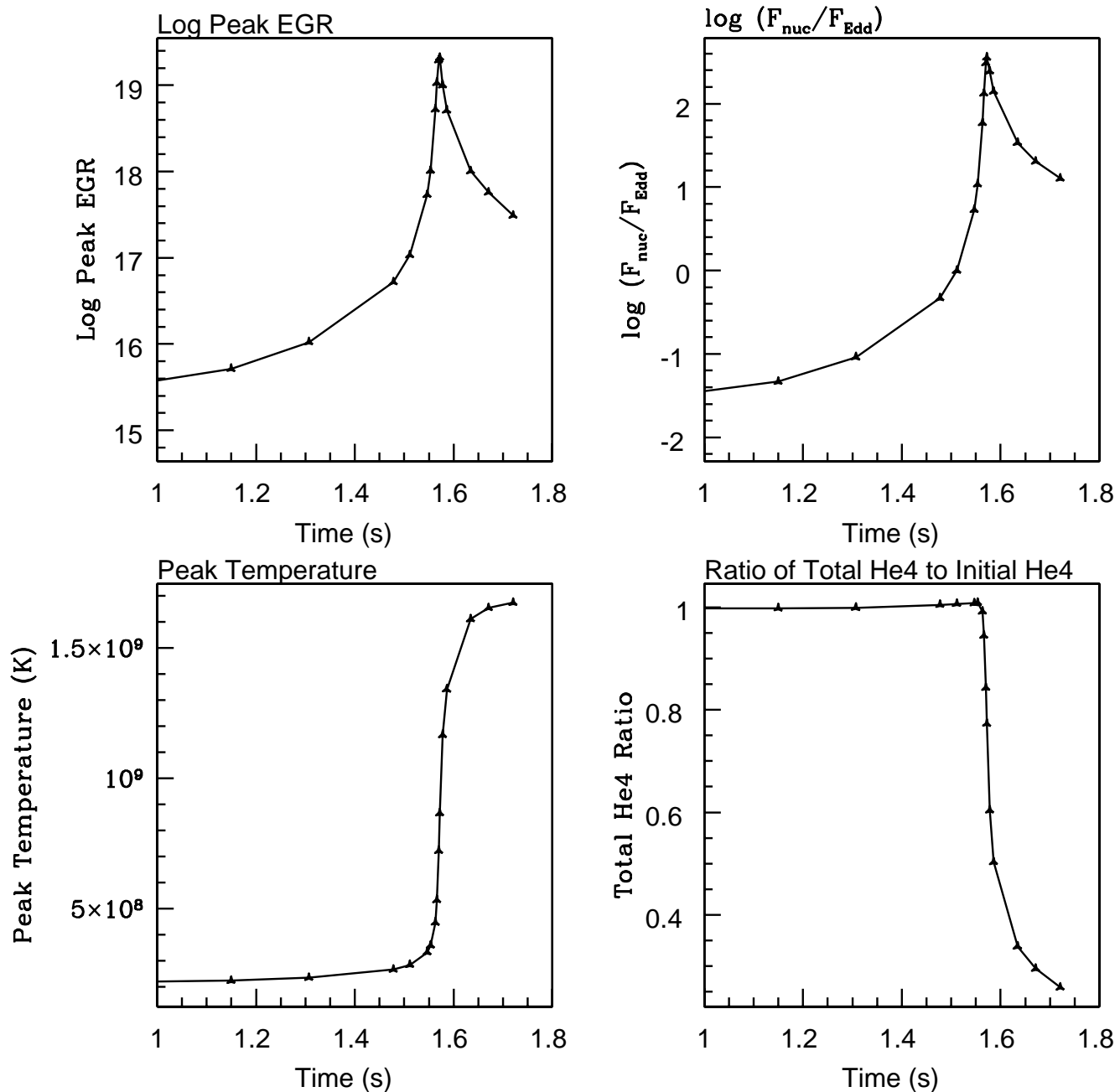


FIGURE 4.4. Global Thermodynamic Quantities vs. Time  
 Log of peak EGR (upper left), ratio of nuclear flux to the Eddington flux (upper right),  
 peak temperature (lower left), and ratio of total He4 to initial He4 (lower right). Note that  
 the peak value over the domain may be associated with different zones at different times.

is about 60% of its initial value. Due to the semi-degenerate conditions of the part of the domain where the EGR is greatest, the density has decreased only about 25%, while the temperature has increased over 400%. As will be discussed in more detail below, convective cell sizes and peak velocities reach their maximum values at burst peak.

Post-burst peak (Figure 4.6), the temperature continues to rise for the next 0.114 s even while the EGR begins to diminish, due to the dominance of heating over cooling factors near the region of maximum EGR during this time. Evidently, the peak value of the EGR occurs momentarily at a relatively confined depth due to the relative scarcity of fuel below  $z = 500$  cm and the rapidly diminishing concentration of fuel elsewhere as the burst consumes most of the available fuel, resulting in a well-defined, sharp peak in the EGR vs. time profile in Figure 4.4. As the domain continues to cool, more of the upper domain reaches a uniform EGR level. The temperature profile eventually peaks at  $t = 1.686$  s, when cooling begins to dominate, diffusing heat away from the peak region. As the temperature becomes more uniform in the upper part of the domain, the profile becomes sub-adiabatic, and convective motions subsequently cease.

**4.6.2. Dynamical Quantities.** To summarize the quantitative aspects of the resulting flows in the calculation, four important dynamical indicators are presented in the panel of four plots of Figure 4.7. In the upper left and upper right are plotted  $\rho$ -weighted average values of the vertical and lateral velocities, respectively, as a function of time. Over the entire burst sequence, these values have averages close to zero, but at any given time, they may be positively or negatively biased. For instance, the  $\rho$ -weighted vertical component tends to be negative throughout the rise to the burst peak, suggesting a net downward flow in the domain during this phase of the evolution, while it becomes positive post-burst peak. The lateral component does not show such a pronounced bi-polar behavior, but tends to be more non-directional on average, shifting between positive and negative values with no apparent pattern. Notably, while the  $\rho$ -averaged components of the velocity never exceeds peak values of  $10^5 \text{ cm s}^{-1}$ , the peak value of the total instantaneous velocity in the domain is over two

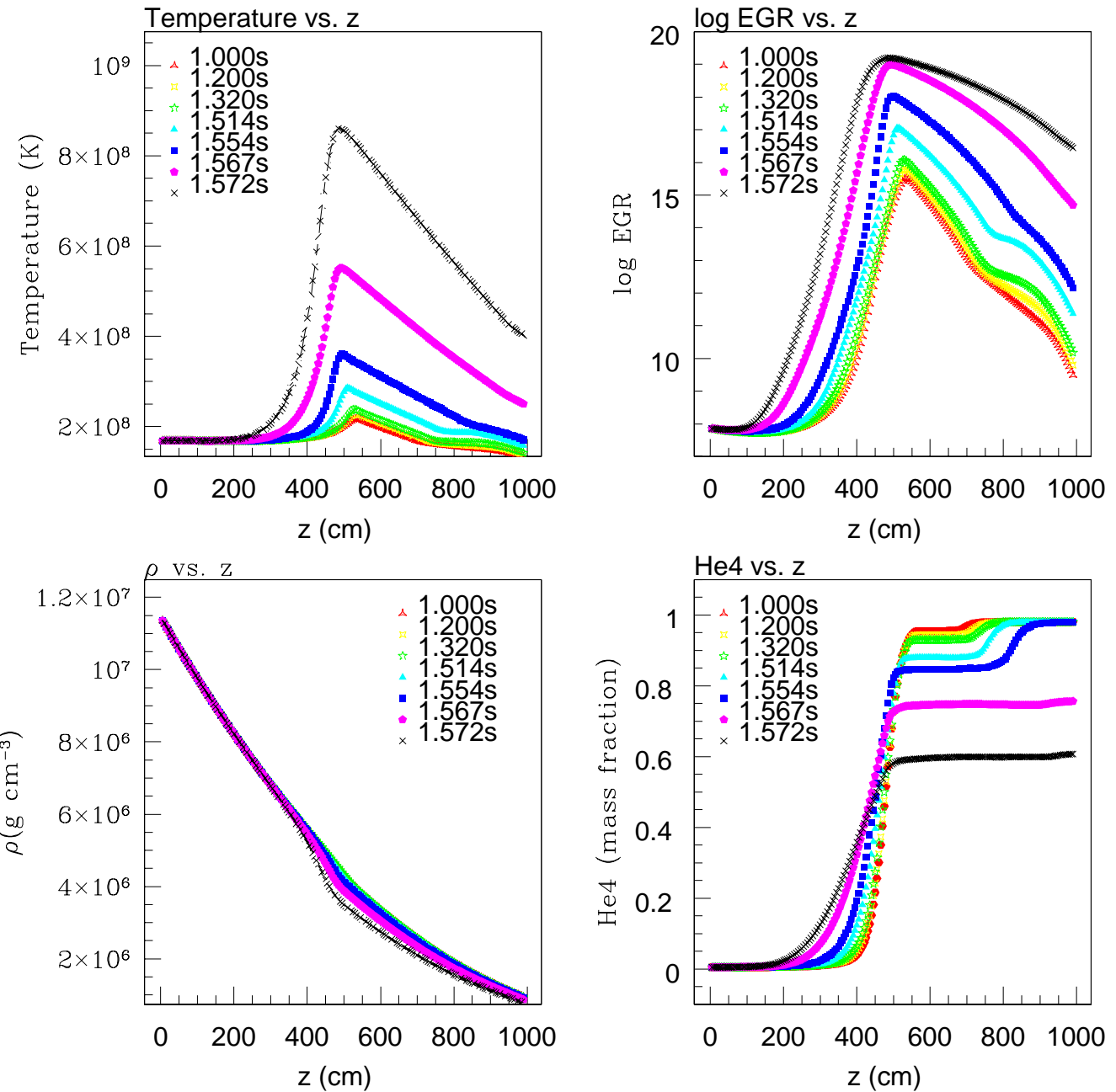


FIGURE 4.5. Thermodynamical Quantities vs.  $z$ , Pre-Burst Peak  
At 7 times leading up to burst peak:  $T$  (upper left), log EGR (upper right),  $\rho$  (lower left),  
and  $Y$ , the mass fraction of He4 (lower right).

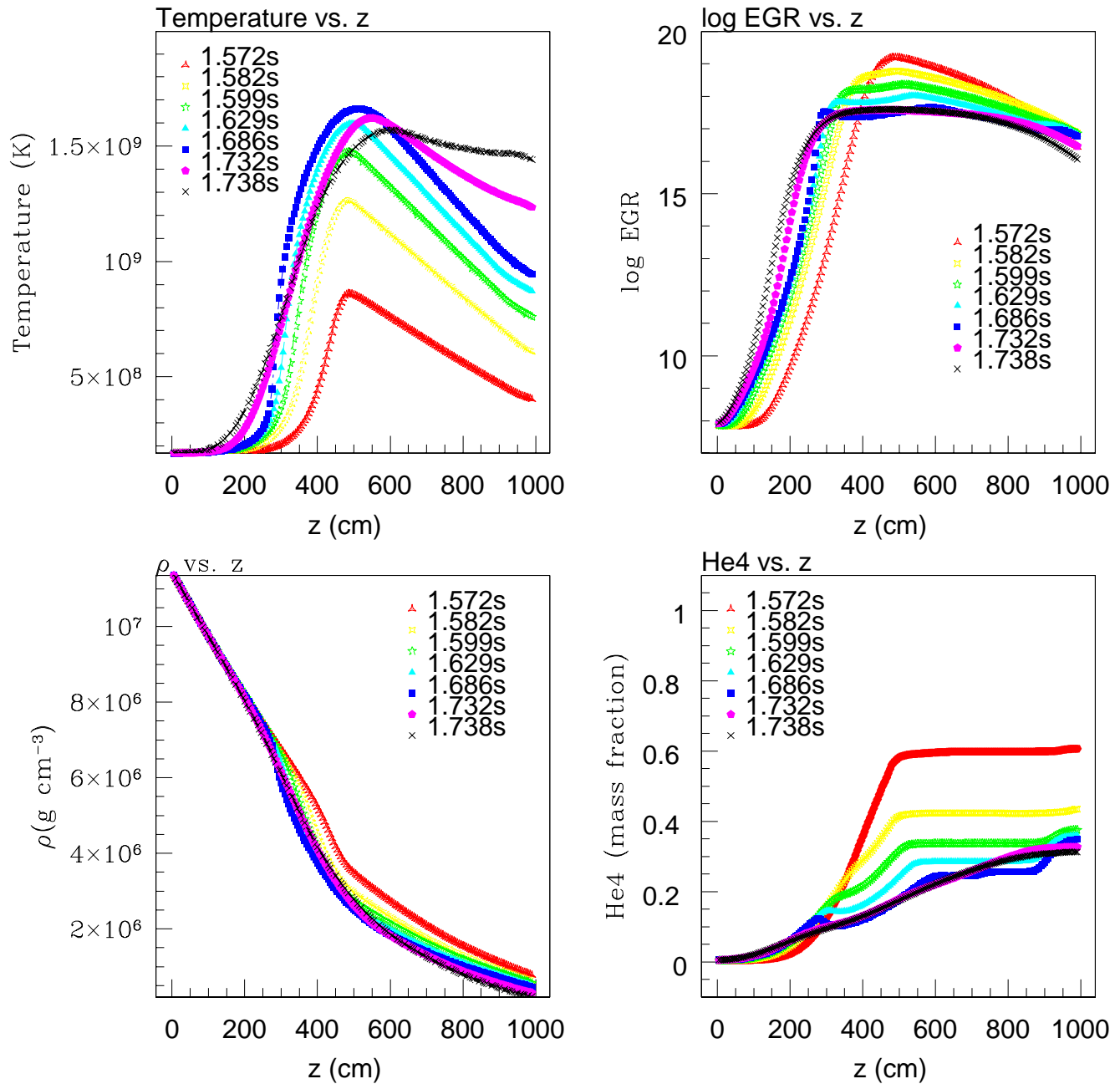


FIGURE 4.6. Thermodynamical Quantities vs.  $z$ , Post-Burst Peak  
At 7 times post-burst peak:  $T$  (upper left), log EGR (upper right),  $\rho$  (lower left), and  $Y$ ,  
the mass fraction of He4 (lower right).

orders of magnitude greater (lower left plot). Nevertheless, as seen in the lower right plot, the peak Mach number never exceeds 0.085 throughout the evolution of the burst.

**4.6.3. Convective Layer Expansion.** To measure the speed at which the convective layer boundaries vertically expand from the burning layer, which is located at the latitude where the instantaneous EGR is maximum, diagnostics involving the laterally averaged, vertical profiles of the He4 fractional abundance at numerous times throughout the burst sequence are examined in the panel of four plots of Figure 4.8. The upper left plot shows the laterally averaged He4 profile, while the upper right figure plots the vertical slope of this profile. The positions of the lower and upper boundaries are taken to be where the slopes of the He4 profile are greatest, because for each boundary, this position represents approximately one-half the distance between where the He4 is at its original value (unmixed regions) and where it is homogenized due to the expanding convective layer (mixed regions). This demarcation helps to track the progress of the convective boundaries both downward and upward in the domain during the burst sequence.

As a function of time, the lower left figure shows the upper-boundary's position as a function of time, and the lower right panel shows the log of the upper-boundary's speed as a function of time. During the initial bursting phase ( $t < 1.5$  s), the speeds of both the lower and upper boundaries are fairly constant, on the order of  $10^2$  cm s $^{-1}$ . This corresponds to the time when the peak EGR is less than a few times  $10^{16}$  erg g $^{-1}$ s $^{-1}$ . However, when the peak EGR approaches  $10^{17}$  erg g $^{-1}$ s $^{-1}$  and beyond ( $t > 1.5$  s), the upper boundary's speed increases by two orders of magnitude to  $10^4$  cm s $^{-1}$ . In contrast, no corresponding acceleration of the lower boundary's downward advancement appears to occur, as its speed never increases beyond  $10^2$  cm s $^{-1}$  downward. The upper boundary advances faster than the lower boundary because density decreases with increasing height, and the upper boundary pushes into regions which offer less dynamical inertia compared to the relatively denser regions which exist at depth.

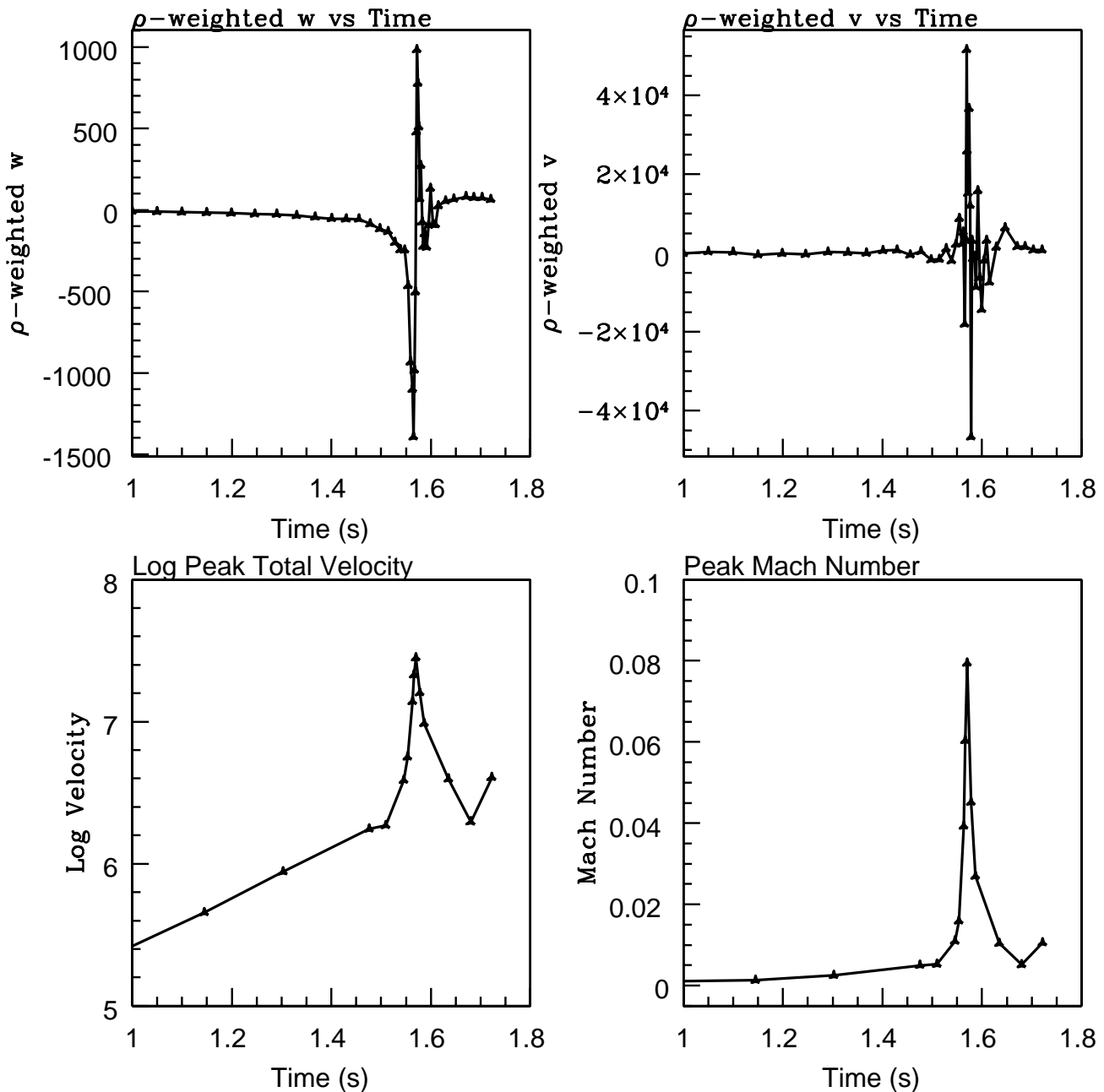


FIGURE 4.7. Global Velocity Quantities vs. Time

$\rho$ -weighted average of vertical velocity (upper left),  $\rho$ -weighted average of lateral velocity (upper right), log of total velocity (lower left), and peak Mach number (lower right). Note that the peak value over the domain may be associated with different zones at different times.

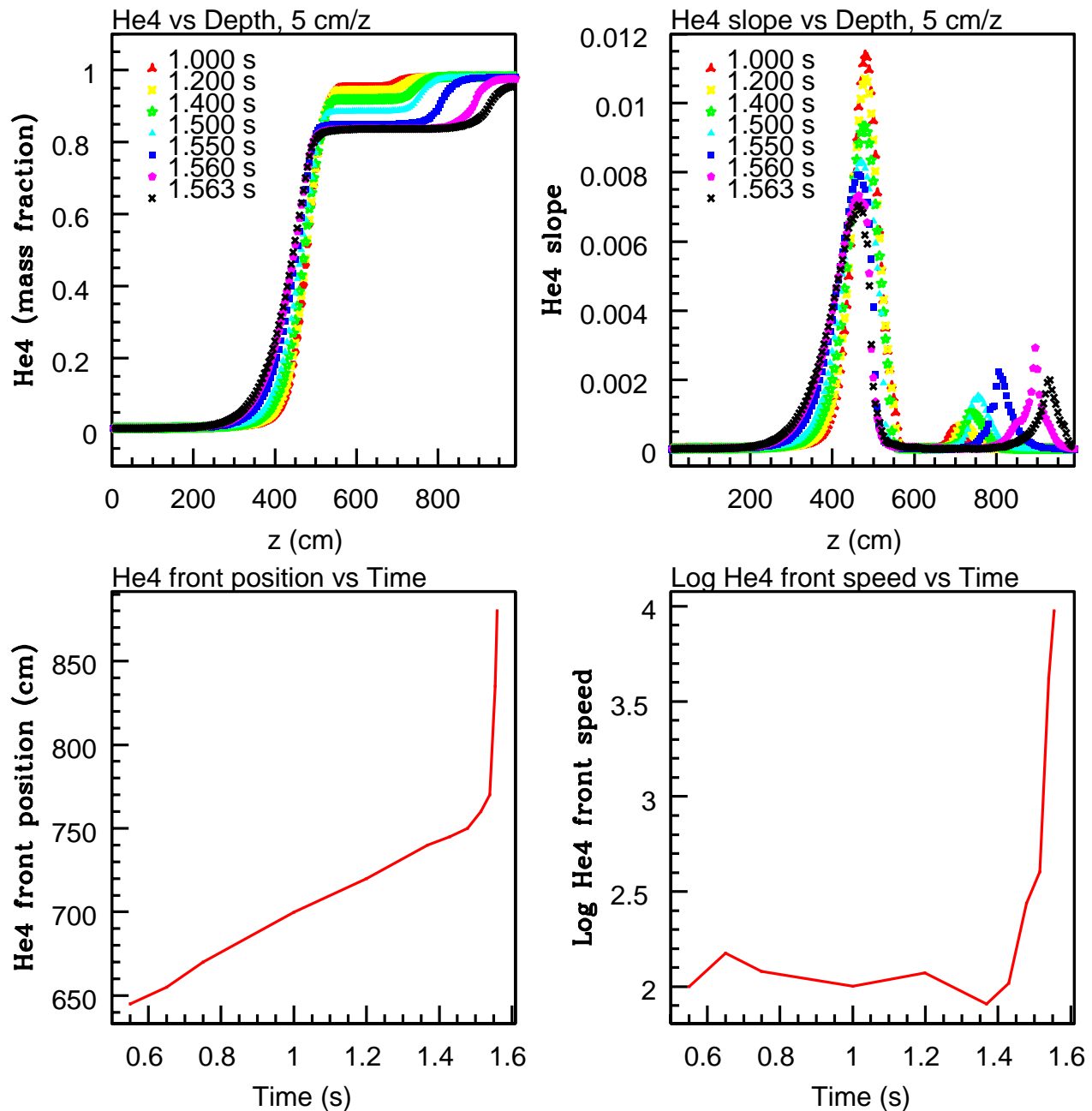


FIGURE 4.8. He4 Front Position and Speed

Laterally averaged He4 profile (upper left), spatial first derivative of He4 profile (upper right), position of the upper He4 front vs. time (lower left), and velocity of the upper He4 front vs. time (lower right). The He4 fronts indicate the positions of the convective layer boundaries.

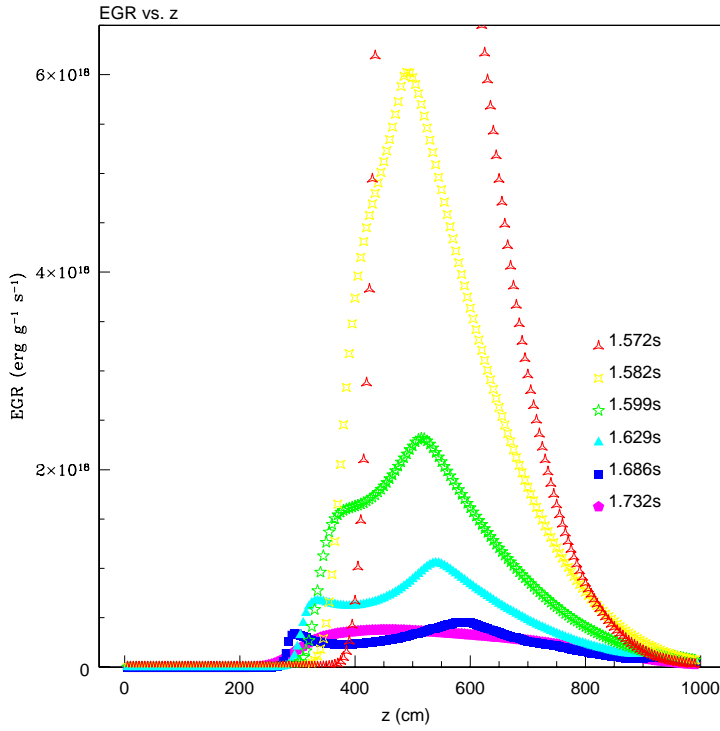


FIGURE 4.9. EGR vs.  $z$ , Post-Burst Peak

The EGR is plotted as a function of height (cm) at several times post-burst peak in linear scale. Upper and lower burning fronts propagate away from the burning layer.

**4.6.4. Burning Front Propagation.** The location of the burning front is defined to be where the EGR is locally maximum at a given time. As defined, the burning front is relatively stationary during the rise to burst peak, as seen in the EGR profiles of Figure 4.5, which show that the latitude corresponding to the maximum EGR is always roughly  $z = 500$  cm during this period. Pre-burst peak, the temperature at this latitude is also locally maximum. Henceforth, this hottest layer is referred to as the *burning layer*, and its latitude as a function of time is shown in the upper right plot of Figure 4.10.

After the peak of the burst, however, the EGR profiles in Figure 4.6 show that two burning fronts, above and below the burning layer, vertically propagate away from it. The upper and lower burning fronts are more clearly discernible in Figure 4.9, which plots the same EGR profiles in linear scale.

The double burning fronts can be understood to originate from a spreading temperature wave, the magnitude of which is still rising throughout the domain post-burst peak due to the dominance of heating over cooling factors during this period. (The panels in Figure 4.6 also show the temperature, density and composition profiles post-burst peak.) After burst peak, as the EGR diminishes in the burning layer due to fuel exhaustion and decreasing density, the still-rising temperature wave pushes into deeper regions where densities are increasing with depth but fuel supply is decreasing. Thus, a lower burning front forms where conditions cause a local maximum in EGR as the temperature wave advances downward. Similarly, the upper burning front results from the temperature wave pushing upward toward less dense regions which have relatively more fuel supply. Due to convective mixing, the composition is roughly uniform above the burning layer, but rapidly diminishes below it. Thus, as the temperature wave increases in magnitude and spreads upward toward regions of relatively greater fuel supply, conditions give rise to a local maximum in the EGR, which propagates upward in the form of a distinct burning front.

On average, the two burning fronts each propagate vertically at speeds of order  $10^3 \text{ cm s}^{-1}$ . However, soon after the fronts travel  $\sim 10^2 \text{ cm}$ , the flame extinguishes due to fuel depletion, as seen in the EGR profile taken at  $t = 1.732 \text{ s}$  in Figure 4.9 and the composition profile in Figure 4.6. Notably, the upper front extinguishes far from the surface. However, as is discussed in Section 6.1 of Chapter 6, including the energy generation rate due to carbon reactions in helium burning is necessary to better account for post-burst peak energetics and more completely model the entire X-ray burst, along with its flame dynamics. For now, the present model suggests that during the rise to burst peak, the burning front is relatively stationary, but afterward, because the temperature is still rising while the EGR is diminishing, a spreading temperature wave into deeper regions (where density increases and fuel decreases) and higher regions (where density decreases and fuel increases) causes two burning fronts to advance vertically away from the burning layer at roughly  $10^3 \text{ cm s}^{-1}$ .

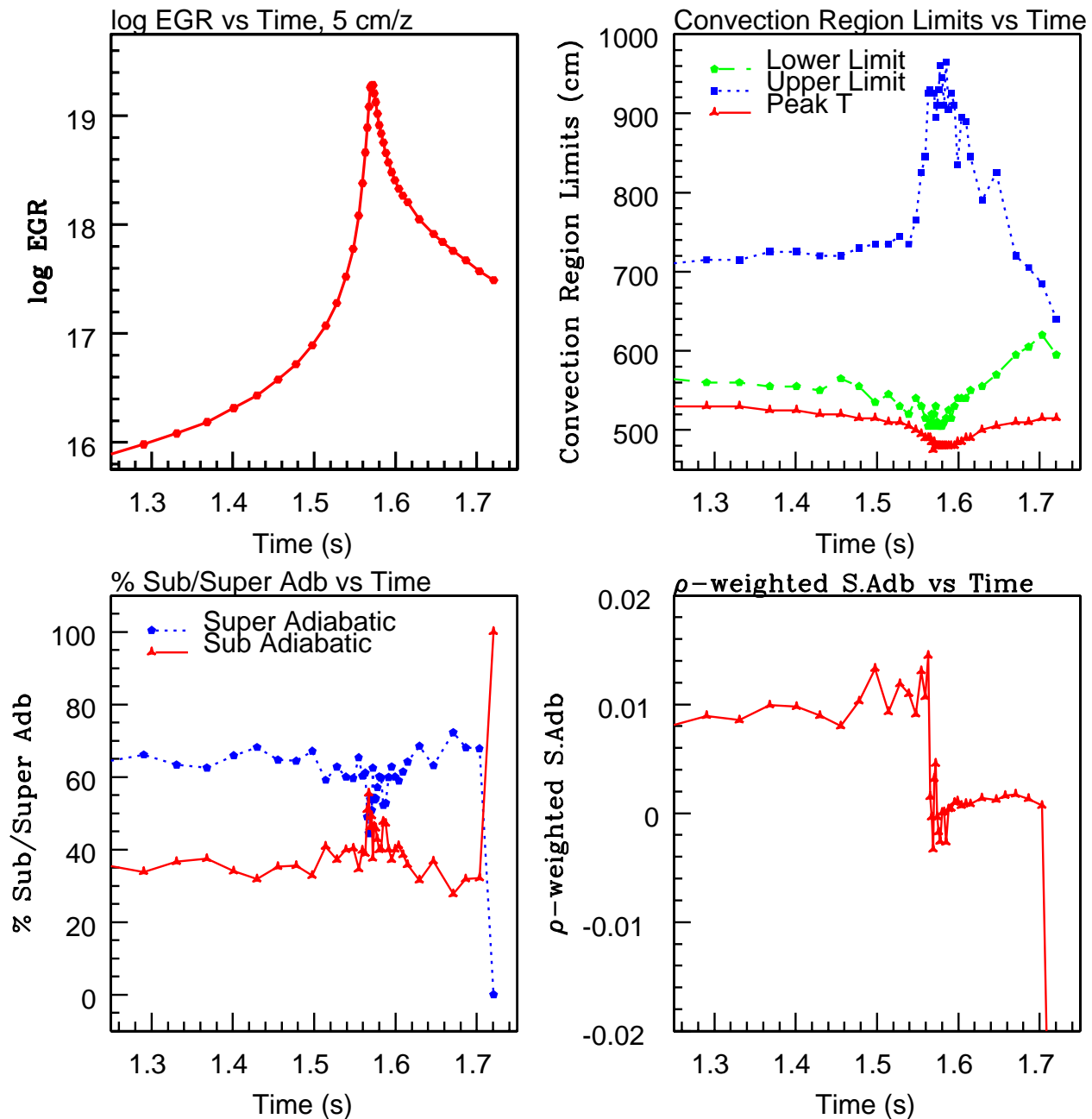


FIGURE 4.10. Convective Quantities vs. Time  
 Log EGR vs. time (upper left); convective zone boundaries vs. time (upper right), percentage of convective region which is sub- and superadiabatic vs. time (lower left),  $\rho$ -averaged superadiabaticity vs. time (lower right).

**4.6.5. Convective Quantities.** In the panel of four plots in Figure 4.10, the time evolution of key convective indicators are presented. The time-frame of the plots is between  $t = 1.25$  s, when the EGR level is barely  $10^{16}$  erg g $^{-1}$ s $^{-1}$ , through the burst rise, peak, and decay, ending at  $t = 1.74$  s. For reference, the upper left plot displays the log EGR evolution during the time period under consideration. The upper right plot shows the time evolution of the upper and lower limits of the convectively unstable region as defined by the Schwarzschild criteria, where the lateral average of  $\nabla$  is calculated to determine the adiabaticity of a given vertical level. Also plotted is the vertical location of the peak temperature, which is always found to occur below the base of the convectively unstable region as expected. As the plot shows, the vertical depth of the convectively unstable region is fairly constant in height (around 150 cm) for all times before  $t = 1.55$  s (corresponding to  $\log \text{EGR} < 17$ ). During the 0.10 s rise from  $\log \text{EGR} 17$  to the burst peak, the extent of the convectively unstable region rapidly expands more than three-fold to 400 cm, reaching its maximum expansion at burst peak. Immediately after the burst peak, the convectively unstable regions quickly diminishes in height, and essentially fades away by the end of the calculation.

While on average, the zones in a given vertical layer may be superadiabatic, and thus theoretically convectively unstable by the Schwarzschild criteria, as well as practically convectively unstable by the development of convective cells in these layers, a significant number of zones in these layers are in fact sub-adiabatic. In the lower left plot of Figure 4.10, the percentage of zones in the convectively unstable region (as defined in the upper right plot) which are sub- or superadiabatic is plotted as a function of time. Prior to the burst peak, the superadiabatic zones dominate, but during the burst peak, the fraction of sub- versus superadiabatic zones becomes nearly 50/50, with brief instances when the fraction of sub-adiabatic zones is slightly greater. After the burst peak, the superadiabatic fraction is dominant until the very end, when convection is lost and sub-adiabaticity becomes 100%. The sub-adiabaticity of significant portions of the convectively unstable region is best understood in light of the very dynamic nature of the convective flows in the region, which

causes very rapid fluctuations in the local temperature gradient, and consequently, a particular zone's adiabaticity as defined by the Schwarzschild criteria. Nevertheless, the lateral average of a given convectively unstable layer is definitely superadiabatic, as expected.

Finally, the lower right plot of Figure 4.10 casts the nature of the sub- or superadiabaticity in a slightly different way. Here, the  $\rho$ -weighted average of the superadiabaticity in the convectively unstable region is plotted against time. This indicator shows that overall, the convectively unstable region is clearly superadiabatic before the burst peak (averaging around +0.01), much less superadiabatic after the peak (averaging about +0.001), and becoming very sub-adiabatic at the conclusion of the calculation.

In comparison, Deupree (2000), using a fully implicit method to study the hydrogen-burning convective cores of zero-age-main-sequence stellar models where convective speeds are on the order of  $10^6 \text{ cm s}^{-1}$ , finds  $\rho$ -weighted, time, angle, and radius averages of the superadiabatic excess on the order of  $10^{-3}$ . The differences are not surprising, since Deupree studies a model which is physically dissimilar in many respects, such as the nuclear burning mechanism and the value of  $\vec{g}$ . Nevertheless, local, instantaneous values were found to vary significantly from the averages, in agreement with the significant thermodynamic fluctuations found in the present results, to be presented in Section 4.8 below.

## 4.7. Flow Fields

Figures 4.11 and 4.12, display snap-shots of the velocity flow fields of the  $5 \text{ cm zone}^{-1}$  models at four log EGR levels: 16, 17, 18, and 19. Only the upper-most 775 cm of the computational domain is shown, since the lower 225 cm is relatively calm ( $|v_{ave}| < 10^3 \text{ cm s}^{-1}$ ) compared to the convectively unstable region ( $|v_{ave}| < 10^5$  to  $10^7 \text{ cm s}^{-1}$ , depending on the EGR level). To enhance the clarity of the main features in the flow, the resolution of the vector field is  $30 \text{ cm zone}^{-1}$ , that is, every 6th velocity vector is plotted .

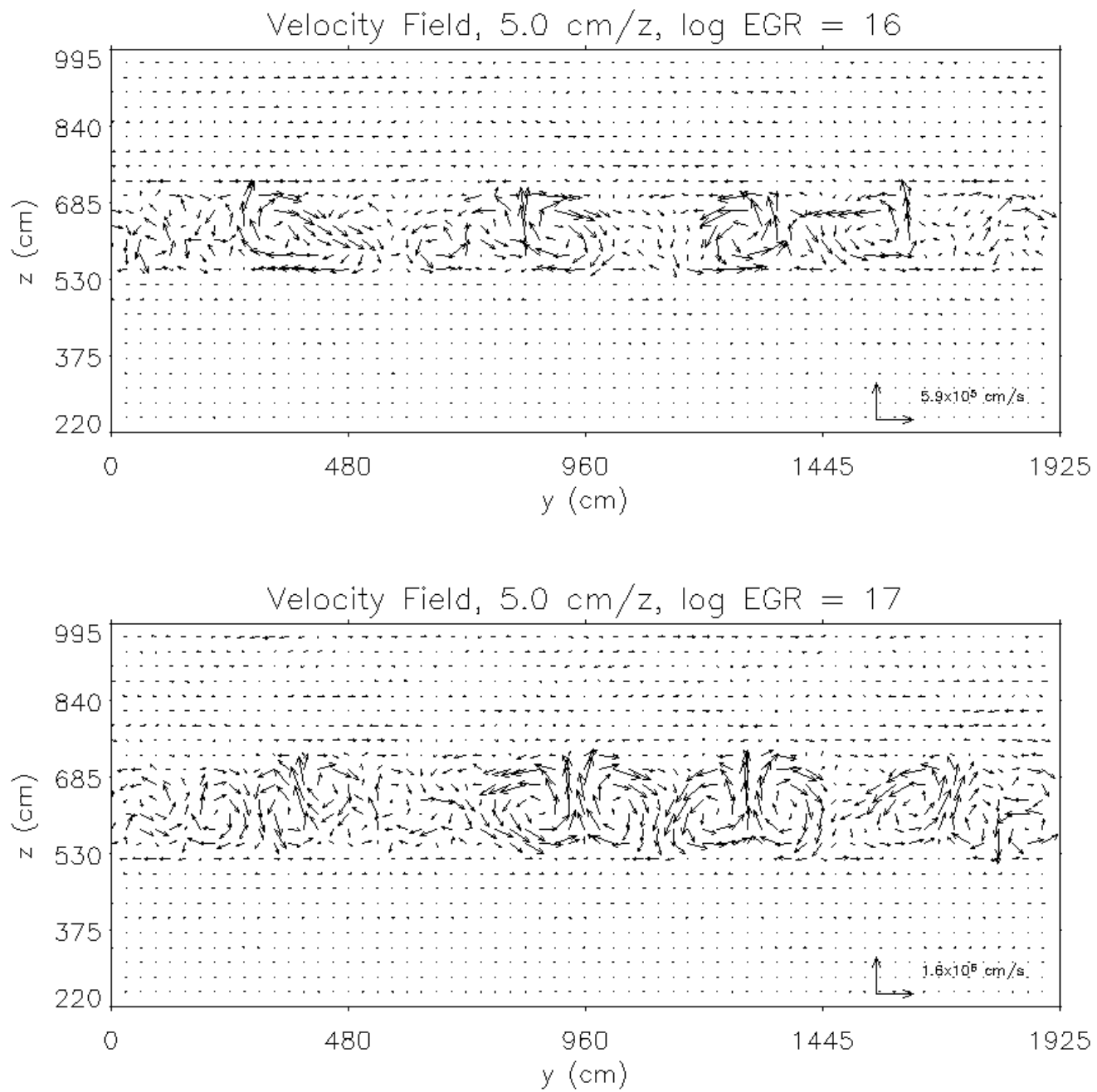


FIGURE 4.11. Velocity Flow Fields, log EGR 16, 17  
5 cm zone $^{-1}$  domain resolution. (30 cm zone $^{-1}$  vector resolution.)

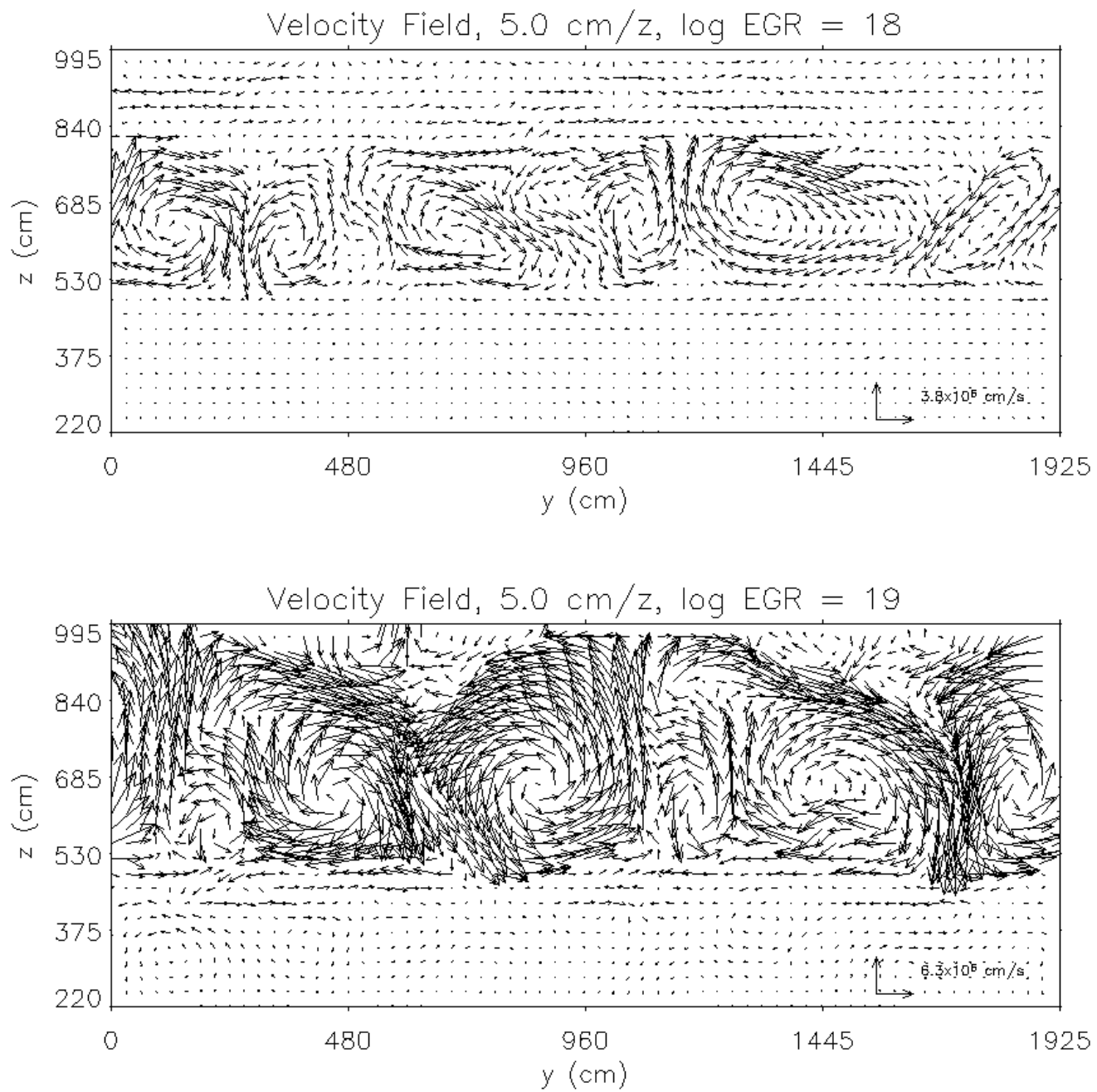


FIGURE 4.12. Velocity Flow Fields, log EGR 18, 19  
5 cm zone<sup>-1</sup> domain resolution. (30 cm zone<sup>-1</sup> vector resolution.)

Beginning at  $\log \text{EGR} = 16$ , the flow fields clearly show well-formed, convective cells (Benard cells). Initially ( $\log \text{EGR} = 16$  and 17), the major cells are approximately symmetric with aspect ratios close to 1:1, although the cells are always dynamically changing and evolving. The major cells are characterized by well-defined updrafts, which mark the center of each cell, channeling material from the base of the convectively unstable region through vertical chimneys up to the top of the region. Once there, the flows bifurcate left and right to form more diffuse downdrafts. The downdrafts of neighboring cells eventually merge, recirculating the fluid flow to the base of the convectively unstable region. In general, a major cell appears roughly to trace the outlines of butterflies, where the left and right wings represent convective cells of opposite rotational sense, separated by the butterfly's central body which is a major updraft.

Due to the dynamical nature of the evolution, the flow fields continuously change into a variety of patterns, and an entirely different arrangement of convective cells may emerge within a few convective times. For example, the major cells may break up into minor cells, which are just as well-defined and symmetric, but a fraction of the size. Several minor cells may later merge to reconstitute a major cell. The direction of updrafts and downdrafts may become skewed toward the left or right to form diagonal channels of flow. The aspect ratio of a cell may momentarily change significantly, as the cell takes on a variety of shapes and forms, but maintaining its overall outline as a complete cell. An updraft occurring at one time at a certain lateral location may develop into a downdraft at the same location within a few convective times. No obvious bulk motion of the cells appears to exist in the lateral direction, as the individual cells do not hold their integrity long enough to noticeably drift as a unit.

By the later stages of the burst ( $\log \text{EGR} = 18$  and 19), the major convective cells rapidly grow in vertical height as the convectively unstable region expands primarily in the upward direction toward the surface of the star. Correspondingly, the horizontal widths of the cells also increase to sustain the roughly 1:1 aspect ratio. Updrafts and downdrafts become much

Log EGR	$ v_{ave} $ (cm s <sup>-1</sup> )	major cell height (cm)	$t_{convective}(\mu\text{s})$
16	$5 \times 10^5$	150	1000
17	$1 \times 10^6$	150	500
18	$4 \times 10^6$	300	250
19	$1 \times 10^7$	475	150

TABLE 4.2. Summary of Dynamical Parameters at Four EGR levels.

The characteristic convective timescale  $t_{convective} = \frac{2\pi h}{|v_{ave}|}$ , where  $h$  = the major cell height.

more pronounced than before, as the domain space is filled up by clearly defined circulation patterns. Rapid dynamical fluctuations are always present, and the cells continue to morph into a variety of shapes and sizes as the convectively unstable region churns and rolls on a convective timescale.

Table 4.2 summarizes certain key parameters ( $|v_{ave}|$ , major cell height, and  $t_{convective}$ ) of the flow fields at representative instances at the four EGR levels examined. The characteristic convective timescale  $t_{convective}$  is defined as:

$$(4.1) \quad t_{convective} = \frac{2\pi h}{|v_{ave}|}$$

where  $h$  = the major cell height.

#### 4.8. Thermodynamical Fluctuations

To better describe the dynamics of the system, contours of temperature and He4 fluctuations from the lateral averages at each vertical height are plotted for four EGR levels in the following panels of plots. That is, for each zone:

$$(4.2) \quad d(A)_{j,k} = A_{j,k} - A_{k\ ave}$$

where  $A$  represents either the temperature,  $T$ , or the mass fraction of He4,  $Y$ ; and  $A_{k\ ave} = (\sum_{j=1}^{j_{max}-1} A_{j,k}) / (j_{max} - 1)$ , the lateral average of  $A$  at a given vertical height with coordinate  $k$ .

A similar set of panels of plots depicts the fluctuations in the adiabatic-excess and Ledoux-excess of a given zone:

$$(4.3) \quad SAd_{j,k} = \nabla - \nabla_{ad}$$

$$(4.4) \quad SLed_{j,k} = \nabla - \nabla_{Led}$$

These fluctuations occur on timescales which are fractions of the convective timescales. For each EGR level, two panels of six contour plots spanning a total of several convective times are presented for each quantity examined. The sequence of plots also displays how the convective patterns in the flow field change on the short timescales on which the fluctuations evolve. For clarity, every other velocity vector is plotted to make up the flow fields in the plots for log EGR 16 and 17, every third for log EGR 18, and every fourth for log EGR 19. For each EGR level, the value of the EGR increases by much less than 0.1% during the time

Color	Relative Value
Black	very negative
Dark Gray	slightly negative
Gray	close to zero
Light Gray	slightly positive
White	very positive

TABLE 4.3. General Guidelines of 5-shade Scheme

Figure	log EGR	Value	Time-span	$d(T)$ limits	f.d. limits
4.13	16	$d(T)$	0.0-1.9 CTs	$\pm 6 \times 10^5$	$\pm 4 \times 10^{-3}$
4.14	16	$d(T)$	2.3-4.0	$\pm 6 \times 10^5$	$\pm 4 \times 10^{-3}$
4.15	17	$d(T)$	0.0-1.4	$\pm 1.2 \times 10^5$	$\pm 8 \times 10^{-3}$
4.16	17	$d(T)$	1.7-3.2	$\pm 1.2 \times 10^5$	$\pm 8 \times 10^{-3}$
4.17	18	$d(T)$	0.0-1.4	$\pm 6 \times 10^6$	$\pm 3 \times 10^{-2}$
4.18	18	$d(T)$	1.7-3.1	$\pm 6 \times 10^6$	$\pm 3 \times 10^{-2}$
4.19	19	$d(T)$	0.0-1.3	$\pm 9 \times 10^6$	$\pm 3 \times 10^{-2}$
4.20	19	$d(T)$	1.5-3.0	$\pm 9 \times 10^6$	$\pm 3 \times 10^{-2}$

TABLE 4.4.  $d(T)$  Figures

Time-span is given in fractions of convective-times (CTs) with respect to the time of the first plot. The “f.d. limits” is the fractional difference based on the lateral average for a given height.

elapsed for the series of plots, and thus, the EGR can be effectively regarded as constant throughout the sequence.

For the figures, a 5-scale shading scheme is used. The caption of each figure details the specific values which correspond to these five shades, and a table summarizing this information is provided in the appropriate sub-sections below. In general, the 5-scale shading scheme can be summarized with the following guidelines in Table 4.3:

Tables 4.4, 4.5, 4.6, and 4.7 summarize important information regarding the following sub-sections of figures.

At each EGR level, plots for all quantities are at the same time slices. That is, the time-index of the first plot of the  $d(T)$  sequence for  $\log \text{EGR} = 16$  is the same as that of the first plot of the  $d(Y)$  sequence at the same EGR level. The same is true for every plot in the sequence at each EGR level for all quantities  $d(T)$ ,  $d(Y)$ , SAd, and SLed. Moreover, the dimensions of each plot, while different at different EGR levels in response to the changing

Figure	log EGR	Value	Time-span	$d(Y)$ limits	f.d. limits
4.21	16	$d(Y)$	0.0-1.9 CTs	$\pm 7 \times 10^{-3}$	$\pm 7 \times 10^{-3}$
4.22	16	$d(Y)$	2.3-4.0	$\pm 7 \times 10^{-3}$	$\pm 7 \times 10^{-3}$
4.23	17	$d(Y)$	0.0-1.4	$\pm 1 \times 10^{-2}$	$\pm 1 \times 10^{-2}$
4.24	17	$d(Y)$	1.7-3.2	$\pm 1 \times 10^{-2}$	$\pm 1 \times 10^{-2}$
4.25	18	$d(Y)$	0.0-1.4	$\pm 5 \times 10^{-2}$	$\pm 5 \times 10^{-2}$
4.26	18	$d(Y)$	1.7-3.1	$\pm 5 \times 10^{-2}$	$\pm 5 \times 10^{-2}$
4.27	19	$d(Y)$	0.0-1.3	$\pm 3 \times 10^{-2}$	$\pm 3 \times 10^{-2}$
4.28	19	$d(Y)$	1.5-3.0	$\pm 3 \times 10^{-2}$	$\pm 3 \times 10^{-2}$

TABLE 4.5.  $d(Y)$  Figures

Time-span is given in fractions of convective-times (CTs) with respect to the time of the first plot. The “f.d. limits” is the fractional difference based on the lateral average for a given height.

Figure	log EGR	Value	Time-span	SAd limits
4.29	16	SAd	0.0-1.9 CTs	$\pm 0.25$
4.30	16	SAd	2.3-4.0	$\pm 0.25$
4.31	17	SAd	0.0-1.4	$\pm 0.25$
4.32	17	SAd	1.7-3.2	$\pm 0.25$
4.33	18	SAd	0.0-1.4	$\pm 0.25$
4.34	18	SAd	1.7-3.1	$\pm 0.25$
4.35	19	SAd	0.0-1.3	$\pm 0.25$
4.36	19	SAd	1.5-3.0	$\pm 0.25$

TABLE 4.6. SAd Figures

Time-span is given in fractions of convective-times (CTs) with respect to the time of the first plot. No “f.d. limits” is calculated, since no lateral averages were used in making plots of SAd.

Figure	log EGR	Value	Time-span	SLed limits
4.37	16	SLed	0.0-1.9 CTs	$\pm 0.25$
4.38	16	SLed	2.3-4.0	$\pm 0.25$
4.39	17	SLed	0.0-1.4	$\pm 0.25$
4.40	17	SLed	1.7-3.2	$\pm 0.25$
4.41	18	SLed	0.0-1.4	$\pm 0.25$
4.42	18	SLed	1.7-3.1	$\pm 0.25$
4.43	19	SLed	0.0-1.3	$\pm 0.25$
4.44	19	SLed	1.5-3.0	$\pm 0.25$

TABLE 4.7. SLed Figures

Time-span is given in fractions of convective-times (CTs) with respect to the time of the first plot. No “f.d. limits” is calculated, since no lateral averages were used in making plots of SLed.

size of the convective region, are the same at a given EGR level for all quantities studied. Thus, while the contour patterns will be different depending on the quantity examined in each of the following sub-sections, the sequence of flow fields which are overlayed against the contour plots at a given EGR level will be the same for all quantities studied. For optimal contrast, the vectors in the flow fields are colored either black or white, depending on the dominant color of the contour plot.

**4.8.1. Temperature Fluctuations  $d(T)$ .** In this sub-section, temperature fluctuations  $d(T)$  are examined as contour plots over several convective timescales. That is, for each zone:

$$(4.5) \quad d(T)_{j,k} = T_{j,k} - T_{k\text{ave}}$$

where  $T_{k\text{ave}} = (\sum_{j=1}^{j_{\max}-1} T_{j,k}) / (j_{\max} - 1)$ , the lateral average of  $T$  at a given vertical height with coordinate  $k$ .

In principle,  $d(T)$  represents the relative temperature of a given zone compared to that of its surroundings. Warmer regions have more positive  $d(T)$ , while cooler regions have more negative  $d(T)$ . While numerous physical factors influence temperature (including thermal diffusion, burning, gravitational potential to do work on the system, and thermal advection), it is thermal advection which is the primary source which drives the temperature fluctuations  $d(T)$  at this timescale. As the contour plots of  $d(T)$  show, the contours of  $d(T)$  appear to form distinct structures which can be correlated with features in the flow field. Spatially localized pockets of  $d(T)$  having similar values and signs appear to be dynamically correlated with the flow field, behaving as if they were particles traveling in the currents.

In general, upflows are associated with positive  $d(T)$ , while downflows are associated with negative  $d(T)$ . This is physically consistent, since zones which have greater magnitudes of  $d(T)$  necessarily have lesser magnitudes of  $d(\rho)$ , and therefore rise due to buoyancy, resulting in upward flows. Conversely, zones with smaller values of  $d(T)$  have correspondingly greater values of  $d(\rho)$ , and thus sink, leading to downward flows. The flow fields and fluctuations vary on the same timescale. Moreover, as the magnitudes of the velocities increase, so do the magnitude of  $d(T)$ .

**4.8.1.1.  $d(T)$  at log EGR 16.** The sequence of plots in Figures 4.13 and 4.14 show the time-evolution of the contours of  $d(T)$  at log EGR 16 between 0.0 - 1.9, and 2.3 - 4.0 convective timescales, respectively, where the times are given with respect to the time of the first plot in Figure 4.13. The convective timescale at log EGR 16 is approximately 1000  $\mu\text{s}$ .

Color	Limits
Black	$d(T) < -4 \times 10^5$
Dark Gray	$-4 \times 10^5 < d(T) < -2 \times 10^5$
Gray	$-2 \times 10^5 < d(T) < +2 \times 10^5$
Light Gray	$+2 \times 10^5 < d(T) < +4 \times 10^5$
White	$d(T) > +4 \times 10^5$

TABLE 4.8. 5-shade Scheme for  $d(T)$  at log EGR 16

Distinct columns of more positive  $d(T)$  extend from the base of the convective region to the top, clearly associated with rising upflows. The return flows downward are characterized by more negative  $d(T)$  and are less distinct compared to the upflows using this particular scaling for the contour lines, but are nevertheless obvious.

The patterns of  $d(T)$  are clearly associated with the directions of the currents. For example, in the first plot of the sequence (upper left plot in Figure 4.13), the upflow is directed diagonally toward the upper right, and the pattern of positive  $d(T)$  is likewise oriented in that direction. As the updraft evolves in the subsequent plots in the same figure to a more vertical direction, the pattern of positive  $d(T)$  likewise shifts to follow the flow. Also, blobs where particularly positive values of  $d(T)$  are concentrated near the center of the base of the updraft can be observed to rise upward in the column, their progress resembling that of particles carried along with the local current. Once at the top of the convective region, the blobs gradually disperse in both directions and become less discernible at this scaling of the contour lines. Similarly, downward flows show organized, but less structured patterns of negative  $d(T)$  returning to the base of the convective region.

The 5-shade scheme for this EGR level is summarized in Table 4.8. For clarity, every other velocity vector is plotted in the flow field.

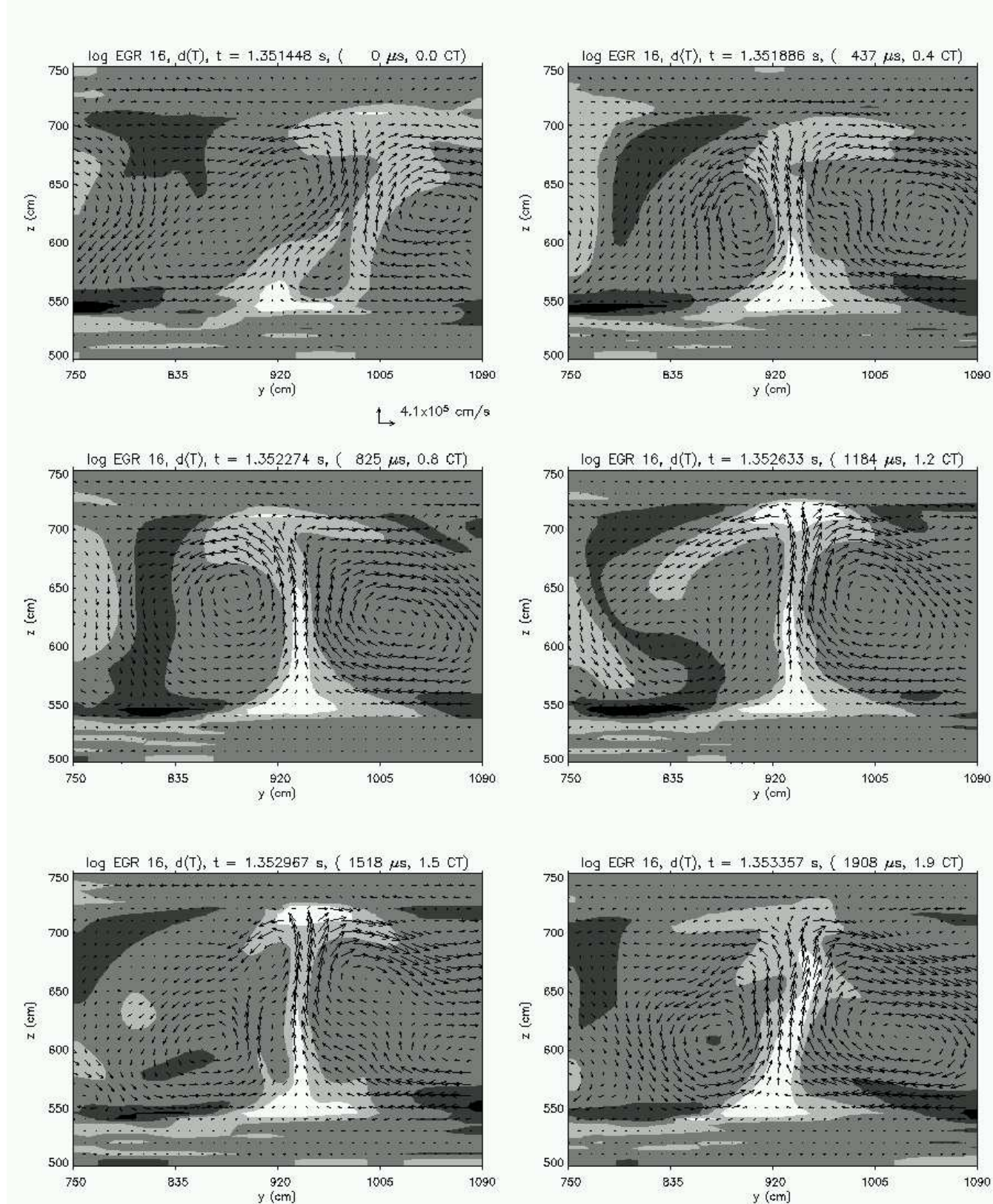


FIGURE 4.13. Contours of  $d(T)$  and Flow Field at log EGR = 16 A  
 $t = 0 - 1.9$  CT. See Table 4.8 for the gray scale legend.

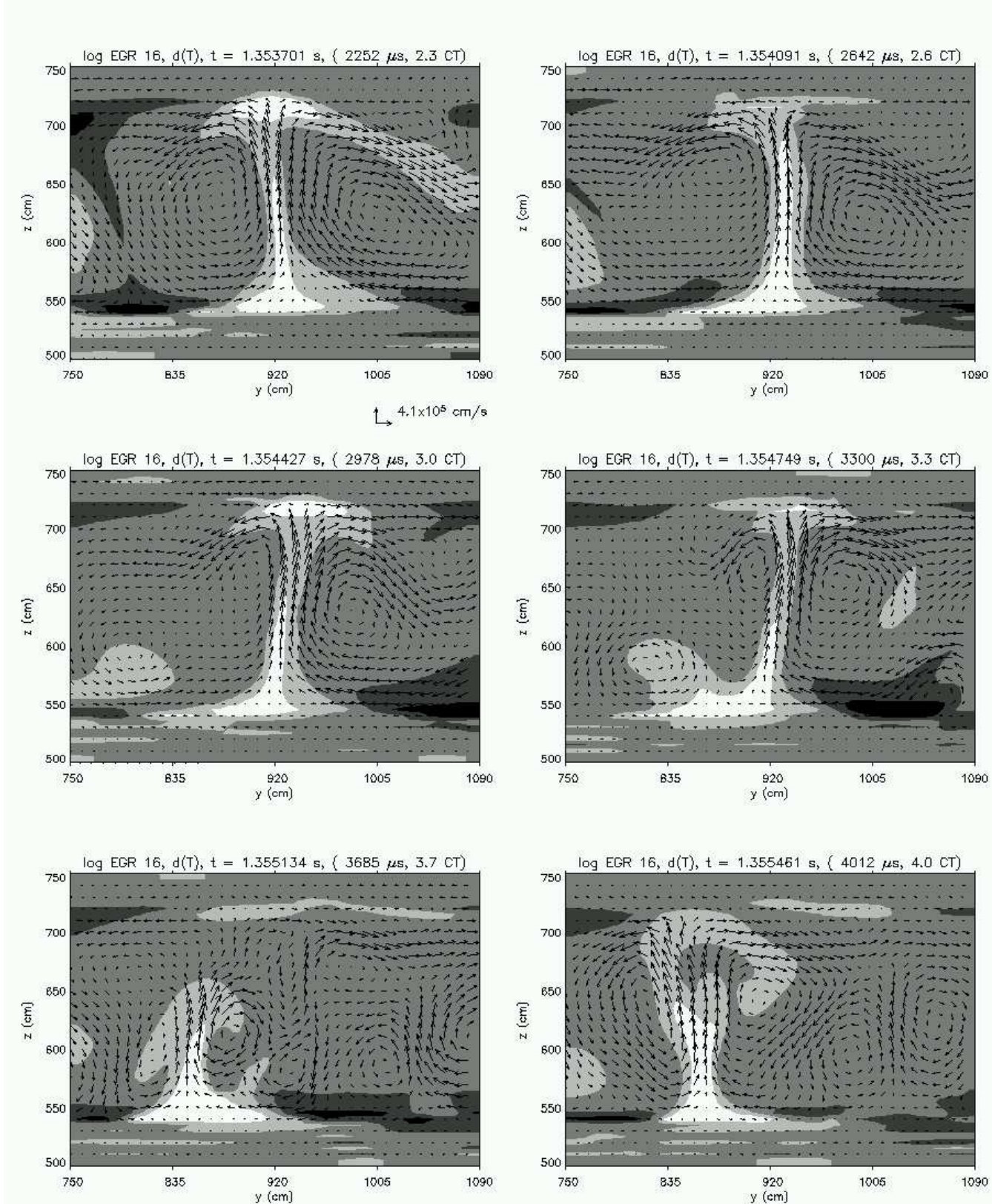


FIGURE 4.14. Contours of  $d(T)$  and Flow Field at log EGR = 16 B  
 $t = 2.3 - 4.0$  CT. See Table 4.8 for the gray scale legend.

4.8.1.2.  *$d(T)$  at log EGR 17.* The sequence of plots in Figures 4.15 and 4.16 show the time-evolution of the contours of  $d(T)$  at log EGR 17 between 0.0 - 1.4, and 1.7 - 3.2 convective timescales, respectively, where the times are given with respect to the time of the first plot in Figure 4.15. The convective timescale at log EGR 17 is approximately  $500 \mu\text{s}$ .

The convectively unstable region has clearly expanded upward. The sizes of major convective cells have likewise increased. The limits of the magnitudes of  $d(T)$  have doubled since the time the log EGR = 16, as have the characteristic magnitudes of the convective velocities ( $\sim 8 \times 10^5 \text{ cm s}^{-1}$ ). Both upflows and downflows are very distinctly characterized by positive and negative patterns of  $d(T)$ . As before, the rising columns of positive  $d(T)$  in upflows are more narrow and well-defined than the patterns of negative  $d(T)$  in downflows, which tend to be broader, more diffuse, and less collimated.

An interesting feature in the sequence of plots in these figures also illustrates one aspect of the nature of the dynamically shifting flow field: a downflow may develop in the exact position where an upflow once existed within a few convective times, and vice versa. Consider the strong upflow developing at longitudinal coordinate  $y = 1400 \text{ cm}$  near the middle of the plots of 4.15. In the sequence of six plots in this figure spanning 1.4 convective times, the upflow has developed from a bud one-third of the height of the convective region into a strongly developed flow extending the entire height of the convective region. The corresponding downward return flow to the left side of the upflow is also very evident at  $y = 1300 \text{ cm}$ . Then, during the next sequence of six plots in 4.16, the flows have dynamically reversed by  $t = 3.0$  convective times, so that now, a strong downflow occurs where an upflow had existed at  $y = 1400 \text{ cm}$ , and an upflow has replaced the downflow at  $y = 1300 \text{ cm}$ . Consistently, positive and negative patterns of  $d(T)$  have likewise switched positions.

Notice that this reversal of flow directions at specific points in the domain is not simply due to a bulk, lateral shifting of a complete cell, but that a very complicated series of reorganization occurs in the flow field, whereby a major cell breaks up into minor cells

Color	Limits
Black	$d(T) < -8 \times 10^5$
Dark Gray	$-8 \times 10^5 < d(T) < -4 \times 10^5$
Gray	$-4 \times 10^5 < d(T) < +4 \times 10^5$
Light Gray	$+4 \times 10^5 < d(T) < +8 \times 10^5$
White	$d(T) > +8 \times 10^5$

TABLE 4.9. 5-shade Scheme for  $d(T)$  at log EGR 17

and reorganizes into another major cell. This type of restructuring is characteristic of the dynamic evolution of the flow field.

The 5-shade scheme for this EGR level is summarized in Table 4.9. For clarity, every other velocity vector is plotted in the flow field.

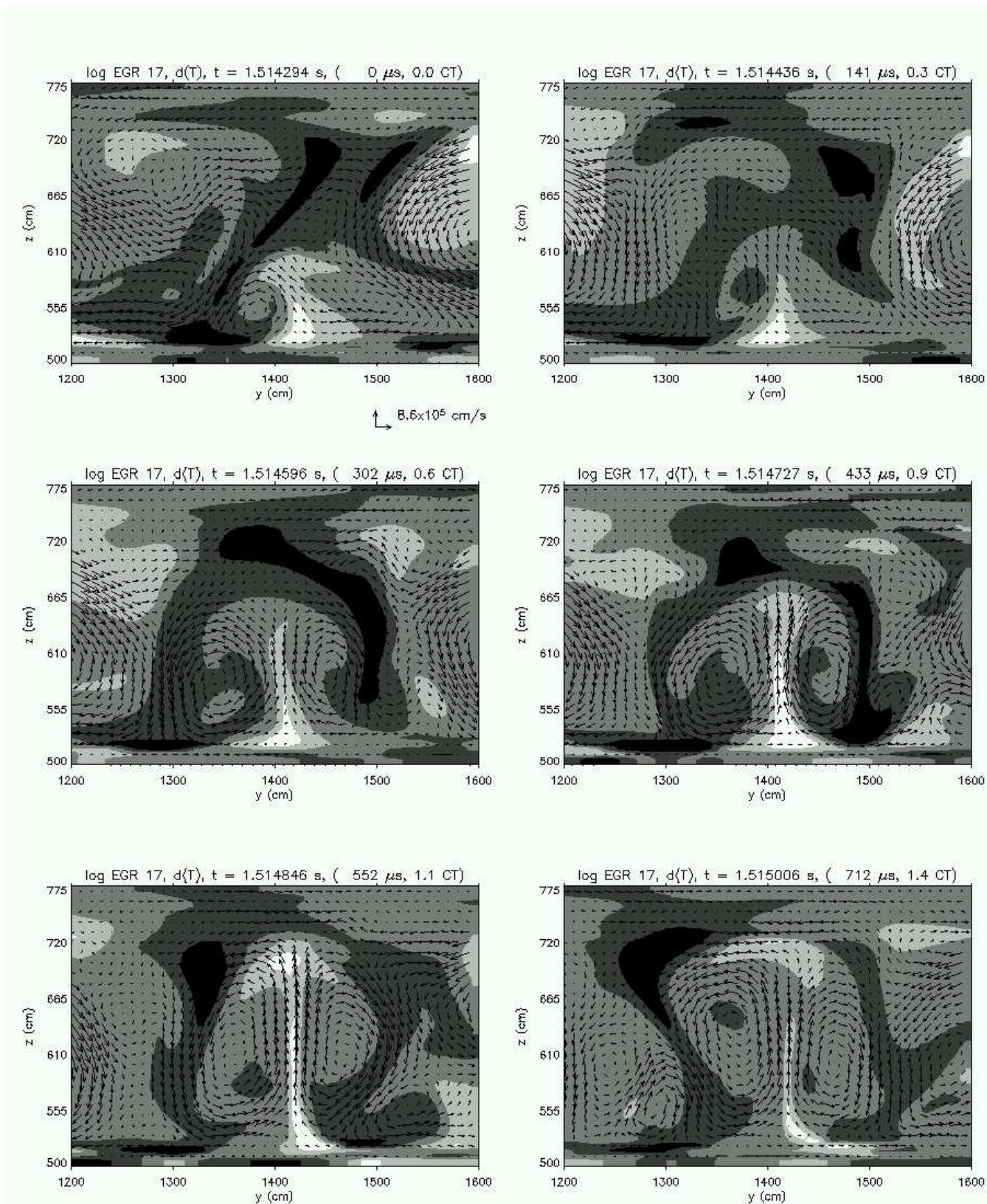


FIGURE 4.15. Contours of  $d(T)$  and Flow Field at log EGR = 17 A  
 $t = 0 - 1.4$  CT. See Table 4.9 for the gray scale legend.

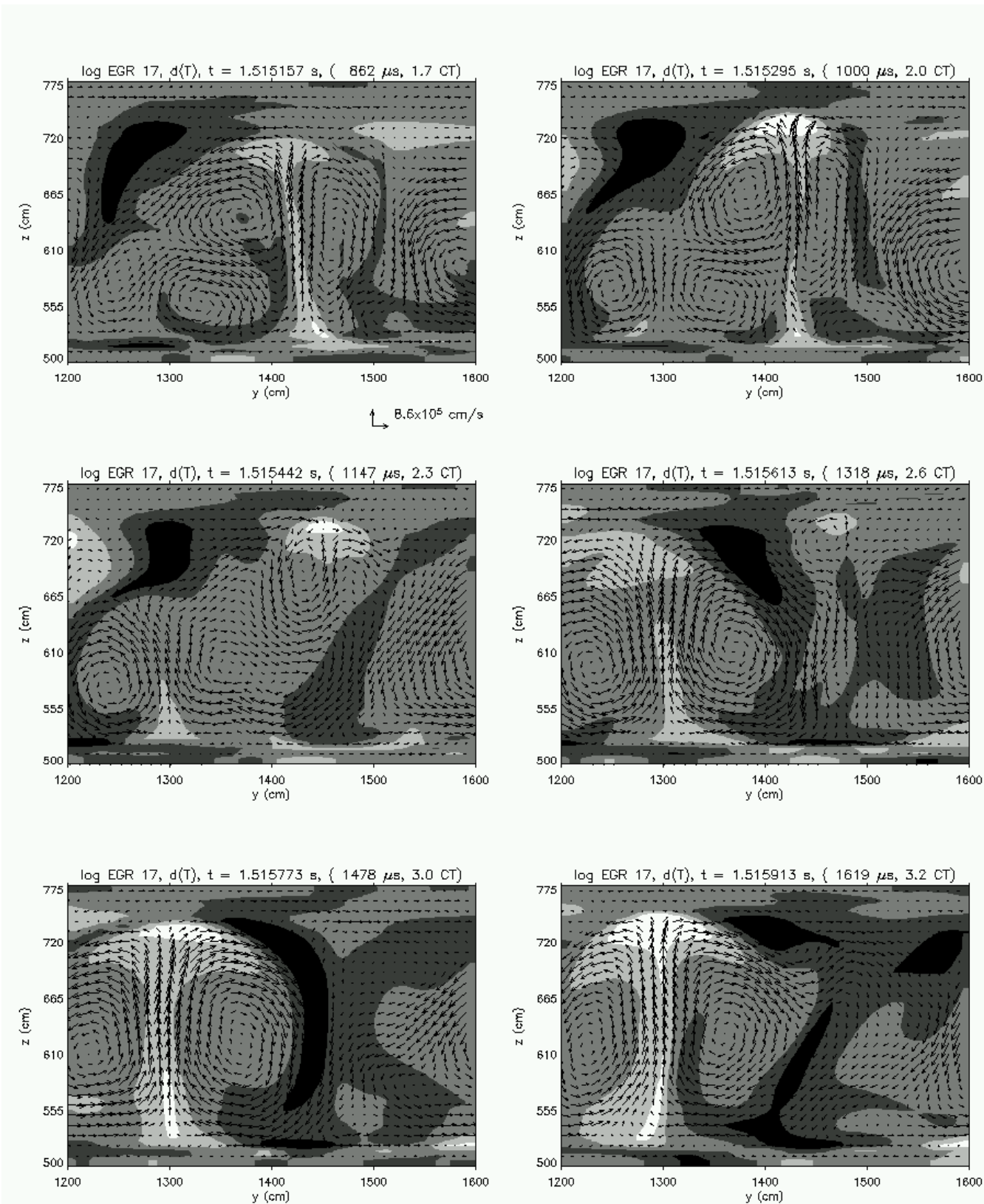


FIGURE 4.16. Contours of  $d(T)$  and Flow Field at  $\log \text{EGR} = 17$  B  
 $t = 1.7 - 3.2 \text{ CT}$ . See Table 4.9 for the gray scale legend.

Color	Limits
Black	$d(T) < -4 \times 10^6$
Dark Gray	$-4 \times 10^6 < d(T) < -2 \times 10^6$
Gray	$-2 \times 10^6 < d(T) < +2 \times 10^6$
Light Gray	$+2 \times 10^6 < d(T) < +4 \times 10^6$
White	$d(T) > +4 \times 10^6$

TABLE 4.10. 5-shade Scheme for  $d(T)$  at log EGR 18

4.8.1.3.  $d(T)$  at log EGR 18. The sequence of plots in Figures 4.17 and 4.18 show the time-evolution of the contours of  $d(T)$  at log EGR 18 between 0.0 - 1.4, and 1.7 - 3.1 convective timescales, respectively, where the times are given with respect to the time of the first plot in Figure 4.17. The convective timescale at log EGR 18 is approximately  $250 \mu s$ .

The extent of the convective region increased another 100 cm closer to the upper boundary of the domain. The limits of the magnitudes of  $d(T)$  have increased five-fold since the time when the log EGR = 17, as have characteristic magnitudes of the convective velocities ( $\sim 5 \times 10^6 \text{ cm s}^{-1}$ ). Rising columns of positive  $d(T)$  can be observed to extend from the base to the top of the region, and as before are better defined than falling patterns of negative  $d(T)$ . Major cells continue to dynamically evolve, changing flow directions rapidly, breaking up into smaller cells of varying aspect ratios, and reconstituting back into larger cells, all within a few convective times. The region below the base of the convective region exhibit more significant extremes of  $d(T)$ , because this is where the EGR and temperature are greatest, ultimately the source of the heating which is driving the convective motions.

The 5-shade scheme for this EGR level is summarized in Table 4.10. For clarity, every third velocity vector is plotted in the flow field.

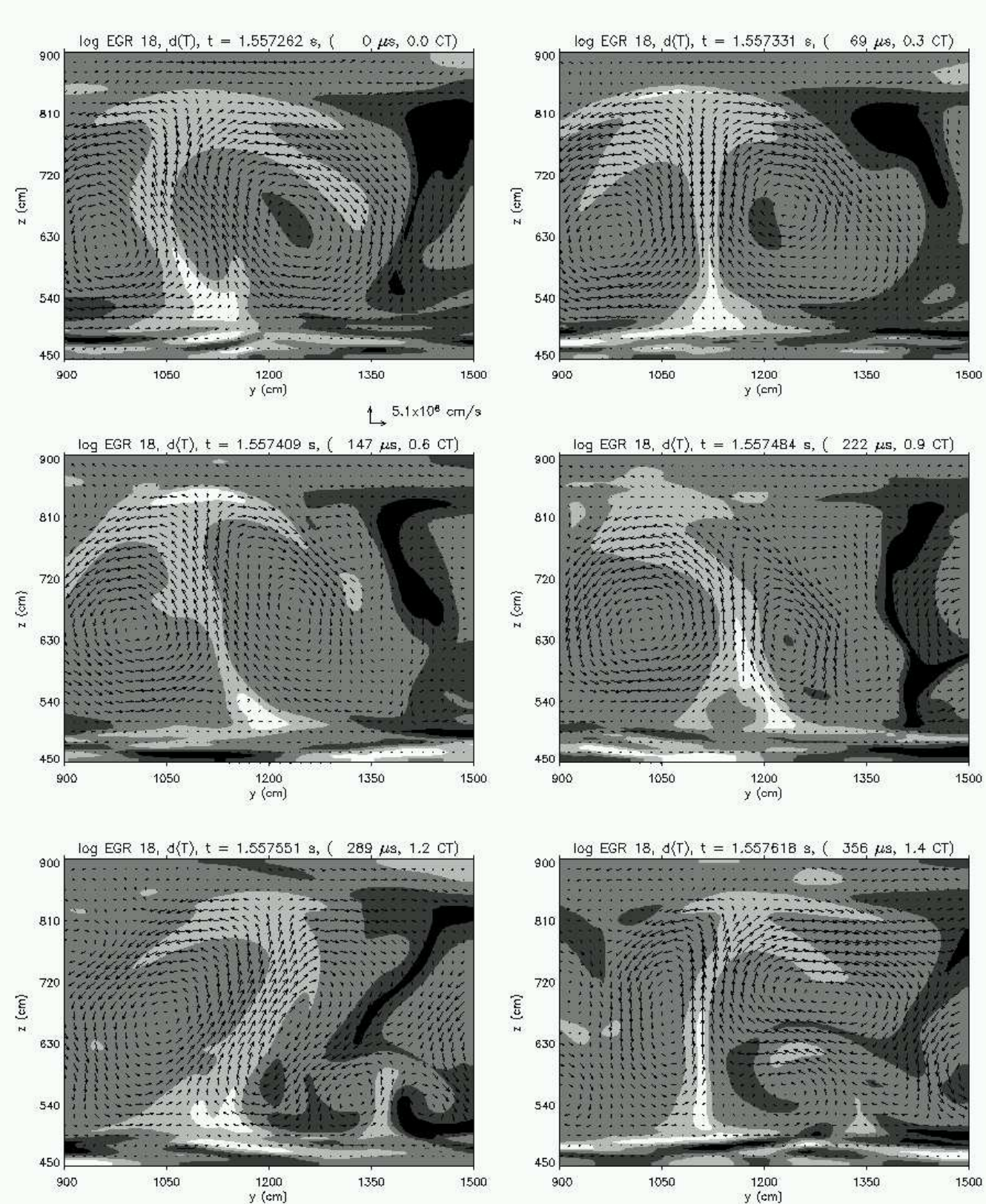


FIGURE 4.17. Contours of  $d(T)$  and Flow Field at  $\log \text{EGR} = 18$  A  
 $t = 0 - 1.4 \text{ CT}$ . See Table 4.10 for the gray scale legend.

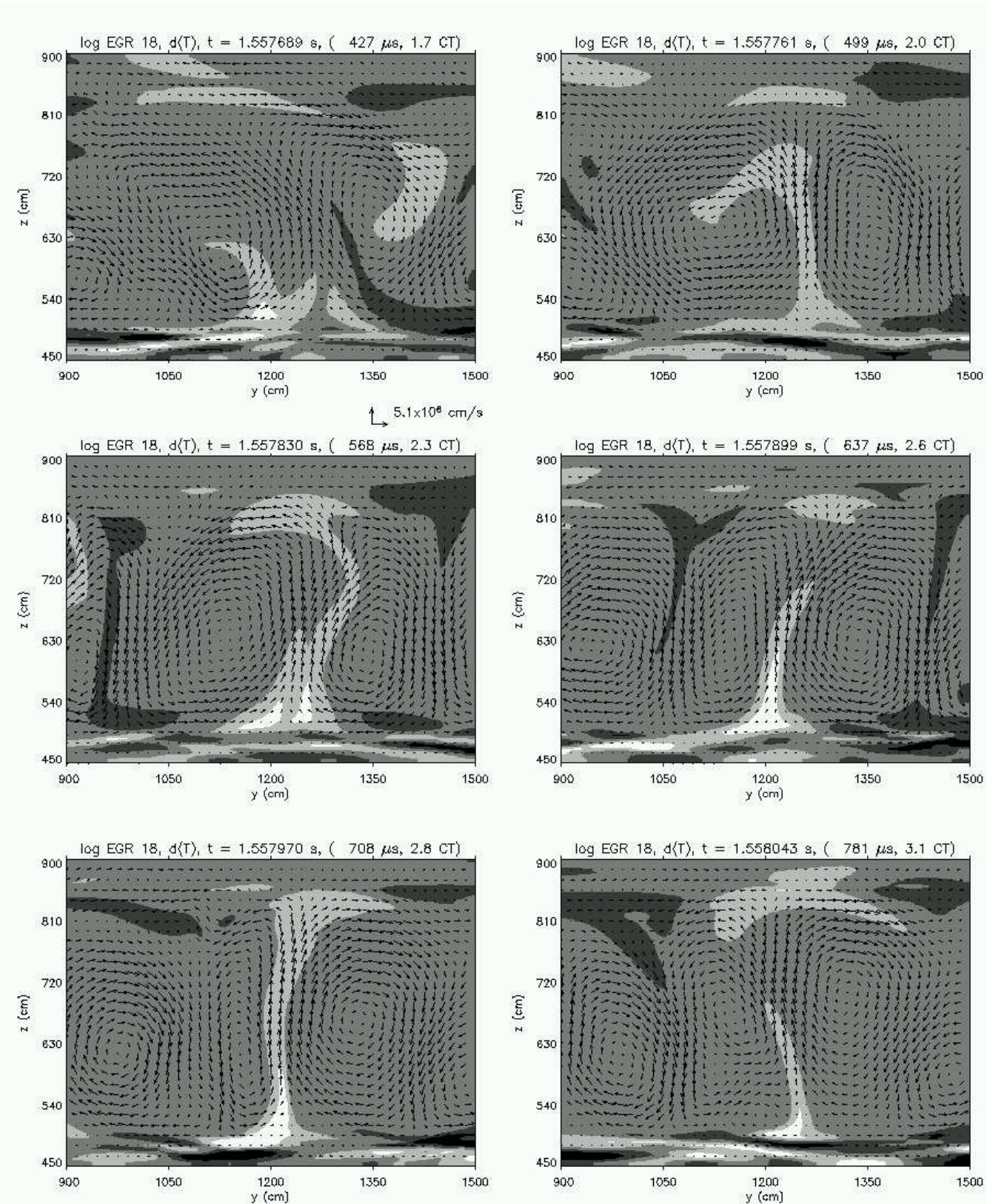


FIGURE 4.18. Contours of  $d(T)$  and Flow Field at  $\log \text{EGR} = 18$  B  
 $t = 1.7 - 3.1 \text{ CT}$ . See Table 4.10 for the gray scale legend.

Color	Limits
Black	$d(T) < -6 \times 10^6$
Dark Gray	$-6 \times 10^6 < d(T) < -3 \times 10^6$
Gray	$-3 \times 10^6 < d(T) < +3 \times 10^6$
Light Gray	$+3 \times 10^6 < d(T) < +6 \times 10^6$
White	$d(T) > +6 \times 10^6$

TABLE 4.11. 5-shade Scheme for  $d(T)$  at log EGR 19

4.8.1.4.  $d(T)$  at log EGR 19. The sequence of plots in Figures 4.19 and 4.20 show the time-evolution of the contours of  $d(T)$  at log EGR 19 between 0.0 - 1.3, and 1.5 - 3.0 convective timescales, respectively, where the times are given with respect to the time of the first plot in Figure 4.19. The convective timescale at log EGR 19 is approximately 150  $\mu$ s.

At log EGR = 19, the peak of the burst is nearly reached. The convective region has expanded to nearly touch the upper boundary of the domain. The limits of the magnitudes of  $d(T)$  have increased 50% from when the log EGR = 18, while characteristic magnitudes of the convective velocities have doubled ( $\sim 1 \times 10^7$  cm s $^{-1}$ ). Updrafts are clearly associated with patterns of positive  $d(T)$ . Patterns of negative  $d(T)$  are still generally found where downdrafts occur, but numerous negative  $d(T)$  regions exist as localized spots of various shapes and sizes near the center of the convective swirls. Sizable regions exhibiting significant contrasts in  $d(T)$  appearing at the upper boundary may be due to boundary effects.

The 5-shade scheme for this EGR level is summarized in Table 4.11. For clarity, every fourth velocity vector is plotted in the flow field.

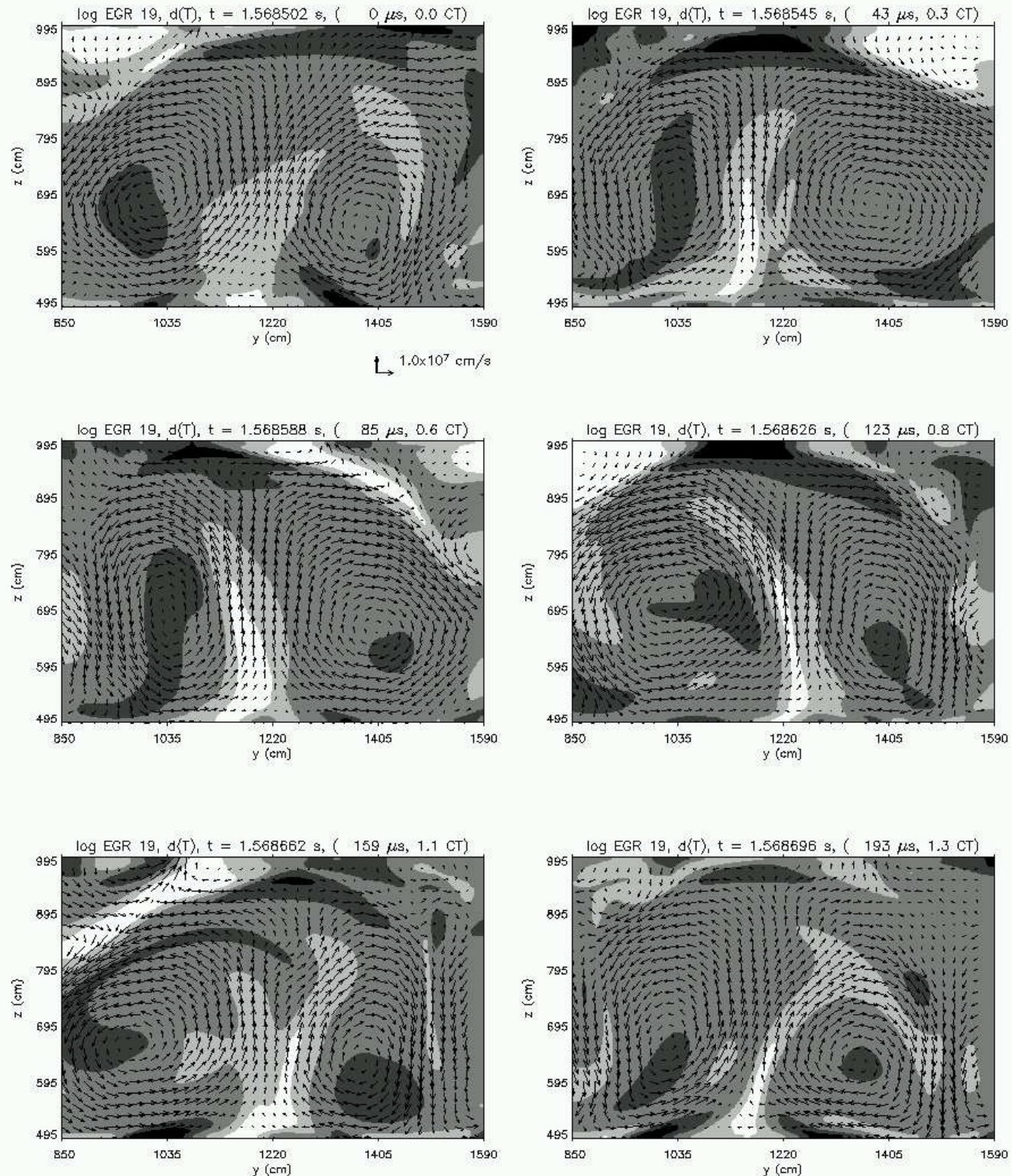


FIGURE 4.19. Contours of  $d(T)$  and Flow Field at  $\log \text{EGR} = 19$  A  
 $t = 0 - 1.3 \text{ CT}$ . See Table 4.11 for the gray scale legend.

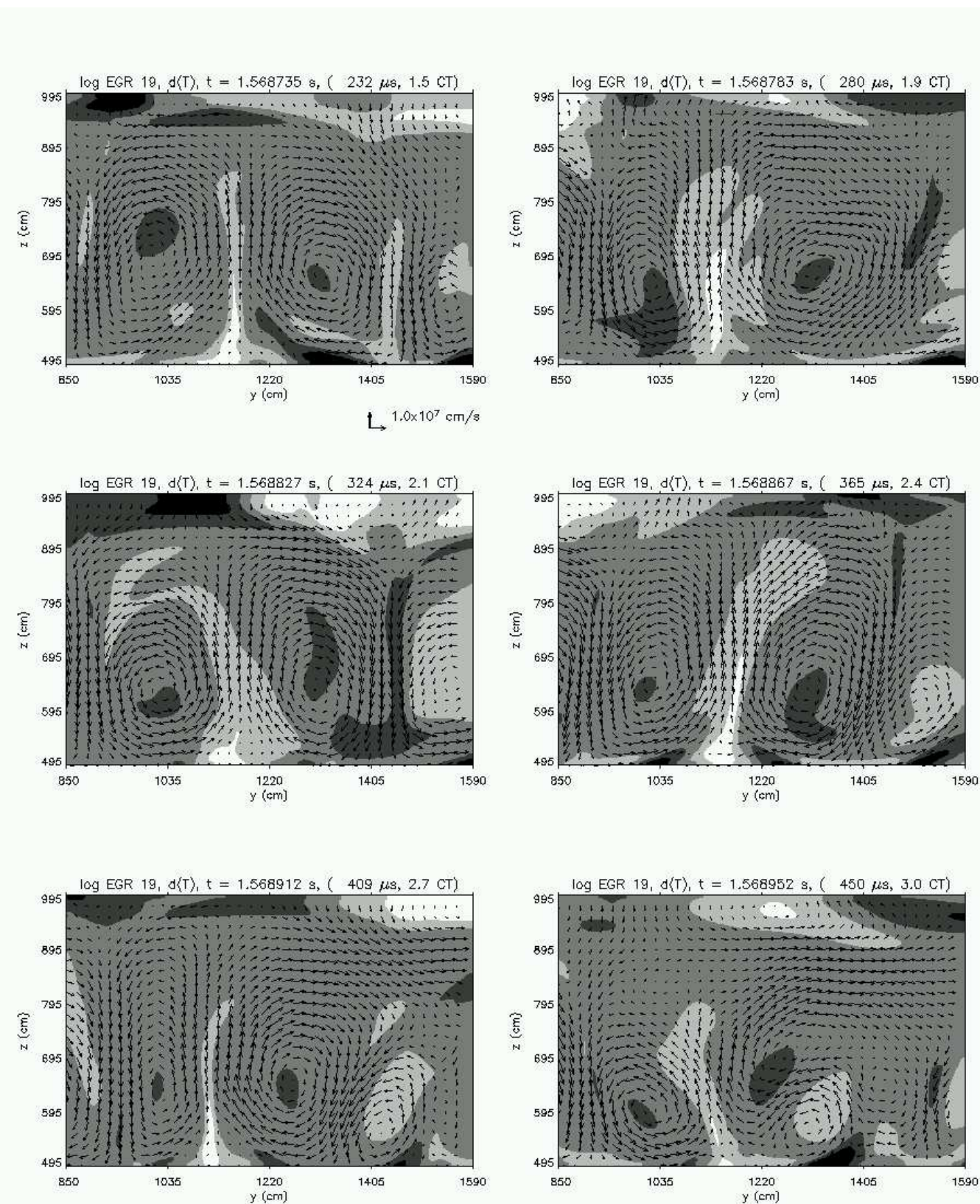


FIGURE 4.20. Contours of  $d(T)$  and Flow Field at log EGR = 19 B  
 $t = 1.5 - 3.0$  CT. See Table 4.11 for the gray scale legend.

**4.8.2. He4 Fluctuations  $d(Y)$ .** In this sub-section, fluctuations in the composition  $d(Y)$  {or  $d(He4)$ } are examined as contour plots over several convective timescales. That is, for each zone:

$$(4.6) \quad d(Y)_{j,k} = Y_{j,k} - Y_{k\text{ave}}$$

where  $Y_{k\text{ave}} = (\sum_{j=1}^{j_{\max}-1} Y_{j,k}) / (j_{\max} - 1)$ , the lateral average of  $Y$  at a given vertical height with coordinate  $k$ .

In the same sense as  $d(T)$  in the previous sub-section, the quantity  $d(Y)$  relates the relative composition of a particular zone to that of its surroundings. The quantity  $d(\rho Y)$ , representing the lateral differences of the actual amount of He4, could in principle equally well be studied, but since the density is essentially laterally uniform, the quantity  $d(Y)$  effectively yields the same information as  $d(\rho Y)$  does. Zones characterized by an excess of He4 compared to its surroundings have positive  $d(Y)$ , while a deficit means  $d(Y)$  is negative. In the present calculations, nuclear burning is due solely to the  $3\alpha$  reaction ( $3\frac{4}{2}He \rightarrow \frac{12}{6}C$ ), and so the nuclear reactants He4 and products C12 are complementary; an excess of one implies a deficit of the other.

Physically, only two factors influence composition in the calculation: burning and advection. Over the times examined in the sequence of plots, advection dominates burning by several orders of magnitude, and is primarily responsible for fluctuations in  $Y$ .

Generally, upflows are associated with negative  $d(Y)$ , while downflows are associated with positive  $d(Y)$ . Interestingly, the reciprocal relationship was observed to be true for  $d(T)$  in the previous sub-section, and comparing the contour patterns of  $d(Y)$  with those of  $d(T)$  reveal this complementarity, feature for feature at all EGR levels. Why upflows are associated with deficits and not excesses of  $Y$  (and vice versa for downflows) is less obvious. In purely diffusional-thermal models, an analytical expression can be derived showing the

complementary relationship between  $T$  and  $Y$  (Matkowsky and Sivashinsky, 1979). Qualitatively, the physical basis for the complementary relationship in this simplified model is due to the effects of burning: relatively warmer regions have greater rates of reaction, and thus, deplete fuel faster. It is tempting to apply this simple picture to the current results which also associate warmer regions as having smaller concentrations of reactants. However, the timescales over which the fluctuations in  $Y$  occur is many orders of magnitudes smaller than the burning time scale, and thus the nature of  $d(Y)$  on these short timescales must be primarily due not to burning, but advection. Burning may play a very minor role, though its effects are insufficient to provide a satisfying explanation for how rapidly the relative amounts of  $d(Y)$  change. Still, the process of advection does not readily explain the polarity of  $d(Y)$  as it pertains to upflows and downflows, since the convective region lacks significant gradients in composition. If advection were the primary cause of the polarity, then  $d(Y)$  should be greater at the tail end of a given flow and smaller at the source of the flow. Yet, in the results, deficits are always associated with upflows, and excesses with downflows. At the time of this writing, exactly what causes this peculiar feature of the results is not fully understood. Nevertheless, both  $d(T)$  and  $d(Y)$  effectively reveal the dynamical nature of the instantaneous, local velocities at all EGR levels.

For clarity, every other velocity vector is plotted to make up the flow fields in the plots for log EGR 16 and 17, every third for log EGR 18, and every fourth for log EGR 19. To help facilitate comparison, the exact same time sequence of plots and the exact same dimensions of the plots are used at each EGR level as are used in the plots of the previous sub-section which examine  $d(T)$ .

Color	Limits
Black	$d(Y) < -4 \times 10^{-3}$
Dark Gray	$-4 \times 10^{-3} < d(Y) < -2 \times 10^{-3}$
Gray	$-2 \times 10^{-3} < d(Y) < +2 \times 10^{-3}$
Light Gray	$+2 \times 10^{-3} < d(Y) < +4 \times 10^{-3}$
White	$d(Y) > +4 \times 10^{-3}$

TABLE 4.12. 5-shade Scheme for  $d(Y)$  at log EGR 16

4.8.2.1.  $d(Y)$  at log EGR 16. The sequence of plots in Figures 4.21 and 4.22 show the time-evolution of the contours of  $d(Y)$  at log EGR 16 between 0.0 - 1.9, and 2.3 - 4.0 convective timescales, respectively, where the times are given with respect to the time of the first plot in Figure 4.21. The convective timescale at log EGR 16 is approximately 1000  $\mu s$ .

As is observed in studying  $d(T)$ , upflows and downflows are associated with definite patterns of  $d(Y)$  having similar values and signs. Now, however, upflows are associated with columns of negative  $d(Y)$ , and downflows are characterized by patterns of positive  $d(Y)$ , opposite of what was observed to be true for  $d(T)$ . A direct comparison of the following sequence of plots of  $d(Y)$  with those in the previous sub-section of  $d(T)$  shows that the outlines of the major features in the contour plots are to a very high degree comparable, except for a reversal of color. Likewise, the dynamical evolution of the localized structures of  $d(Y)$  behave in the same way as those of  $d(T)$  on the same timescale.

Above and below the convective region, regions of significant  $d(Y)$  already appear to exist. This suggests substantial, dynamical fluctuations occur even at this relatively low EGR level. As the EGR continues to rise, the magnitude of these fluctuations and the rate at which they develop will also increase.

The 5-shade scheme for this EGR level is summarized in Table 4.12. For clarity, every other velocity vector is plotted in the flow field.

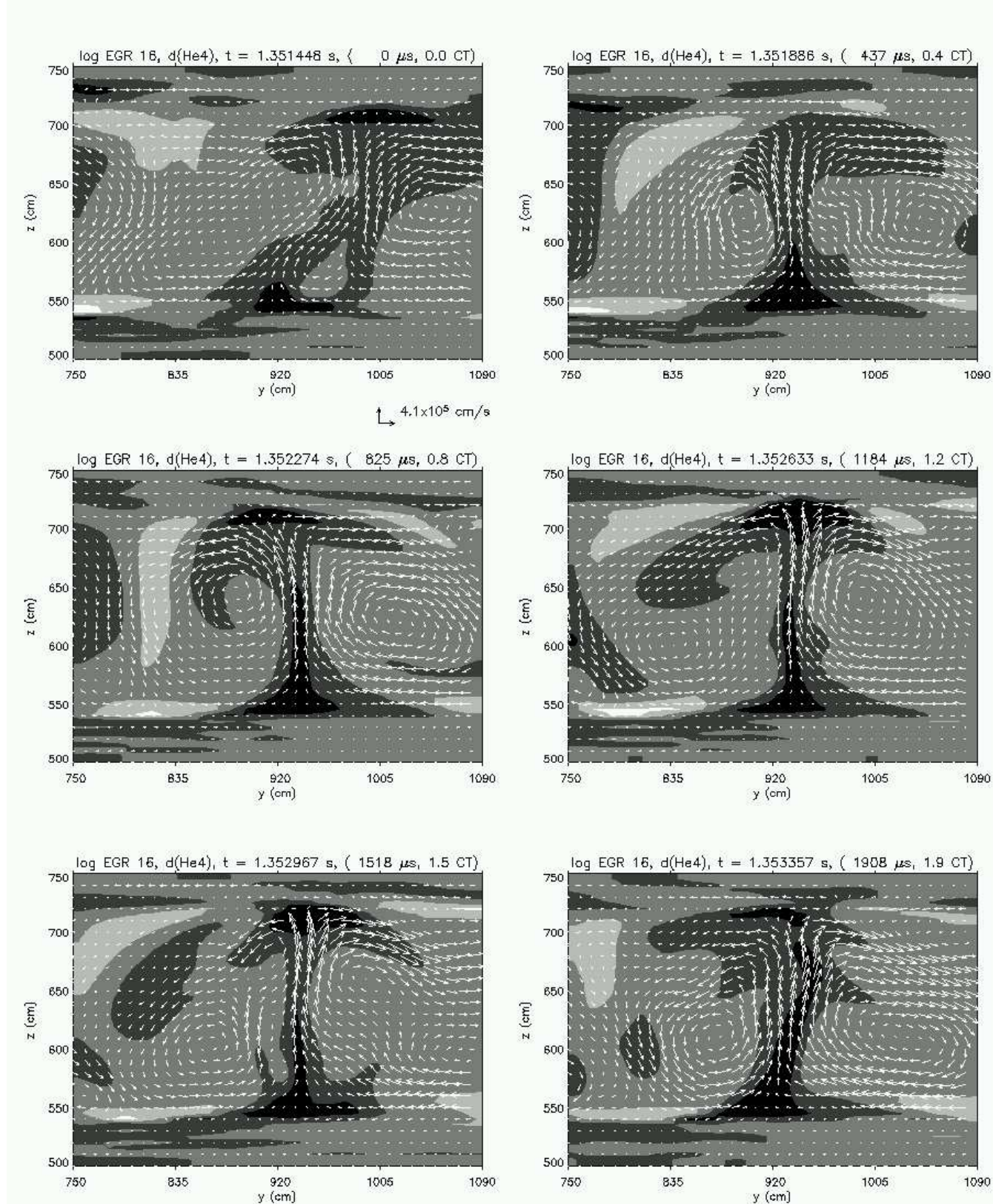


FIGURE 4.21. Contours of  $d(Y)$  and Flow Field at log EGR = 16 A  
 $t = 0 - 1.9$  CT. See Table 4.12 for the gray scale legend.

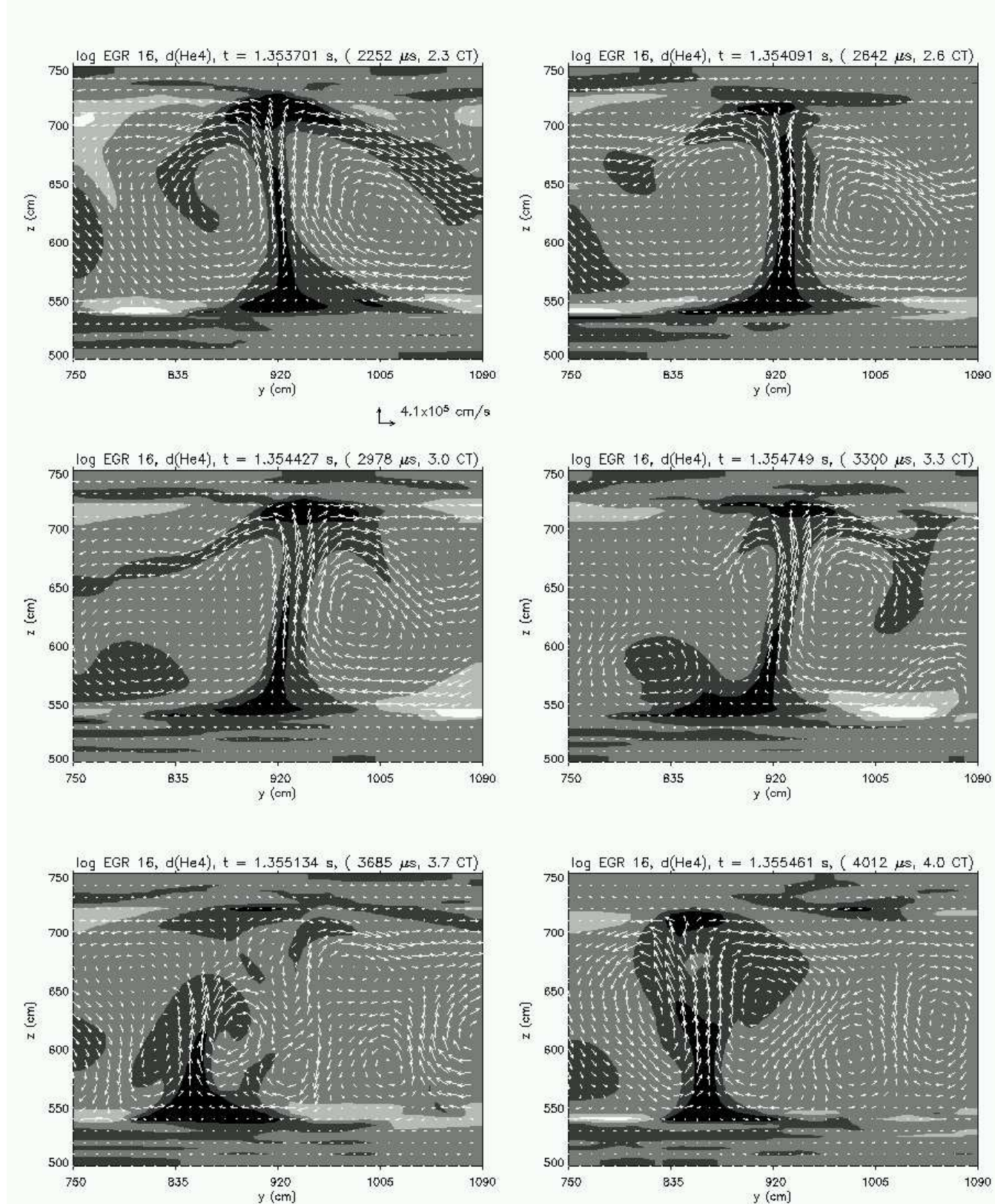


FIGURE 4.22. Contours of  $d(Y)$  and Flow Field at  $\log \text{EGR} = 16$  B  
 $t = 2.3 - 4.0$  CT. See Table 4.12 for the gray scale legend.

Color	Limits
Black	$d(Y) < -6 \times 10^{-3}$
Dark Gray	$-6 \times 10^{-3} < d(Y) < -3 \times 10^{-3}$
Gray	$-3 \times 10^{-3} < d(Y) < +3 \times 10^{-3}$
Light Gray	$+3 \times 10^{-3} < d(Y) < +6 \times 10^{-3}$
White	$d(Y) > +6 \times 10^{-3}$

TABLE 4.13. 5-shade Scheme for  $d(Y)$  at log EGR 17

4.8.2.2.  $d(Y)$  at log EGR 17. The sequence of plots in Figures 4.23 and 4.24 show the time-evolution of the contours of  $d(Y)$  at log EGR 17 between 0.0 - 1.4, and 1.7 - 3.2 convective timescales, respectively, where the times are given with respect to the time of the first plot in Figure 4.23. The convective timescale at log EGR 17 is approximately  $500 \mu s$ .

The limits of the magnitudes of  $d(Y)$  have increased over 40%, while the magnitudes of the characteristic velocities have doubled ( $\sim 8 \times 10^5 \text{ cm s}^{-1}$ ). The general association that upflows generally have negative  $d(Y)$  and downflows, positive  $d(Y)$ , still holds. Comparison with the sequence of plots of  $d(T)$  at log EGR = 17 clearly exhibit the complementary relationship between  $d(T)$  and  $d(Y)$ .

The 5-shade scheme for this EGR level is summarized in Table 4.13. For clarity, every other velocity vector is plotted in the flow field.

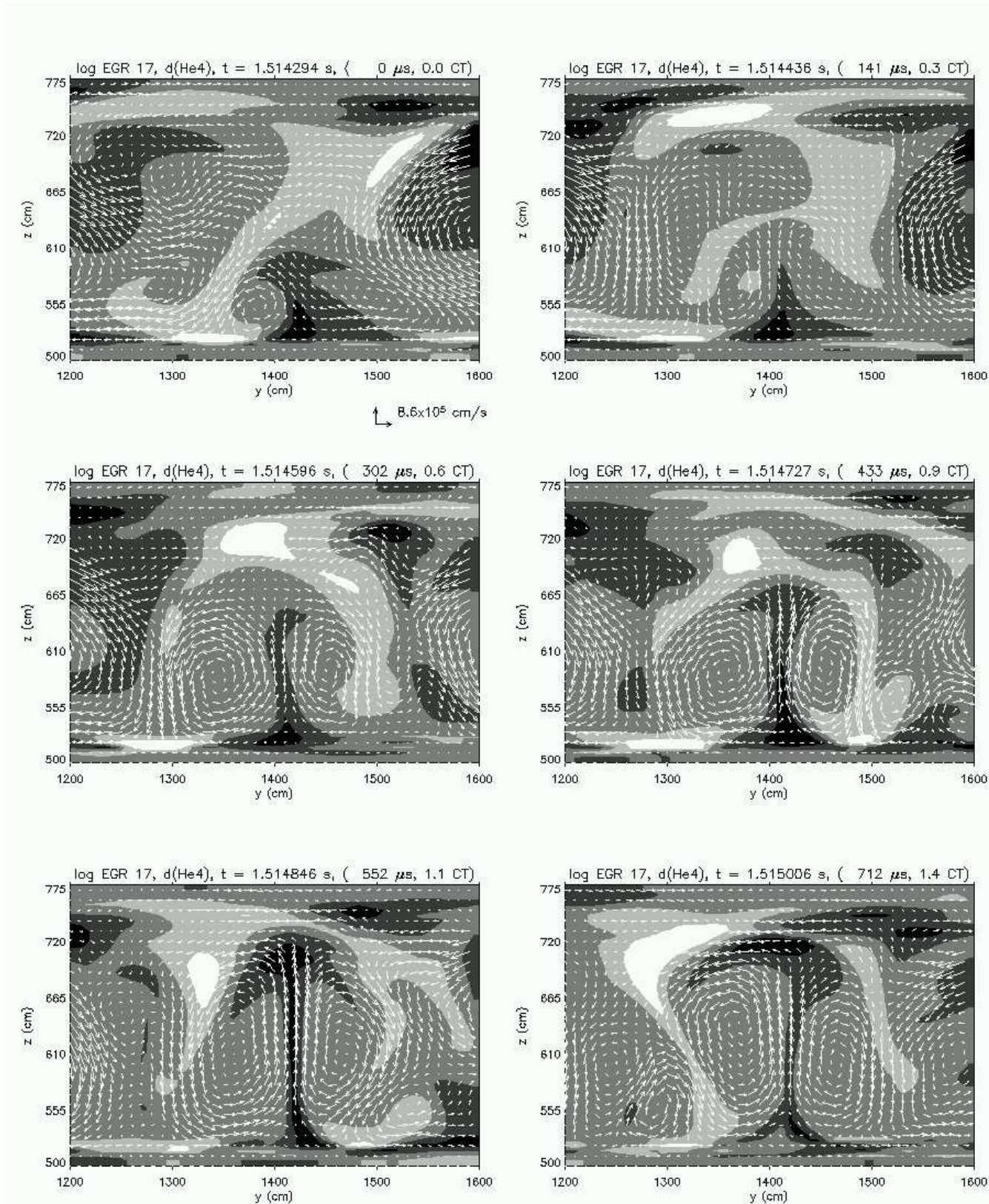


FIGURE 4.23. Contours of  $d(Y)$  and Flow Field at  $\log \text{EGR} = 17$  A  
 $t = 0 - 1.4 \text{ CT}$ . See Table 4.13 for the gray scale legend.

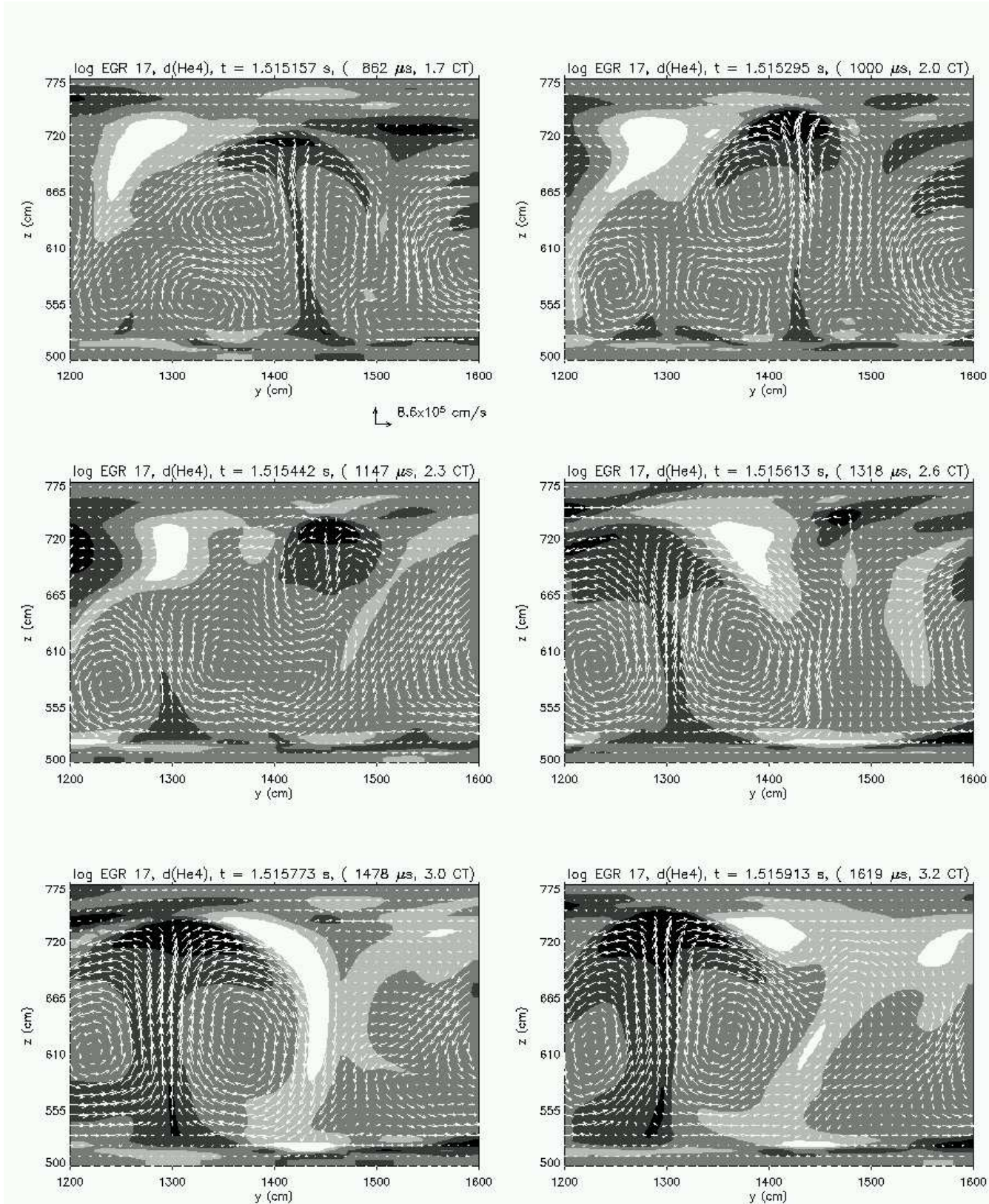


FIGURE 4.24. Contours of  $d(Y)$  and Flow Field at  $\log \text{EGR} = 17$  B  
 $t = 1.7 - 3.2 \text{ CT}$ . See Table 4.13 for the gray scale legend.

Color	Limits
Black	$d(Y) < -3 \times 10^{-2}$
Dark Gray	$-3 \times 10^{-2} < d(Y) < -1.5 \times 10^{-2}$
Gray	$-1.5 \times 10^{-2} < d(Y) < +1.5 \times 10^{-2}$
Light Gray	$+1.5 \times 10^{-2} < d(Y) < +3 \times 10^{-2}$
White	$d(Y) > +3 \times 10^{-2}$

TABLE 4.14. 5-shade Scheme for  $d(Y)$  at log EGR 18

4.8.2.3.  $d(Y)$  at log EGR 18. The sequence of plots in Figures 4.25 and 4.26 show the time-evolution of the contours of  $d(Y)$  at log EGR 18 between 0.0 - 1.4, and 1.7 - 3.1 convective timescales, respectively, where the times are given with respect to the time of the first plot in Figure 4.25. The convective timescale at log EGR 18 is approximately  $250 \mu s$ .

The limits of the magnitudes of  $d(Y)$  have increased five-fold since the time the log EGR = 17, as have characteristic magnitudes of the convective velocities ( $\sim 5 \times 10^6 \text{ cm s}^{-1}$ ). The complementary relationship between  $d(Y)$  and  $d(T)$  is still evident.

The 5-shade scheme for this EGR level is summarized in Table 4.14. For clarity, every third velocity vector is plotted in the flow field.

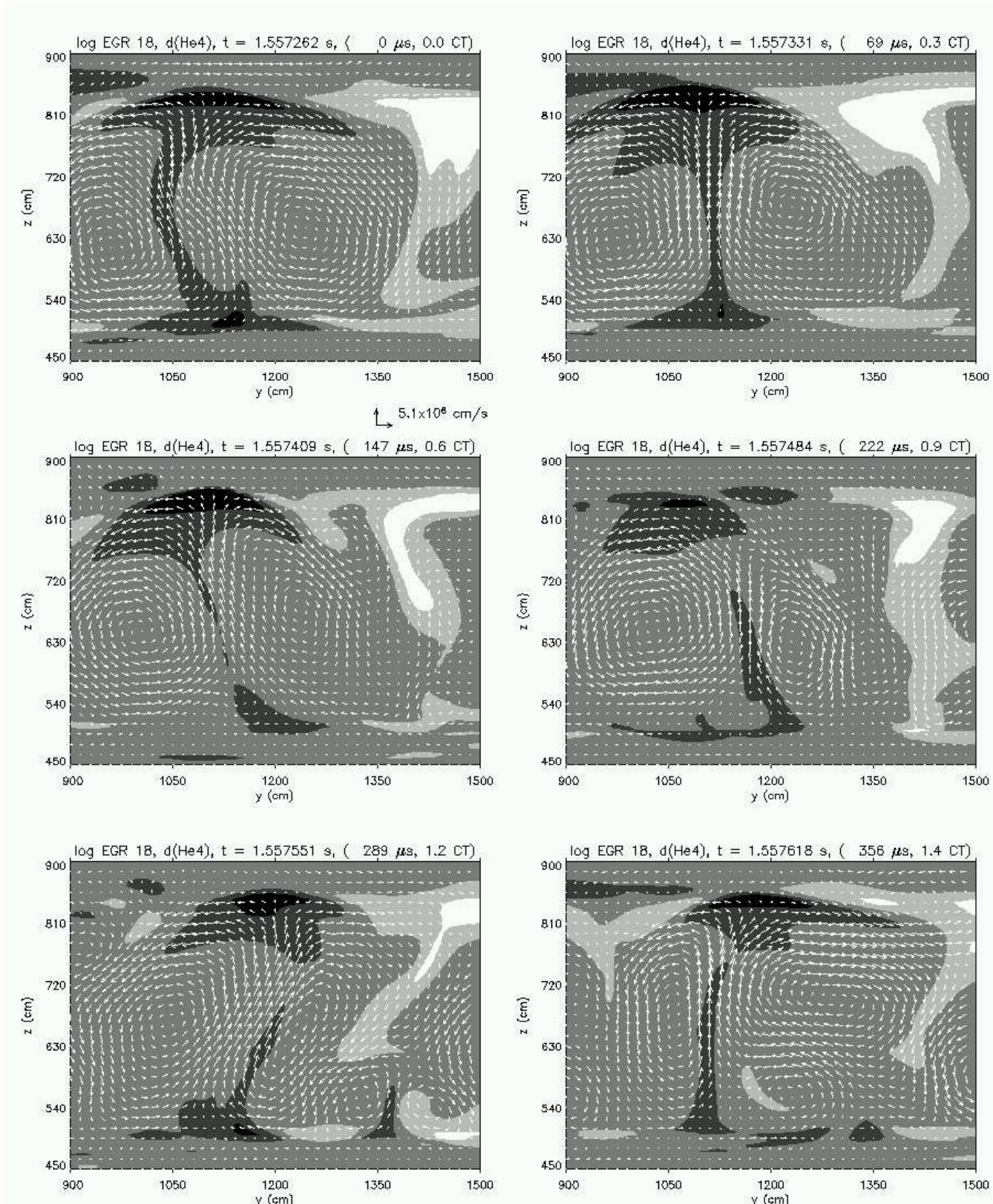


FIGURE 4.25. Contours of  $d(Y)$  and Flow Field at  $\log EGR = 18 A$   
 $t = 0 - 1.4 \text{ CT}$ . See Table 4.14 for the gray scale legend.

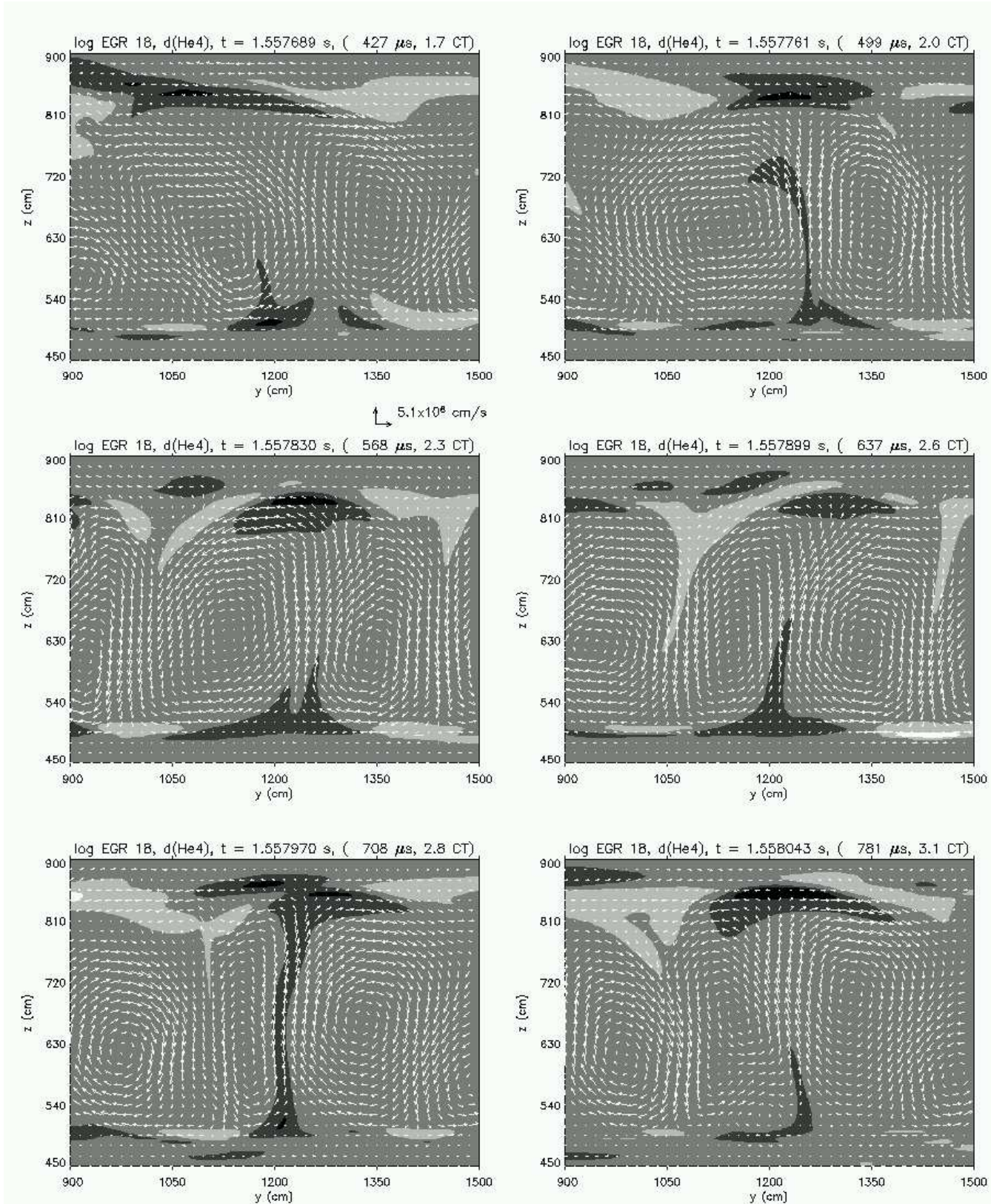


FIGURE 4.26. Contours of  $d(Y)$  and Flow Field at  $\log \text{EGR} = 18$  B  
 $t = 1.7 - 3.1 \text{ CT}$ . See Table 4.14 for the gray scale legend.

Color	Limits
Black	$d(Y) < -2 \times 10^{-2}$
Dark Gray	$-2 \times 10^{-2} < d(Y) < -1 \times 10^{-2}$
Gray	$-1 \times 10^{-2} < d(Y) < +1 \times 10^{-2}$
Light Gray	$+1 \times 10^{-2} < d(Y) < +2 \times 10^{-2}$
White	$d(Y) > +2 \times 10^{-2}$

TABLE 4.15. 5-shade Scheme for  $d(Y)$  at log EGR 19

4.8.2.4.  $d(Y)$  at log EGR 19. The sequence of plots in Figures 4.27 and 4.28 show the time-evolution of the contours of  $d(Y)$  at log EGR 19 between 0.0 - 1.3, and 1.5 - 3.0 convective timescales, respectively, where the times are given with respect to the time of the first plot in Figure 4.27. The convective timescale at log EGR 19 is approximately  $150 \mu s$ .

By  $\log \text{EGR} = 19$ , the star is essentially at the peak of the burst. The convective region has expanded to nearly touch the upper boundary of the domain. The limits of the magnitudes of  $d(Y)$  have actually decreased 60% since the time the  $\log \text{EGR} = 18$ , while characteristic magnitudes of the convective velocities have doubled ( $\sim 1 \times 10^7 \text{ cm s}^{-1}$ ). The decrease in the limits of the magnitudes of  $d(Y)$  is understandable, since by this time, the concentration has dropped over 60% from its initial values, and relative differences of composition between zones are correspondingly less. Still, upflows are generally associated with negative  $d(Y)$ , and the complementary relationship between  $d(Y)$  and  $d(T)$  is still very obvious.

The 5-shade scheme for this EGR level is summarized in Table 4.15. For clarity, every fourth velocity vector is plotted in the flow field.

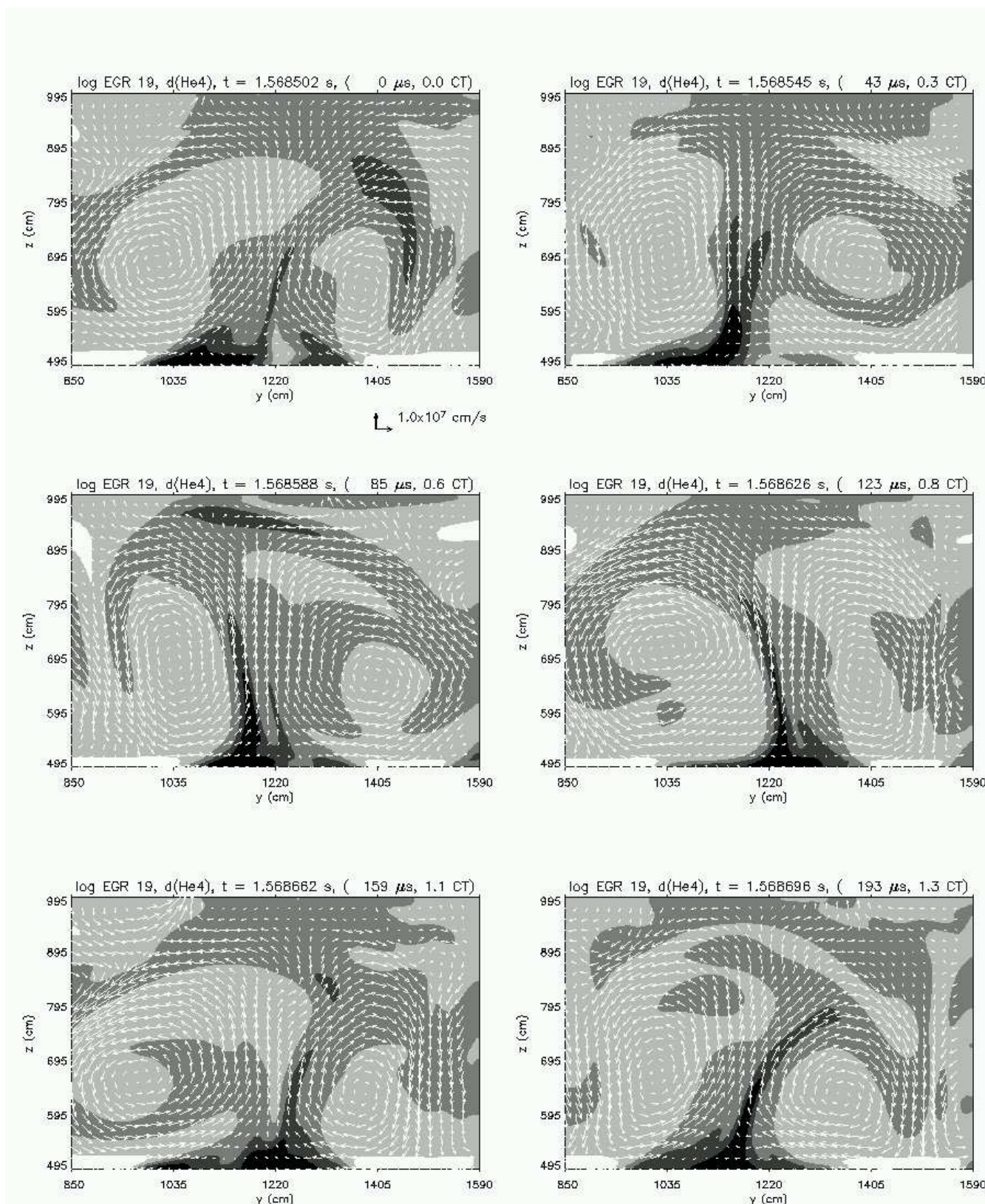


FIGURE 4.27. Contours of  $d(Y)$  and Flow Field at  $\log \text{EGR} = 19 \text{ A}$   
 $t = 0 - 1.3 \text{ CT}$ . See Table 4.15 for the gray scale legend.

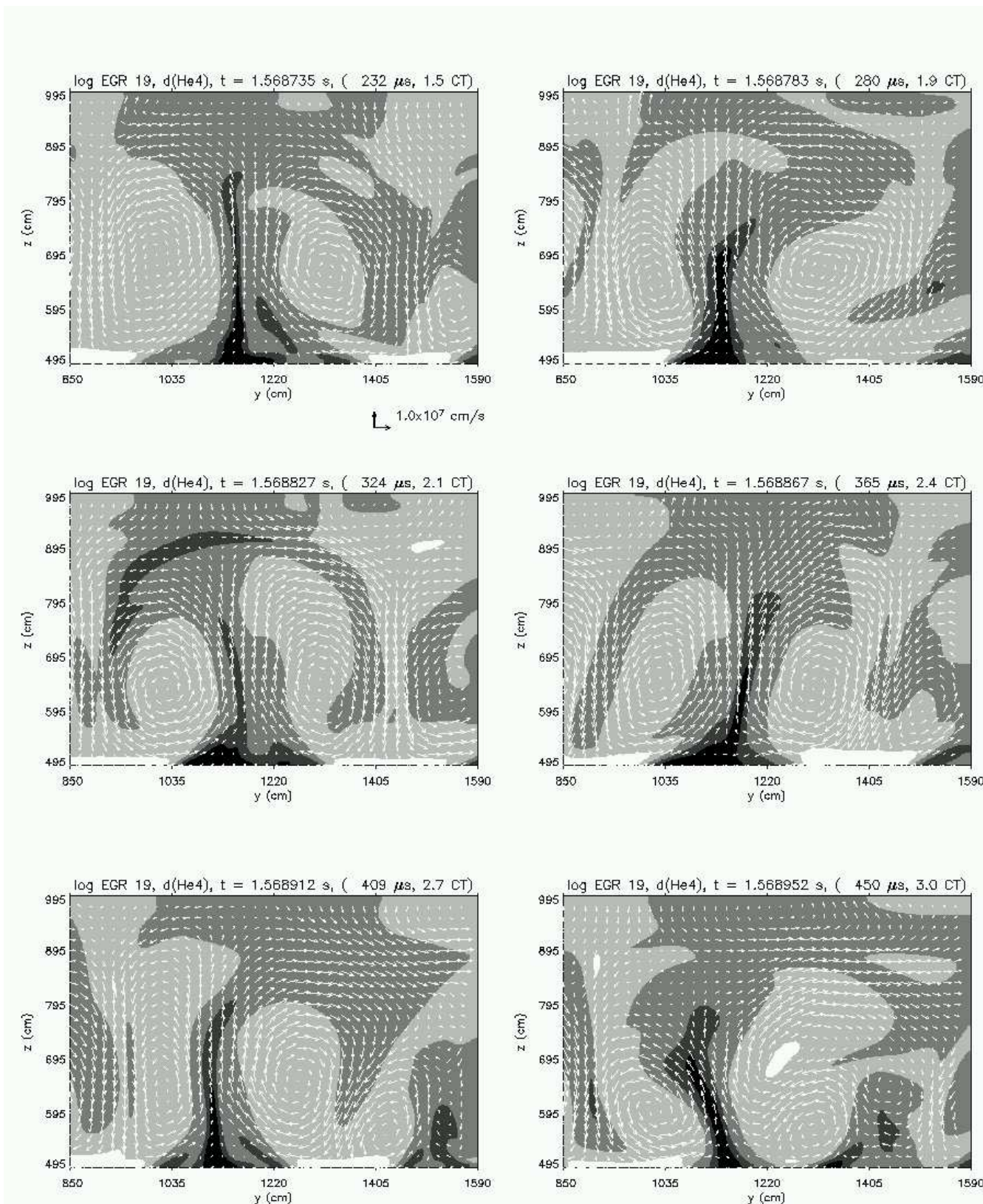


FIGURE 4.28. Contours of  $d(Y)$  and Flow Field at log EGR = 19 B  
 $t = 1.5 - 3.0 \text{ CT}$ . See Table 4.15 for the gray scale legend.

**4.8.3. SAd Fluctuations .** In this sub-section, fluctuations in the sub- or superadiabaticity (SAd), or the adiabatic excess, are examined as contour plots over several convective timescales. That is, for each zone:

$$(4.7) \quad SAd_{j,k} = \nabla_{j,k} - \nabla_{ad,j,k}$$

Locally, the SAd reflects the instantaneous fluctuation in the temperature gradient, and the figures in this section show these instantaneous values. On the other hand, to determine the overall convective tendency of a certain region, an average (over the lateral direction and time) of the SAd throughout the region is required. Such average quantities will be examined in detail in the next section (Section 4.9) to verify whether the Schwarzschild criteria is satisfied in the convective region. Thus, while localized groups of zones may have negative SAd at a specific time, they may still be part of a larger convective layer which is dynamically unstable by the Schwarzschild criteria. The figures in this sub-section should be appreciated in the proper perspective: regions where SAd is negative in the convective region merely indicate where the temperature gradient is momentarily sub-adiabatic. Nevertheless, interesting patterns and trends can be observed, which together provide a more complete understanding of the dynamic nature of the flow field.

Unlike  $d(T)$  and  $d(Y)$ , no obvious association exists between the structure of the patterns of SAd and the presence of upflows and downflows. An investigation to correlate the SAd with accurate predictors demonstrates that the total time-integrated change in the vertical gradient of  $Y$  due to advection is strongly correlated to the SAd of a particular zone. The same investigation also determined that the primary physical factor which influences whether the SAd is instantaneously and locally positive or negative is the total time-integrated effects of temperature advection. Finally, the total time-integrated change due to burning plays a minor but noticeable role, while the effect of thermal diffusion is entirely negligible.

Color	Limits
Black	$SAd < -0.1675$
Dark Gray	$-0.1675 < SAd < -0.0825$
Gray	$-0.0825 < SAd < +0.0825$
Light Gray	$+0.0825 < SAd < +0.1675$
White	$SAd > +0.1675$

TABLE 4.16. 5-shade Scheme for SAd at all EGR levels

To reiterate, the flow field may cause local gradients to become sub-adiabatic in the convective region on a rapid timescale, but the lateral and temporal averages of the temperature gradients in the convective region are superadiabatic by the Schwarzschild criteria, as expected.

The 5-shade scheme for all EGR levels in this sub-section on SAd is summarized in Table 4.16.

For clarity, every other velocity vector is plotted to make up the flow fields in the plots for log EGR 16 and 17, every third for log EGR 18, and every fourth for log EGR 19. To help facilitate comparison, the exact same time sequence of plots and the exact same dimensions of the plots are used at each EGR level as are used in the plots of the previous sub-sections which examine  $d(T)$  and  $d(Y)$ .

4.8.3.1. *SAd at log EGR 16.* The sequence of plots in Figures 4.29 and 4.30 show the time-evolution of the contours of SAd at log EGR 16 between 0.0 - 1.9, and 2.3 - 4.0 convective timescales, respectively, where the times are given with respect to the time of the first plot in Figure 4.29. The convective timescale at log EGR 16 is approximately  $1000 \mu s$ .

At the upper and lower edges of the plots, the black stripes indicating very sub-adiabatic regions of the domain clearly define where the convective region is vertically bounded. Convective cells form exclusively within these bounds.

While most of the convective region is nearly adiabatic, well-formed regions of sub-adiabaticity within the convective region are apparent. The sign of SAd in a given region is not consistently associated with the direction of the flows there, but is correlated with the time-integrated change of temperature and composition due to advection. The shapes and sizes of regions with slightly negative SAd change dynamically and are driven by the flow field.

Long, thin bands characterized by very positive SAd can be found to stretch along the lower and upper vertical limits of the convective region. These bands do not significantly change their shapes and positions during the several convective times depicted in the figures, suggesting they are not fluctuations driven by the flow field, as  $d(T)$  and  $d(Y)$  were demonstrated to be in the previous sub-sections. Rather, in Section 4.9, plots of laterally and temporally averaged SAd as a function of vertical position suggest that these bands occur where the actual gradient deviates from the Schwarzschild criteria to follow the Ledoux criteria instead, and are thus ultimately due to the composition gradients at the edges of the convective region at this low EGR level.

The 5-shade scheme for all EGR levels in this sub-section of SAd is summarized in Table 4.16. For clarity, every other velocity vector is plotted in the flow field.

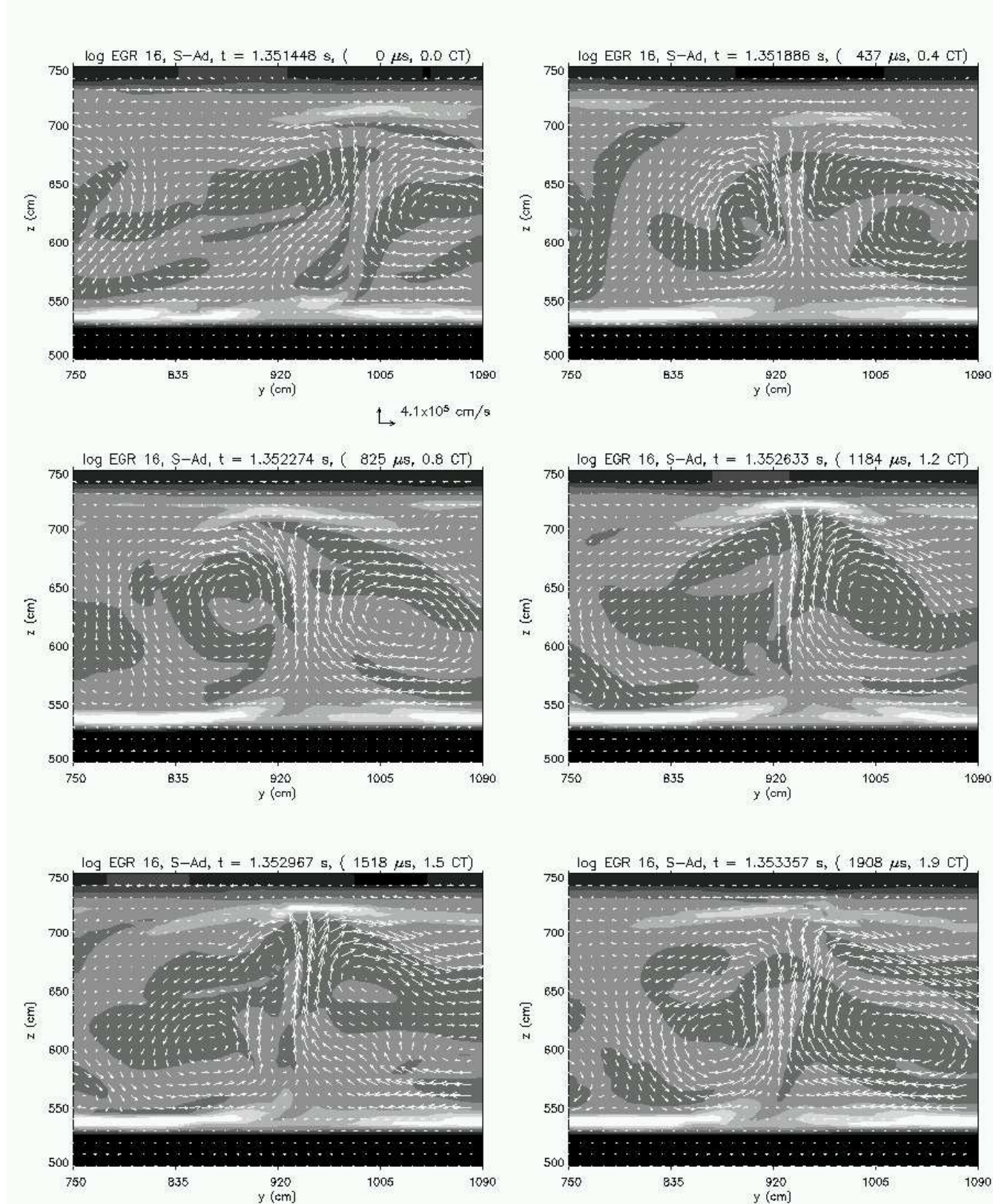


FIGURE 4.29. Contours of SAd and Flow Field at log EGR = 16 A  
 $t = 0 - 1.9 \text{ CT}$ . See Table 4.16 for the gray scale legend.

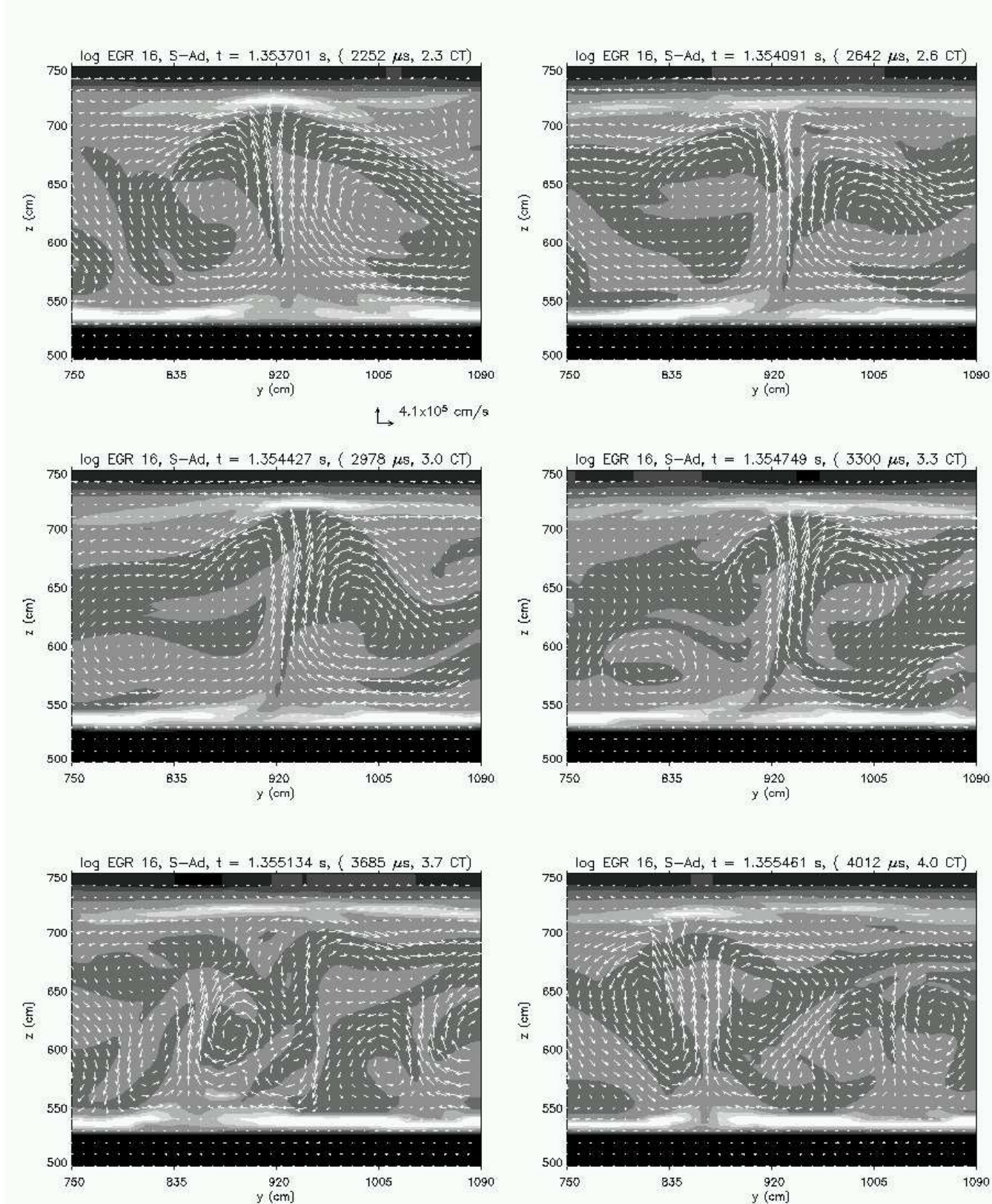


FIGURE 4.30. Contours of SAd and Flow Field at log EGR = 16 B  
 $t = 2.3 - 4.0$  CT. See Table 4.16 for the gray scale legend.

4.8.3.2. *SAd at log EGR 17.* The sequence of plots in Figures 4.31 and 4.32 show the time-evolution of the contours of SAd at log EGR 17 between 0.0 - 1.4, and 1.7 - 3.2 convective timescales, respectively, where the times are given with respect to the time of the first plot in Figure 4.31. The convective timescale at log EGR 17 is approximately 500  $\mu s$ .

The convective layer now shows significantly more regions where the SAd is slightly positive. Regions where SAd are very positive still stably persist at the lower and upper limits of the convective region due to the composition gradients there, but more dynamically changing pockets of positive SAd now emerge throughout the convective region. As before, sizable regions of slightly negative SAd also exist and evolve dynamically. Moreover, small pockets of very negative SAd can be found within the convective region, but they are relatively localized and rare. Still no consistent association between the direction of flow and the sign of SAd in a given region is apparent.

The 5-shade scheme for all EGR levels in this sub-section of SAd is summarized in Table 4.16. For clarity, every other velocity vector is plotted in the flow field.

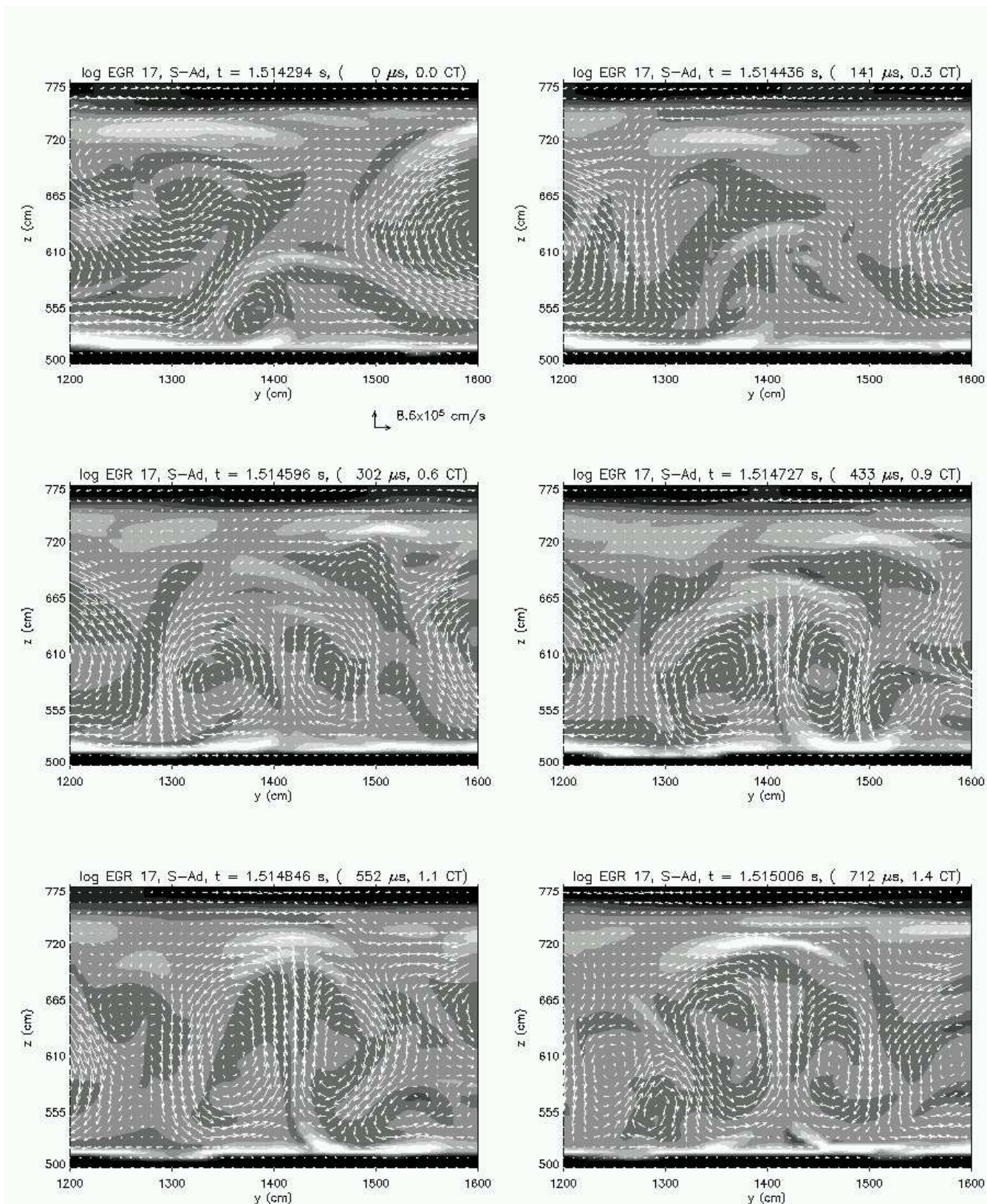


FIGURE 4.31. Contours of SAd and Flow Field at log EGR = 17 A  
 $t = 0 - 1.4$  CT. See Table 4.16 for the gray scale legend.

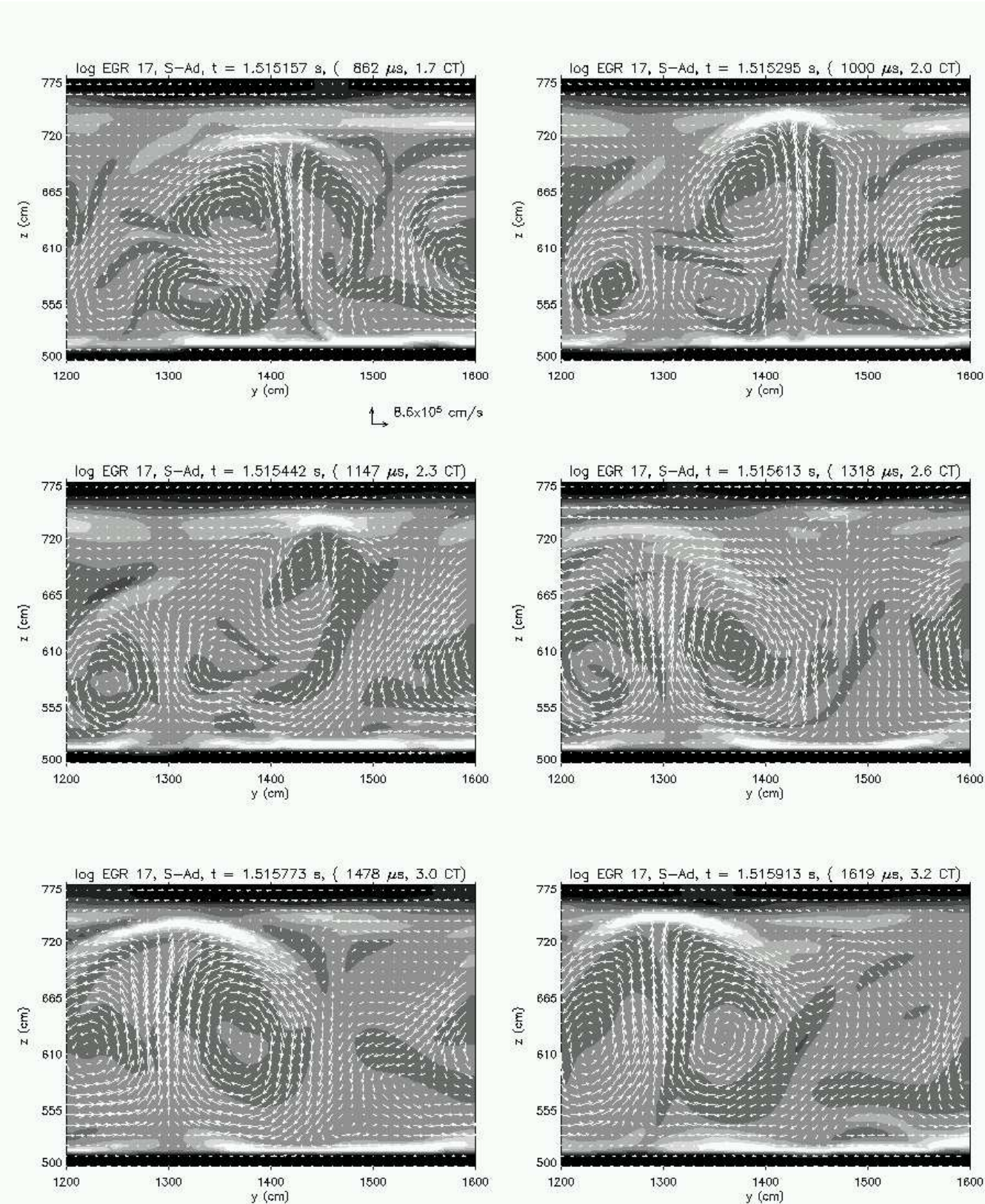


FIGURE 4.32. Contours of SAd and Flow Field at  $\log EGR = 17$  B  
 $t = 1.7 - 3.2$  CT. See Table 4.16 for the gray scale legend.

4.8.3.3. *SAd at log EGR 18.* The sequence of plots in Figures 4.33 and 4.34 show the time-evolution of the contours of SAd at log EGR 18 between 0.0 - 1.4, and 1.7 - 3.1 convective timescales, respectively, where the times are given with respect to the time of the first plot in Figure 4.33. The convective timescale at log EGR 18 is approximately  $250 \mu s$ .

The bands of very positive SAd have become very pronounced at the upper and lower limits of the convective region, as well as within it, and their sizes and shapes change dynamically. Regions characterized by slightly negative SAd appear to take up a sizable proportion of the convective region, and the sizes and frequency of regions with very negative SAd also increase within it.

The 5-shade scheme for all EGR levels in this sub-section of SAd is summarized in Table 4.16. For clarity, every third velocity vector is plotted in the flow field.

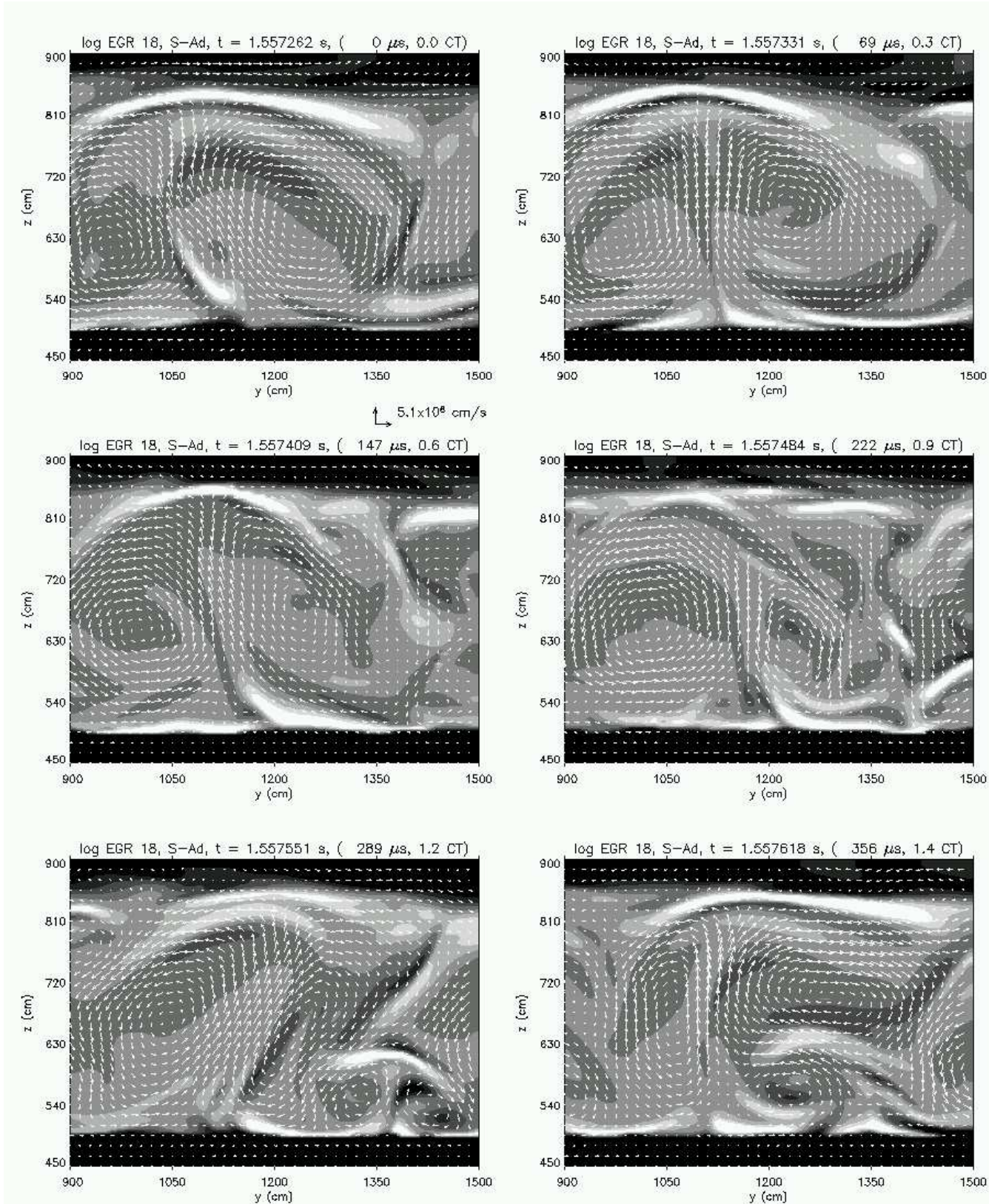


FIGURE 4.33. Contours of SAd and Flow Field at  $\log \text{EGR} = 18 \text{ A}$   
 $t = 0 - 1.4 \text{ CT}$ . See Table 4.16 for the gray scale legend.

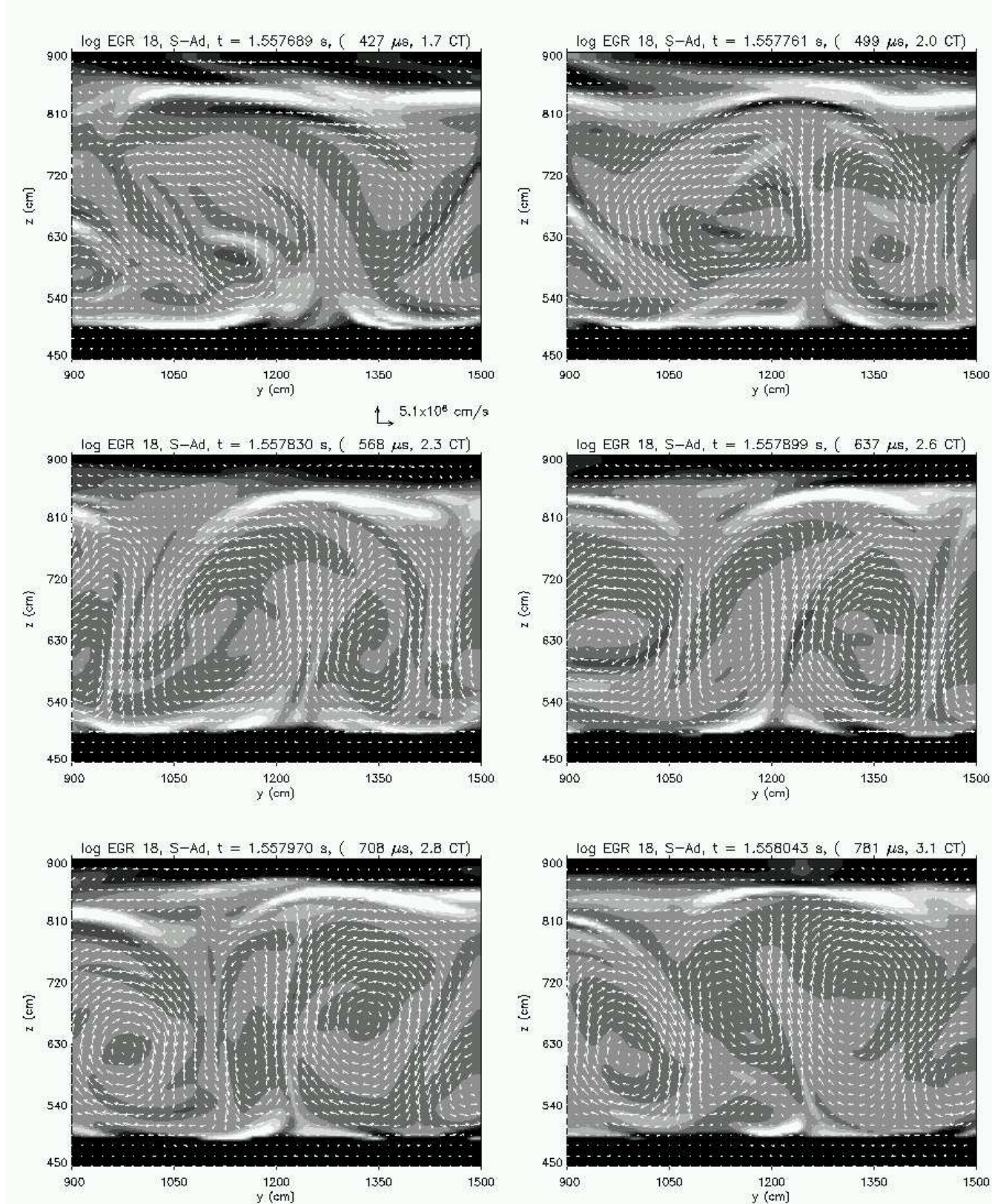


FIGURE 4.34. Contours of SAd and Flow Field at  $\log EGR = 18$  B  
 $t = 1.7 - 3.1$  CT. See Table 4.16 for the gray scale legend.

4.8.3.4. *SAd at log EGR 19.* The sequence of plots in Figures 4.35 and 4.36 show the time-evolution of the contours of SAd at log EGR 19 between 0.0 - 1.3, and 1.5 - 3.0 convective timescales, respectively, where the times are given with respect to the time of the first plot in Figure 4.35. The convective timescale at log EGR 19 is approximately  $150 \mu s$ .

The number of bands characterized by very positive SAd are noticeably fewer in number and smaller in size than before. Moreover, they no longer border the convective region as prominently as at previous EGR levels, primarily because the composition gradients there have greatly diminished at this time. Regions with slightly positive and negative SAd still make up a significant percentage of the convective region and dynamically evolve in time.

The 5-shade scheme for all EGR levels in this sub-section of SAd is summarized in Table 4.16. For clarity, every fourth velocity vector is plotted in the flow field.

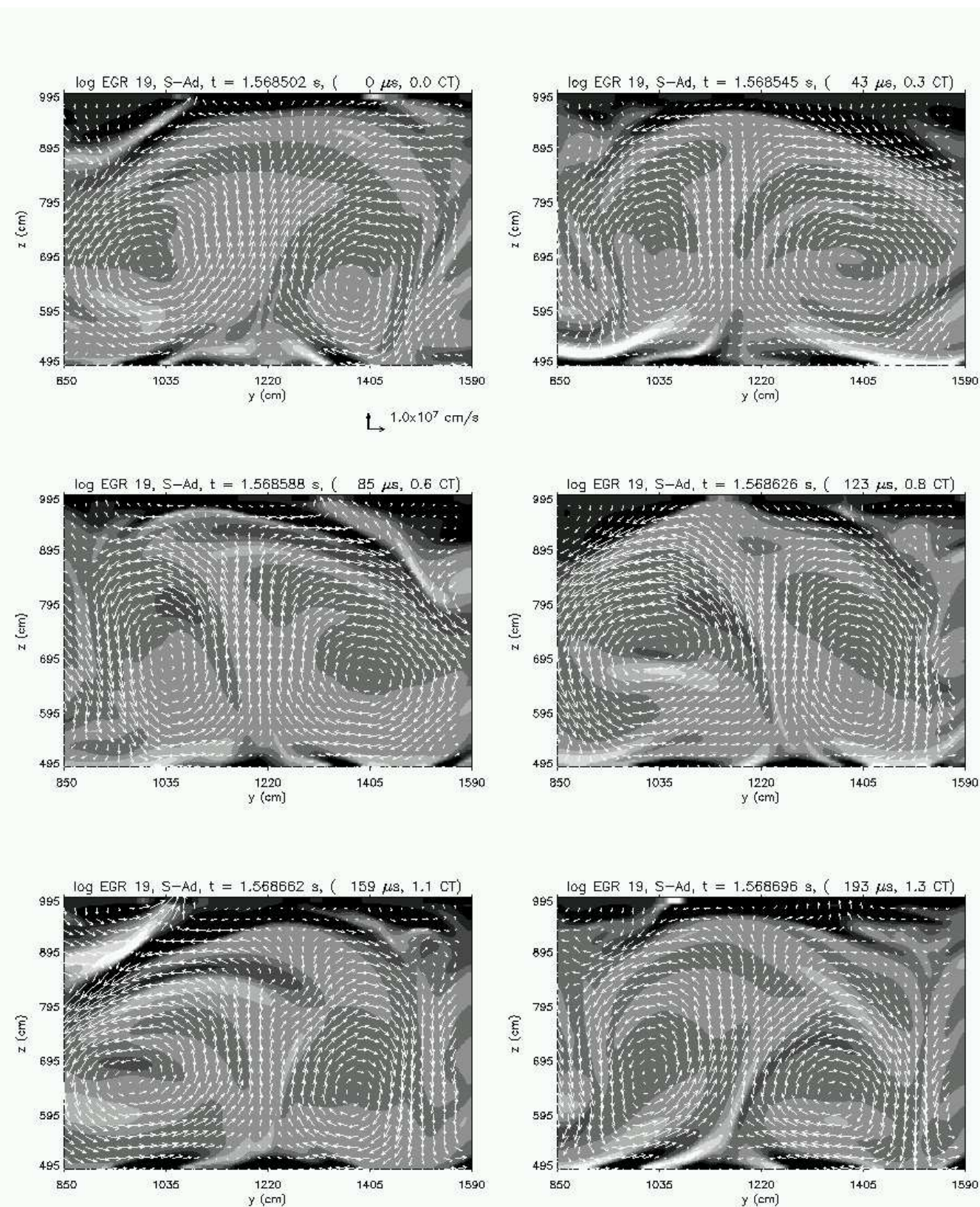


FIGURE 4.35. Contours of SAd and Flow Field at log EGR = 19 A  
 $t = 0 - 1.3$  CT. See Table 4.16 for the gray scale legend.

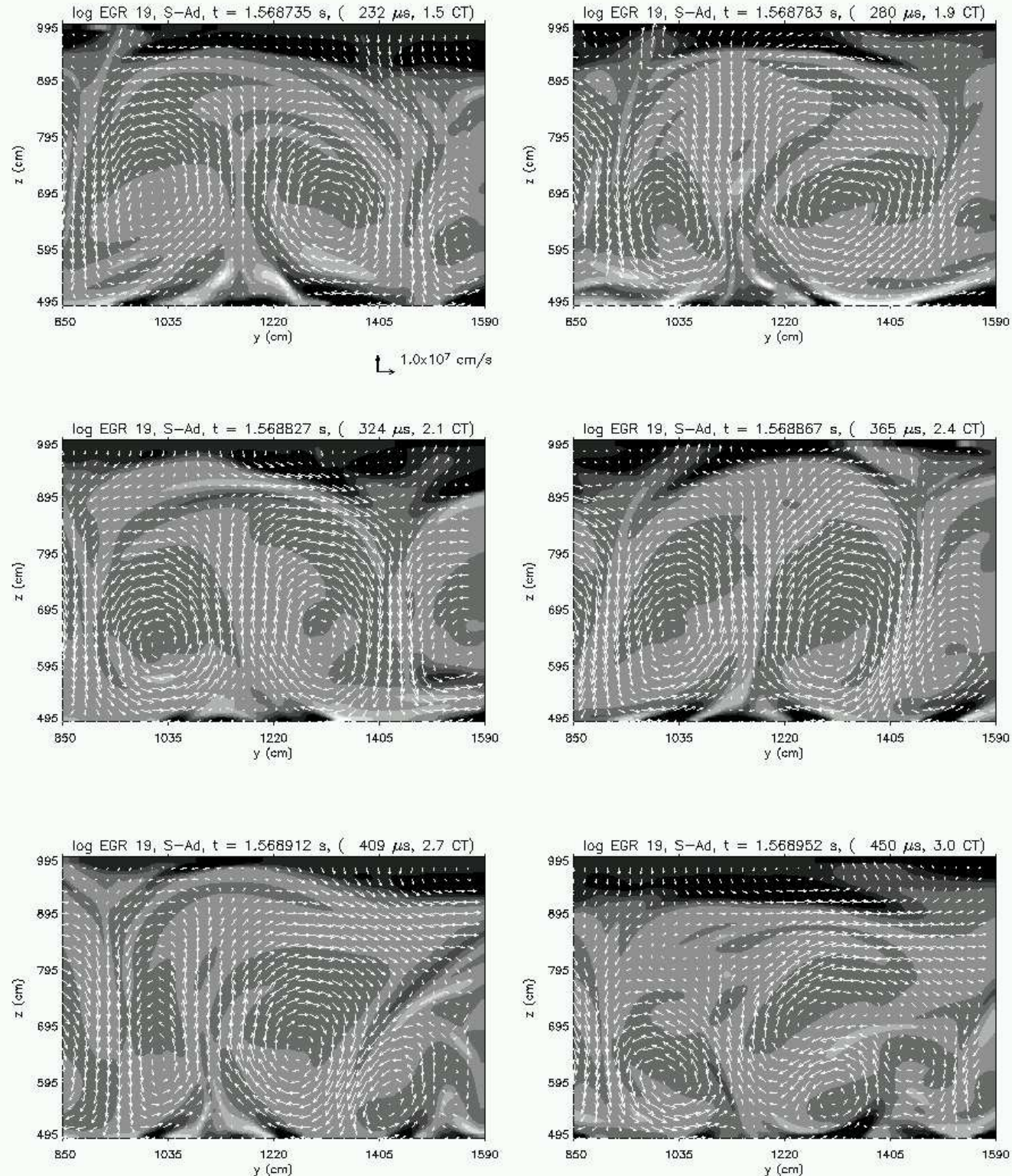


FIGURE 4.36. Contours of SAd and Flow Field at log EGR = 19 B  
 $t = 1.5 - 3.0 \text{ CT}$ . See Table 4.16 for the gray scale legend.

Color	Limits
Black	SLed < -0.1675
Dark Gray	-0.1675 < SLed < -0.0825
Gray	-0.0825 < SLed < +0.0825
Light Gray	+0.0825 < SLed < +0.1675
White	SLed > +0.1675

TABLE 4.17. 5-shade Scheme for SLed at all EGR levels

**4.8.4. SLed Fluctuations.** In this sub-section, fluctuations in the Ledoux-excess (SLed) are examined as contour plots over several convective timescales. That is, for each zone:

$$(4.8) \quad SLed_{j,k} = \nabla_{j,k} - \nabla_{Led,j,k}$$

Because the Ledoux gradient  $\nabla_L \equiv \nabla_{ad} + \frac{c_1}{c_2} \nabla_\mu$  (where  $\nabla_\mu \equiv \left(\frac{d \ln \mu}{d \ln P}\right)$ , and  $c_1 \equiv \left(\frac{\partial \ln \rho}{\partial \ln \mu}\right)_{P,T}$ ,  $c_2 \equiv -\left(\frac{\partial \ln \rho}{\partial \ln T}\right)_{P,\mu}$ ),  $\nabla_L > \nabla_{ad}$  when  $\frac{c_1}{c_2} \nabla_\mu > 0$ . At the upper and lower edges of the convective region where the composition gradient is most steep,  $\nabla_L$  departs significantly from  $\nabla_{ad}$ . On the other hand, away from the edges of the convective region where the composition is well mixed due to convective homogenization,  $\nabla_L \sim \nabla_{ad}$ . The actual gradient appears to satisfy the Ledoux criteria throughout the convective region, most obviously at the upper and lower edges, due to the presence of the non-trivial composition gradients there.

In general, most of the convective region exhibits only slightly negative and positive SLed most of the time, and so the contour plots are comparatively plain compared to the corresponding figures of SAd. Exceptions emerge near burst peak at log EGR = 19, when sizable bands of very negative and positive SLed develop.

To facilitate comparison with the SAd plots in the previous sub-section, the 5-shade scheme for all EGR levels in the following plots of SLed has the same limits as the one used for SAd, and is summarized again in Table 4.17.

For clarity, every other velocity vectors is plotted to make up the flow fields in the plots for log EGR 16 and 17, every third for log EGR 18, and every fourth for log EGR 19. To help facilitate comparison, the exact same time sequence of plots and the exact same dimensions

of the plots are used at each EGR level as are used in the plots of the previous sub-sections which examine  $d(T)$ ,  $d(Y)$ , and SAd.

4.8.4.1. *SLed at log EGR 16.* The sequence of plots in Figures 4.37 and 4.38 show the time-evolution of the contours of SLed at log EGR 16 between 0.0 - 1.9, and 2.3 - 4.0 convective timescales, respectively, where the times are given with respect to the time of the first plot in Figure 4.37. The convective timescale at log EGR 16 is approximately 1000  $\mu s$ .

Most of the convective region exhibits slightly negative SLed. Sizable regions which are less negative than others exist, and evolve dynamically. No consistent association between flow direction and the relative value of SLed is apparent.

The 5-shade scheme for all EGR levels in this sub-section of SLed is summarized in Table 4.17. For clarity, every other velocity vector is plotted in the flow field.

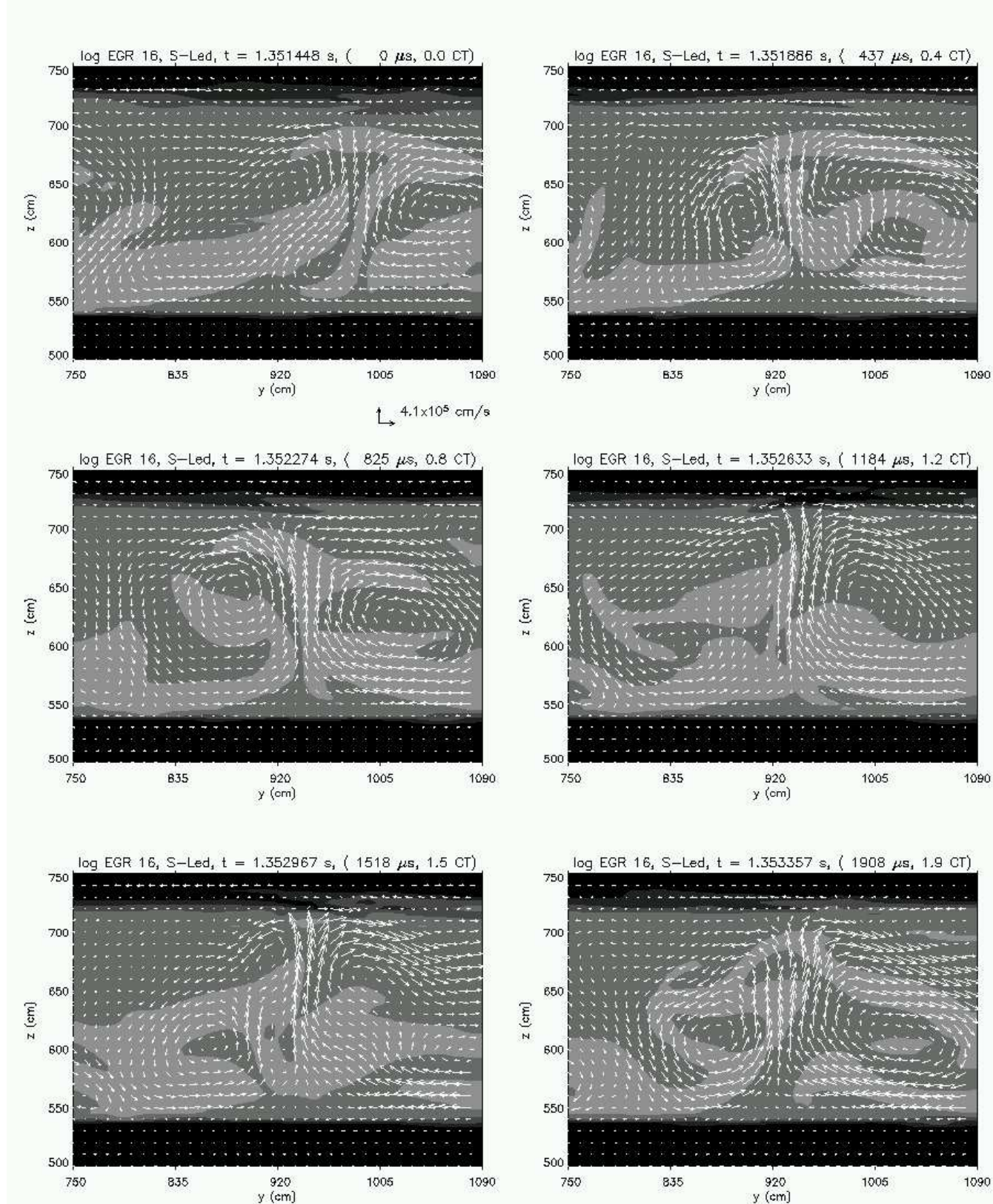


FIGURE 4.37. Contours of SLed and Flow Field at log EGR = 16 A  
 $t = 0 - 1.9$  CT. See Table 4.17 for the gray scale legend.

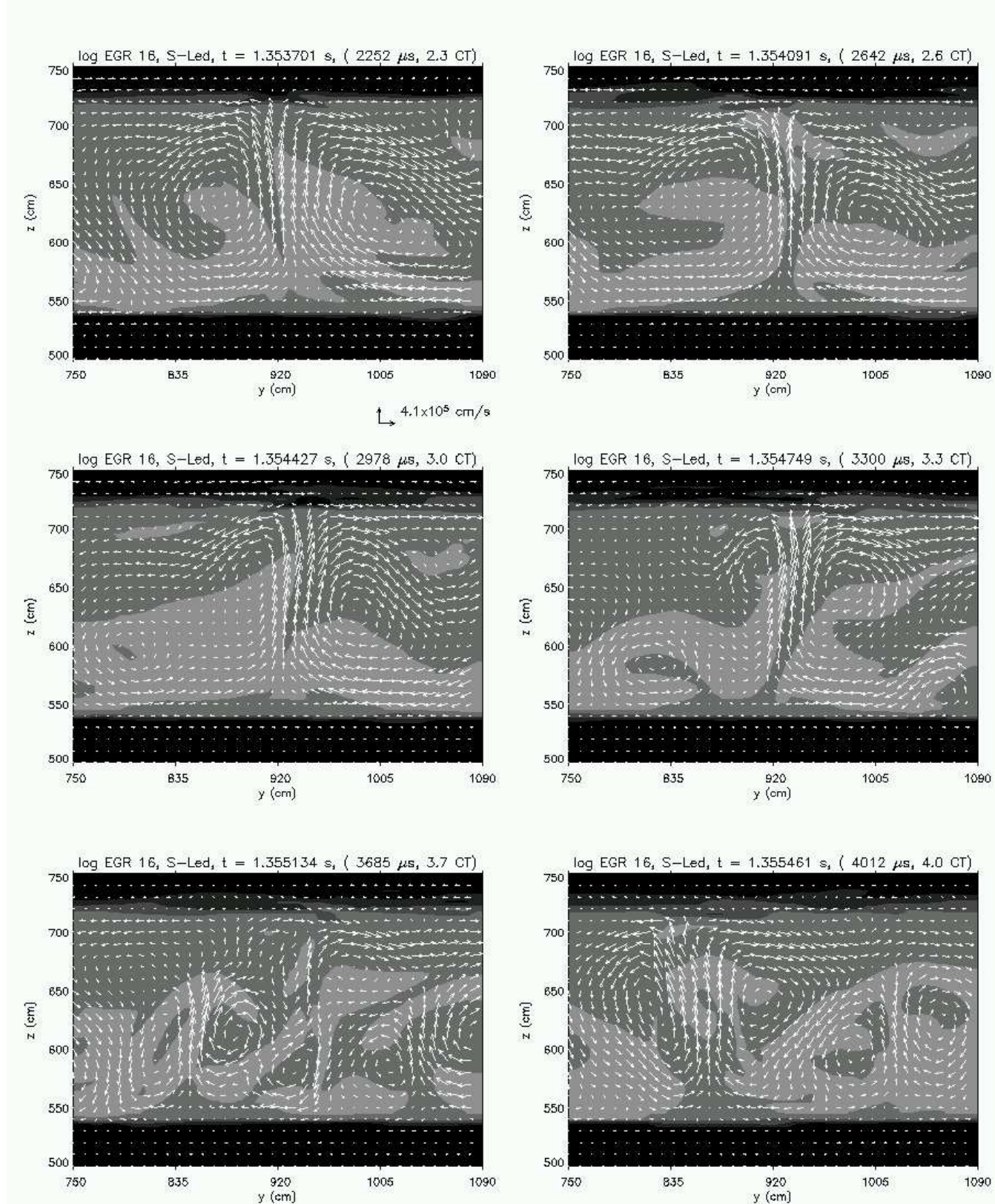


FIGURE 4.38. Contours of SLed and Flow Field at log EGR = 16 B  
 $t = 2.3 - 4.0$  CT. See Table 4.17 for the gray scale legend.

4.8.4.2. *SLed at log EGR 17.* The sequence of plots in Figures 4.39 and 4.40 show the time-evolution of the contours of SLed at log EGR 17 between 0.0 - 1.4, and 1.7 - 3.2 convective timescales, respectively, where the times are given with respect to the time of the first plot in Figure 4.39. The convective timescale at log EGR 17 is approximately  $500 \mu\text{s}$ .

As the extent of the convective region and convective cell sizes grow, so do the sizes of the patterns of similarly valued SLed. For the most part, however, the SLed of most of the convective region still tends to be negatively valued. A strong band of very negative SLed appear to develop at the top of the major convective cell centered at longitudinal position  $y = 1300 \text{ cm}$  in Figure 4.39. No consistent associations between the characteristics of the flow field and the relative values of SLed are apparent.

The 5-shade scheme for all EGR levels in this sub-section of SLed is summarized in Table 4.17. For clarity, every other velocity vector is plotted in the flow field.

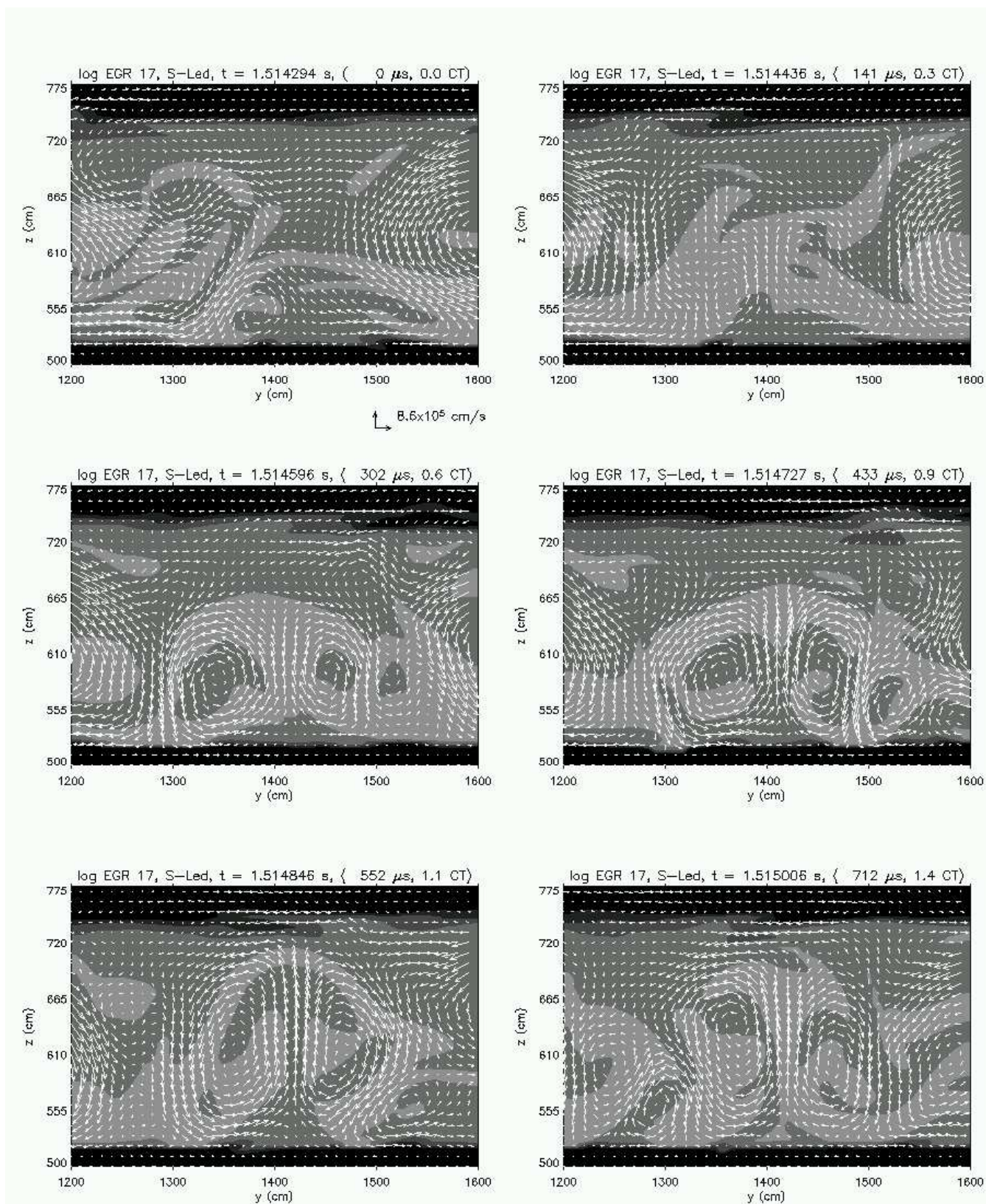


FIGURE 4.39. Contours of SLed and Flow Field at log EGR = 17 A  
 $t = 0 - 1.4$  CT. See Table 4.17 for the gray scale legend.

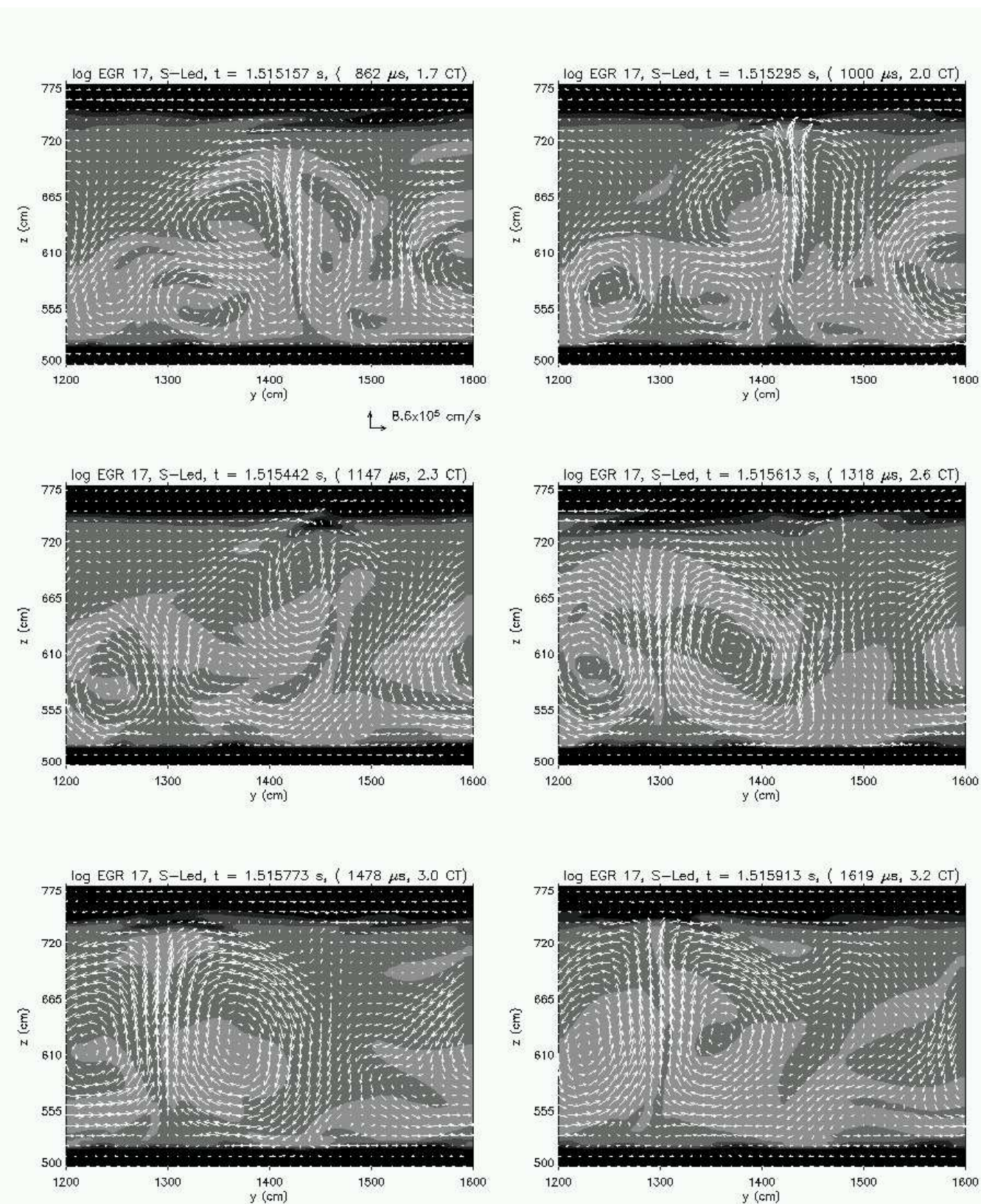


FIGURE 4.40. Contours of SLed and Flow Field at log EGR = 17 B  
 $t = 1.7 - 3.2 \text{ CT}$ . See Table 4.17 for the gray scale legend.

4.8.4.3. *SLed at log EGR 18.* The sequence of plots in Figures 4.41 and 4.42 show the time-evolution of the contours of SLed at log EGR 18 between 0.0 - 1.4, and 1.7 - 3.1 convective timescales, respectively, where the times are given with respect to the time of the first plot in Figure 4.41. The convective timescale at log EGR 18 is approximately  $250 \mu s$ .

The most noticeable change is the development of significant bands of slightly to very positive SLed. However, they are relatively short-lived and quickly evolving back into regions which have more negative SLed. The bands which exhibit the most positive value of SLed tend to form at the base of the convective region. At the top of the convective region, bands of very negative SLed penetrate deeper into the region than was seen to occur at the time the log EGR = 17. These bands tend to occur at the top of convective cells and their shapes follow the bifurcating flows which occur there.

The 5-shade scheme for all EGR levels in this sub-section of SLed is summarized in Table 4.17. For clarity, every third velocity vector is plotted in the flow field.

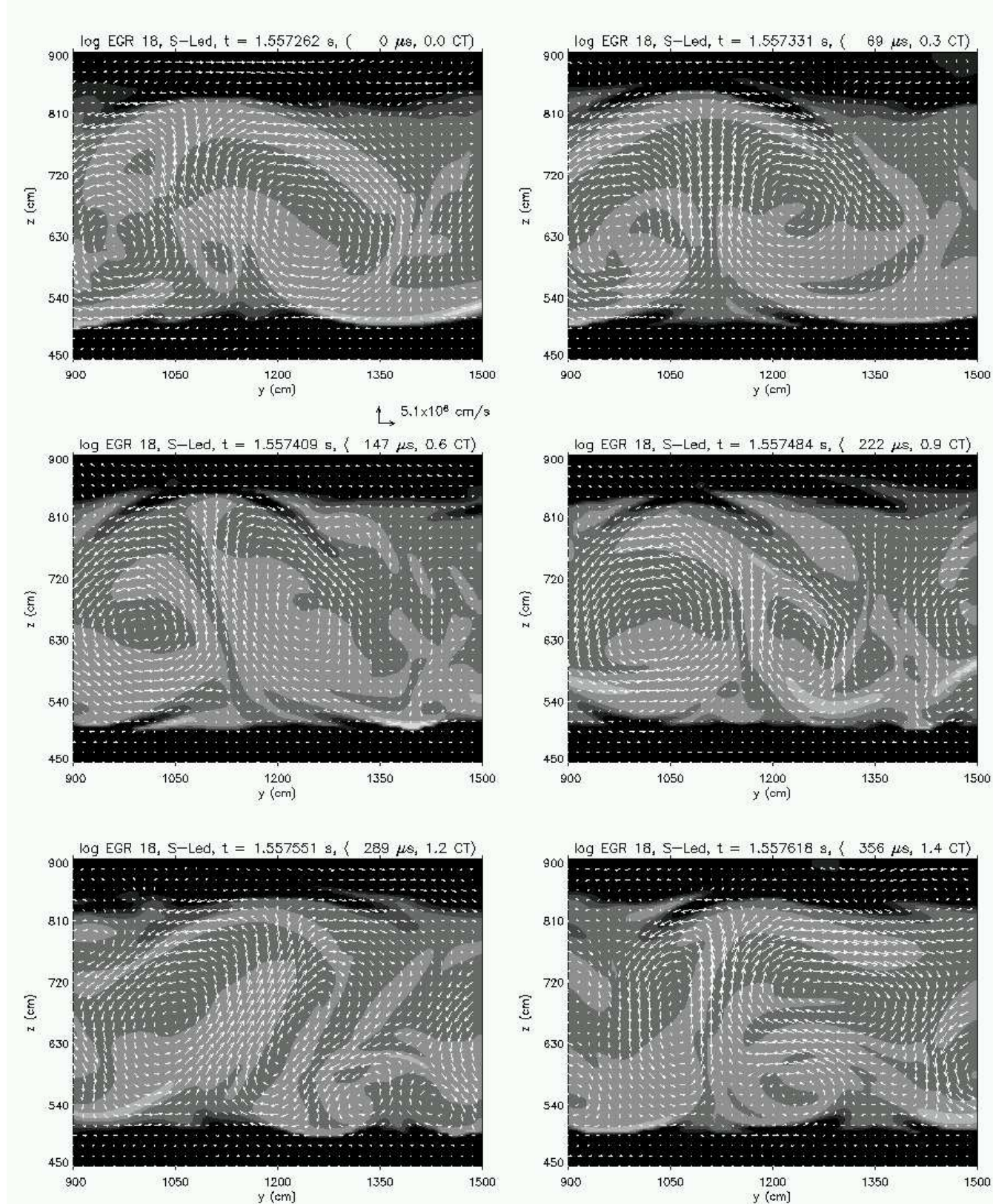


FIGURE 4.41. Contours of SLed and Flow Field at log EGR = 18 A  
 $t = 0 - 1.4$  CT. See Table 4.17 for the gray scale legend.

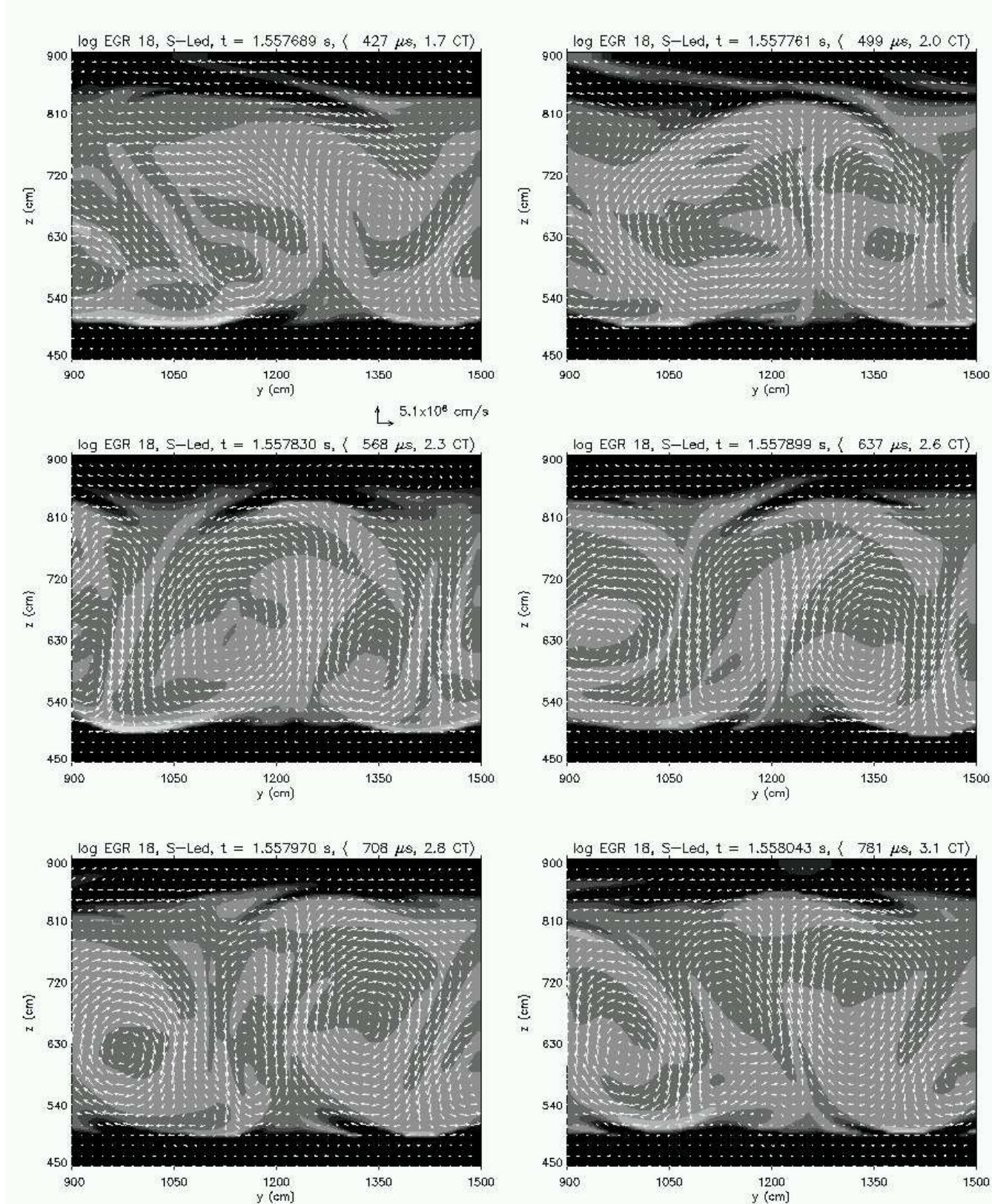


FIGURE 4.42. Contours of SLed and Flow Field at log EGR = 18 B  
 $t = 1.7 - 3.1$  CT. See Table 4.17 for the gray scale legend.

4.8.4.4. *SLed at log EGR 19.* The sequence of plots in Figures 4.43 and 4.44 show the time-evolution of the contours of SLed at log EGR 19 between 0.0 - 1.3, and 1.5 - 3.0 convective timescales, respectively, where the times are given with respect to the time of the first plot in Figure 4.43. The convective timescale at log EGR 19 is approximately  $150 \mu\text{s}$ .

Significant bands of very positive and negative SLed can be found at the upper and lower edges of the convective region, and are observed to evolve dynamically. Pockets of slightly positive and negative SLed also form within the convective region, but the negative regions dominate.

The 5-shade scheme for all EGR levels in this sub-section of SLed is summarized in Table 4.17. For clarity, every fourth velocity vector is plotted in the flow field.

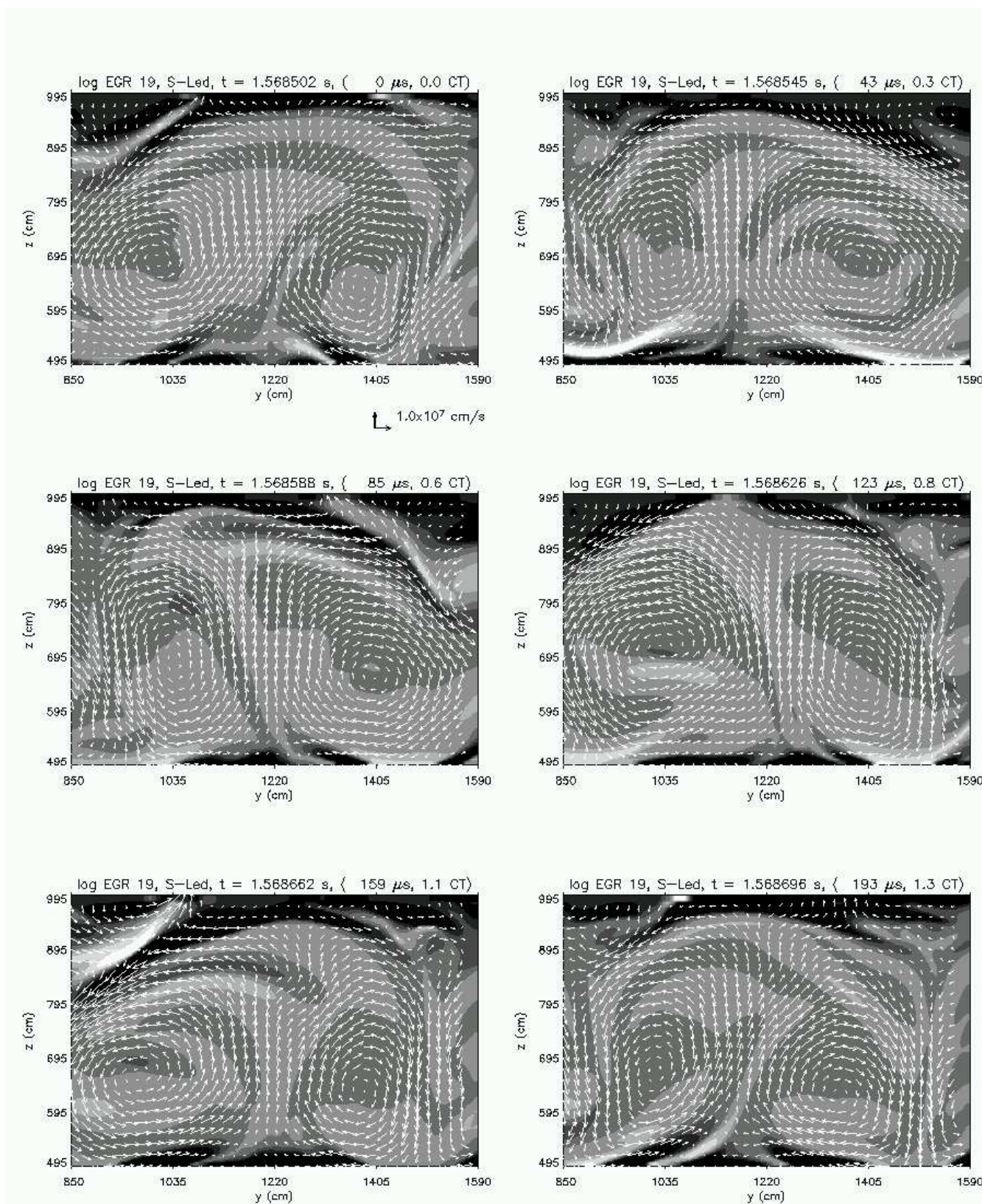


FIGURE 4.43. Contours of SLed and Flow Field at log EGR = 19 A  
 $t = 0 - 1.3$  CT. See Table 4.17 for the gray scale legend.

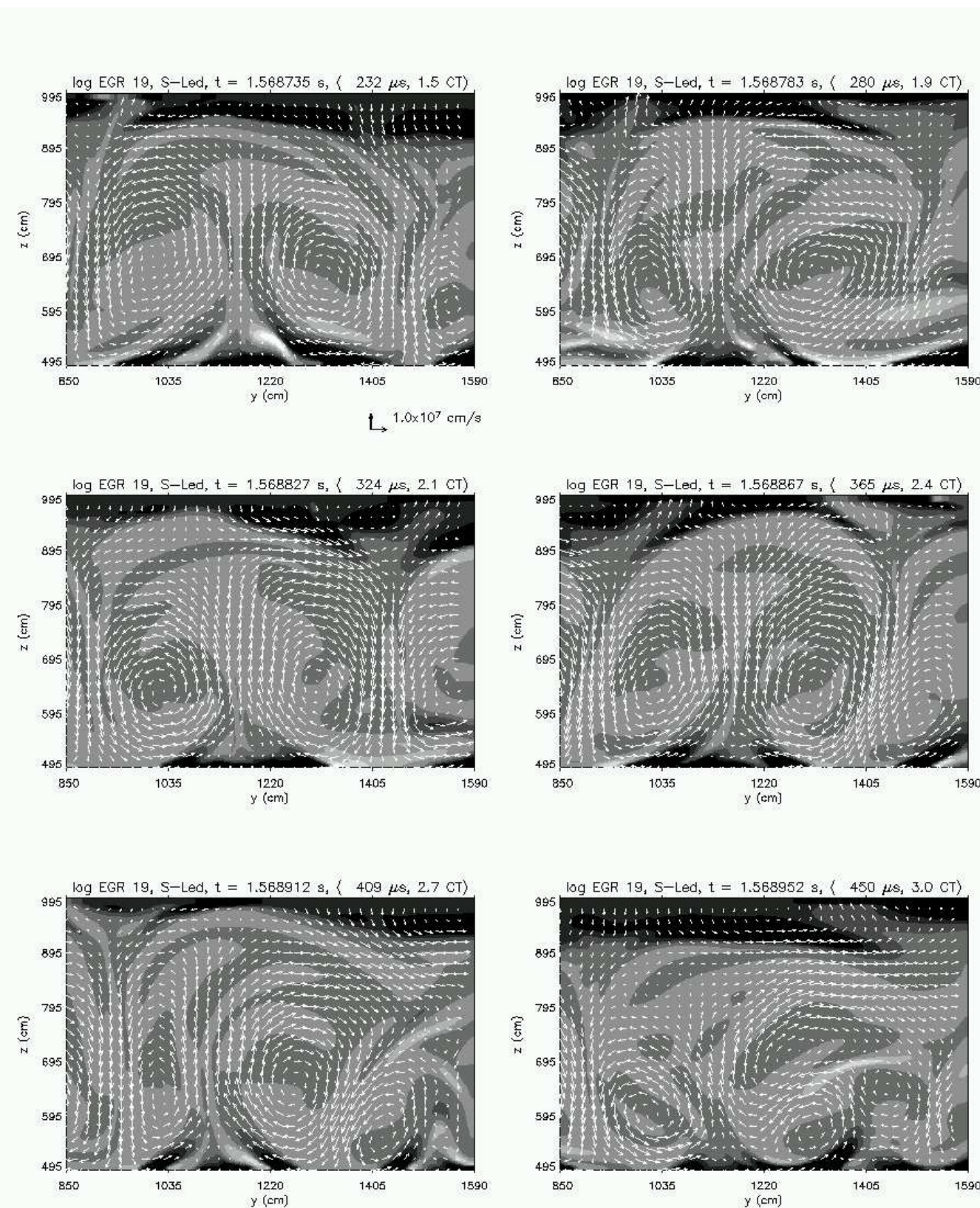


FIGURE 4.44. Contours of SLed and Flow Field at log EGR = 19 B  
 $t = 1.5 - 3.0 \text{ CT}$ . See Table 4.17 for the gray scale legend.

#### 4.9. Velocity Correlations and Thermodynamic Gradients

To help quantify the extent and evolution of the convectively unstable region, the vertical velocity correlation function  $W$  is calculated in the manner of Chan and Sofia (1987).

$$(4.9) \quad W = \frac{\langle w_k w_{ref} \rangle}{\langle w_k \rangle^{1/2} \langle w_{ref} \rangle^{1/2}}$$

The velocity correlation  $W$  is constructed by laterally and temporally averaging the product of the vertical components of velocity at two vertical positions, one of which is a fixed reference position ( $w_{ref}$ ). For each EGR level, this reference position is at the same vertical height, corresponding to the latitude of the center of the convective layer at log EGR = 16. This reference position is always close to the center of the convectively unstable region. The panel of four plots in Figure 4.45 shows  $W$  plotted as a function of the natural log of pressure at four EGR levels. (One pressure scale height is roughly 200 cm.) Also plotted are  $\nabla$ ,  $\nabla_{ad}$ , and  $\nabla_L$  as functions of  $\ln P$ . As indicated in the plots,  $W$  is a very well-defined function with unmistakable tails, and it can be used to quantitatively define the positions of the vertical edges of the Benard cells. The convective layer can be characterized by regions where  $W > 0.10$ . This choice is also consistent with the Schwarzschild criteria, since the plots in Figure 4.45 show that only regions where  $W > 0.10$  are slightly superadiabatic on average.

As expected, the figures show that at all EGR levels, the convectively unstable region (roughly where  $W > 0.10$ ) occurs where  $\nabla$  is essentially adiabatic. Higher and lower than this region, where no significant convective motions develop, the gradient is significantly sub-adiabatic, as expected. Also, at both the upper and lower edges of the convectively unstable region, the actual gradient more closely follows the Ledoux criteria, due to significant composition gradients which occur there. Apparently, convective motions efficiently mix the

composition in the convectively unstable region, effectively eliminating significant composition gradients within it. However, mixing is less efficient at the convective boundaries, so composition gradients may persist there.

Figure 4.46 summarizes the velocity correlation at the four EGR levels as a function of vertical position ( $z$ ) and  $\ln P$ . The figure illustrates the expansion of the convective region as the burst progresses, as the vertical extent of the convectively unstable region increases from less than one pressure scale-height to about two pressure scale-heights.

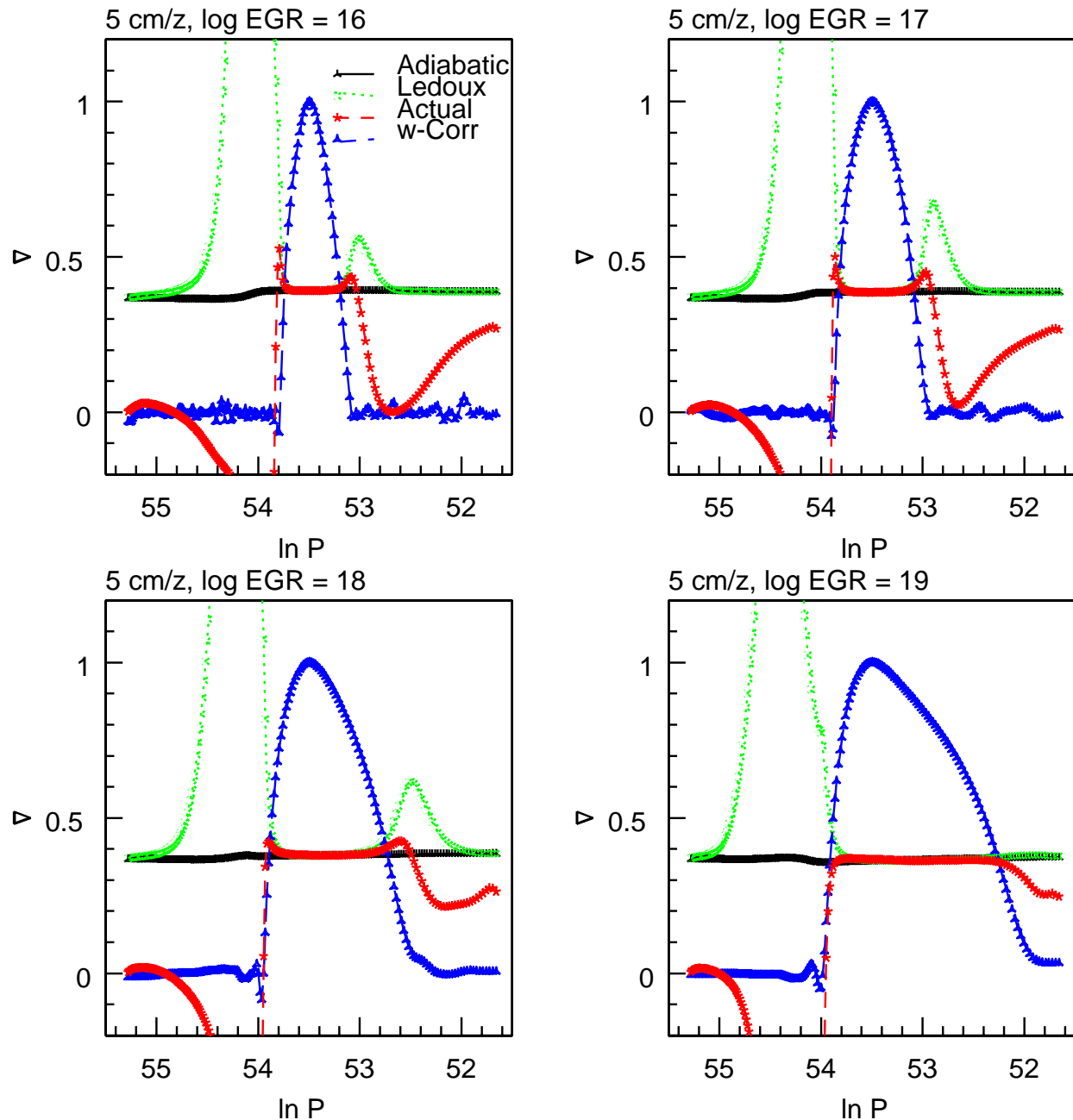


FIGURE 4.45. Vertical Velocity Correlation  $W$  and  $\nabla$ 's  
 $5 \text{ cm zone}^{-1}$  model at four EGR levels.

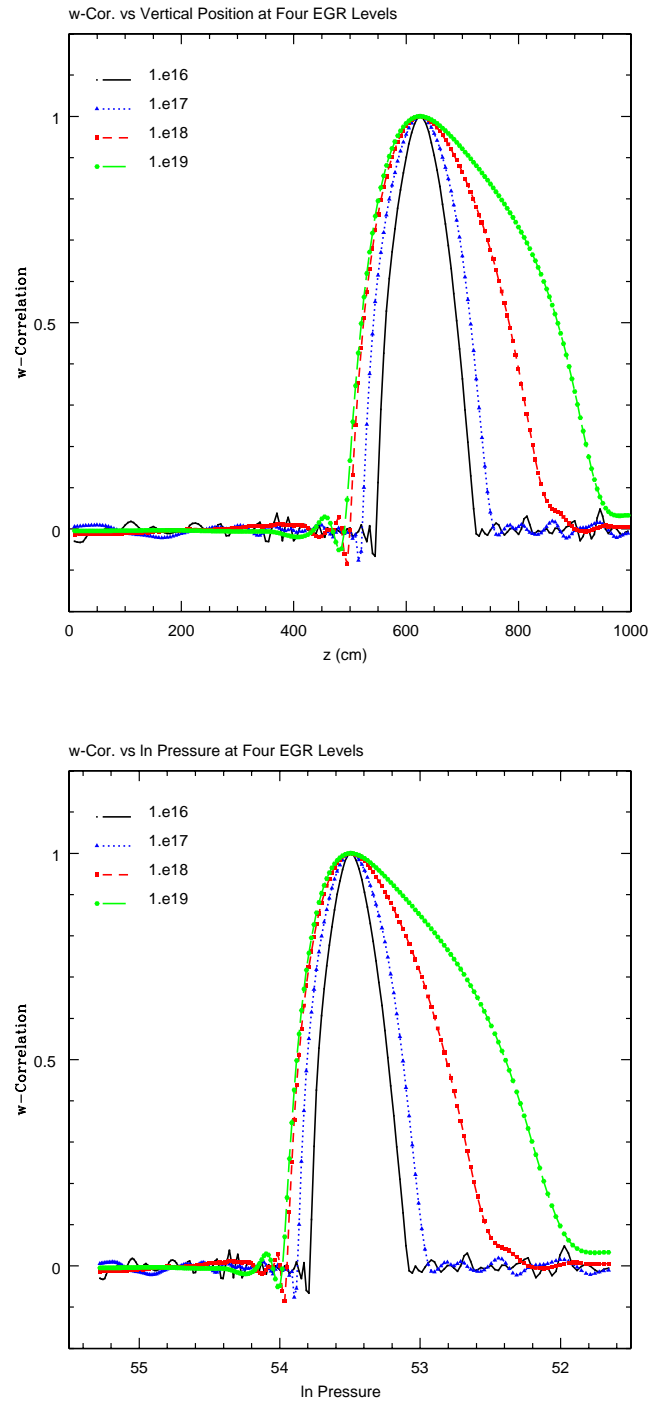


FIGURE 4.46. Vertical Velocity Correlation  $W$   
Vertical velocity correlation  $W$  vs. vertical position (top) and  $\ln P$  (bottom) of the  $5 \text{ cm zone}^{-1}$  model at four EGR levels.

Analogously, the lateral velocity correlation function  $V$  is calculated in the same manner as  $W$ , but with averaging in the vertical direction. The reference longitude in this case is taken to be the center-line, which separates the left and right halves of the computational domain. Figure 4.47 exhibits  $V$  as a function of lateral position for the central 800 cm of the domain at the four EGR levels. The results quantitatively demonstrate that on average, the aspect ratio of the major cells in the convectively unstable region is always roughly 1:1. The lateral velocity correlation is also more symmetric than the vertical velocity correlation, a feature which reflects the lateral uniformity in the domain.

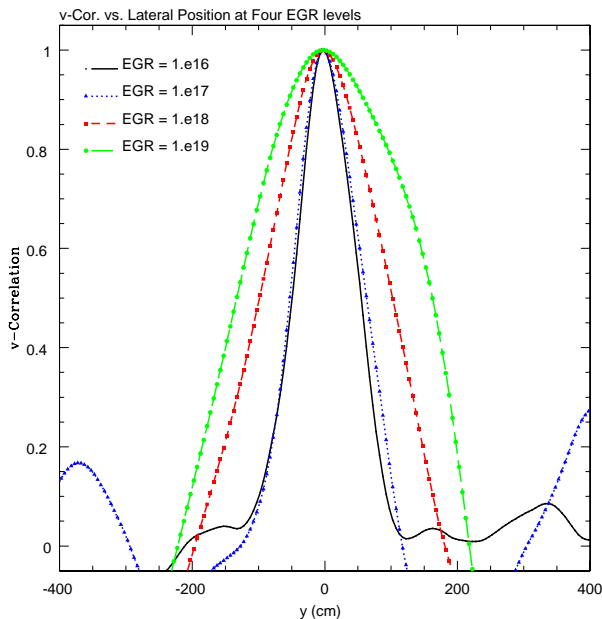


FIGURE 4.47. Lateral Velocity Correlation  $V$   
Lateral velocity correlation  $V$  at four EGR levels.

## 4.10. Tracer Particle Analyses

In this section, convective transport of material is studied from two perspectives. First, the transport of particles originally within the convectively unstable region beyond the formal boundaries of the convective layer (*under- or over-penetration*) is examined in Sub-section 4.10.1. Conversely, in Sub-section 4.10.2, the analysis shifts to consider whether particles initially bordering the exterior of the convective region are able to penetrate the boundaries and be carried into it (*bottom- or top-penetration*). The results suggest that penetration in both directions does occur, mostly at higher EGR levels, though in a limited, temporary, and downwardly-biased manner.

**4.10.1. Penetration from the inside to outside the convective region.** First, as a point of definition, *under- or over-penetration* occurs when particles initially found within the convective region are carried by local currents below or above the formal convective boundaries as defined by the Schwarzschild criteria.

To track the trajectory of tracer particles, the following procedure is performed at five points in time during the burst sequence ( $\log \text{EGR} = 16, 17, 18, 18.5$ , and  $19$ ). First, the entire velocity field is calculated with the LMNA code at every time-step for 1230 steps, corresponding to a physical time-span of several convective times at the corresponding EGR level. Then, this time-dependent velocity information is inputted into a separate analysis code, which evolves the positions of massless tracer particles using the forward-Euler method. Linear, two-dimensional interpolation is utilized to determine approximate velocities when positions of particles fall between grid-points on the domain. For each analysis, the position of two particles for each of the 385 zones in the lateral direction are tracked, one in the upper-half of the convective region, and the other in the lower half. Thus, the positions of 770 tracer particles are followed per analysis. Particle trajectories respect the lateral periodicity of the domain, allowing for continuity in tracking at the right edge if a particle flies off the left edge, and vice versa.

At each EGR level examined, the results are presented in three ways: 1) a 2D plot of the complete trajectories of ten representative particles with initial positions in strong up- and down-flows, to establish the general behavior of particle motion; 2) a 2D plot of the highest and lowest points in the trajectories of each of the 770 particles, to visually identify instances where penetration occurs; and, 3) a 1D plot of the projection of the highest and lowest points superimposed against plots of the velocity correlation and thermodynamic gradients, to quantify the extent of penetration.

First, Figure 4.48 ( $\log \text{EGR} = 16$  and 17) and Figure 4.49 ( $\log \text{EGR} = 18$  and 19) show the complete trajectories of ten representative particles against the velocity field and contour plot of the final time slice in the analysis sequence. The variable displayed in the contour plot is the superadiabaticity, where the black regions are very sub-adiabatic, and the lighter regions are slightly sub- to superadiabatic. (The scaling scheme for the plots is similar to those presented previously in Sub-section 4.8.3 on SAd fluctuations.) Using this scheme, the convective region clearly stands out between the stable regions above and below it. The initial positions of the tracer particles are indicated with large, black diamonds, and particle trajectories are depicted with thick, white lines. Nearly all of the ten representative particles at each EGR level have initial positions in strong down- or up-drafts, thus maximizing the chance they will be carried beyond the convective boundaries.

The figures show insignificant penetration occurs at the lower EGR levels. All particles are observed to consistently make sharp turns when they reach the convective boundaries, abruptly reversing direction or traveling along the edge of the boundaries before making their way back into the convective region. On numerous occasions, the particles were carried in strong down- or up-drafts as they approached the boundaries, situations which should maximize the possibility of penetration. However, as the trajectories clearly show, particles never travel beyond the boundaries, behaving as though an impenetrable barrier existed there. At the higher EGR levels, some instances of penetration can be found, but only momentarily and to a very small extent. Moreover, due to the rapid fluctuations in the

gradients, the formal boundaries of the convective region are dynamically shifting, blurring the transition between stable and unstable regions. Nevertheless, as observed at the lower EGR levels, particle trajectories appear to eventually reverse upon reaching the convective boundaries and are ultimately well-contained within the convective region on average.

More comprehensively, Figure 4.50 (log EGR = 16 and 17), Figure 4.51 (log EGR = 18 and 18.5), and Figure 4.52 (log EGR = 18.5 and 19) show the highest and lowest positions which each of the 770 particles attained during the entire analysis period. The extremes for each trajectory are displayed as small, white diamonds against the velocity field and contour plot of the adiabaticity. Actual trajectory paths are omitted for clarity, since the general behavior of the trajectories has been previously established. The figures vividly demonstrate the rather impenetrable nature of the convective boundaries. At lower EGR levels, over-penetration does not occur, and only a few instances of minuscule under-penetration are observed (for instance, at roughly  $y = 1200$  cm at log EGR = 17). At higher EGR levels, more instances of under- and over-penetration are observed for a small fraction of the particles ( $\sim 5$  to 10%), and even then, the extent of the penetration is relatively limited. Notably, much of the under-penetration appears to occur in rather localized aggregations, rather than uniformly distributed along the entire edge of the convective region. The positions of the aggregations appear to roughly correspond to the bases of significant down-flows.

To quantify the extent of penetration, Figure 4.53 (log EGR = 16 and 17), Figure 4.54 (log EGR = 18 and 18.5), and Figure 4.55 (log EGR = 19) projects the highest and lowest vertical position of each of the 770 tracer particles against a one-dimensional vertical axis. For reference, the laterally and temporally averaged vertical velocity correlation  $W$ , adiabatic gradient  $\nabla_{ad}$ , Ledoux gradient  $\nabla_L$ , and actual gradient  $\nabla$  at each EGR level are also plotted. The tracer particle positions are the data points above the  $\nabla_{ad}$  line. By the Schwarzschild criteria, the formal convective boundaries occur where  $\nabla$  crosses below  $\nabla_{ad}$ , which also corresponds to where  $W > 0.1$ .

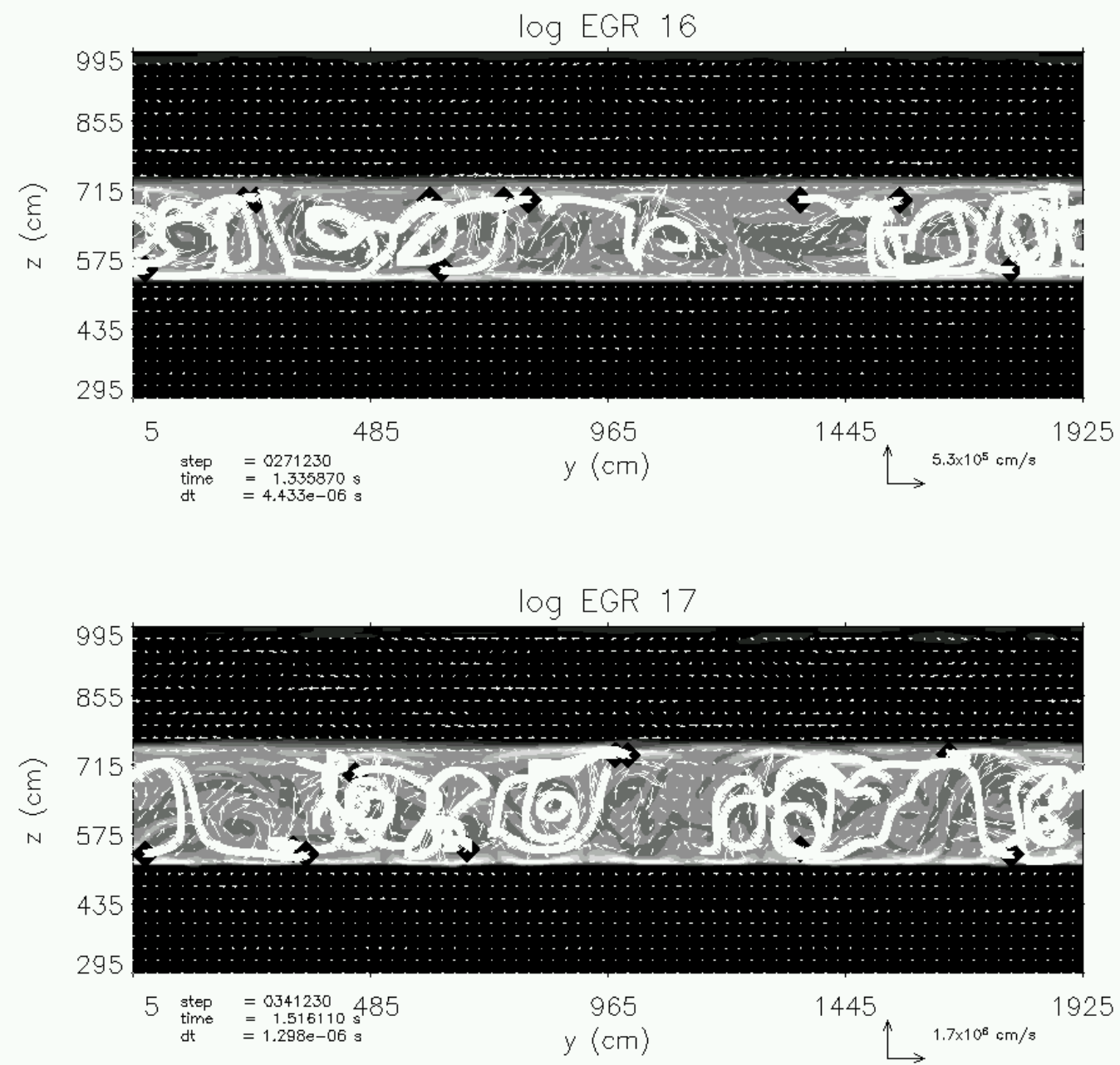


FIGURE 4.48. Ten Particle Trajectories, log EGR = 16 and 17  
 Ten representative particle trajectories, starting from positions within the convective region.

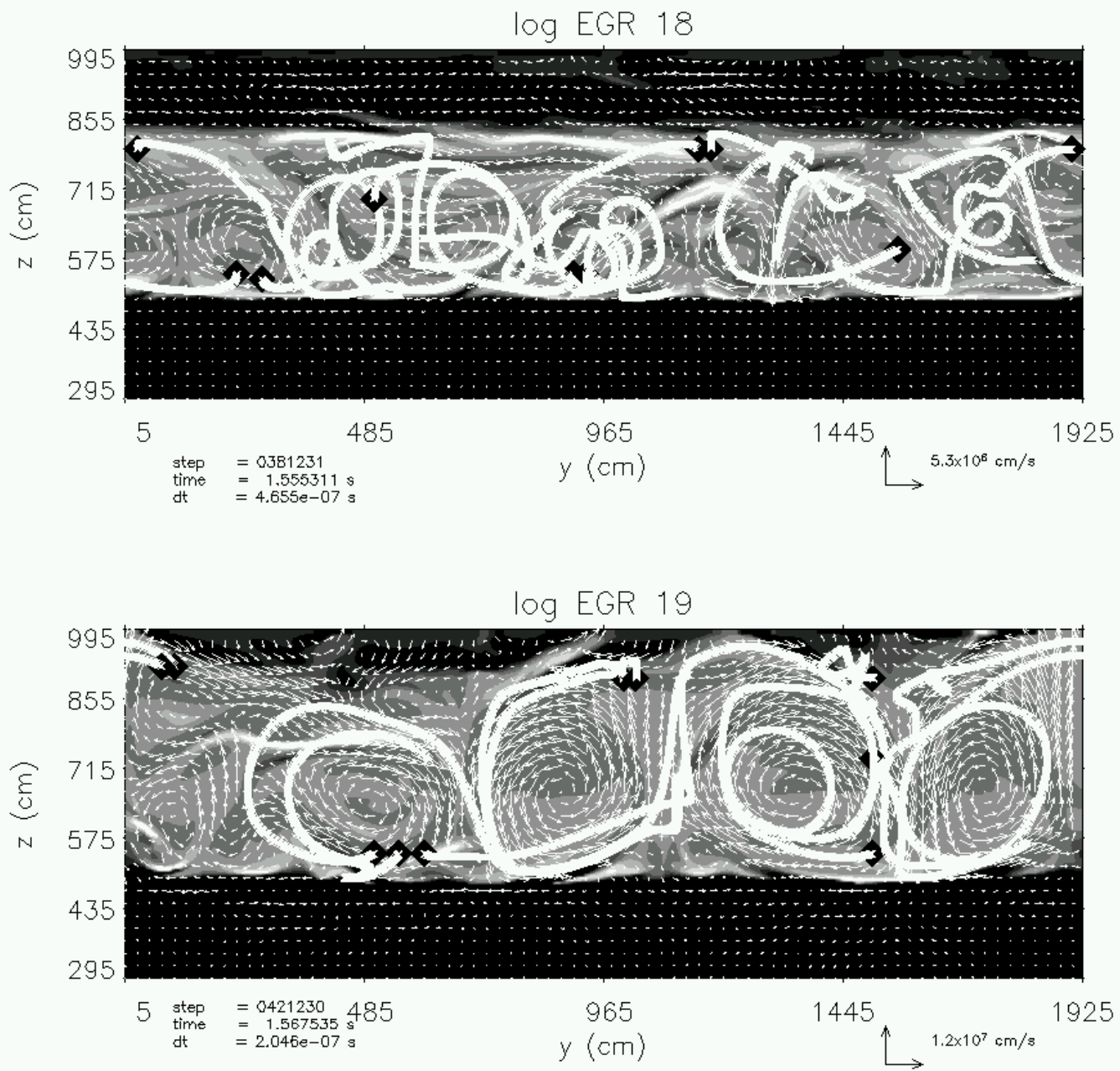


FIGURE 4.49. Ten Particle Trajectories, log EGR = 18 and 19  
 Ten representative particle trajectories, starting from positions within the convective region.

log EGR	Under-Penetration	Over-Penetration
16	none	none
17	5 cm (1/40)	none
18	10 cm (1/20)	none
18.5	20 cm (1/10)	40 cm (1/5)
19	60 cm (1/3)	indeterminate

TABLE 4.18. Extent of Under- and Over-Penetration

Extent of under- and over-penetration based on particle tracer studies. Value in parentheses is the fraction of pressure scale heights (1 scale height  $\sim 200$  cm).

The figures show that at  $\log \text{EGR} = 16$  and  $17$ , the tracer particle positions are clearly well contained within the formal convective boundaries, with only one or two points extending below the lower boundary by one zone's length at  $\log \text{EGR} = 17$ . Under-penetration increases steadily as the EGR increases, reaching 60 cm, or one-third of a scale height by  $\log \text{EGR} = 19$ . In terms of the number of penetration events, under-penetration occurs much more frequently than over-penetration. Some over-penetration ( $\sim 40$  cm, one-fifth of a scale height) seems to occur at  $\log \text{EGR} = 18.5$ . However, when referenced to Figure 4.54, these instances appear to involve just a handful of particles in a spotty manner. The extent of over-penetration at  $\log \text{EGR} = 19$  is indeterminate, because by this time, the upper convective boundary is so close to the upper computational domain boundary that dynamical integrity may be questionable due to numerical artifacts. Still, it is reasonable to extrapolate the general trend that as velocities increase in magnitude as the burst progresses, the extent of under- and over-penetration increases.

Table 4.18 summarizes the extent of under- and over-penetration at each of the EGR levels examined.

Taken together, the results suggest that particle penetration from the inside of the convective region to the outside is insignificant at the lower EGR levels ( $\log \text{EGR} < 17$ ). At these times, a particle cannot travel very far beyond the boundaries before lateral convective motions deflect it at the edge, eventually sweeping it back into the convective region. Thus, at the convective boundaries, lateral flows dominate the vertical.

At the higher EGR levels ( $\log \text{EGR} > 18$ ), the convective motions become vigorous enough to momentarily transport  $\sim 5$  to 10% of the tracer particles less than one-third of a scale height in localized aggregations below the convective boundaries, and in a more random manner above, before sweeping them back into the heart of the convective region.

The results are physically reasonable, since the magnitude of the vertical velocities diminish very rapidly at the convective boundaries, over two orders of magnitude within half of a scale height, as evidenced by the steep drop in the W-correlation at the boundaries. Consequently, material originally inside the convective region appears for the most part to be effectively trapped within it.

**4.10.2. Penetration from the outside to inside the convective region.** In this sub-section, the analysis shifts to consider whether particles originally outside the convective region will be carried by local currents into it. To avoid confusion with the previously defined terms which describe the direction of penetration, two new terms are defined: *bottom-* and *top-penetration*, referring to the two situations where particles enter the convective region through the bottom and top boundaries from regions outside of it.

The same numerical procedure which had been employed in the previous penetration analysis (Sub-section 4.10.1) is used here, that is, evolve the positions of 770 tracer particles using forward-Euler over 1230 pre-generated, sequential velocity fields, and utilize linear, 2D interpolation for intermediate trajectory positions. As before, two particles are introduced for every lateral zone of the domain. However, now the initial vertical positions of the tracer particles are above and below the formal convective boundaries, as defined by the Schwarzschild criteria. Moreover, since the previous penetration analysis has already established the vertical extents of under- and over-penetration at each EGR level, the initial vertical positions of the particles in the present analysis are strategically positioned beyond those extents. (Refer to Table 4.18 for the under- and over-penetration extents.)

Two representative EGR levels are considered:  $\log \text{EGR} = 17$  and 18.5, and for each EGR level, two studies, A and B, are performed. The difference between the studies lies in

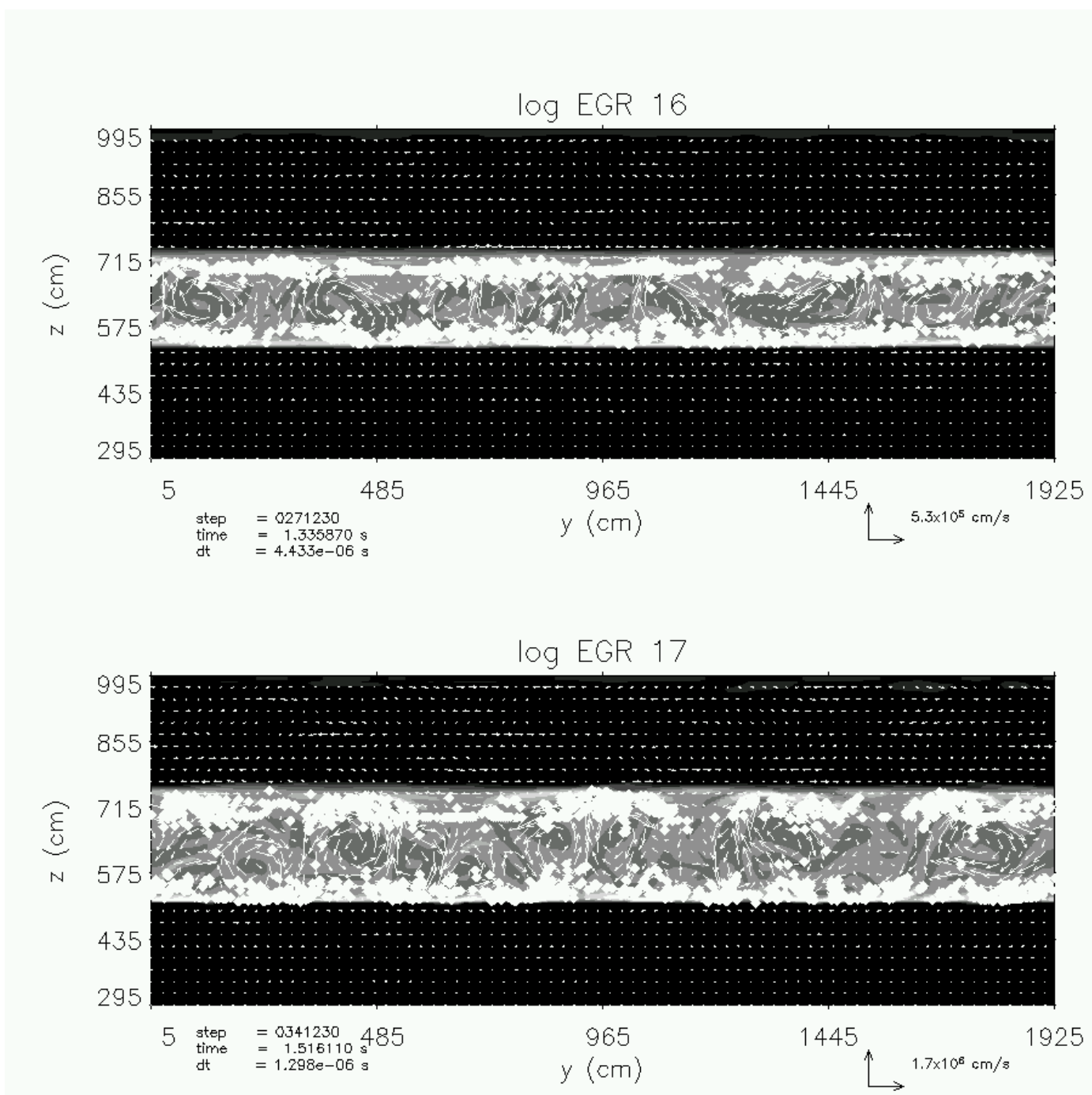


FIGURE 4.50. Particle Trajectory Limits (inside-out), log EGR = 16, 17  
 Highest and lowest positions of 770 tracer particles are plotted as small, white diamonds.  
 Initial positions of particles are inside the convective region.

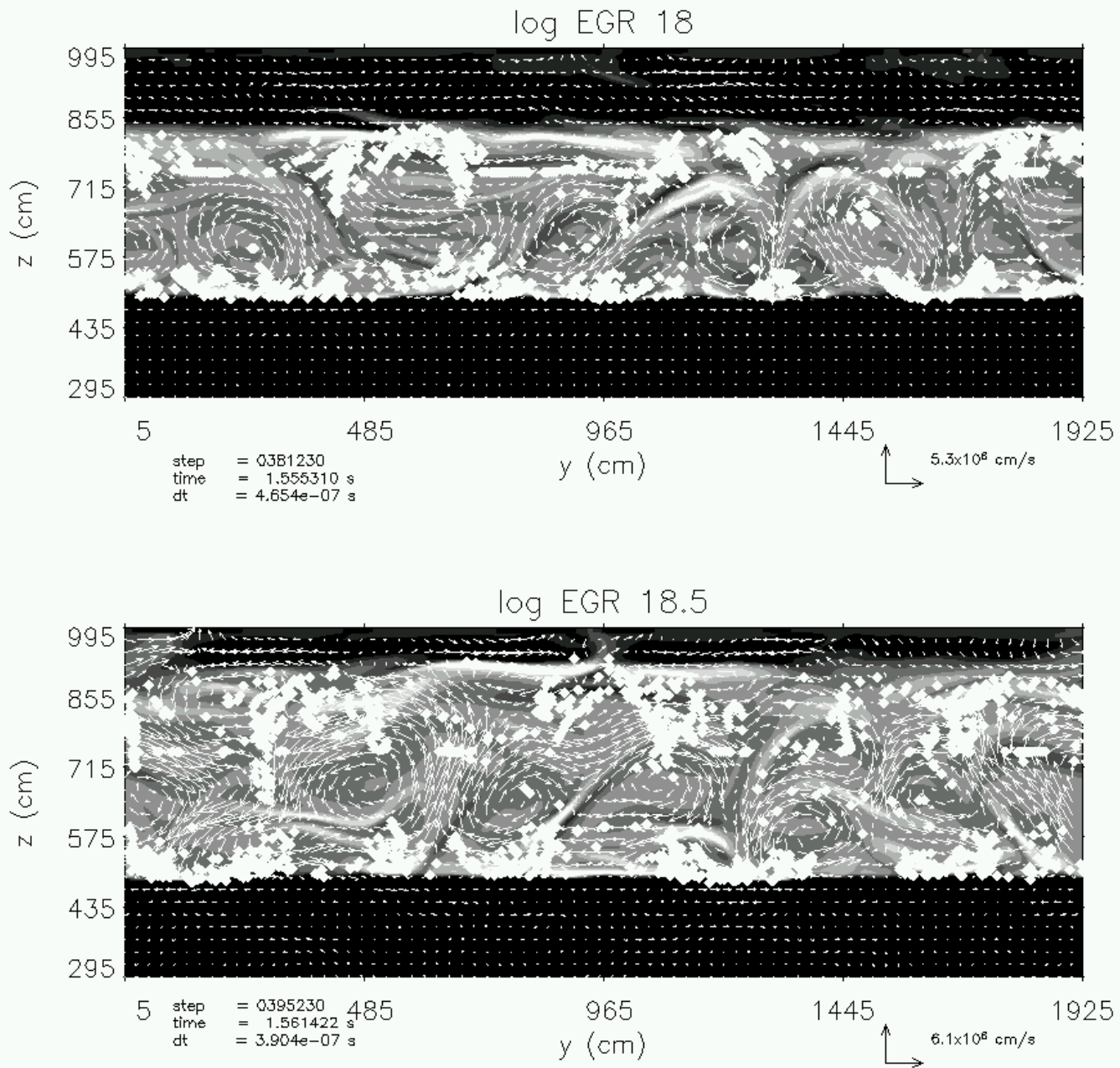


FIGURE 4.51. Particle Trajectory Limits (inside-out), log EGR = 18, 18.5  
 Highest and lowest positions of 770 tracer particles are plotted as small, white diamonds.  
 Initial positions of particles are inside the convective region.

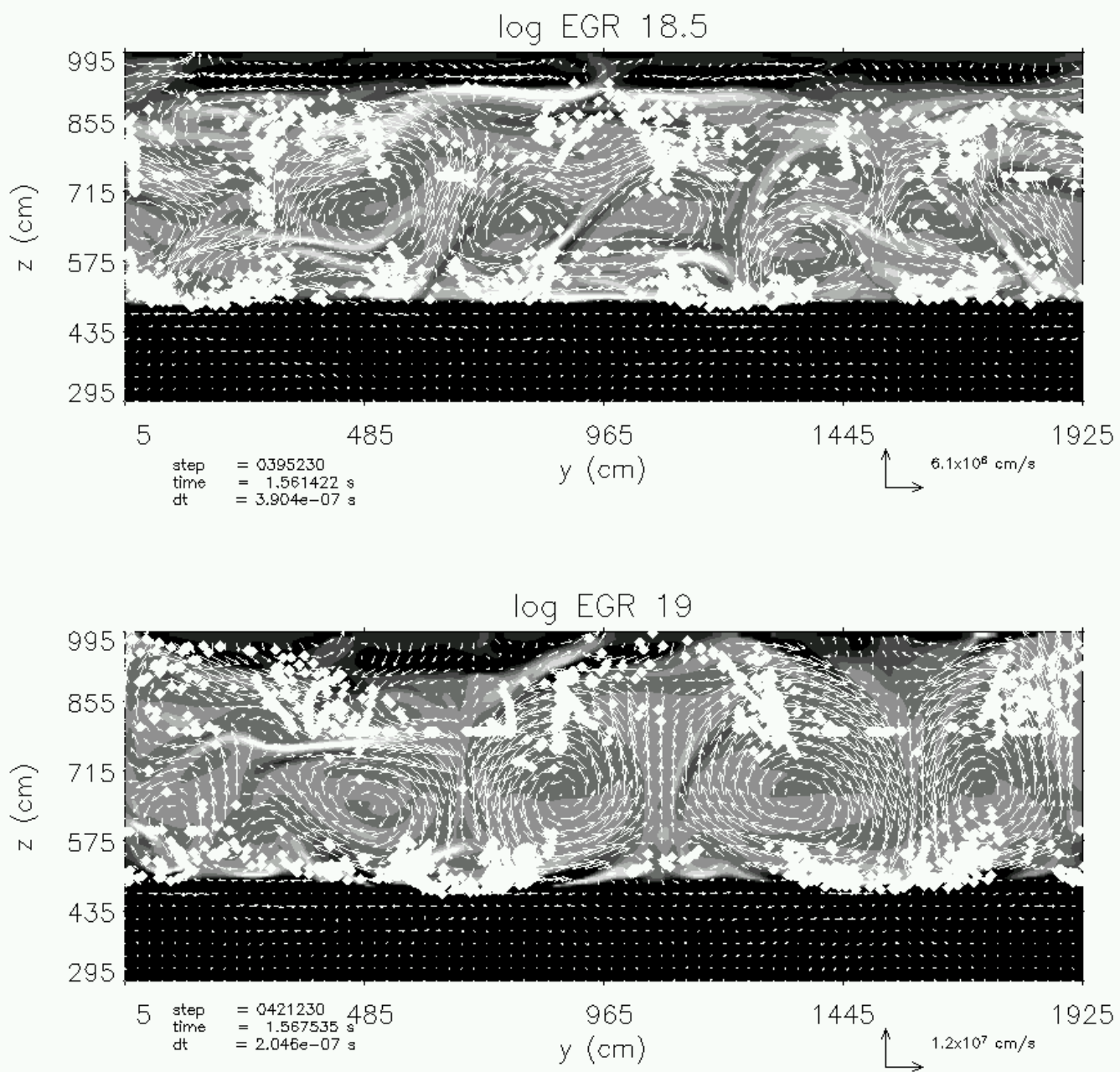


FIGURE 4.52. Particle Trajectory Limits (inside-out), log EGR = 18.5, 19  
 Highest and lowest positions of 770 tracer particles are plotted as small, white diamonds.  
 Initial positions of particles are inside the convective region.

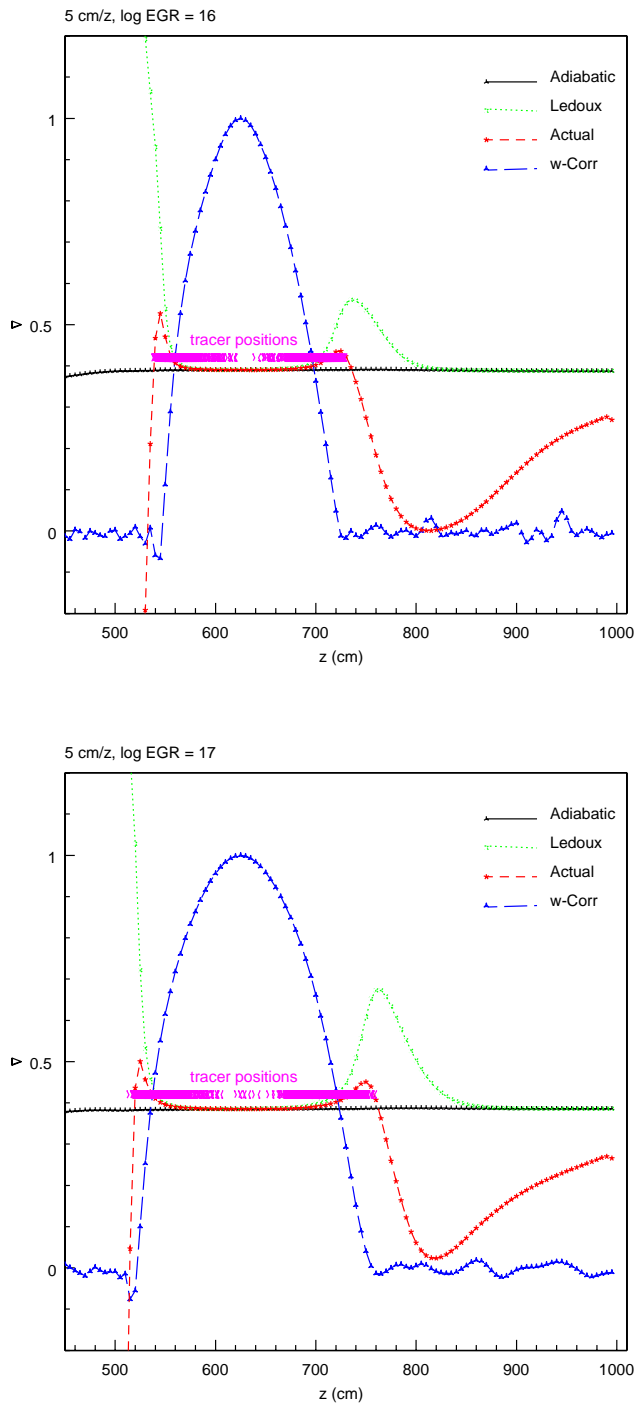


FIGURE 4.53. Penetration at  $\log \text{EGR} = 16$  and 17  
 Highest and lowest positions of 770 tracer particles (collection of points above the adiabatic line) plotted against the velocity correlation and various gradients. Initial positions of particles are inside the convective region.

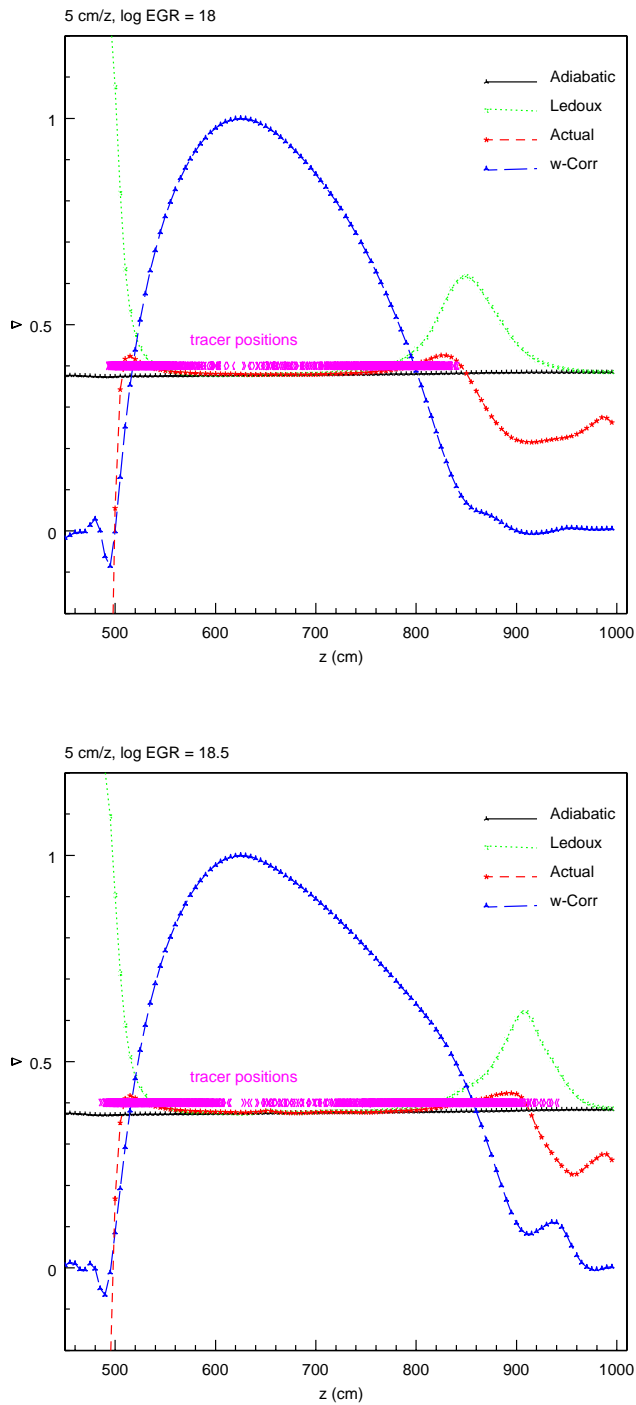


FIGURE 4.54. Penetration at  $\log \text{EGR} = 18$  and  $18.5$ .  
 Highest and lowest positions of 770 tracer particles (collection of points above the adiabatic line) plotted against the velocity correlation and various gradients. Initial positions of particles are inside the convective region.

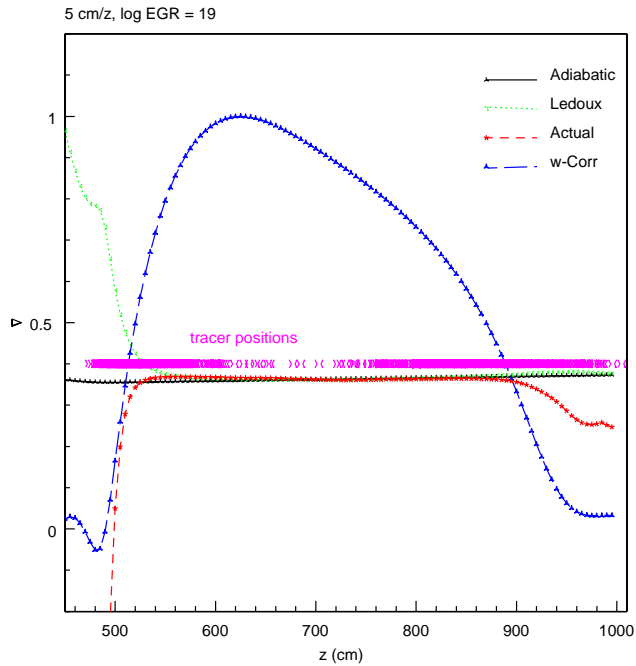


FIGURE 4.55. Penetration at  $\log \text{EGR} = 19$

Highest and lowest positions of 770 tracer particles (collection of points above the adiabatic line) plotted against the velocity correlation and various gradients. Initial positions of particles are inside the convective region.

the initial vertical positions of the rows of tracer particles, where Study A's initial vertical positions are 5 cm (one zone) farther from the formal convective boundaries than Study B's. Together, the two studies demonstrate that the difference of the initial placement by just one vertical zone may significantly affect whether and by how much bottom- and top-penetration occurs. Table 4.19 summarizes the initial vertical positions of the particles, quoted as distances in cm above or below the formal convective boundaries. For each position, another value is quoted in parenthesis, which is the distance above or below the appropriate under- and over-penetration limits. For example, in Study A of  $\log \text{EGR} 17$ , a row of 385 tracer particles is initially positioned 15 cm above the formal convective boundary, which is also 15 cm above the over-penetration extent (since there is no over-penetration at this EGR), while another row of 385 tracer particles is positioned 10 cm below the convective boundary,

log EGR	Study	Upper $z_i$ in cm	Lower $z_i$ in cm
17	A	+15 (+15)	-10 (-5)
17	B	+10 (+10)	-5 (0)
18.5	A	+45 (+5)	-25 (-5)
18.5	B	+40 (0)	-20 (0)

TABLE 4.19. Initial Vertical Positions of Tracer Particles.

Upper and lower initial positions ( $z_i$ ) of tracer particles. Units are in cm, quoted with respect to the position of the formal convective boundary as defined by the Schwarzschild criteria. Values in parenthesis are with respect to under- and over-penetration extents. 1 computational zone = 5 cm.

which is also 5 cm below the under-penetration extent (since the under-penetration extent is 5 cm below the convective boundary at this EGR).

Figure 4.56 shows the results at log EGR = 17. The highest and lowest positions which each of the 770 tracer particles ultimately attains during the entire analysis period are plotted against a background which show the velocity field and contour plot of the superadiabaticity of the final time-slice, in the same manner as had been presented in the previous analysis. To achieve optimal contrast for the purpose of display, *black* diamond-shaped data points on the plots signify the *lowest* positions attained by the particles starting *above* the convective region, and the *highest* positions attained by the particles starting *below* the convective region. In contrast, *white* diamonds are used for the complementary positions in each case. Thus, black dots appearing inside the convective region distinctly signify penetration events. Thus, in Study A at log EGR = 17 (top plot of Figure 4.56), virtually no penetration events occur, with the exception that some of the particles at the far left of the domain have begun to penetrate the top of the convective boundary. In this study, the initial vertical positions of the top row of tracer particles are 15 cm (three zones) from the top of the convective boundary, and since no upper-penetration occurs at this EGR level, this is also the distance from the upper-penetration extent. Nevertheless, some top-penetration is apparent. In contrast, the initial vertical position of the bottom row of tracer particles are only 5 cm (one zone) from the lowest under-penetration extent for this EGR level, and no bottom-penetration whatsoever appears to occur.

To show the sensitivity of the likelihood of penetration events on the initial vertical placement of the tracer particles, Study B at log EGR 17 (bottom plot of Figure 4.56) initially positions the tracer particles one zone closer toward the top and bottom convective boundaries compared to Study A. Thus, the particles are now initially placed at the same under-penetration extent found previously, but still a couple of zones above the top convective boundary, which is effectively the same as the over-penetration extent at this EGR level. This very slight change results in significantly more penetration events. Detailed analysis of the data reveals that while the rate at which penetration occurs increases at both boundaries, it occurs roughly three times more often at the bottom compared to the top boundary. The results suggest the bottom boundary is effectively impenetrable beyond a distance equivalent to the lowest extent of under-penetration, since penetration occurs only when particles are initially placed within this critical distance. On the other hand, the upper boundary is significantly more “leaky,” since even though no over-penetration was observed at this EGR level, top-penetration occurs when particles are initially placed several zones above the top convective boundary.

Similar results are found at log EGR 18.5 (Figure 4.57). Study A (top plot), initially places the particles 5 cm (one zone) beyond the under- and over-penetration extents for this EGR level. Some top-penetration occurs, but no bottom-penetration. However, in Study B (bottom plot), the tracer particles are initially positioned at the under- and over-penetration extents, and both top- and bottom-penetration become evident. Thus, as is observed at log EGR = 17, the top boundary appears to be much more permeable than the bottom boundary. Indeed, particles which are initially found in regions beyond the under-penetration extent appear unable to enter the convective region within a time-frame of a few convective timescales.

In principle, the nature of bottom- and top-penetration may be sensitive to the proximity of the upper convective boundary to the top edge of the computational domain. For instance, artificial motions which arise due to upper boundary interactions may influence particle

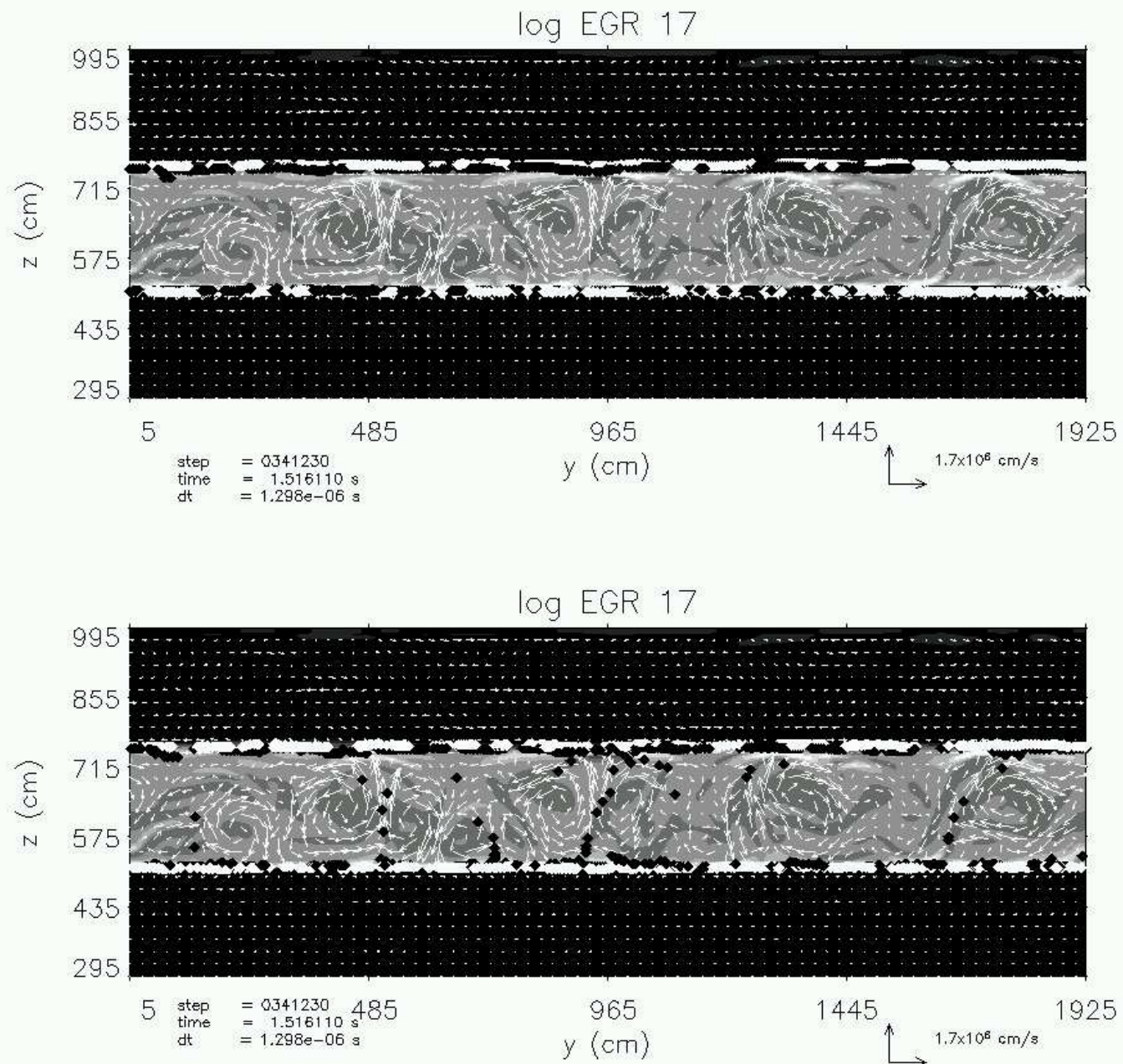


FIGURE 4.56. Particle Trajectory Limits (outside-in), log EGR = 17  
 Highest and lowest positions of 770 tracer particles are plotted as small, white or black diamonds. Initial positions of particles are outside the convective region. Study A: top plot. Study B: bottom plot.

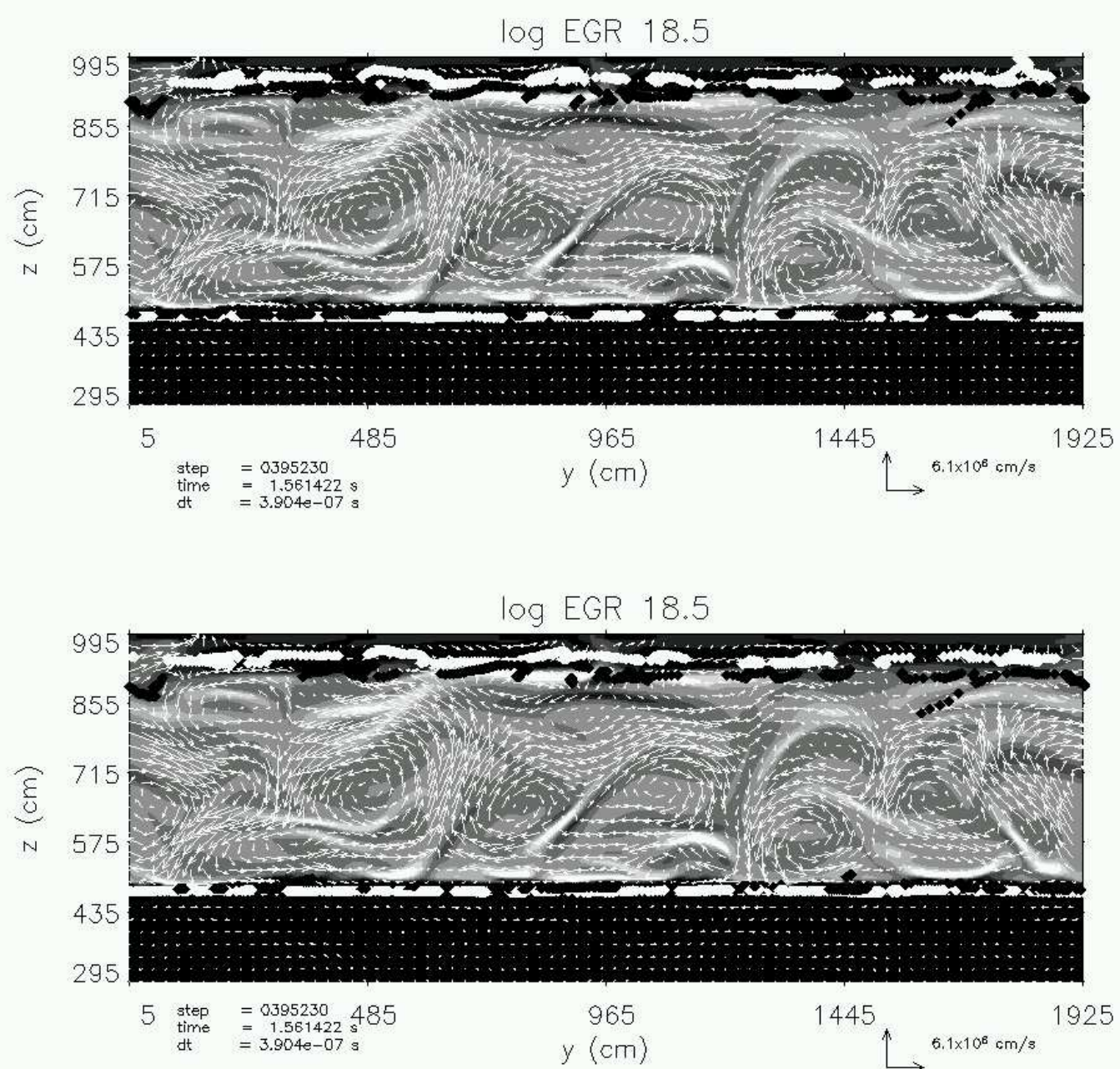


FIGURE 4.57. Particle Trajectory Limits (outside-in), log EGR = 18.5  
Highest and lowest positions of 770 tracer particles are plotted as small, white or black diamonds. Initial positions of particles are outside the convective region. Study A: top plot. Study B: bottom plot.

behavior there. To examine this possibility, the same series of tests of bottom- and top-penetration as previously described are also performed for models with extended vertical domains ( $386 \times 205$ ). The extended models have 5 more zones (25 cm) at the top of the domain. Plotted in the same manner as before, the extended domain results are shown in Figures 4.58 (log EGR = 17) and 4.59 (log EGR = 18.5), and are very similar to the results obtained from the shorter,  $386 \times 200$  standard domain, suggesting that the general nature of bottom- and top-penetration is not affected by the location of the upper boundary. Notably, while the average vertical height of the convective cells at log EGR = 17 is the same for both domains, the cells which form in the extended domain at log EGR = 18.5 are roughly 90% of the height compared to those in the standard domain. (This difference in cell sizes during the advanced stages of the burst will be quantified in Chapter 5, where the standard and extended models will be carefully compared as part of a series of validation studies.) Consequently, a repositioning of the initial positions of the tracer particles for the extended model analysis at log EGR = 18.5 is necessary to yield comparable results. Thus, while changing the height of the vertical dimension of the domain slightly affects the size of the convective cells at later stages of the burst, it does not noticeably affect the previously established nature of bottom- and top-penetration into the convective region.

**4.10.3. Summary of Tracer Particle Analyses.** Overall, the results of the tracer particle analyses show that the actual number of particles which penetrate the convective boundaries is very small, less than 5% of the total number of particles. The vast majority of particles with initial positions outside the convective layer stay outside. On the other hand, all particles starting within the convective region are permanently trapped within it. Penetration does occur, but only very rarely, and in the case of under- and over-penetration, only temporarily. This behavior may be partly understood by considering the dominance of lateral over vertical flows at the convective boundaries. Vertical progress of particles inside the convective region is effectively halted at the boundaries, since the vertical components of velocities diminish several orders of magnitude there. Lateral flows deflect the particles

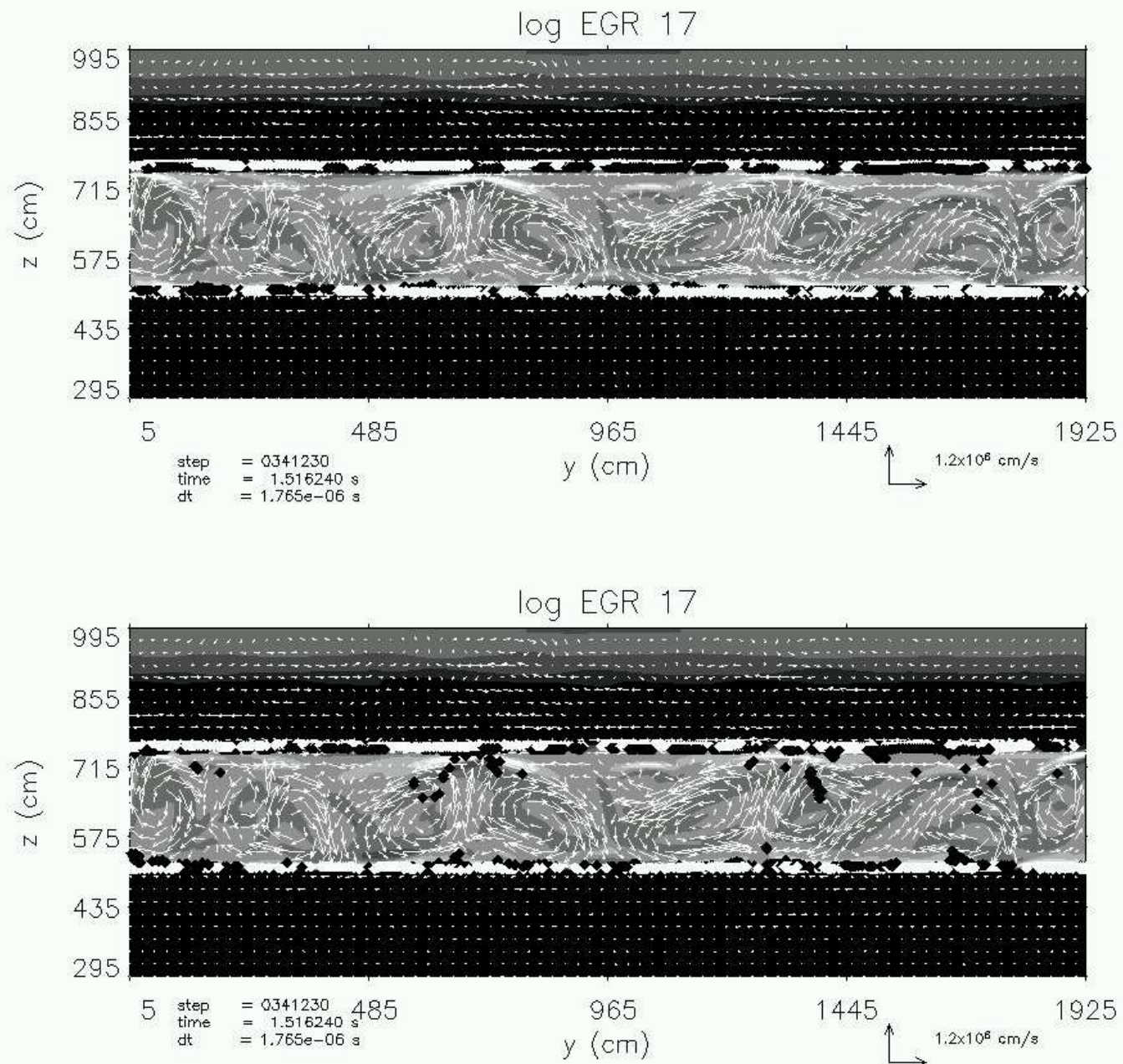


FIGURE 4.58. Particle Trajectory Limits (extended domain),  $\log \text{EGR} = 17$   
 Extended domain ( $386 \times 205$ ). Highest and lowest positions of 770 tracer particles are plotted as small, white or black diamonds. Initial positions of particles are outside the convective region. Study A: top plot. Study B: bottom plot.

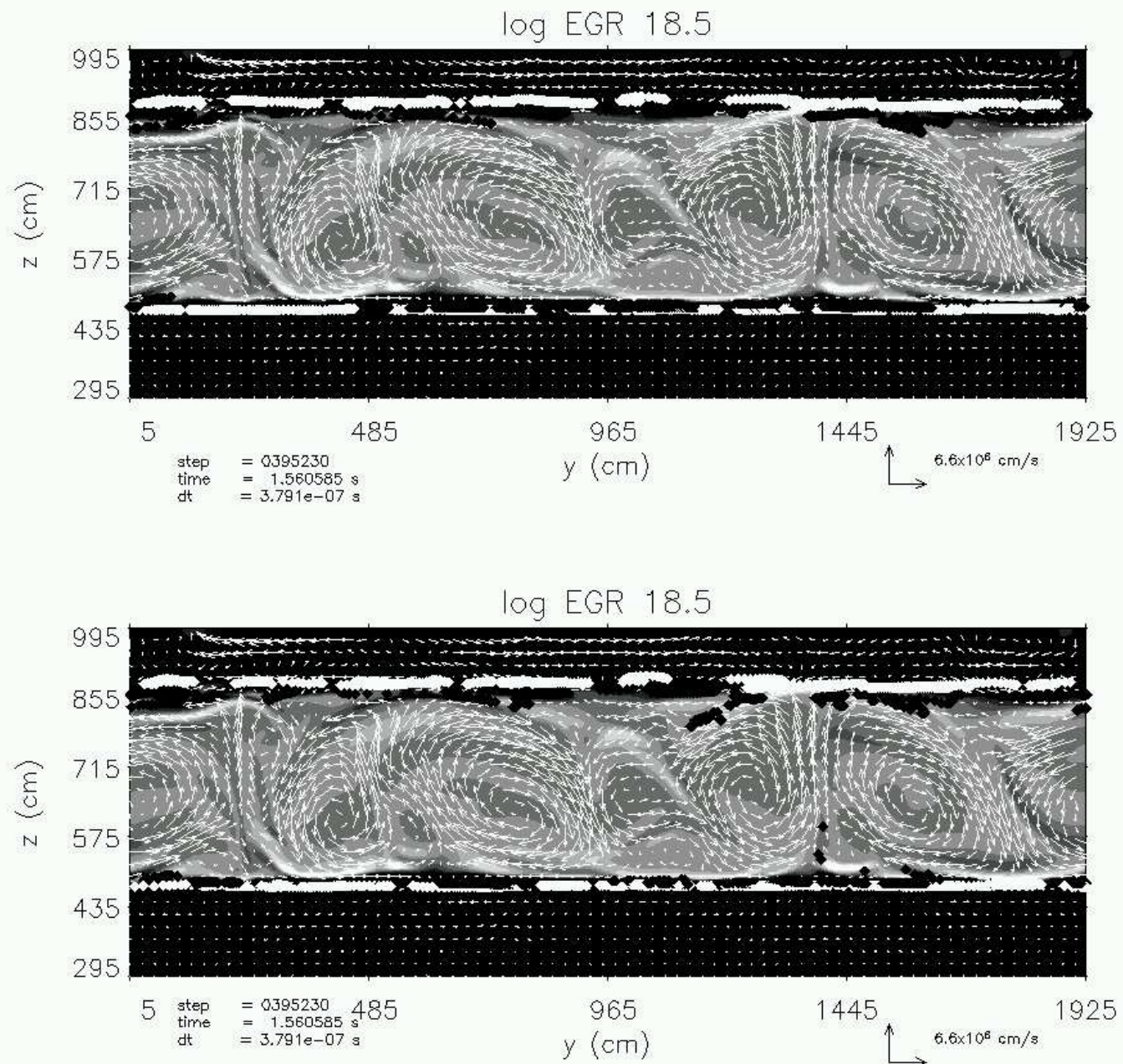


FIGURE 4.59. Particle Trajectory Limits (extended domain),  $\log \text{EGR} = 18.5$   
Extended domain ( $386 \times 205$ ). Highest and lowest positions of 770 tracer particles are plotted as small, white or black diamonds. Initial positions of particles are outside the convective region. Study A: top plot. Study B: bottom plot.

until they are eventually swept back into the convective region. Likewise, once particles initially outside the convective region reach the convective boundary, they may be carried by the lateral flows and eventually become trapped within the convective layer when much stronger, inwardly directed, convective currents consequently dictate their future paths.

The maximum extent of penetration is found to be 1/3 of a scale height in pressure, which occurs at the bottom boundary near the peak of the burst when the magnitudes of the velocities were greatest. This value is comparable to what Deupree (2000) reports (0.3–0.45 pressure scale heights, depending on mass) when studying hydrogen-burning convective cores of zero-age-main-sequence stars .

A downward bias for top-penetration appears to exist. Particles initially outside the convective region more easily fall down into the convective region from above it, rather than rise up into it from below. Examining the laterally and time-averaged vertical velocities  $\langle w \rangle$  as a function of depth helps to explain this downward bias. In Figure 4.60,  $\langle w \rangle$  is plotted against the vertical position  $z$  at  $\log \text{EGR} = 16, 17, 18$ , and  $19$ . Overlayed on each plot is the lateral and time-averaged vertical velocity correlation  $\langle W\text{-corr} \rangle$ , which helps delineate the vertical extent of the convective region ( $W\text{-corr} > 0.1$ ). Notably, while the peak vertical velocities are two orders of magnitude greater than the averages,  $\langle w \rangle$  in the convective region are on average comparable in magnitude with  $\langle w \rangle$  in the regions above and below it. While slight irregularities in the behavior of  $\langle w \rangle$  occur at the convective boundaries, the function is remarkably continuous there.

The plots in Figure 4.60 show that at each EGR level,  $\langle w \rangle$  is negative in the regions above the upper convective boundary, negative in the upper part of the convective region itself, positive in the lower part of the convective region, and slightly negative (of order  $10^2 \text{ cm s}^{-1}$ , not discernible on the scale of the plots) in the regions below the lower convective boundary. As the burst progresses,  $\langle w \rangle$  in a greater proportion of the lower part of the convective region becomes positive.

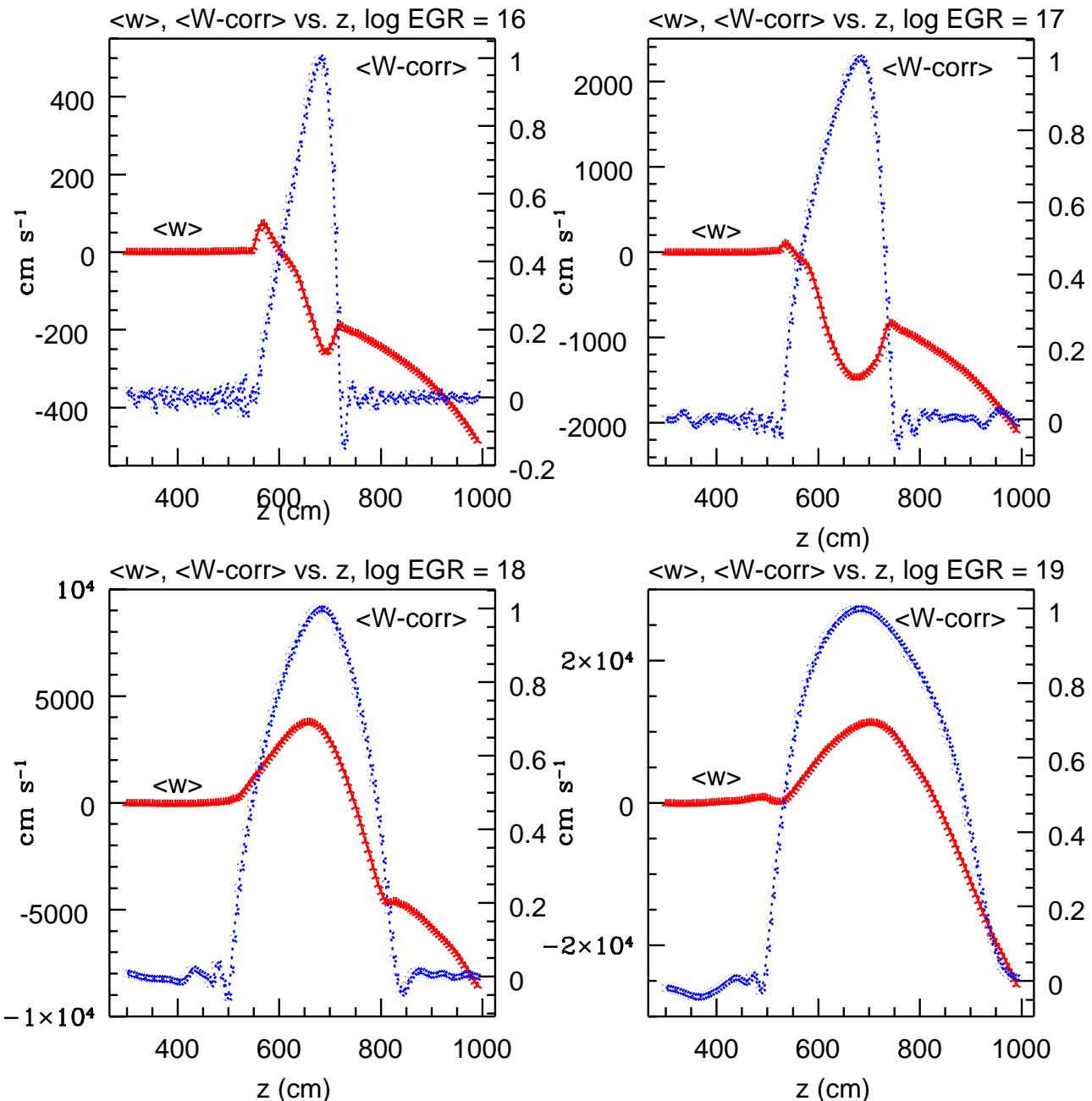


FIGURE 4.60. Average Vertical Velocity at Major EGR Levels  
 Laterally and time-averaged vertical velocities ( $\langle w \rangle$ ) as a function of depth ( $z$  in cm) at four log EGR levels (16, upper left; 17, upper right; 18, lower left; 19, lower right). Laterally and time-averaged vertical velocity correlations ( $\langle W\text{-corr} \rangle$ ) are overlaid. Left axis of each plot measures velocity ( $\text{cm s}^{-1}$ ), while the right axis measures velocity correlation (dimensionless).

These results help to explain the apparent downward bias of the general behavior of the tracer particles. Because  $\langle w \rangle$  is negative above the convective region, a net downward flow may carry particles which are initially above the upper convective boundary into the convective region. Once inside, these particles become trapped, because the net flow in the upper portion of the convective region itself is still downward, despite momentarily strong upward surges. At the lower convective boundary, the reverse is true:  $\langle w \rangle$  is slightly negative below the lower convective edge, inhibiting particles from rising up through it, but  $\langle w \rangle$  is slightly positive in the lower convective region, effectively helping to prevent particles from permanently escaping the convective region through the bottom boundary. Localized, strong downward surges may momentarily carry particles beyond the formal convective boundary, but such incursions are temporally and spatially limited. Thus, the downward bias in the overall dynamics of the tracer particles can be partly understood to result from average flows which exist both within and without the convective region.

As initially mentioned in Sub-section 4.6.1, the net downward flow also explains why the total amount of He4 by mass in the domain increases slightly until  $t = 1.55$  s ( $\log EGR = 18$ ). The downward flow effectively advects fuel deeper into the domain where the densities are greater. Consequently, the total mass of He4, which is the summation of the product  $\rho Y \Delta V$  over the entire domain, increases.

In the next section, modal analysis is performed to determine the role of gravity- and/or convective-modes in regions where penetration occurs.

## 4.11. Modal Analysis

As has been described thus far, two distinct dynamical regions in the domain can be identified: a vigorously churning convective region, which is laterally and temporally superadiabatic on average, sandwiched above and below by much calmer sub-adiabatic, non-convective regions. At the interface of these two regions, a small amount of penetration is observed, as had been previously established in Section 4.10 using tracer particles. At the lower EGR levels ( $\log \text{EGR} < 17$ ), the transition between convective and non-convective regions appears to be very well defined, the interface occurring over only a few computational zones. At the higher EGR levels ( $\log \text{EGR} > 18$ ), the transition becomes more blurry on sub-convective time scales, because localized, rapidly evolving convective surges may temporarily bend and flex the instantaneous convective boundaries significantly beyond their otherwise straight, laterally- and temporally-averaged limits. Since penetration is found to occur mostly at the higher EGR levels, the presence of convective modes (c-modes), as opposed to gravitational modes (g-modes), may be reasonably hypothesized to be the cause of penetration, when it does occur.

Previous studies support this hypothesis. For example, in a study which hydrodynamically simulates He-shell flash convection in low-mass asymptotic giant branch stars, both g- and c-modes were also found to cross the formal convective boundaries, leading to mixing across the boundaries (Herwig et al., 2006). Hydrodynamical instabilities were also found to generate weak turbulence which may result in mixing between the surface and deeper layers on an accreting neutron star (Urpin, 2005). Notably, these studies involved fully explicit hydrodynamics, which admitted acoustic (pressure, p-) modes.

By design, p-modes are naturally and completely excluded from the domain by the LMNA method. The present study is designed to test the hypothesis that c-modes are necessarily associated with penetration. The goal is to reveal the dominant dynamical modes of select lateral slices at certain vertical heights of the domain using  $k-w$  diagrams, making it possible to positively correlate the presence of c-modes in regions where penetration occurs.

The modal analysis requires a straightforward data processing procedure. For each vertical height examined, the vertical component of the velocity in all 385 lateral zones at that height is recorded at every time-step, the duration and total number of which depends on the EGR level examined, information which will be detailed below. This 2D array of data ( $y$  vs.  $t$ ) is transformed into Fourier space ( $k$  vs.  $w$ ) using a standard Fast Fourier Transform routine. Taking the square of the resulting amplitudes yields the power spectrum of the original data, which is the final  $k - w$  diagram. (For convenience, the values of the wave-number  $k$  and frequency  $w$  already have the constant  $2\pi$  factored out, such that  $k_n = \frac{1}{\lambda_n}$ , and  $w_n = \frac{1}{t_n}$ , where  $\lambda_n$  is the  $n$ -th multiple of the lateral zone size of 5 cm, and  $t_n$  is the  $n$ -th multiple of the appropriate time-step.) Two EGR levels are considered:  $\log \text{EGR} = 17$  and 18.5. At  $\log \text{EGR} = 17$ , the duration of the time-step is fixed at a constant  $dt_{17} = 1.0 \times 10^{-6}$  s, and the analysis spans 2000 time-steps, or, a total period of 4 convective times. At  $\log \text{EGR} = 18.5$ ,  $dt_{18.5} = 1.0 \times 10^{-7}$  s, and 4000 time-steps are covered for a total analysis period of 2 convective times. (A Hanning filter is applied to the time-axis of the original data, a standard procedure which very slightly improves the clarity of the final results.)

For reference, the Brunt-Väisälä frequency as a function of vertical position for  $\log \text{EGR} = 17$  and 18.5 is plotted in Figure 4.61. The Brunt-Väisälä frequency  $w_{BV}$ , is the natural frequency of a displaced element in a dynamically stable layer, and it is derived by considering the buoyancy force per unit volume which a displaced element in a dynamically stable layer experiences, for example, in Kippenhahn and Weigert (1990):

$$(4.10) \quad w_{BV}^2 = \frac{g\delta}{H_P} \left( \nabla_{ad} - \nabla + \frac{c_1}{c_2} \nabla_\mu \right)$$

All variables are defined at the beginning of this chapter, and  $H_P = -\frac{dr}{d\ln P}$  is the pressure scale height. As the figures show,  $w_{BV}$  is on the order of  $10^4 \text{ s}^{-1}$  in the non-convective regions, and this is the expected frequency of g-modes. Note that when  $w_{BV}$  becomes zero

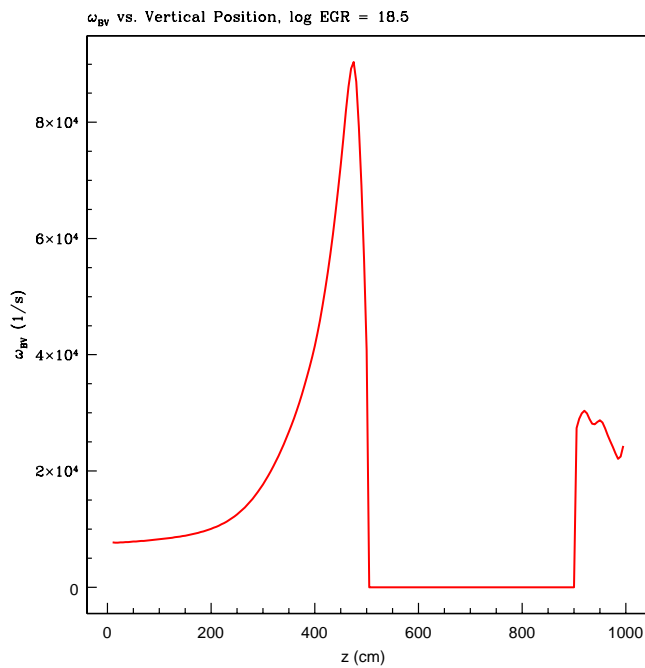
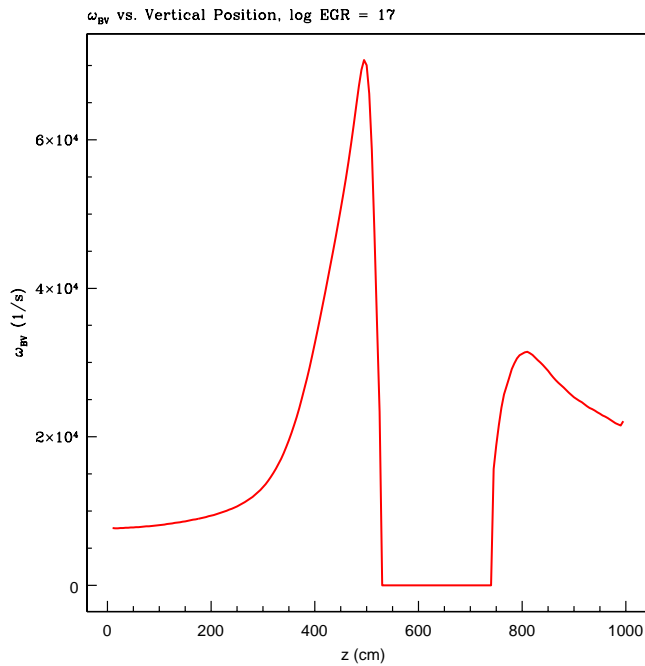


FIGURE 4.61. Brunt-Väisälä Frequency vs. Vertical Position  
Brunt-Väisälä Frequency vs. Vertical Position for log EGR = 17 and 18.5

(or imaginary), the region is convectively unstable, offering another way to quantify the exact limits of the convective boundaries

Figures 4.62 (lower convective boundary) and 4.63 (upper convective boundary) show the resulting  $k - w$  diagrams at log EGR 17, and Figures 4.64 (lower convective boundary) and 4.65 (upper convective boundary), at log EGR 18.5. Each figure consists of four  $k - w$  diagrams, where each diagram represents a lateral slice at different vertical heights in the domain as follows: 1) the upper left diagram, where it is dynamically stable; 2) the upper right diagram, where the most extreme limits of particle penetration occurs, based on the tracer particle analysis of Section 4.10; 3) the lower left diagram, where the boundary of the convective region lies; and, 4) the lower right diagram, fully within the convective layer. (The specific vertical height considered is given in the label above each diagram.) The value of the power spectrum is presented in a linear scale, and the legend bar shows the range of the scale of values plotted. Each diagram shows only a small fraction of the entire phase space, specifically, the lowermost left corner; that is, most of the power occurs at relatively longer timescales (small  $w$ ) and relatively larger structures (small  $k$ ).

The  $k - w$  diagrams consistently show higher frequency modes in the non-convective regions (upper left plots in each figure), where  $w$  is roughly in the range of  $w_{BV}$  as expected. Moreover, the outlines of a dispersion-relation-like curve can be discerned, more clearly at log EGR 17, faintly present at log EGR 18.5. These features can be interpreted as characterizing g-modes in the domain. Generally, smaller dynamical structures ( $< 100$  cm) oscillate with a period on the order of roughly  $10 \mu s$  or less, while larger structures ( $> 200$  cm),  $20 \mu s$  or more.

Within the convective regions (lower right plots in each figure), the features in the  $k - w$  diagrams become very different. Most of the power is now concentrated at the bottom of the diagram, corresponding to periods approaching the total limits of the analysis, about  $2000 \mu s$  for log EGR 17, and  $400 \mu s$  for log EGR 18.5, that is, on the order of the appropriate convective times. The length-scales which oscillate with these periods appear to have

dimensions between 100-400 cm, agreeing with the sizes of the convective cells in the flow field diagrams which are presented in Section 4.7. No dispersion-like curves are evident here. Thus, these features can be interpreted as characterizing c-modes.

At and near the convective boundaries (lower left and upper right plots in each figure), the  $k - w$  diagrams appear to show mixed features of both g- and c-modes. As evidenced by a complete analysis where the  $k - w$  diagrams of all vertical heights were examined (from which the four representative diagrams at each boundary and EGR level were chosen to be presented in this chapter), the regions near the convective boundaries are characterized by a gradual transition of dynamical modes, where g- and c-modes both contribute. Modally, the bridge between non-convective and convective regions is a gradual slope, not a sharp step.

Since the extent of penetration is limited to a very small distance beyond the convective boundary, the results suggest that penetration of trace particles, and thus mixing of material, occurs where both g- and c-modes are present. Moreover, since no over-penetration is found at  $\log \text{EGR} = 17$ , even though c-modes are evident at the upper convective boundary at this time, c-modes may exist where penetration does not. Also, where top-penetration occurs at  $\log \text{EGR} = 17$ , c-modes do exist. Thus, c-modes are apparently necessary but not sufficient for penetration to occur.

The results support the original hypothesis that convective motions play an important role in driving penetration events, temporary and limited though they may be. Modal analysis reveals both g- and c-modes near the convective boundaries where penetration occurs. The transition between non-convective to convective regions is thus gradual, in terms of dynamical modes, unlike the formal convective boundaries which are quite sharp and distinct. Physically, the disparity can be explained by the rapid, dynamical nature of the evolution of the flow field, which often features sudden, strong surges that break through the formal convective boundaries. The extent and frequency of this penetration increases as the burst rises to greater EGR levels, pushing material originally within the convective layer into the

adjacent regions. However, the incursion is only momentary, as the flows just as rapidly reverse direction, sweeping up the material which had just spilled outside the unstable region back inside.

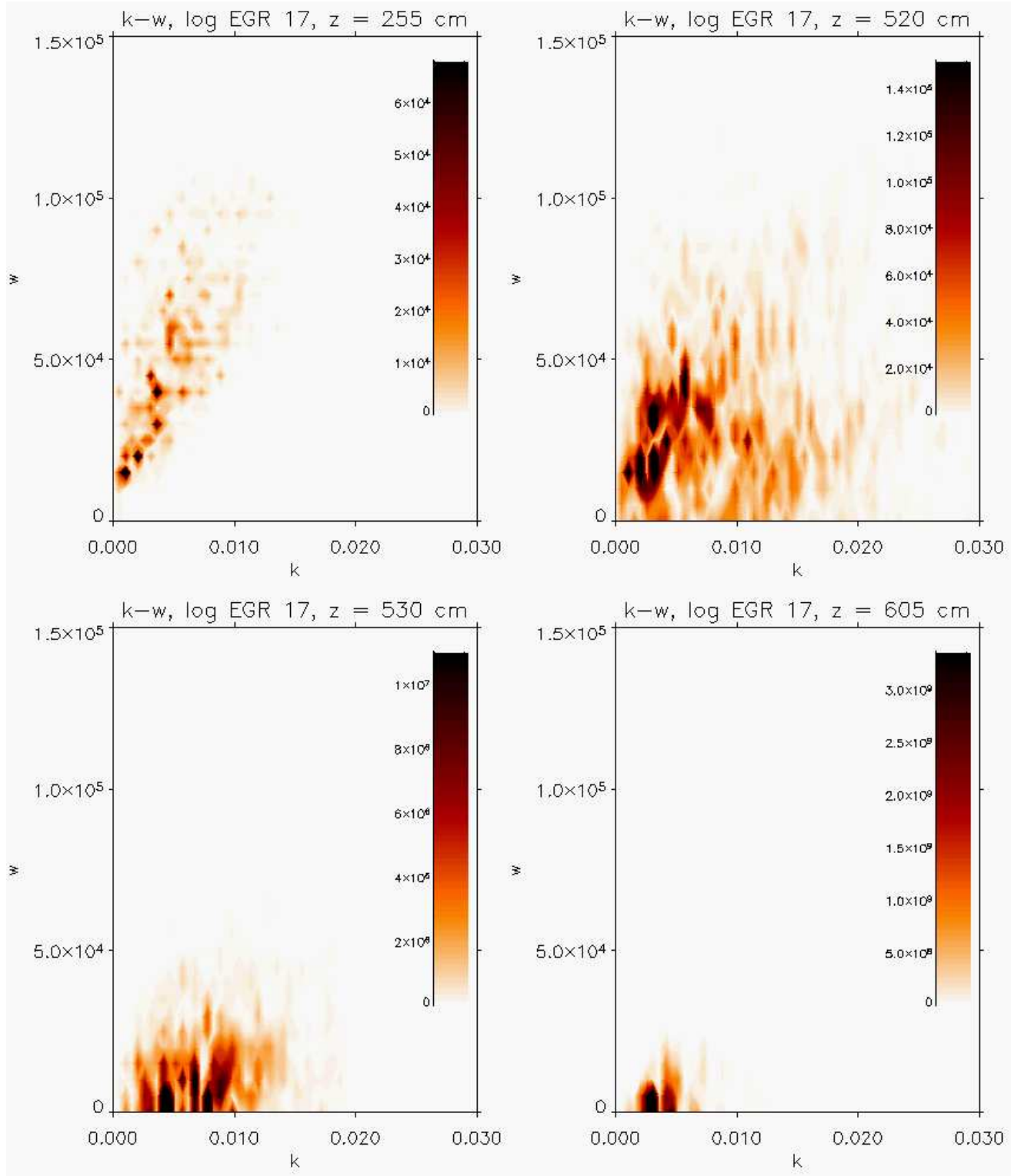


FIGURE 4.62.  $k - w$  Diagrams, Lower Convective Boundary,  $\log \text{EGR} = 17$   
 Upper left, dynamically stable region ; upper right, limit of penetration extent; lower left,  
 convective boundary; lower right, within the convective layer. Linear scale.

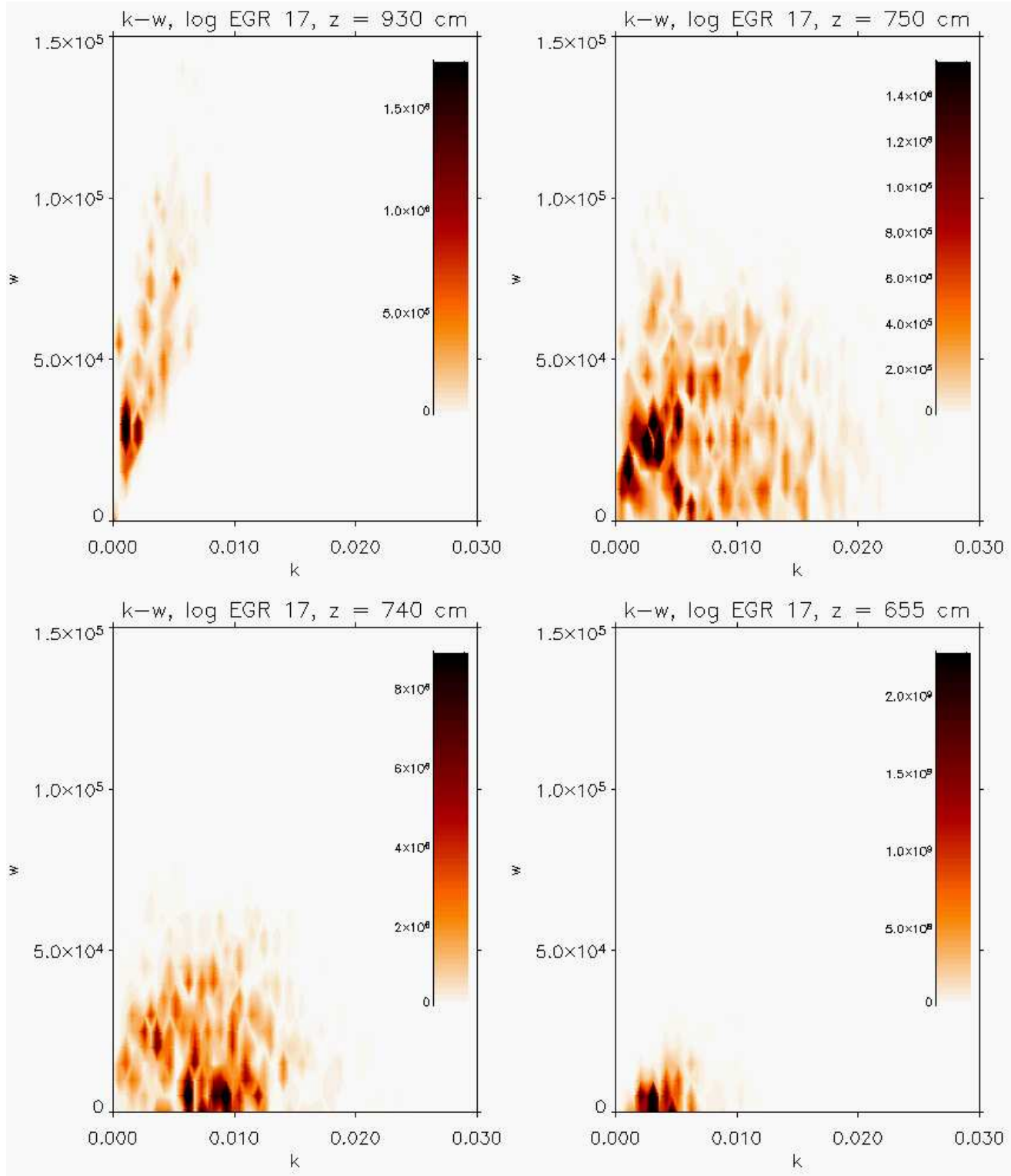


FIGURE 4.63.  $k - w$  Diagrams, Upper Convective Boundary,  $\log \text{EGR} = 17$   
 Upper left, dynamically stable region ; upper right, limit of penetration extent; lower left,  
 convective boundary; lower right, within the convective layer. Linear scale.

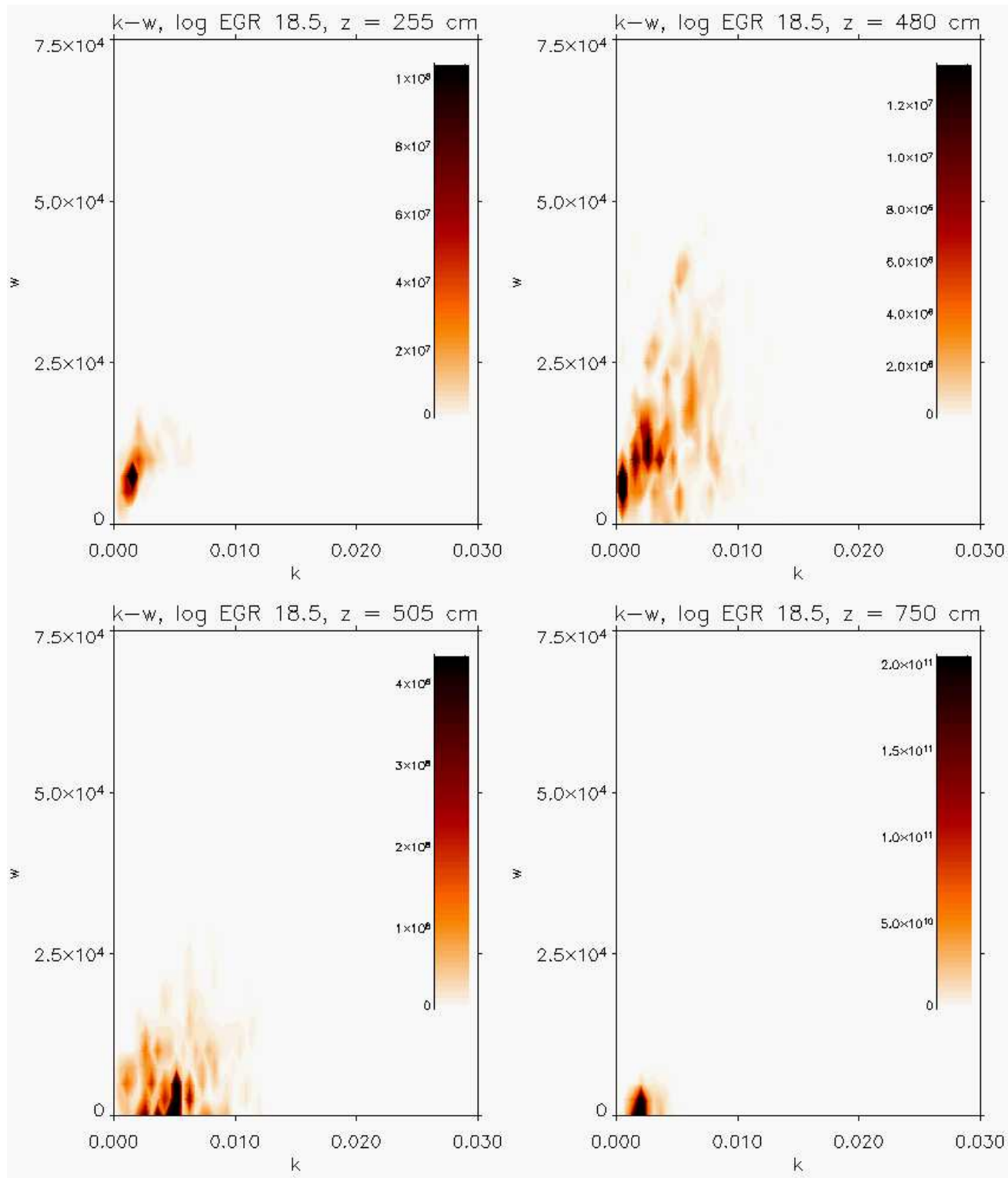


FIGURE 4.64.  $k - w$  Diagrams, Lower Convective Boundary,  $\log \text{EGR} = 18.5$   
Upper left, dynamically stable region ; upper right, limit of penetration extent; lower left,  
convective boundary; lower right, within the convective layer. Linear scale.

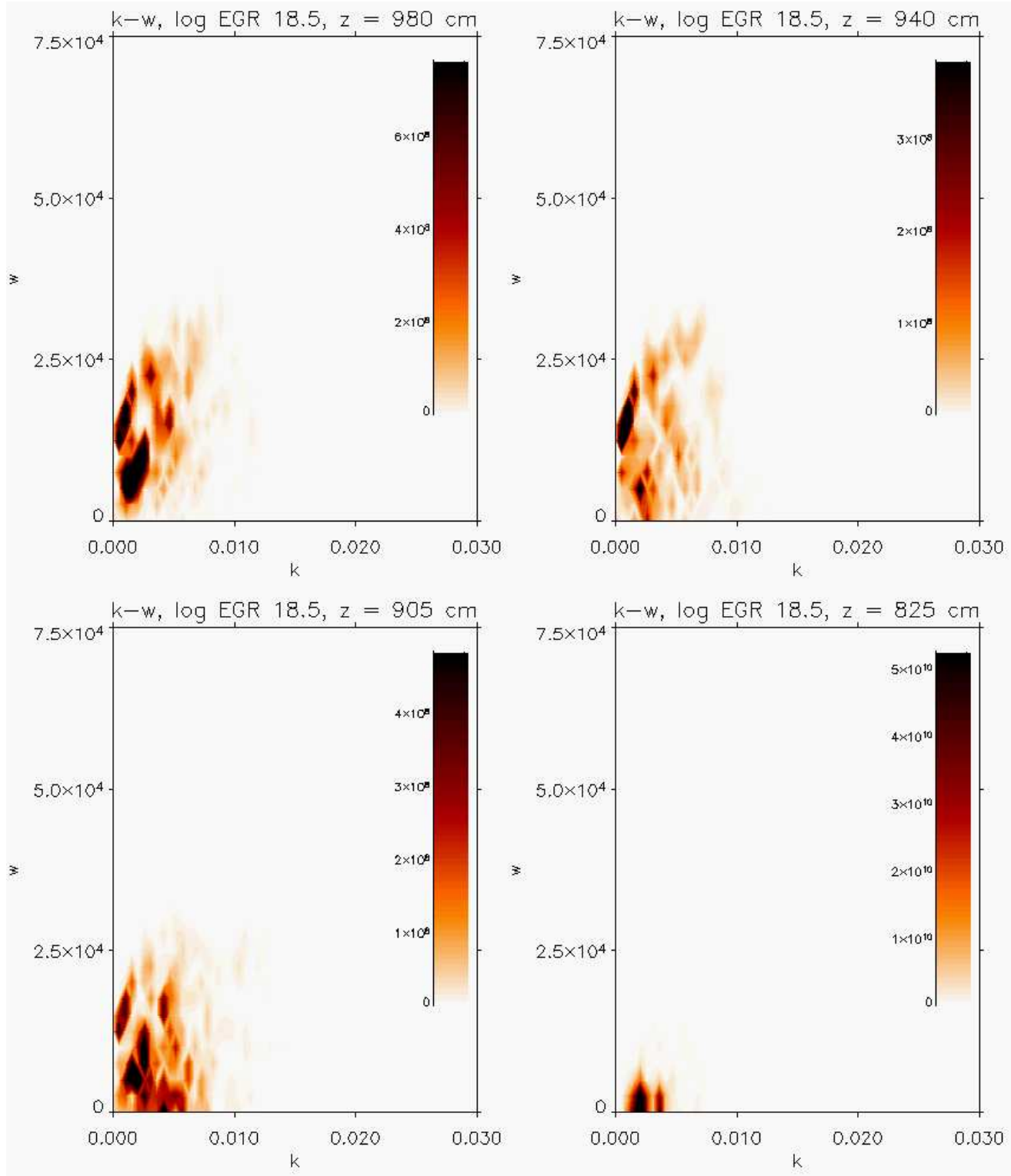


FIGURE 4.65.  $k - w$  Diagrams, Upper Convective Boundary,  $\log \text{EGR} = 18.5$   
Upper left, dynamically stable region ; upper right, limit of penetration extent; lower left,  
convective boundary; lower right, within the convective layer. Linear scale.

## 4.12. Mixing-Length Theory

The mixing-length theory (MLT) is used extensively in astrophysical computations as a local model for convection (Kippenhahn and Weigert, 1990; Steffen and Jordan, 2001). It is based on a simplistic picture of a buoyant bubble which rises a certain mixing-length  $l = \alpha H_p$  (defined in terms of the local pressure scale height  $H_p$  and the mixing-length parameter  $\alpha$ ) and then diffuses into its surroundings. With MLT,  $\alpha$  can be straightforwardly related to quantities such as the convective energy flux  $F_c$ , the superadiabatic excess ( $\Delta\nabla = \nabla - \nabla_{ad}$ ), the magnitude of the average temperature  $T'$  and velocity  $w'$  fluctuations, and the average flow speed  $w$ . For example,

$$(4.11) \quad w \propto \alpha^2 \Delta\nabla$$

$$(4.12) \quad T' \propto \alpha T \Delta\nabla$$

$$(4.13) \quad F_c \propto \frac{w'}{\alpha}$$

$$(4.14) \quad F_c^2 \propto \alpha T'^3$$

Numerous 2D and 3D hydrodynamical simulations of solar convection (Chan and Sofia, 1986, 1987; Kim et al., 1996; Abbott et al., 1997; D.H. and Woodward, 2000; Steffen and Jordan, 2001) show good agreement between their results and the predictions of MLT, and  $\alpha$  is found to be of order 1. Agreement generally worsens at the convective boundaries, since MLT, being a local theory of convection, is not able to account for convective flows

which extend beyond the formal convective region. For example, elemental mixing between convectively stable and unstable regions would not be possible in MLT.

A diligent attempt was made to compare the results of the present LMNA calculations with the predictions of MLT, for example, with the relationships expressed in Equations 4.11, 4.12, 4.13, and 4.14. However, no consistent value for  $\alpha$  could be determined, perhaps due to the very small value of the superadiabaticity present in the domain.

The failure to agree with MLT is not altogether unreasonable. The dynamic nature of the present results clearly demonstrate the non-local nature of convection; there is no apparent reason why the dynamic and thermodynamic values of a given position in the domain should be determined by local conditions.

## CHAPTER 5

### 2D Validation Studies

Extensive validation studies were performed to demonstrate convergence of qualitative and quantitative results of the Low Mach Number Approximation model. In this chapter, the results of several important validation studies are presented: 1) the Grid Refinement Study tests three models having different zone sizes; 2) the Time Resolution Study examines three models having different time-step restrictions; and, 3) the Extended Vertical Boundary Study compares two models with different vertical extents. Comparisons of the different models are based on qualitative flow field plots, dynamical animation comparisons, time-evolution of important thermodynamic and velocity quantities, and vertical profiles of velocity correlations and important gradients ( $\nabla \equiv (\frac{d \ln T}{d \ln P})_{actual}$ ,  $\nabla_{ad} \equiv (\frac{d \ln T}{d \ln P})_s$ ,  $\nabla_L \equiv \nabla_{ad} + \frac{c_1}{c_2} \nabla_\mu$ , where  $\nabla_\mu \equiv (\frac{d \ln \mu}{d \ln P})$ ,  $c_1 \equiv \left(\frac{\partial \ln \rho}{\partial \ln \mu}\right)_{P,T}$ ,  $c_2 \equiv -\left(\frac{\partial \ln \rho}{\partial \ln T}\right)_{P,\mu}$ ). Other consistency studies involved testing isolated pieces of the Low Mach Number Approximation model, such as advecting composition and temperature in artificial flow fields, diffusing an artificial temperature gradient, burning nuclear fuel in a certain time interval, and solving analytical functions with the elliptic solver. All of these validation studies show that the results are convergent, consistent, and physically reasonable.

#### 5.1. 2D Domains

As is explained in Chapter 4, the 2D domains consist of an  $m \times n$  Cartesian grid of uniformly sized zones, where  $m$  and  $n$  refer to the number of zones in the lateral ( $j$  or  $y$ ) direction and vertical ( $k$  or  $z$ ) directions respectively. Each zone has an aspect ratio of 1:1 at all times for all models. The main computational domain, whose zones are laid out on a Cartesian coordinate system  $(j, k)$ , consists of all the zones between the coordinates  $j, k = 2$ , and  $j = m - 1$  and  $k = n - 1$ . The rows and columns corresponding to  $j, k = 1$ , and  $j$

$= m, k = n$  consist of guardcells which bound the main computational domain on all sides (upper, lower, left, right).

If the lateral extent of the domain is too small, one Benard cell forms and takes up the entire width of the computational domain, and the size of the cell correlates with the width of the computational domain. Thus, an insufficient lateral extent may cause numerical artifacts, because the periodic boundary condition is influencing the natural evolution of dynamical features. By increasing the lateral extent of the domain sufficiently, multiple cells begin to develop and fit in the domain, and beyond a certain domain width, the lateral sizes of the cells become independent of the domain width, a sign that the lateral boundaries are sufficiently distant to avoid influencing the results. For the 2D models used in this chapter, the width of the domains ( $m = 386$  for the  $5 \text{ cm zone}^{-1}$  model) is wide enough to include at least four large Benard cells. Furthermore, the evolution of characteristic thermodynamic and velocity values (such as peak EGR, peak temperature, peak Mach number, etc.) is not significantly sensitive to the width of the lateral domain provided it is sufficiently large.

The boundary conditions imposed on the main domain and constraints on the time-step are identical to those presented in Chapter 4.

## 5.2. Grid Refinement Study

Three zone sizes were used to test for convergence of results under zone refinement: 5, 7.5, and  $10 \text{ cm zone}^{-1}$ . Table 5.1 gives the dimensions of three 2D domains of varying resolutions used in the grid refinement study. To equalize time-steps, the CFL for each model was adjusted appropriately.

Figures 5.1, 5.2, 5.3, and 5.4 compare the velocity flow fields of the 5, 7.5, and  $10 \text{ cm zone}^{-1}$  models at four log EGR levels (16, 17, 18, and 19), which show snap-shots of the dynamical evolution up to the peak of the burst. Only the upper-most 775 cm of the computational domain is shown, since the lower 225 cm is calm compared to the convectively unstable region. To facilitate ease of comparison between the results of the different models,

Zone Size (cm)	$m$ (zones)	$n$ (zones)	CFL
10	194	100	0.5 / 2.0
7.5	258	154	0.5 / 1.5
5	386	200	0.5 / 1.0

TABLE 5.1. 2D Domain Sizes in Grid Refinement Study

the effective resolution of the flow fields in the figures has been scaled to the lowest-common-multiple ( $= 30 \text{ cm zone}^{-1}$ ) of the three models.

Qualitatively, the flow fields show that all models yield similarly sized Benard cells (Koschmieder, 1993) of approximately the same peak velocities at each EGR level. Moreover, the lateral distribution and aspect ratios of the cells are quite comparable between the different resolutions. In all cases, the convective motions appear confined between well-defined bands which extend the full lateral width of the domain. These bands widen vertically as the burst progresses. Convective motions naturally develop within these bands, and the velocities of the convective flows increase as the EGR increases. As was shown, these convectively unstable regions are characterized by superadiabaticity as defined by the Schwarzschild criteria ( $\nabla \geq \nabla_{ad}$ ) (Kippenhahn and Weigert, 1990).

To help quantify the extent and evolution of the convectively unstable region, the vertical velocity correlation function  $W$  is calculated in the manner of Chan and Sofia (1987) as explained in Section 4.9 of Chapter 4. The convective region is characterized by  $W > 0.10$ . Figures 5.5, 5.6, 5.7, 5.8 show  $W$  plotted as a function of  $\ln P$  for the three grid refinement models at four EGR levels. (One pressure scale height is about 200 cm.) Also plotted are  $\nabla$ ,  $\nabla_{ad}$ , and  $\nabla_L$  as functions of  $\ln P$ . As expected, the figures show that for all models at all EGR levels, the convectively unstable region occurs where  $\nabla$  is essentially adiabatic. Outside this region, where no significant convective motions develop, the gradient is clearly sub-adiabatic. Also, at both the upper and lower edges of the convectively unstable region, the actual gradient more closely follows the Ledoux criteria. Notably, the velocity correlations of all the models show considerable agreement at each EGR level when overlayed on top of each other, suggesting convergence of the dynamical features in terms of spatial resolution.

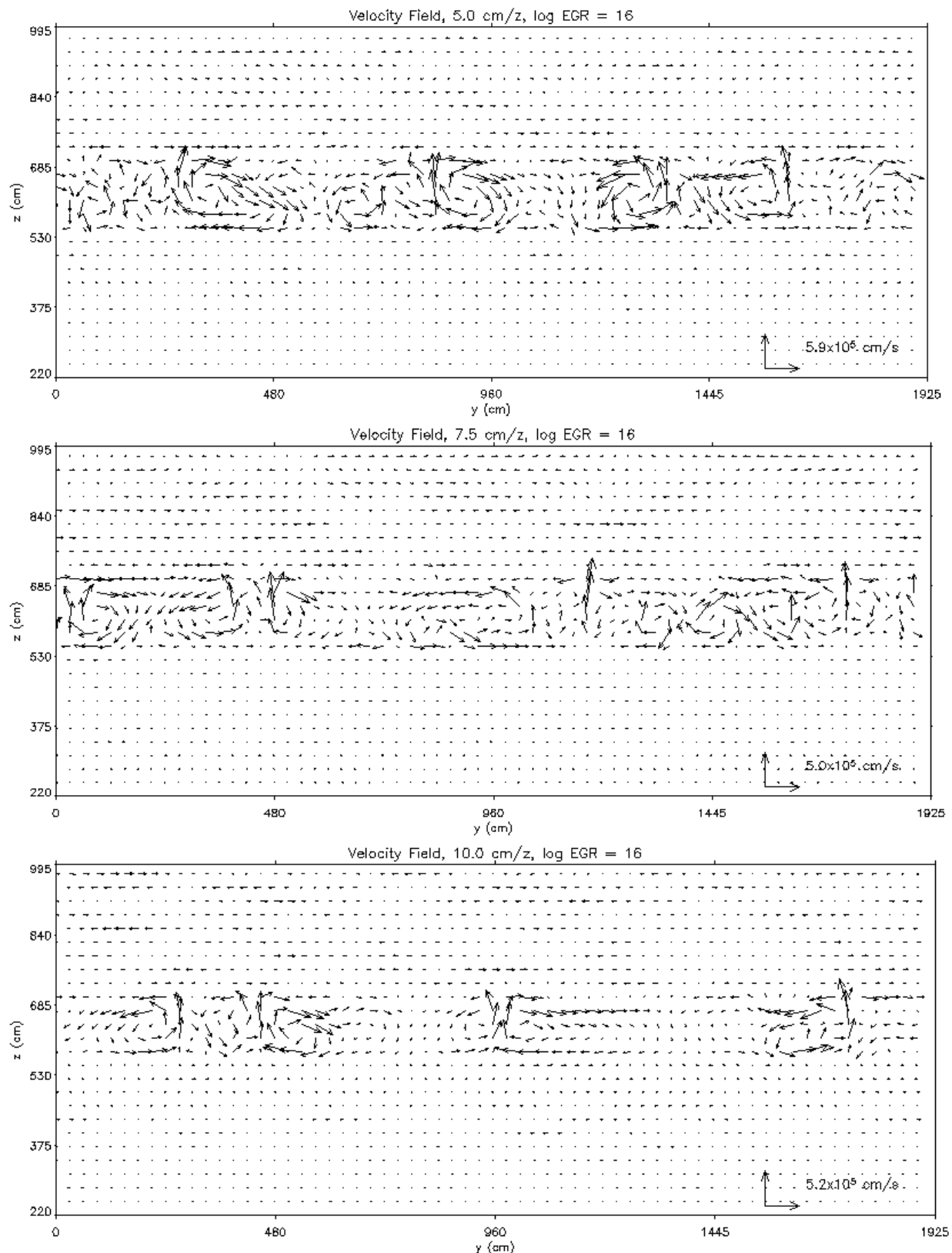


FIGURE 5.1. Grid Refinement:  $\log EGR = 16$   
Velocity flow fields (top 5, middle 7.5, bottom 10  $\text{cm zone}^{-1}$ ).

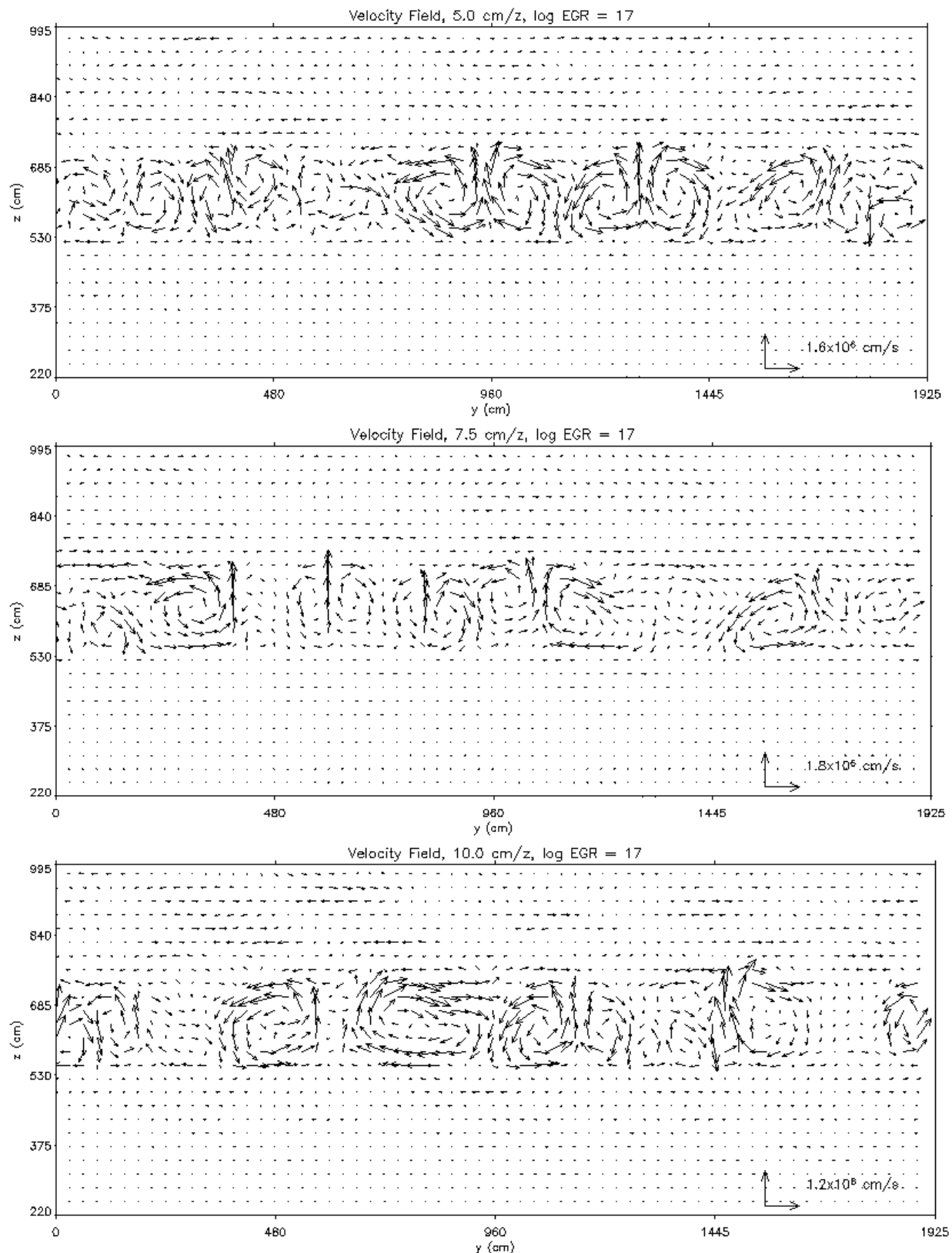


FIGURE 5.2. Grid Refinement:  $\log \text{EGR} = 17$   
Velocity flow fields (top 5, middle 7.5, bottom  $10 \text{ cm zone}^{-1}$ ).

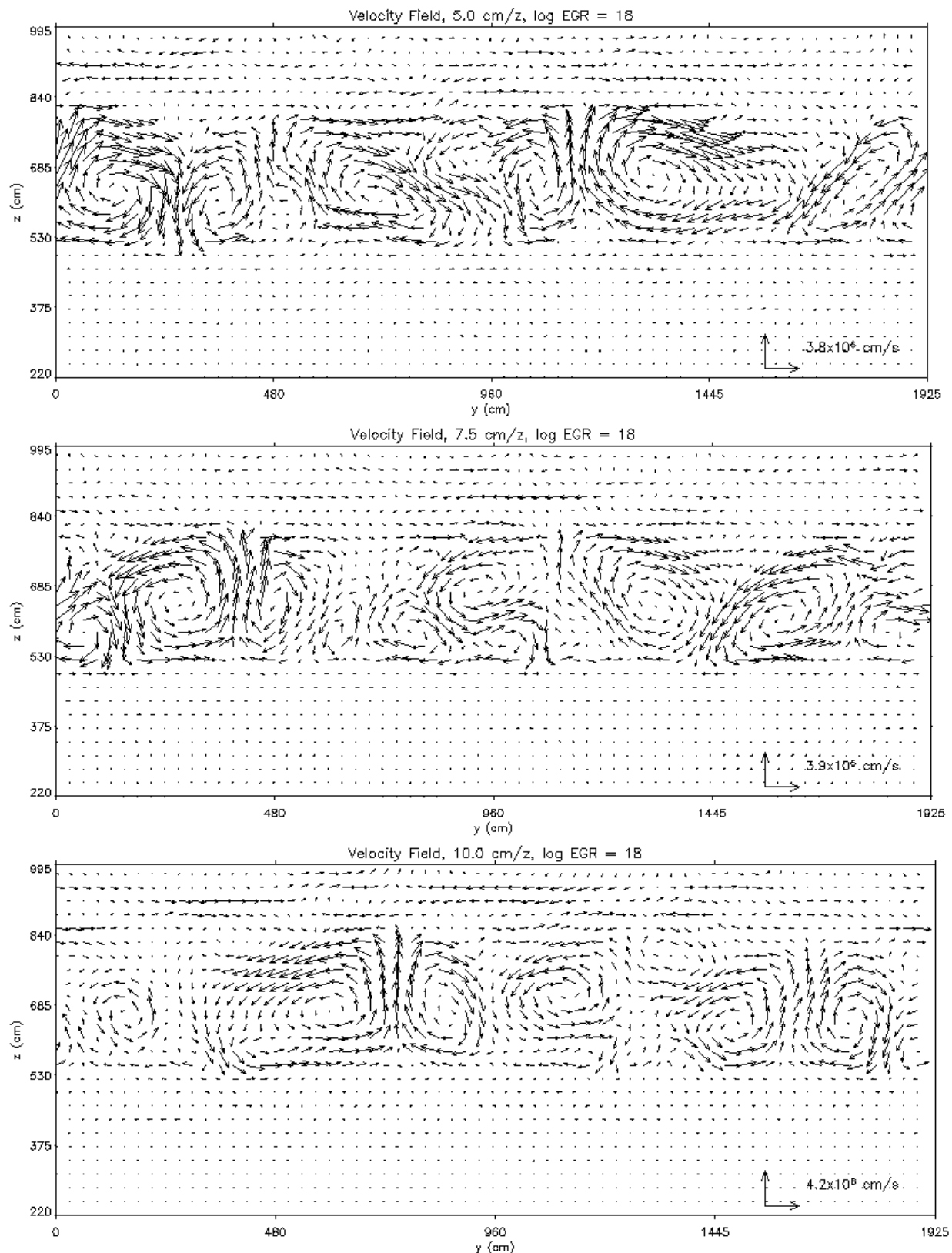


FIGURE 5.3. Grid Refinement: log EGR = 18  
Velocity flow fields (top 5, middle 7.5, bottom 10 cm zone<sup>-1</sup>).

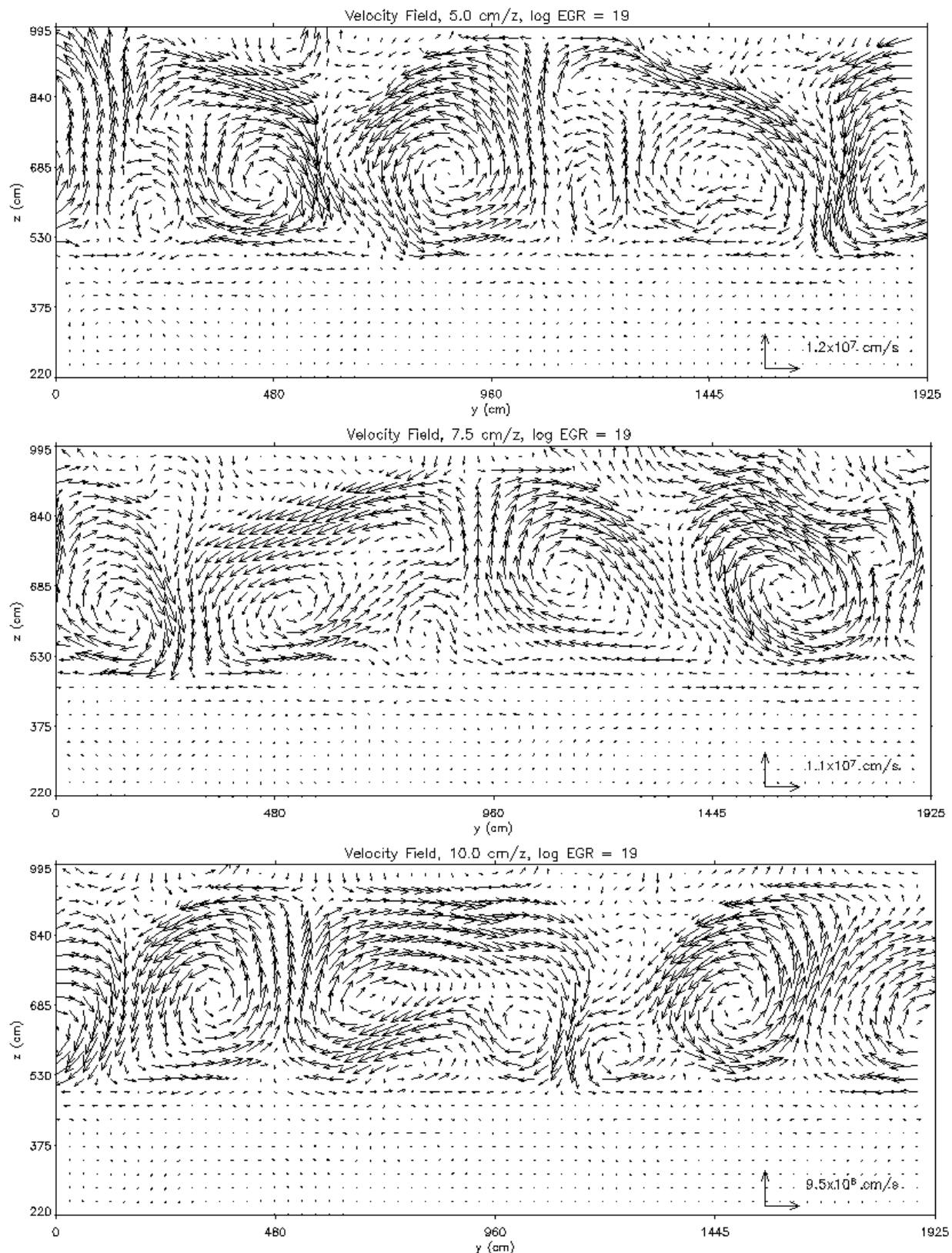


FIGURE 5.4. Grid Refinement:  $\log \text{EGR} = 19$   
Velocity flow fields (top 5, middle 7.5, bottom 10  $\text{cm zone}^{-1}$ ).

More evidence for spatial resolution convergence can be seen in Figures 5.9 and 5.10, which compare global thermodynamic and velocity quantities as a function of time for the different resolutions. For all models, the peak values of EGR,  $T$ , flux, He4 composition,  $v$ ,  $w$ , total velocity, and Mach number all behave similarly throughout the burst sequence. The results indicate less time (up to 0.1 s) is needed to reach the burst peak with greater zone resolution. This effect can be explained by considering the effects of numerical dissipation: the greater the resolution, the less the dissipation of heat, and hence, the faster the burning can commence.

Based on the peak value of EGR and flux, the burst rise-time is about  $1.6 \pm 0.1$  s, subsequently followed by a rapid decay in about 0.1-0.2 s. The general features of the bursts at all resolutions are the same as is presented in Section 4.5 of Chapter 4.

To compare the speeds at which the convective layer boundaries expand above and below the ignition layer, the laterally averaged, vertical profile of He4 at numerous times through the burst sequence is examined in the manner explained in Sub-section ?? of Chapter 4. The upper left plot of Figure 5.11 shows a sample of such a profile for the  $5 \text{ cm zone}^{-1}$  model. The two boundaries of the burning are taken to be where the slope of the He4 profile is greatest (upper right plot of Figure 5.11, since it represents roughly one-half the distance between where the He4 is at its original value (unmixed regions) and where it is homogenized due to the expanding convectively unstable region (mixed regions)). As a function of time, the lower left plot of Figure 5.11 shows the upper-boundary's position for each of the three models used in the grid refinement study, and the lower right plot shows the upper-boundary's speed vs. time. All models show comparable behavior over time. Consistent with the log EGR vs. Time plot in Figure 5.9, the results show a delay in the burst for models with larger zone sizes. However, the magnitude of the speed of the upper-boundary at equivalent phases in the burst is approximately the same for all resolutions. Taken together, the grid refinement results indicate that the domain is sufficiently well-resolved at zone sizes equal to or less than

$10 \text{ cm zone}^{-1}$ . Consequently, the resolution of the standard model used for more detailed analysis reported in Chapter 4 on the Standard Model Results is chosen to be  $5 \text{ cm zone}^{-1}$ .

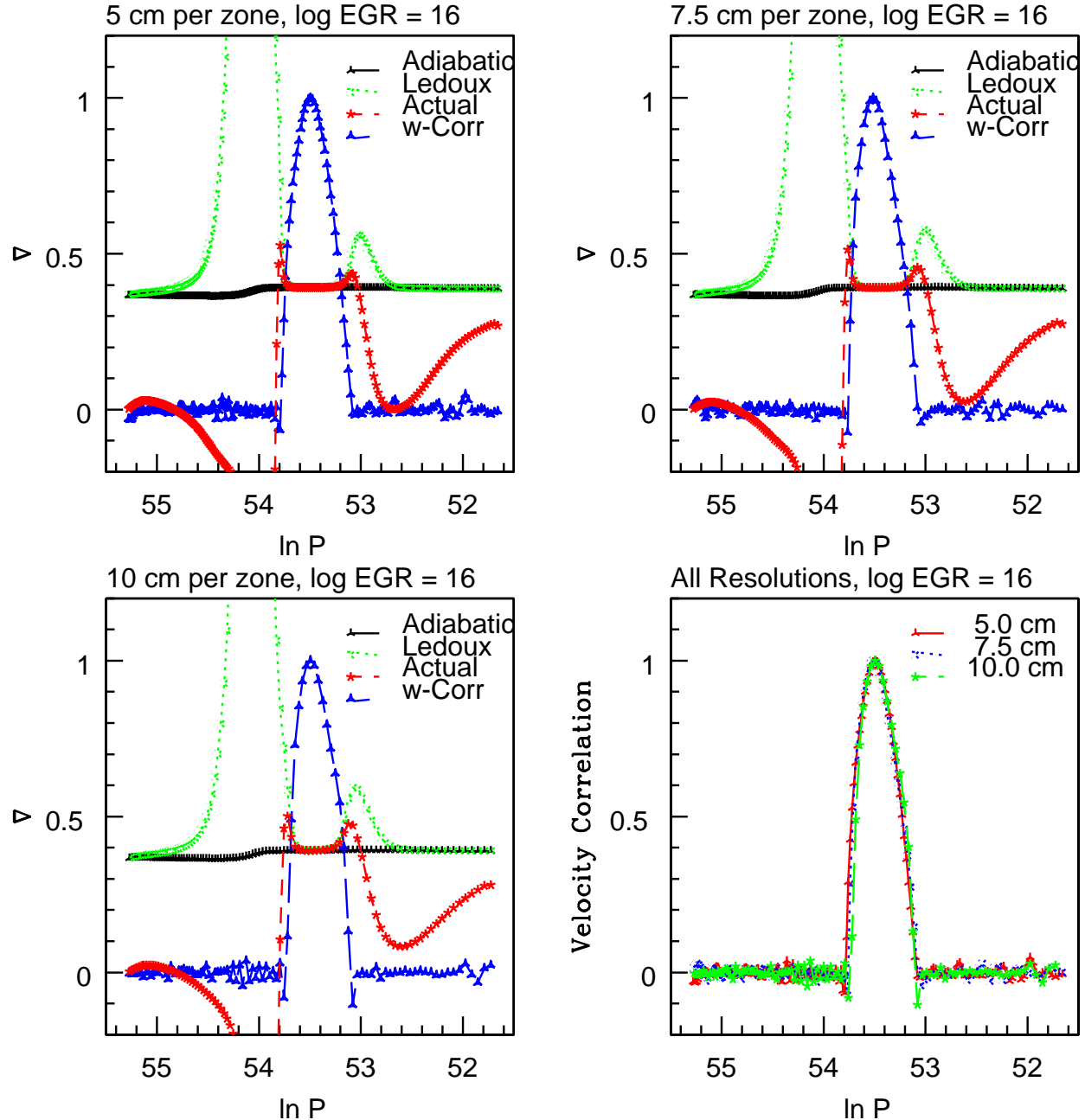


FIGURE 5.5. Grid Refinement:  $W$  vs  $\nabla$ 's, log EGR = 16  
Velocity correlation and various  $\nabla$ 's at log EGR=16, models using resolutions of 5.0, 7.5,  
 $\text{and } 10.0 \text{ cm zone}^{-1}$ .

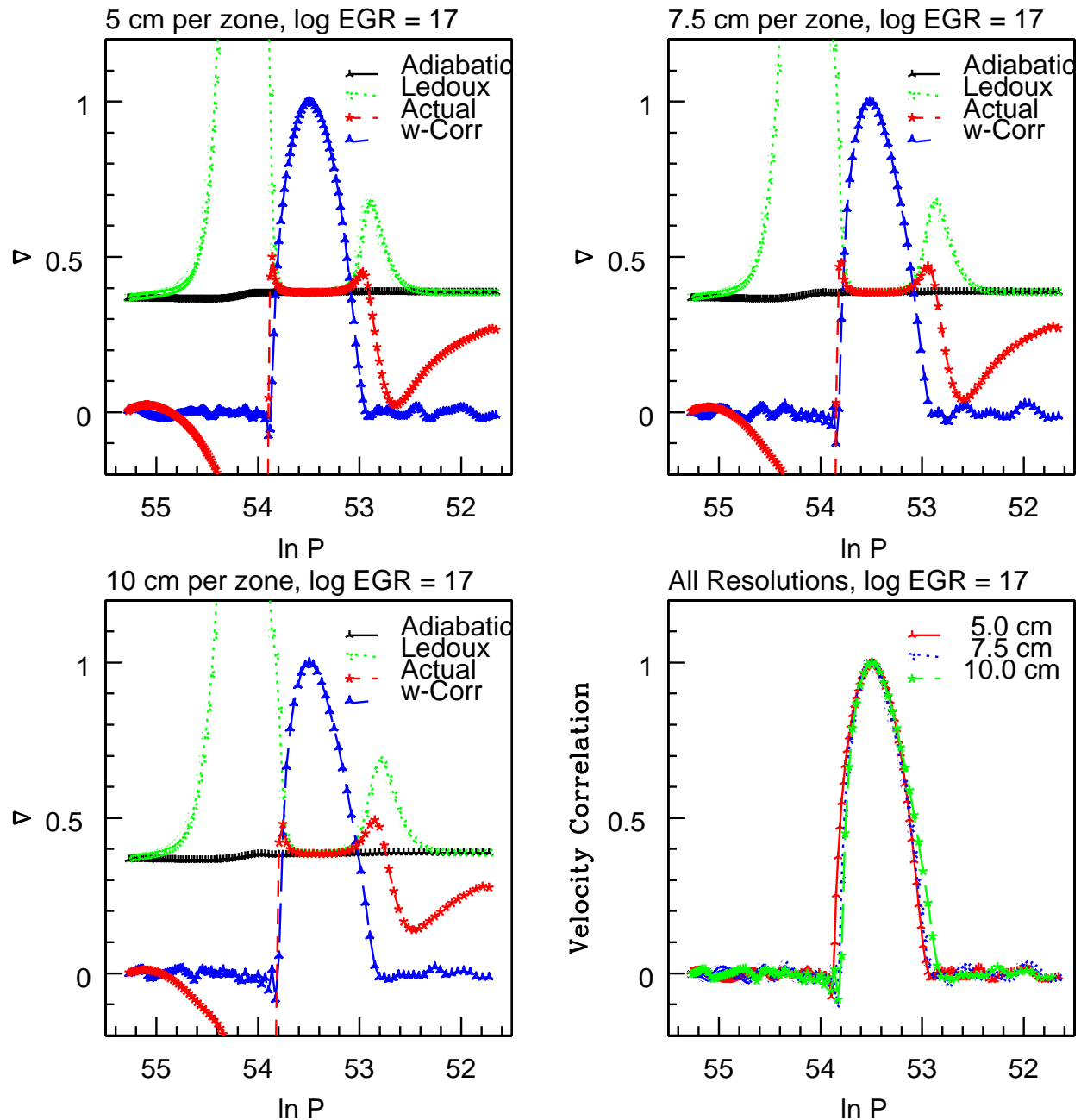


FIGURE 5.6. Grid Refinement:  $W$  vs  $\nabla$ 's, log EGR = 17  
Velocity correlation and various  $\nabla$ 's at log EGR=17, models using resolutions of 5.0, 7.5,  
and  $10.0 \text{ cm zone}^{-1}$ .

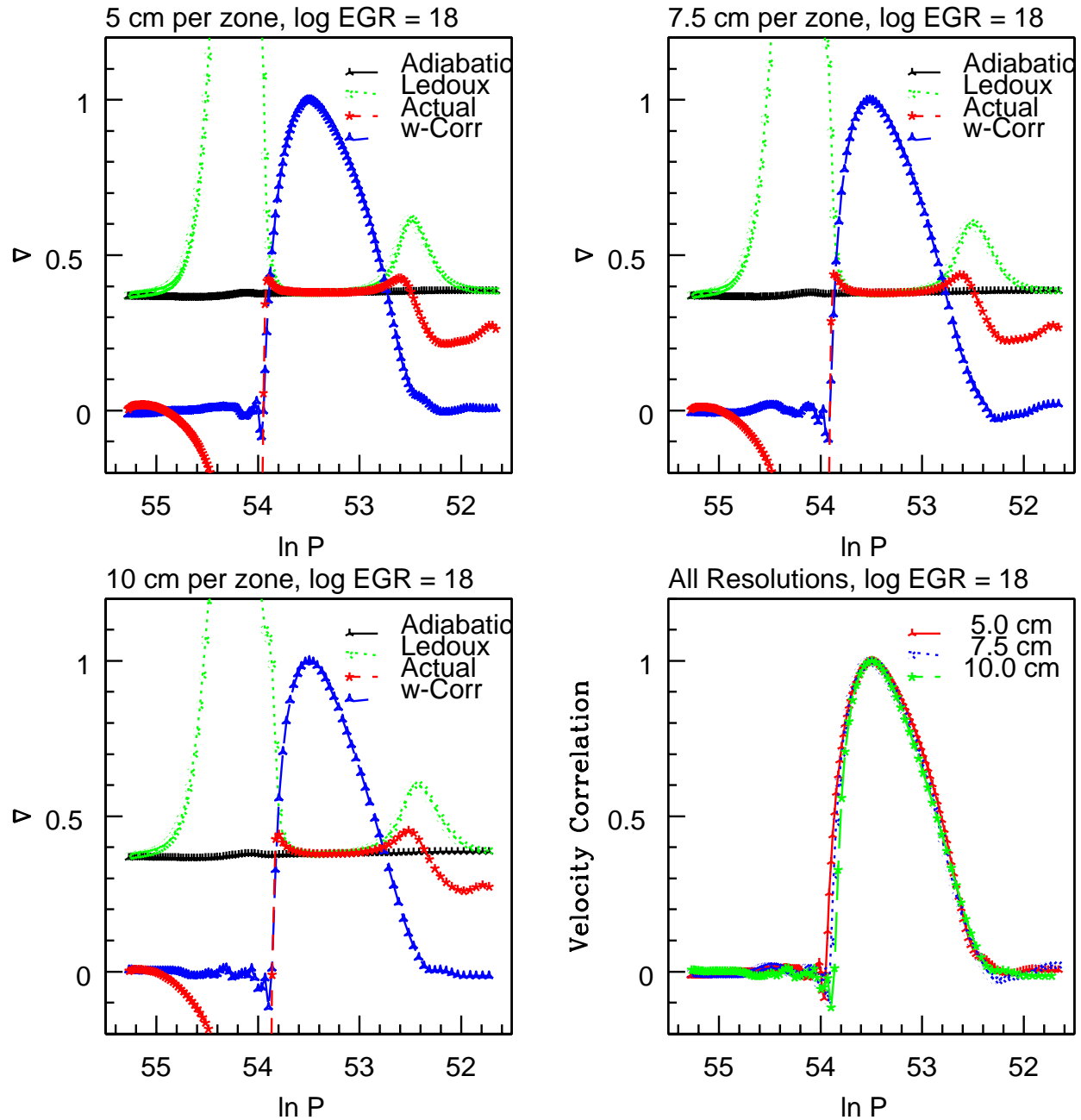


FIGURE 5.7. Grid Refinement:  $W$  vs  $\nabla$ 's, log EGR = 18  
Velocity correlation and various  $\nabla$ 's at log EGR = 18, models using resolutions of 5.0, 7.5,  
and  $10.0 \text{ cm zone}^{-1}$ .

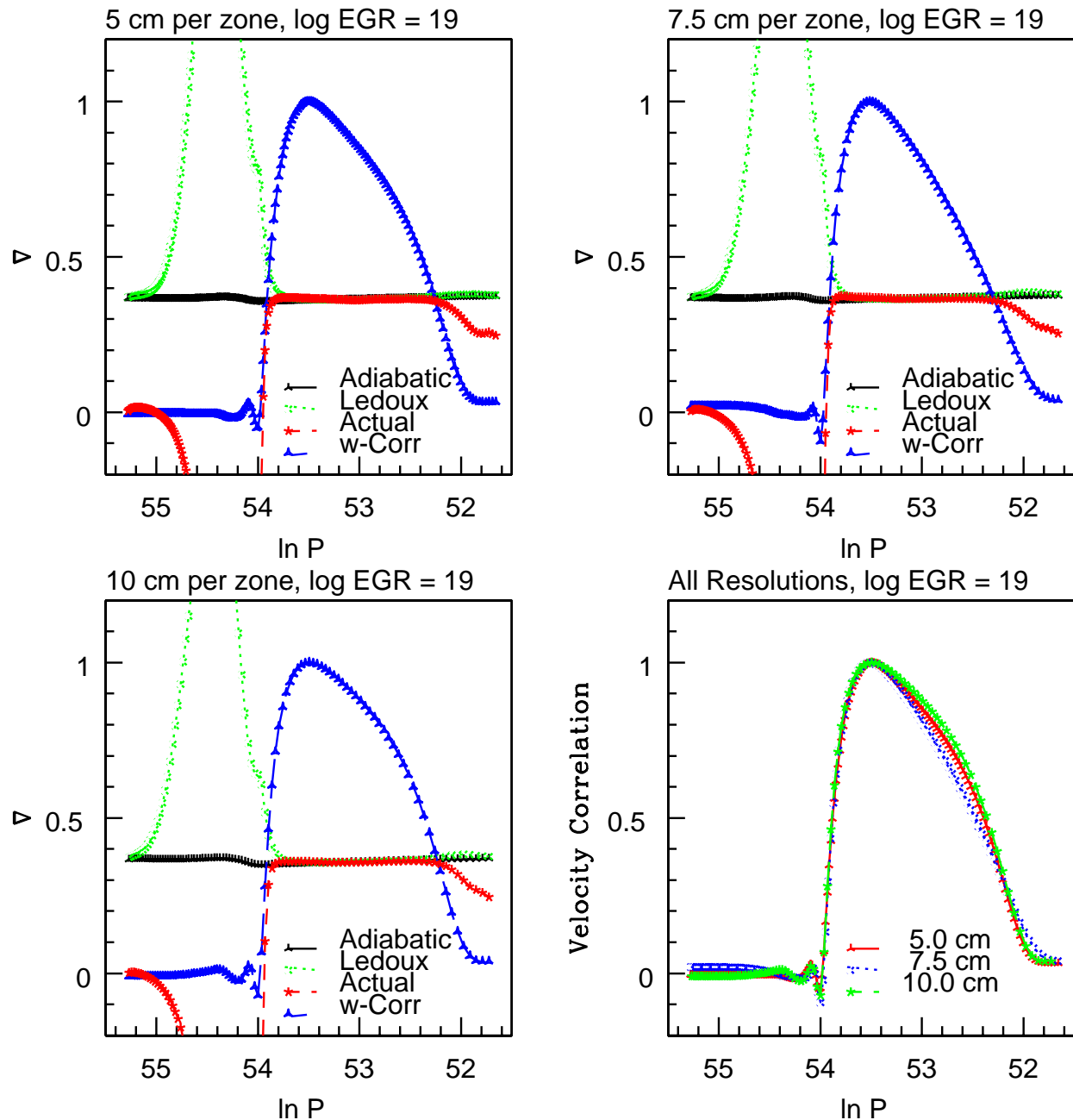


FIGURE 5.8. Grid Refinement:  $W$  vs  $\nabla$ 's, log EGR = 19  
Velocity correlation and various  $\nabla$ 's at log EGR=19, models using resolutions of 5.0, 7.5,  
and  $10.0 \text{ cm zone}^{-1}$ .

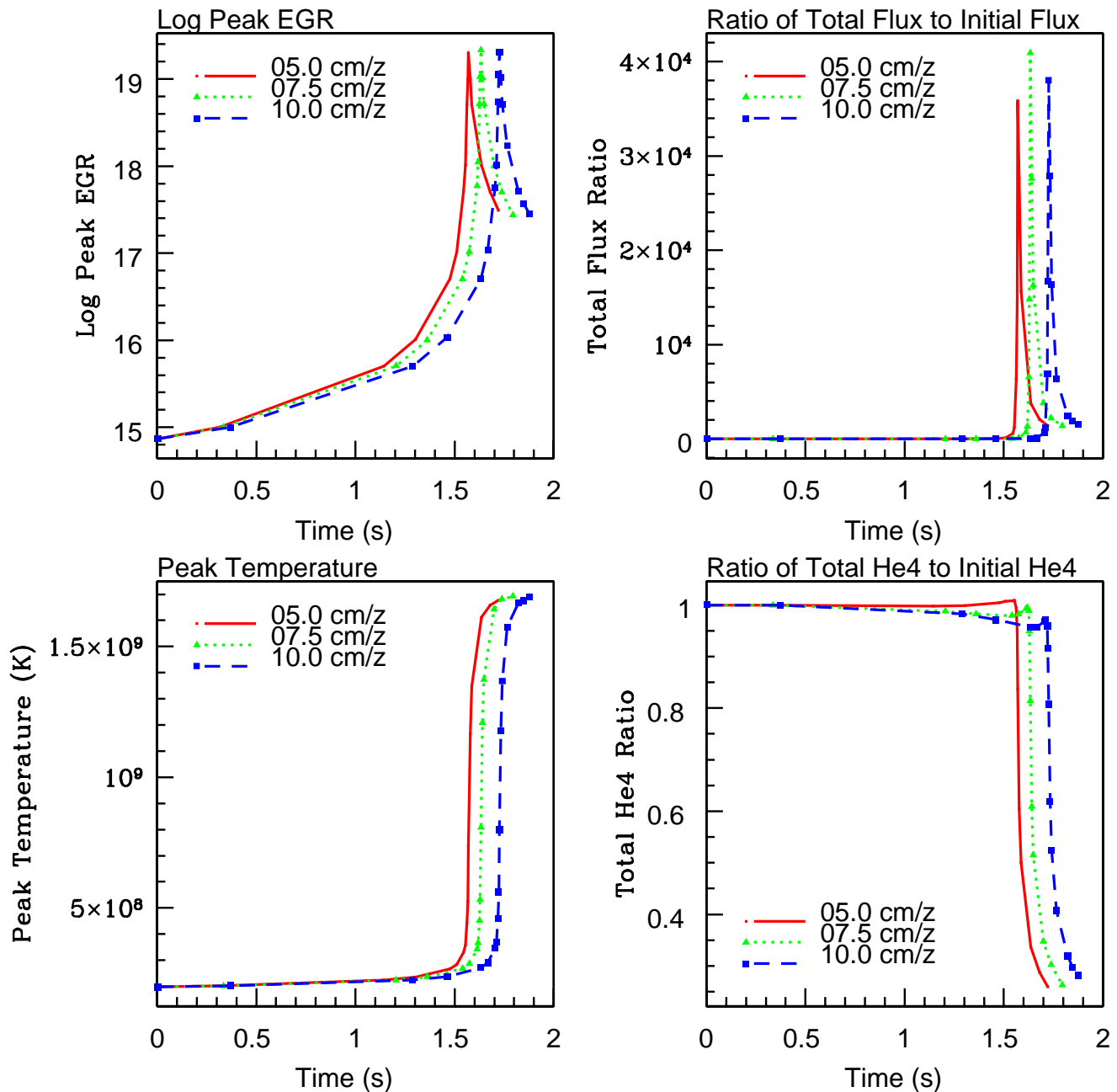


FIGURE 5.9. Grid Refinement: Global Thermodynamic Quantities vs. Time  
 Log of peak EGR (upper left), ratio of total flux to initial flux (upper right), peak temperature (lower left), and ratio of total He4 to initial He4 (lower right). Note that the peak value over the domain may be associated with different zones at different times.

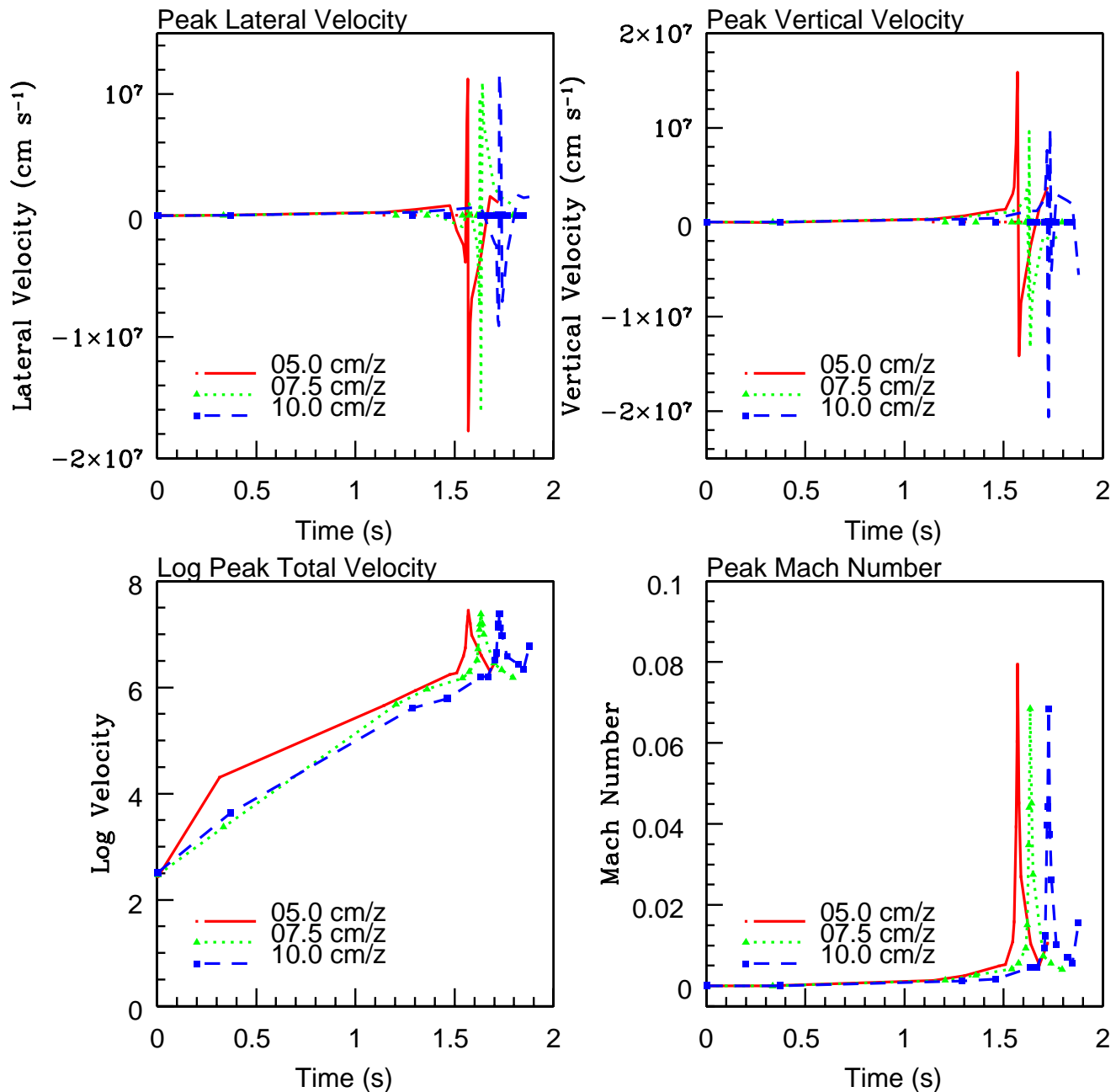


FIGURE 5.10. Grid Refinement: Global Velocity Quantities vs. Time  
 Peak lateral velocity (upper left), peak vertical velocity (upper right), log of total velocity (lower left), and peak Mach number (lower right). Note that the peak value over the domain may be associated with different zones at different times.

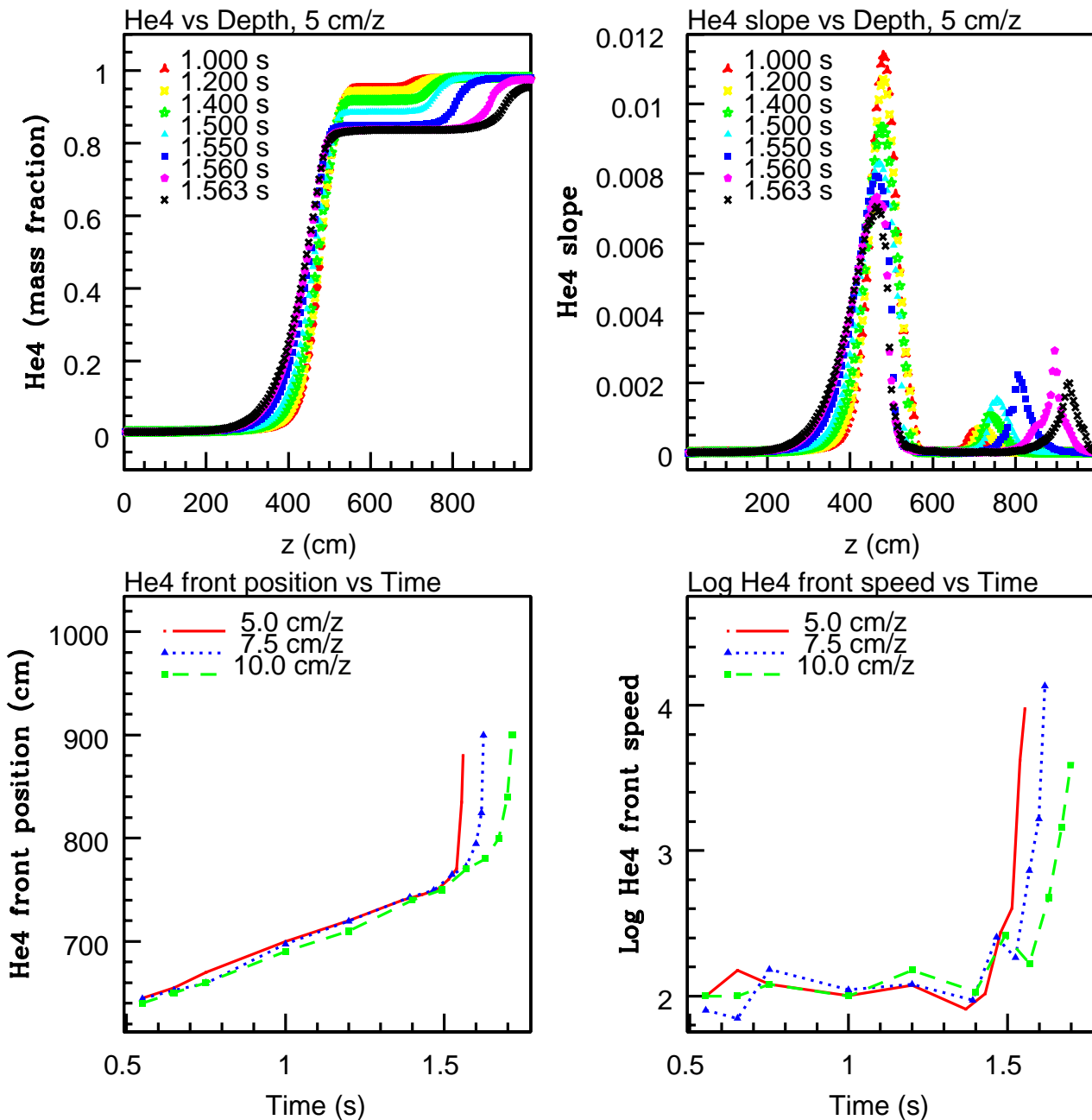


FIGURE 5.11. Grid Refinement: He4 Front Position and Speed  
 Laterally averaged He4 profile for  $5 \text{ cm}^{-1}$  model (upper left), spatial first derivative of He4 profile (upper right), position of upper He4 front vs. time for three resolutions (lower left), and velocity of upper He4 front vs. time for three resolutions (lower right). The He4 fronts indicate the positions of the convective layer boundaries.

### 5.3. Time Resolution Study

In addition to the zone refinement study of the previous section, three  $10 \text{ cm zone}^{-1}$  models using different CFL conditions ( $\text{CFL} = 0.50$ ,  $0.50/2$ , and  $0.50/4$ ) were calculated to test for reproducibility of results under time-step refinements. All other restrictions on the time-step as described in the previous section apply to these calculations as well. Having established the equivalence between the models in terms of zone size in the previous study, the  $10 \text{ cm zone}^{-1}$  resolution was chosen for this study to save computational time.

Figures 5.12 and 5.13 show the flow fields of the  $\text{CFL} = 0.50/2$  and  $0.50/4$  models at three representative EGR levels, which can be compared to the  $\text{CFL} = 0.50$  model's flow fields in Figures 5.2, 5.3, and 5.4 of the previous section. (Again, for ease of comparison, the flow fields are scaled to a grid resolution of  $30 \text{ cm zone}^{-1}$ .) Qualitatively, the results of each model are indistinguishable from each other, signifying time-step convergence in the overall dynamical features.

More quantitatively, as had been compared in the zone refinement studies, the velocity correlation and various  $\nabla$ 's are laterally and temporally averaged at four EGR levels in Figures 5.14, 5.15, 5.16, and 5.17. Also, global thermodynamic and velocity quantities are compared between the time-step resolution models in Figures 5.18 and 5.19. Additionally, the results of the  $5 \text{ cm zone}^{-1}$ ,  $\text{CFL} = 0.50$  model are also presented in these figures. (Note that the  $5 \text{ cm zone}^{-1}$ ,  $\text{CFL} = 0.50$  model effectively shares the same CFL condition as the  $10 \text{ cm zone}^{-1}$ ,  $\text{CFL} = 0.50/2$  model.) Not surprisingly, considerable agreement exists between the models. Consult the previous section for a description of the results, as they are virtually identical to that of the present study.

In terms of time-step refinement, this study indicates that a CFL condition of 0.50 is sufficient to produce qualitatively and quantitatively consistent results.

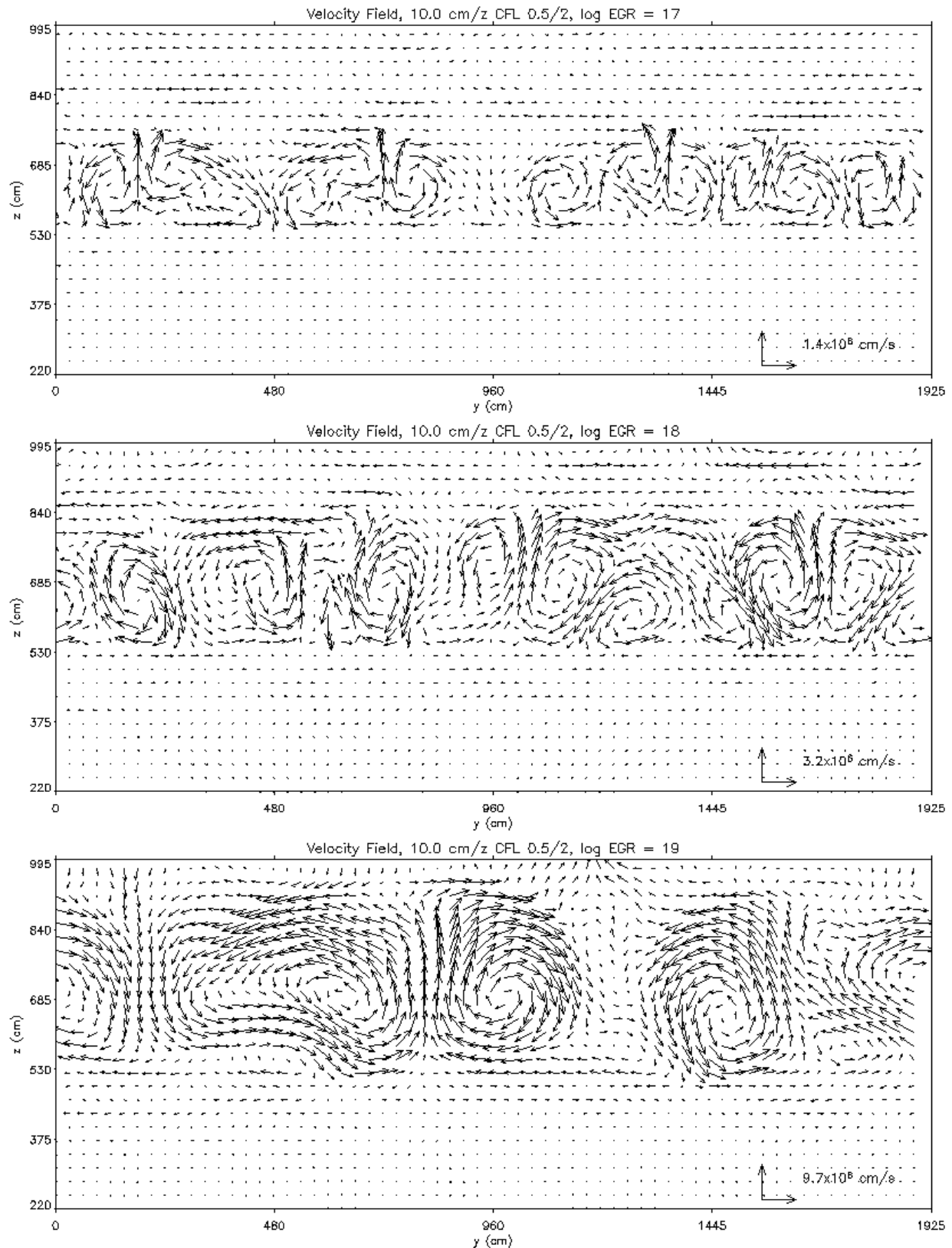


FIGURE 5.12. Time-Step Refinement A  
Three representative EGR levels of the  $10 \text{ cm zone}^{-1}$  model,  $\text{CFL}=0.50/2.0$

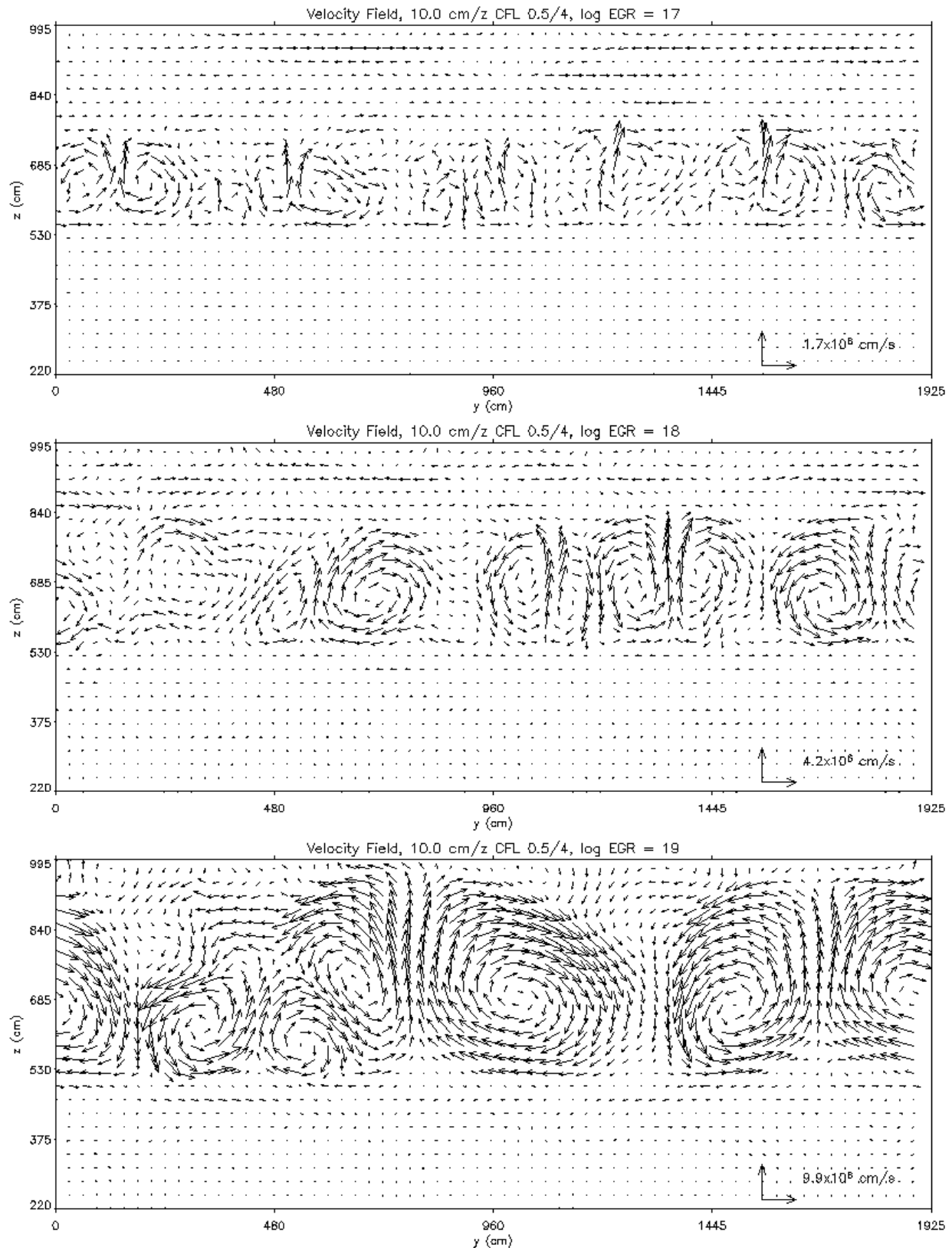


FIGURE 5.13. Time-Step Refinement B  
Three representative EGR levels of the  $10 \text{ cm zone}^{-1}$  model,  $\text{CFL}=0.50/4.0$

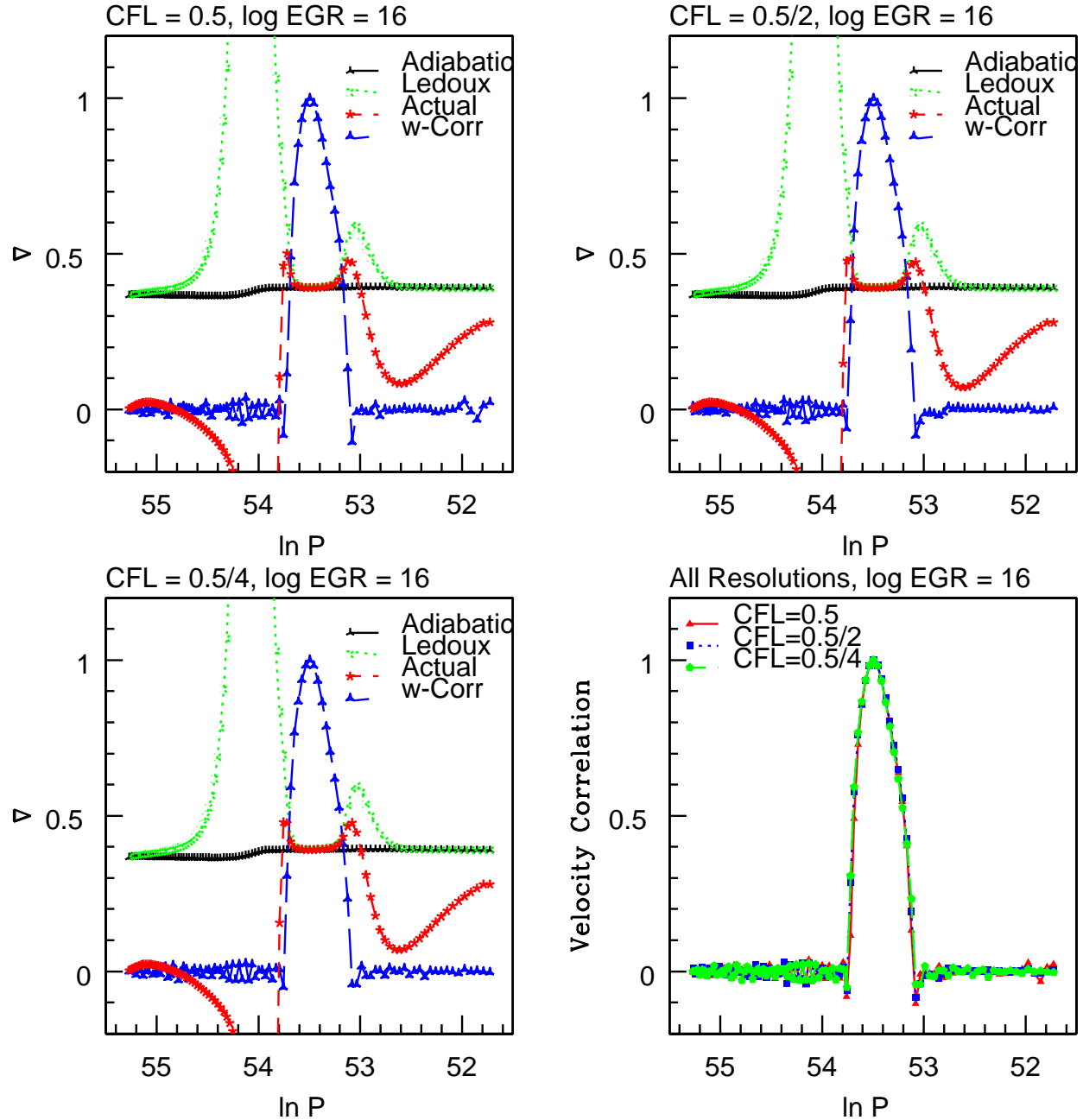


FIGURE 5.14. Time-Step Refinement,  $\log EGR = 16$   
Velocity correlation and various  $\nabla$ 's at  $\log EGR=16$ ,  $10 \text{ cm zone}^{-1}$  models using  $CFL = 0.50, 0.50/2$ , and  $0.50/4$

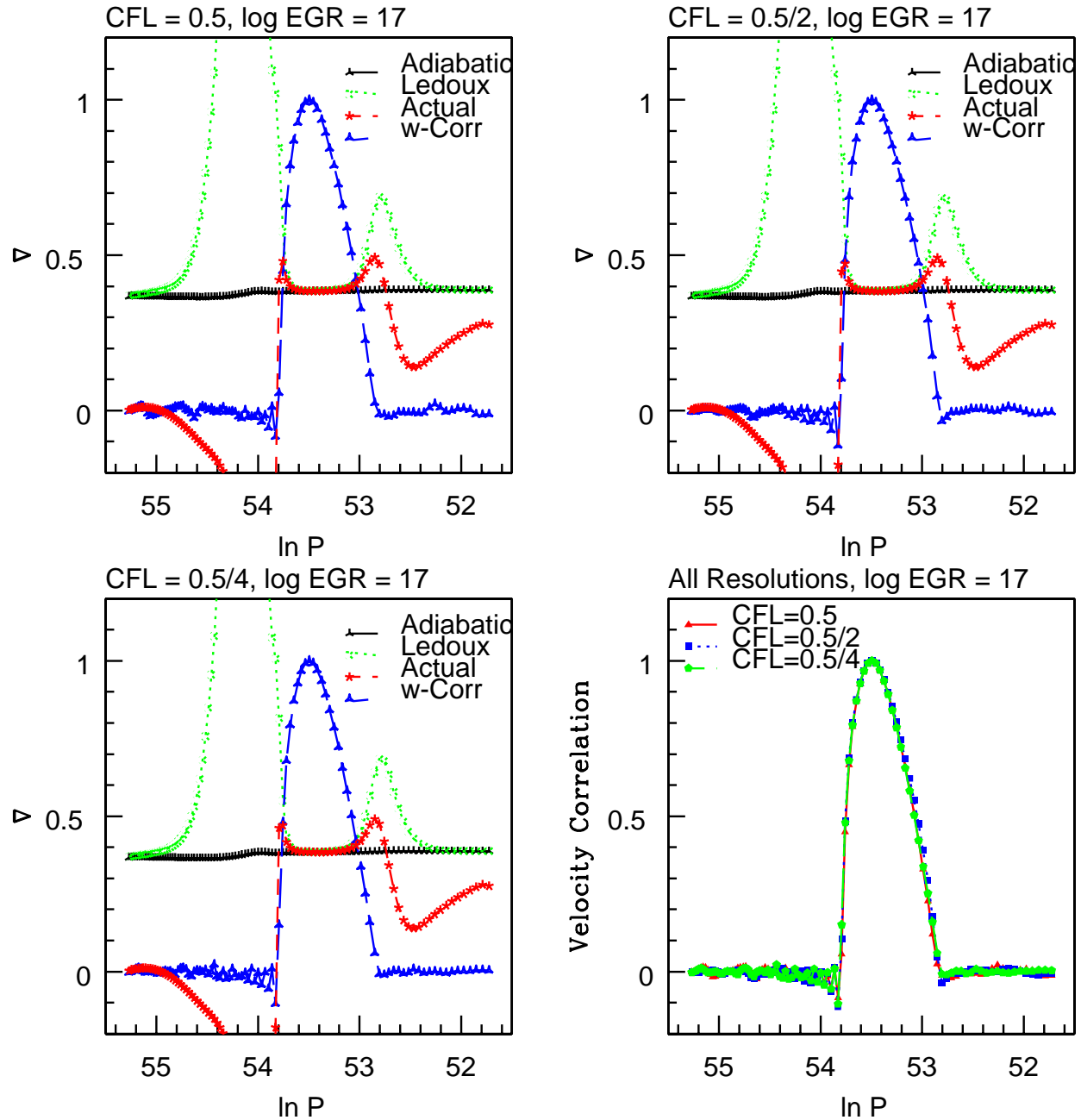


FIGURE 5.15. Time-Step Refinement,  $\log EGR = 17$   
Velocity correlation and various  $\nabla$ 's at  $\log EGR=17$ ,  $10 \text{ cm zone}^{-1}$  models using  $CFL = 0.50, 0.50/2$ , and  $0.50/4$

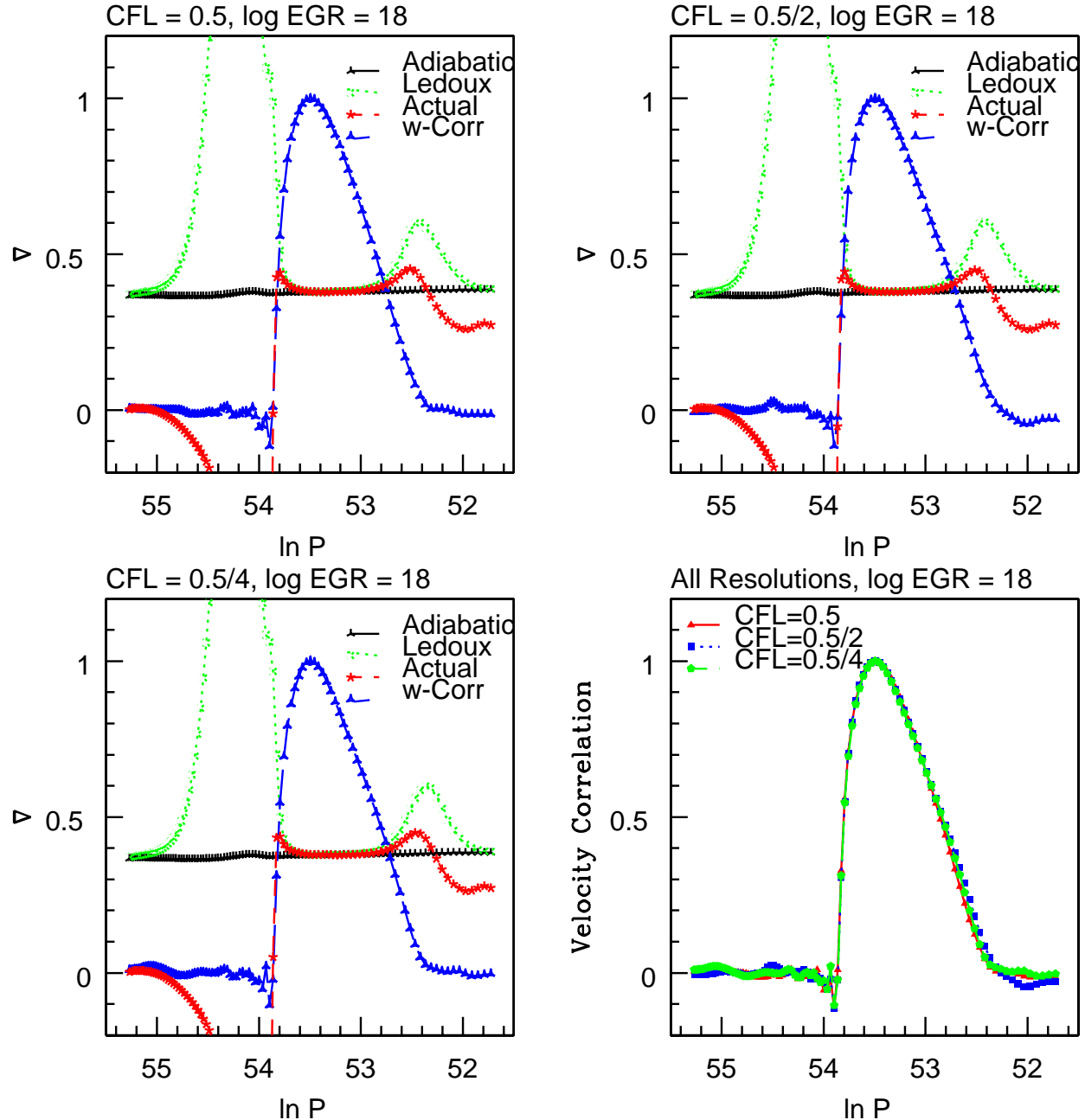


FIGURE 5.16. Time-Step Refinement,  $\log \text{EGR} = 18$   
Velocity correlation and various  $\nabla$ 's at  $\log \text{EGR}=18, 10 \text{ cm zone}^{-1}$  models using  $\text{CFL} = 0.50, 0.50/2$ , and  $0.50/4$

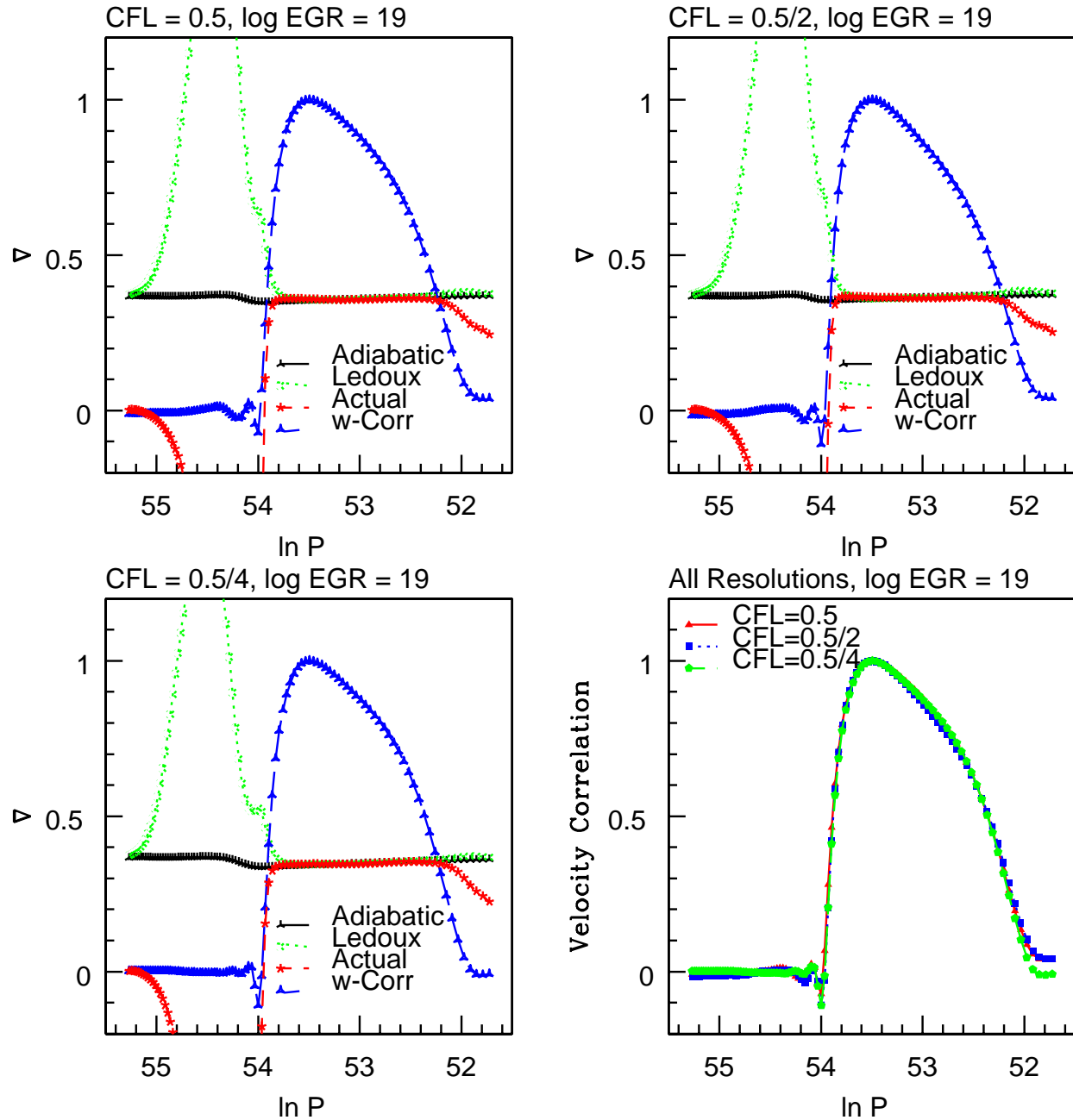


FIGURE 5.17. Time-Step Refinement,  $\log EGR = 19$   
Velocity correlation and various  $\nabla$ 's at  $\log EGR=19$ ,  $10 \text{ cm zone}^{-1}$  models using  $CFL = 0.50, 0.50/2$ , and  $0.50/4$

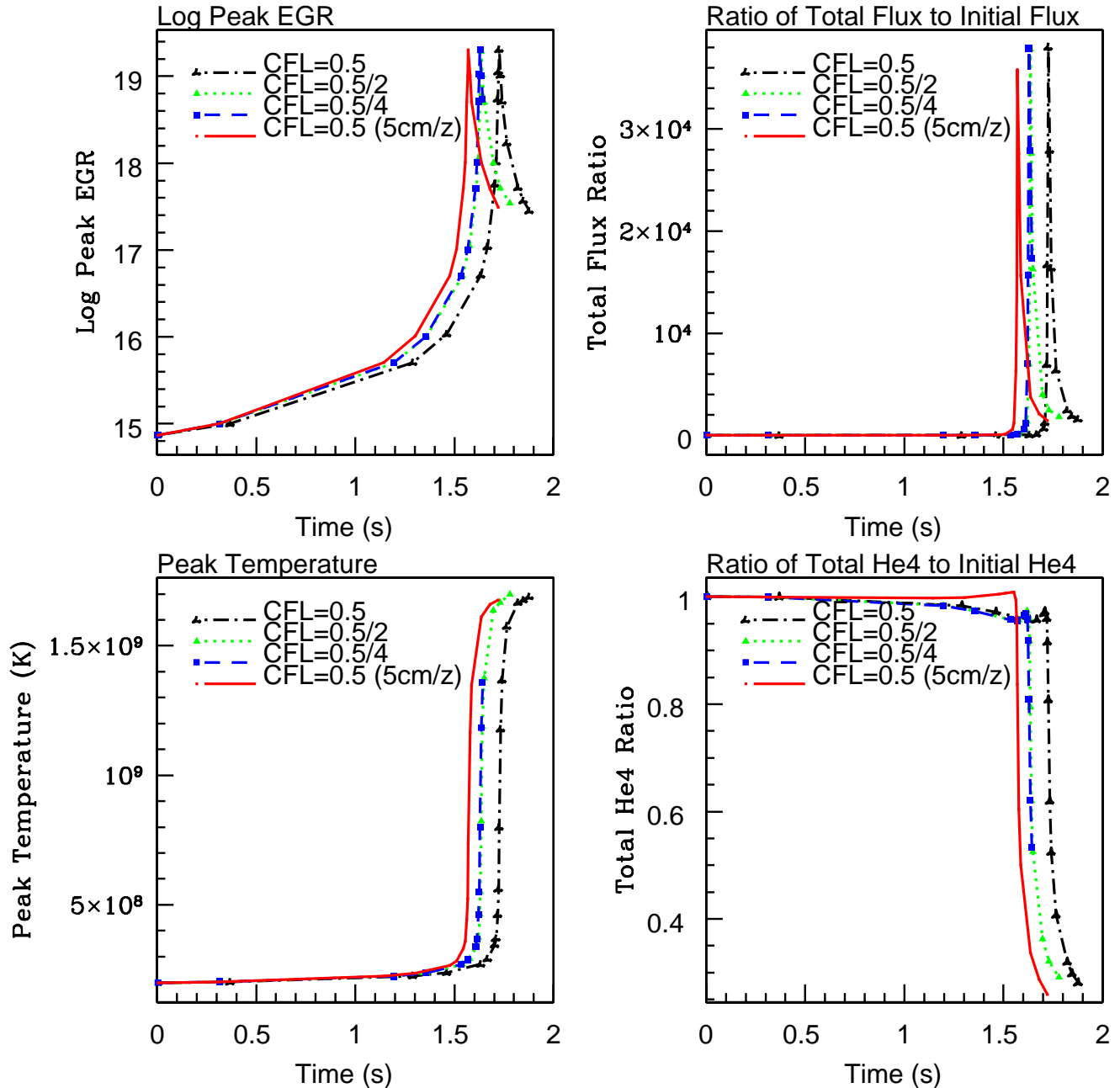


FIGURE 5.18. Time-Step Refinement: Global Thermodynamic Quantities vs. Time  
Log of peak EGR (upper left), ratio of total flux to initial flux (upper right), peak  
temperature (lower left), and ratio of total He4 to initial He4 (lower right). Note that the  
peak value over the domain may be associated with different zones at different times.

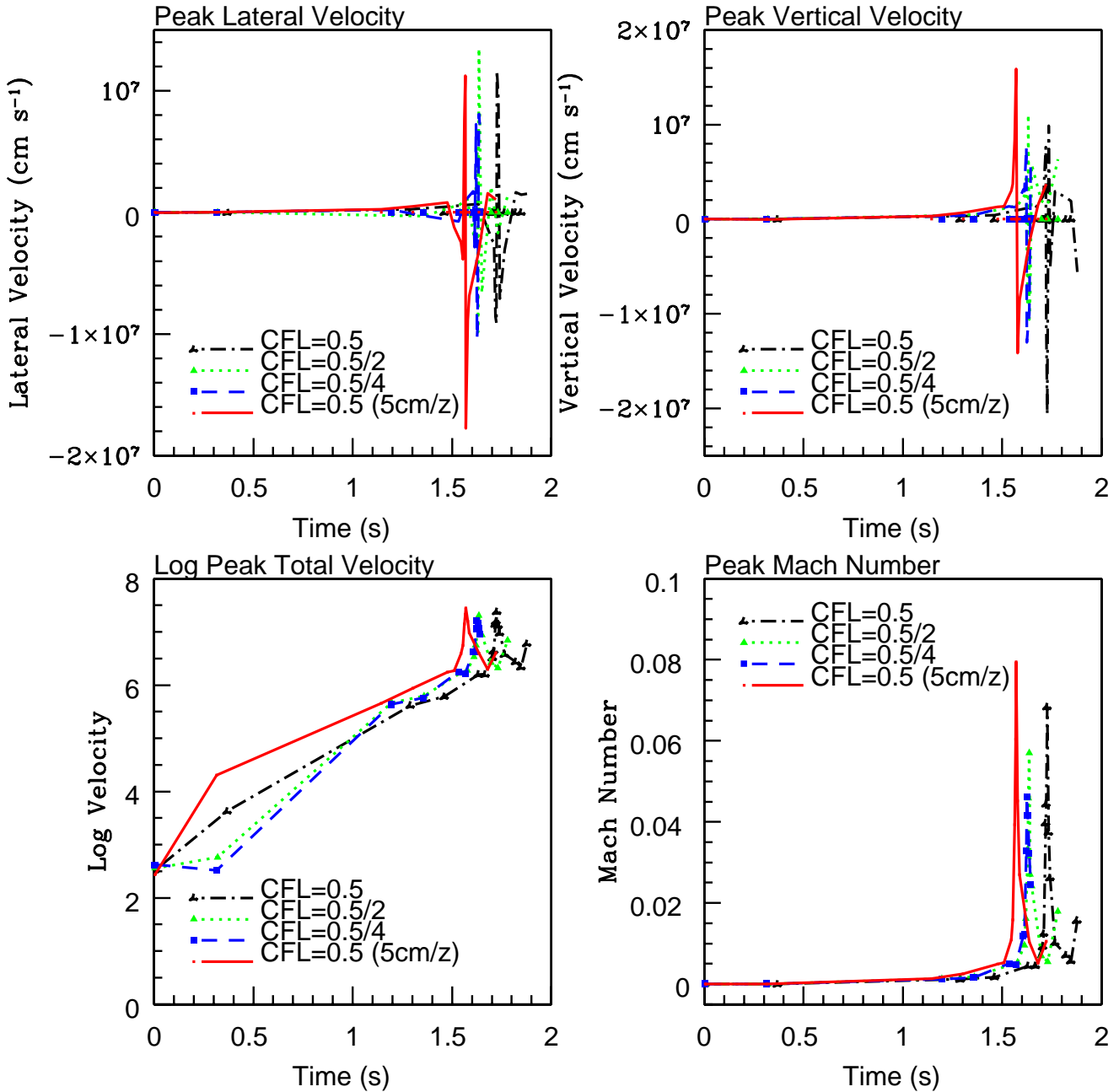


FIGURE 5.19. Time-Step Refinement: Global Velocity Quantities vs. Time  
 Peak lateral velocity (upper left), peak vertical velocity (upper right), log of total velocity (lower left), and peak Mach number (lower right). Note that the peak value over the domain may be associated with different zones at different times.

#### 5.4. Extended Vertical Boundary Study

To examine whether the upper boundary significantly influences the results, another 5 cm zone<sup>-1</sup> model was calculated having 25 additional centimeters above the upper boundary of the previously examined 5 cm zone<sup>-1</sup> model. That is, instead of the 386×200 zones of the standard 5 cm zone<sup>-1</sup> model, the extended model has a domain consisting of 386×205 zones.

Figure 5.20 shows the flow field of the extended model at three representative EGR levels. These results can be compared to the standard 5 cm zone<sup>-1</sup> model's flow fields in Figures 5.2, 5.3, and 5.4 of Section 5.2 on the grid refinement study. The nature of the present flow fields' characteristics, distributions, and evolution show considerable qualitative agreement with the standard model, indicating that the influence of the upper boundary on the qualitative features of the dynamic evolution is minimal.

As in the previous studies, the quantitative aspects of the flow fields are described by determining lateral and temporal averages of the velocity correlation and various  $\nabla$ 's. Figure 5.21 shows these results for the extended domain model at four representative EGR levels. For ease of comparison with the normal domain model, Figure 5.22 overlays the two models' velocity correlations at four different EGR levels. Clearly, the two models show considerable agreement, providing further confirmation that the upper boundary's influence upon the results of the normal domain model is insignificant at EGR levels less than log EGR = 19. However, at log EGR = 19, a slight deviation appears near the upper boundary. This suggests that at this advanced stage of the burst, the upper convective boundary's proximity to the upper computational boundary noticeably influences the subsequent dynamics. While the deviation is relatively minor, its existence suggests upper boundary effects must be taken into consideration at this stage of the calculation.

Time evolution of the global thermodynamic and velocity quantities of the extended model are indistinguishable from that of the normal model. Consult the 5 cm zone<sup>-1</sup> data points in Figures 5.9 and 5.10 for the time-dependent nature of these quantities.

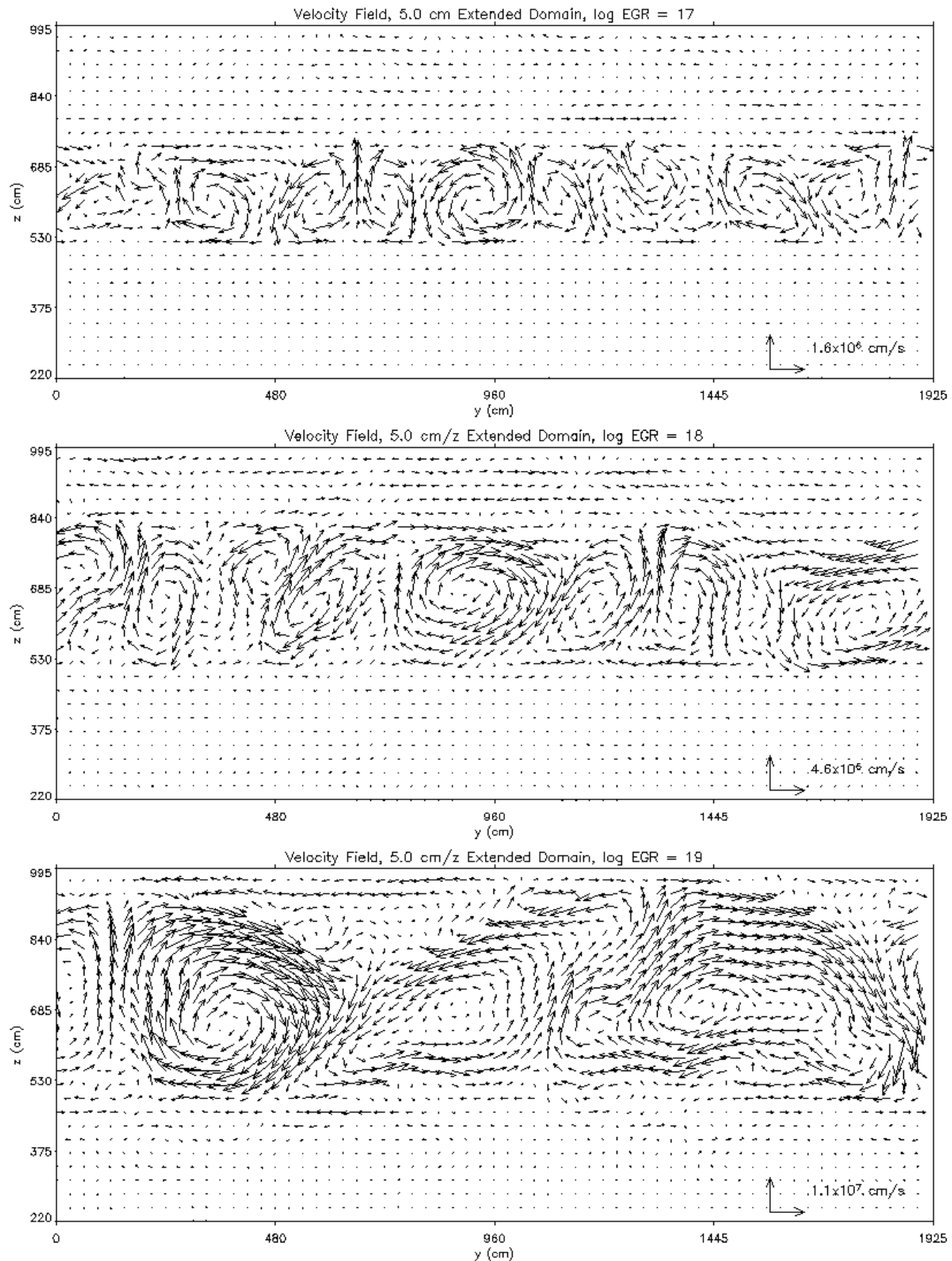


FIGURE 5.20. Extended Vertical Boundary: Flow Fields  
Flow fields of three representative EGR levels of the extended model.

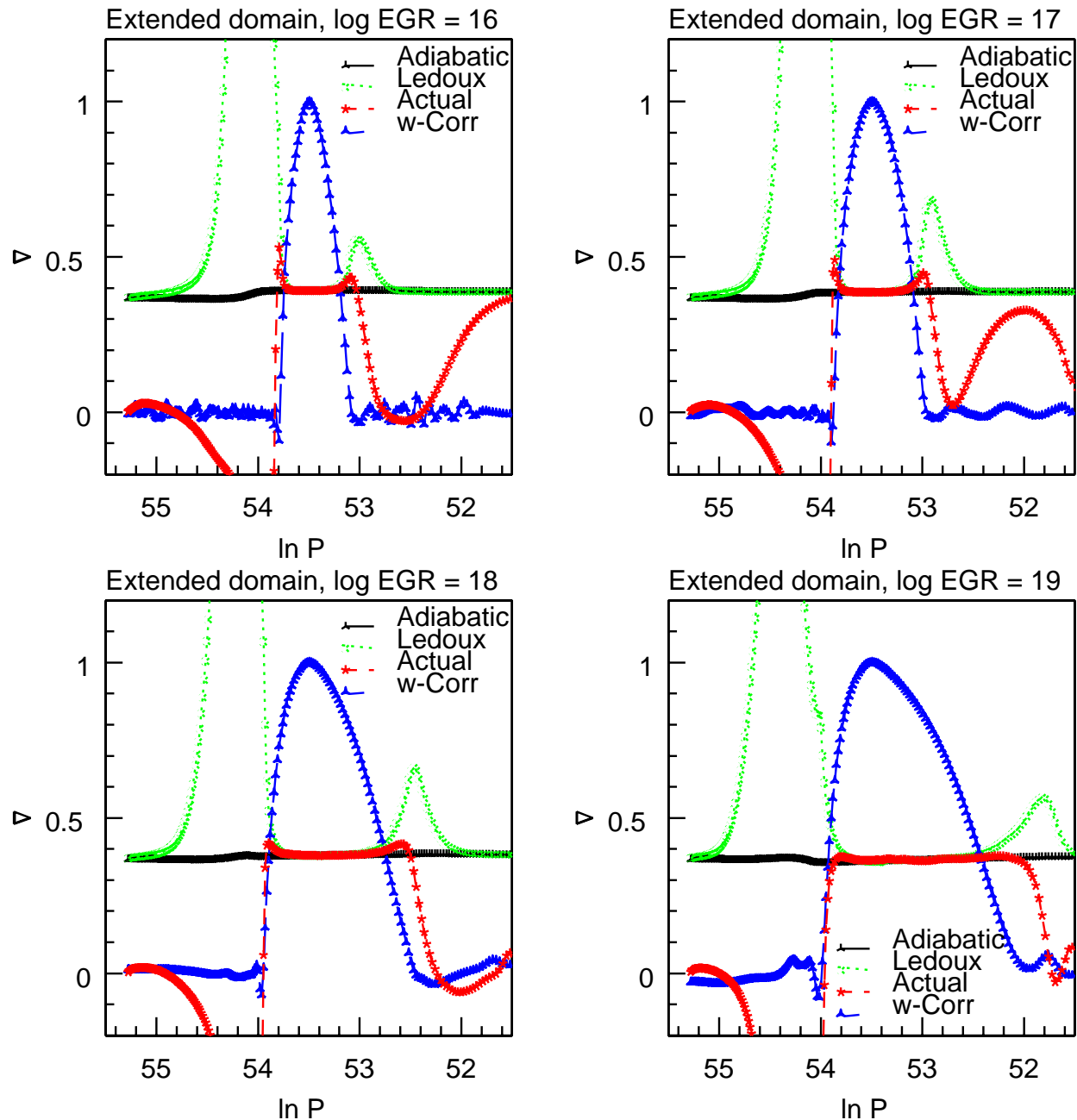


FIGURE 5.21. Extended Vertical Boundary:  $W$  vs  $\nabla$ 's  
Velocity correlation and various  $\nabla$ 's of the extended  $5 \text{ cm zone}^{-1}$  ( $386 \times 205$ ) model at four representative EGR levels.

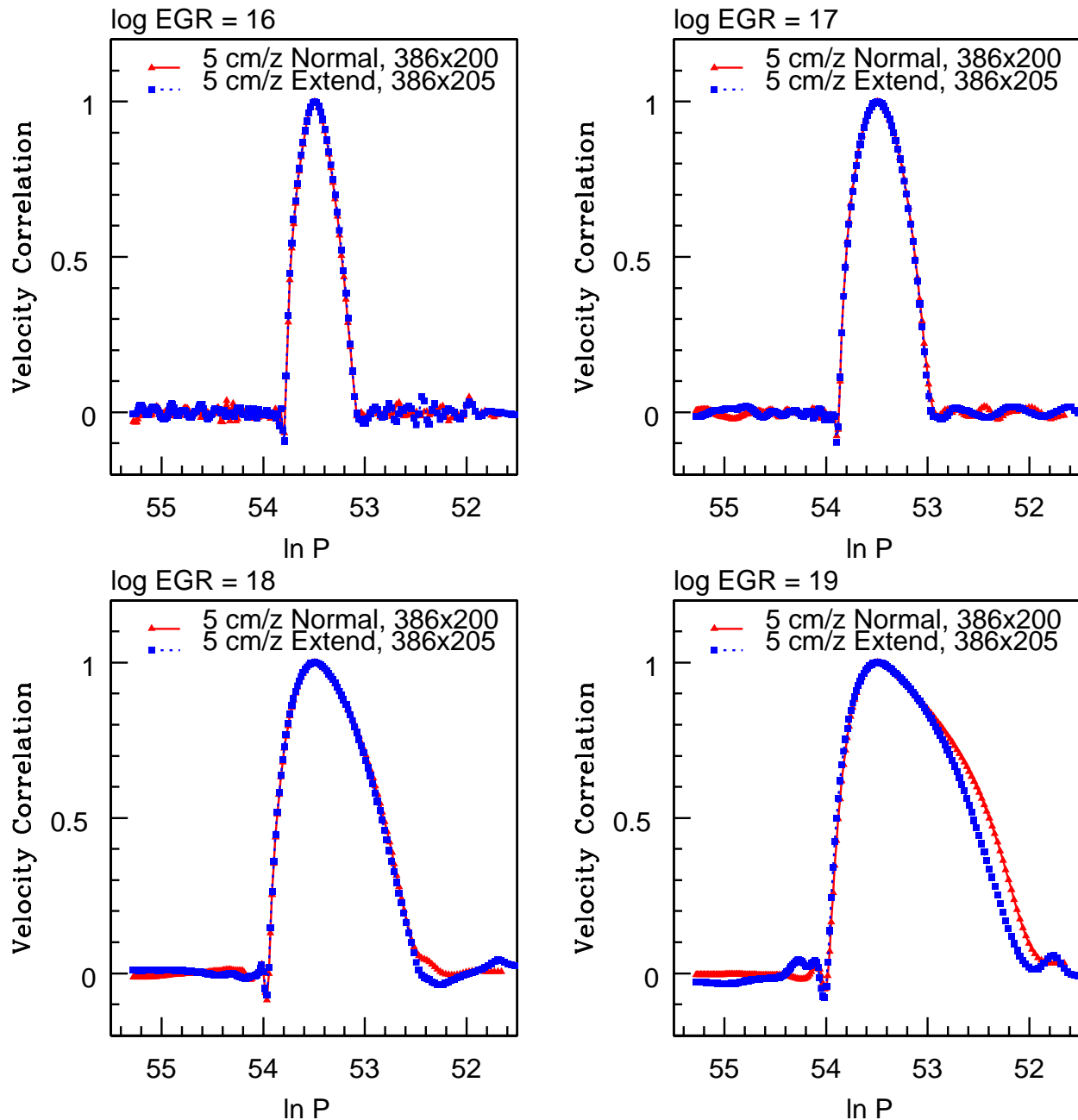


FIGURE 5.22. Extended Vertical Boundary:  $W$  Comparison  
Comparison of velocity correlation at four representative EGR levels,  $5 \text{ cm zone}^{-1}$  normal ( $386 \times 200$ ) vs. extended ( $386 \times 205$ ) model.

### 5.5. Other tests

Other tests were rigorously performed on individual pieces of the LMNA model during programming development. The purpose of the tests was to ensure all critical parts of the model yielded physically reasonable results. For example, advection of composition and temperature were tested by introducing a perturbation of the tested quantity in an artificial flow-field, such as a circular flow around the domain. Similarly, thermal diffusion was tested by examining how an artificial temperature gradient spread as a function of time. As well, the nuclear burning module was tested by monitoring changes in temperature, energy generation rate, and nuclear reactants and by-products as a function of time. Moreover, the implementation of the elliptic solver and boundary conditions was tested by solving multi-variable functions with analytical solutions against which the numerical results could be quantitatively compared. Another aspect of the model which underwent considerable testing was the parallel-processing structure. Individually, these consistency tests on all critical pieces of the LMNA model yielded reasonable and realistic results, which validate the integrity of the the coding.

### 5.6. Summary

The 2D LMNA model has been extensively tested both on the piecewise level of its individual, critical components (advection, diffusion, burning, elliptic solver, parallel-processing structure), and on the integrated level of long-term time evolution using several different spatial and temporal resolutions, as well as with domains of different dimensions. Results are physically reasonable, consistent, and convergent. Taken together, they help validate the overall integrity of the 2D LMNA model.

## CHAPTER 6

### Discussion

This thesis involved the development and implementation of a low Mach number model of deflagrations in a highly stratified environment, which has been applied to modeling Type I X-ray bursts on neutron stars. The LMNA model is valid where the bulk motions are substantially less than that of sound, so that acoustic effects do not significantly affect the deflagration. The low Mach number approximation effectively filters out acoustic waves from the hydrodynamical evolution, allowing a substantial decrease in the time needed to perform a calculation. Although routinely employed in terrestrial combustion problems (McGrattan et al., 2004), the model is presently applied to an astrophysical setting where strong gravitational forces causes significant stratification. Terrestrially, the gravitational acceleration  $g$  is of order 1, so there is little stratification in pressure and density. However, on the surface of a neutron star where  $g$  is of order  $10^{14}$ , significant stratification exists. Thus, adapting the LMNA to highly stratified environments such as neutron stars requires the unique computational methods presented in this thesis.

In this final chapter, the contribution of carbon reactions in helium burning beyond  $3\alpha$  to the energetics of the burst simulation is first examined, and it is shown that prior to burst peak, carbon reactions may be neglected, but after burst peak, they should be included to more completely account for the total energy released. In the next section, the behaviors of the nuclear, radiative, and advective fluxes of the 1D and 2D models are examined and compared, and the results have important implications on the expected light curves of X-ray bursts. Next, the interesting behavior of the calculated temperature gradient and how it compares to the Schwarzschild and Ledoux criteria will be highlighted. Finally, the major results of this thesis are summarized, and several avenues of future development

and application of the LMNA model will be offered to demonstrate its potential as a useful tool in astrophysical modeling.

### 6.1. Contribution of Carbon Reactions in Helium Burning

The combustive process considered in the current LMNA model is the  $3\alpha$  reaction ( $3\frac{4}{2}He \rightarrow \frac{12}{6}C$ ), where two species are considered,  $\frac{4}{2}He$  and  $\frac{12}{6}C$ .



The ash of the  $3\alpha$  reaction is  $\frac{12}{6}C$ , and its concentration rises as helium burning progresses. Consequently, further  $\alpha$  captures may commence to form heavier nuclei:



The energy generation rate of these reactions ( $\dot{s}_{12,\alpha}$  and  $\dot{s}_{16,\alpha}$ ) are *not* included in the present LMNA model. A more complete model of X-ray bursts powered by helium burning should include these rates. Further reactions beyond  $\frac{20}{10}Ne$  can occur, but have very low probability due to the very small cross sections involved (Duorah and Duorah, 1985). To estimate the error from neglecting these energy sources from the model, the reaction rates for the three main helium burning reactions can be expressed in the manner of Duorah and Duorah (1985):

$$(6.5) \quad \dot{s}_{3\alpha} = A Y^3 Q_{3\alpha}/\rho$$

$$(6.6) \quad \dot{s}_{12,\alpha} = B Y Z Q_{12,\alpha} / \rho$$

$$(6.7) \quad \dot{s}_{16,\alpha} = C Y Z Q_{16,\alpha} / \rho$$

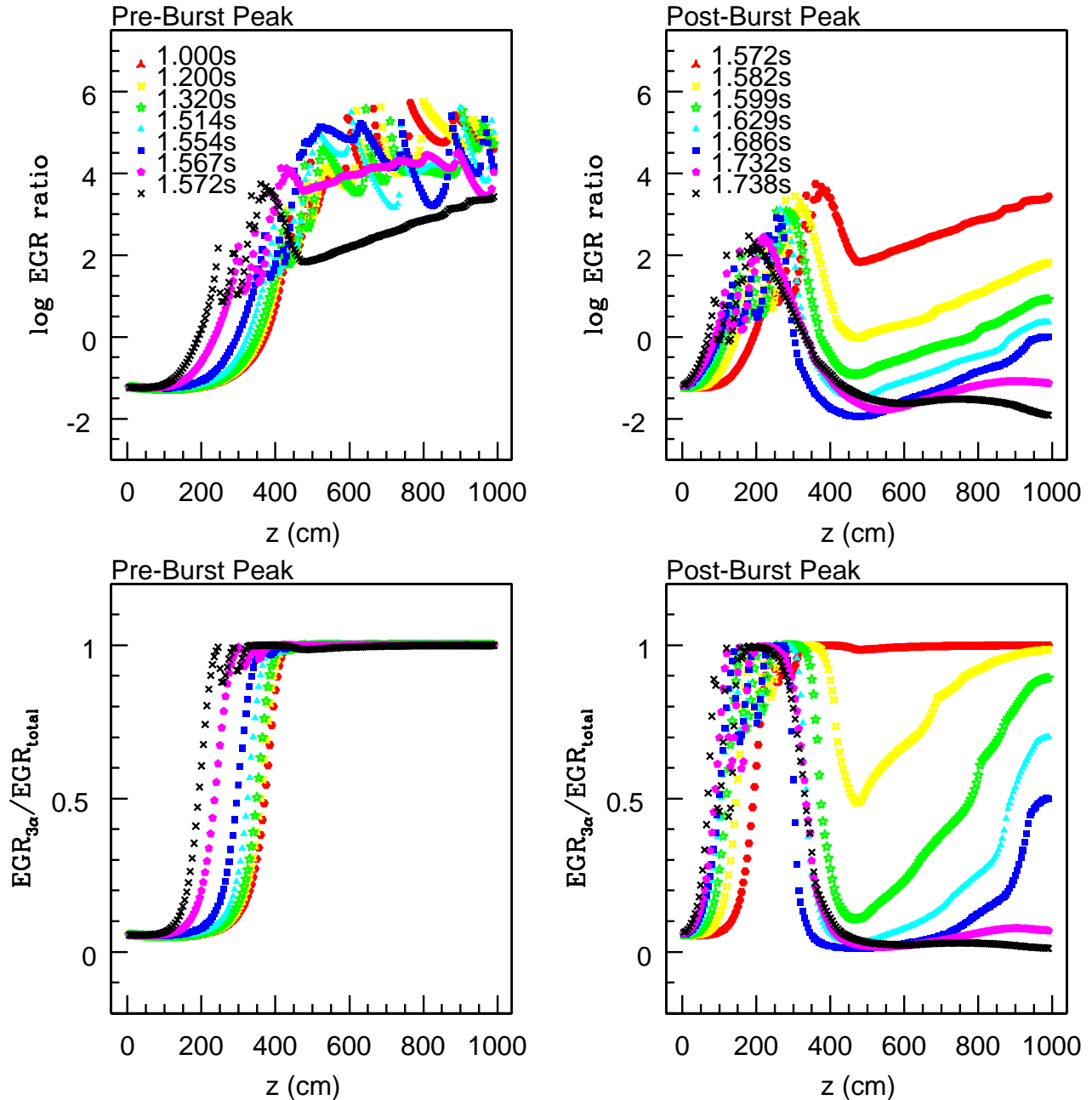
where  $Z$  is the fractional abundance of  $^{12}_6C$ ; and,  $Q_{3\alpha} = 7.281$  MeV or  $1.165 \times 10^{-5}$  erg,  $Q_{12,\alpha} = 7.162$  MeV or  $1.147 \times 10^{-5}$  erg, and  $Q_{16,\alpha} = 4.73$  MeV or  $7.578 \times 10^{-6}$  erg. The coefficients  $A$ ,  $B$ , and  $C$  are functions of density and temperature:

$$(6.8) \quad A = \frac{4.376 \times 10^{16-(19.12/T_8)} \rho^3}{T_8^3} E(\rho, T)$$

$$(6.9) \quad B = \frac{\rho^2}{48} N_A (N_A < \sigma V >) E(\rho, T)$$

$$(6.10) \quad C = \frac{\rho^2}{64} N_A (N_A < \sigma V >) E(\rho, T)$$

where  $T_8$  is the temperature in units of  $10^8$  K,  $E(\rho, T)$  is an enhancement factor,  $N_A$  is Avogadro's number, and  $N_A < \sigma V >$  is the reaction rate as calculated with the Maxwell-Boltzmann distribution of  $\alpha$  particles in units of  $\text{cm}^3 \text{ mol}^{-1} \text{ s}^{-1}$ .

FIGURE 6.1. EGR Ratios vs.  $z$ , Pre- and Post-Burst Peak

The log of  $\dot{s}_{3\alpha}/\dot{s}_{12,\alpha}$  pre-burst peak (upper-left) and post-burst peak (upper-right) as a function of vertical position. The fraction  $\dot{s}_{3\alpha}/\dot{s}_{total}$  pre-burst peak (lower-left) and post-burst peak (lower-right) as a function of vertical position. Laterally averaged values of  $\rho$ ,  $T$ ,  $Y$ , and  $Z$ , and values of  $N_A < \sigma V >$  from the most recent  $^{12}C(\alpha, \gamma)^{16}O$  reaction rate calculations from Kunz et al. (2002) are used for these calculations.

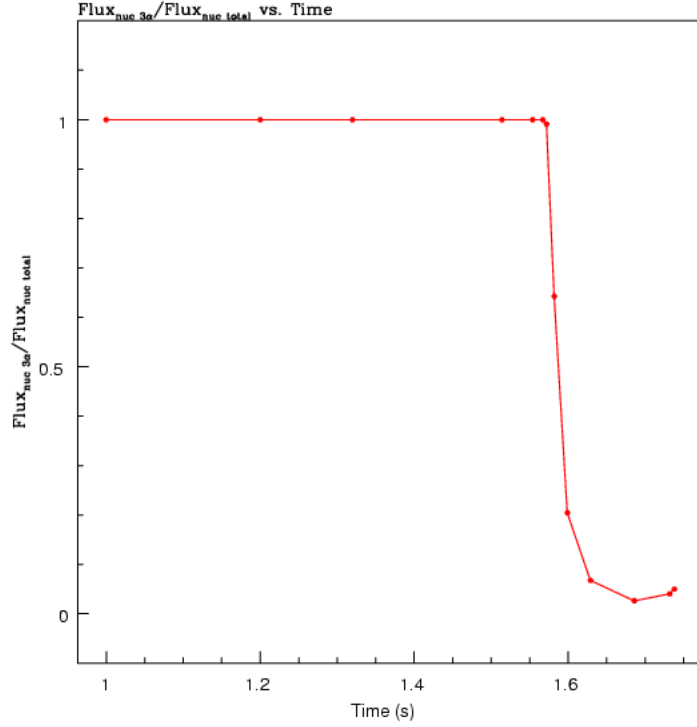


FIGURE 6.2.  $F_{3\alpha}/(F_{3\alpha} + F_{12,\alpha})$  vs. Time

As an approximation, let the total energy generation rate be  $\dot{s}_{total} = \dot{s}_{3\alpha} + \dot{s}_{12,\alpha}$ . If the enhancement factors are assumed to be roughly the same, the ratio  $R_{EGR} \equiv \dot{s}_{3\alpha}/\dot{s}_{12,\alpha}$  is approximately:

$$(6.11) \quad R_{EGR} \approx \frac{48 \times 4.376 \times 10^{16-(19.12/T_8)} \rho Y^2}{T_8^3 N_A (N_A < \sigma V >) Z} \frac{Q_{3\alpha}}{Q_{12,\alpha}}$$

With laterally averaged values of  $\rho$ ,  $T$ ,  $Y$ , and  $Z$ , and values of  $N_A < \sigma V >$  from the most recent  $^{12}C(\alpha, \gamma)^{16}O$  reaction rate calculations from Kunz et al. (2002), the log of  $R_{EGR}$  is plotted as a function of height at different times pre- and post-burst peak in the upper-left and upper-right plots in Figure 6.1. (The times examined in these plots are the same times examined in certain figures of Chapter 4, such as in Figures 4.5 and 4.6.) The fraction  $\dot{s}_{3\alpha}/\dot{s}_{total}$  can be straightforwardly shown to be equal to be  $R_{EGR}/(1 + R_{EGR})$ , and

this fractional contribution of the energy generation due to the  $3\alpha$  reaction is plotted as a function of height in the lower-left (pre-burst peak) and lower-right (post-burst peak) plots of Figure 6.1. These plots show that before the burst peak,  $\dot{s}_{3\alpha}$  dominates in most of the domain, except where  $Y$  is small (c.f. Figure 4.6 in Chapter 4). This arises from the  $Y^2$  dependence of equation 6.11. Moreover, after burst peak, as nuclear fuel is consumed and  $Y$  diminishes,  $\dot{s}_{12,\alpha}$  begins to dominate in a greater portion of the domain. Energetically, the more appropriate value to consider is the nuclear flux, which is considered next.

The instantaneous nuclear flux of a given reaction is the vertically integrated product  $F_{nuc} = \sum_{z=0}^{z_{top}} \rho \dot{s} \Delta z$ . Thus, the fractional contribution of  $F_{3\alpha}$  to the total nuclear flux is:

$$(6.12) \quad \frac{F_{3\alpha}}{F_{3\alpha} + F_{12,\alpha}} = \frac{\sum_{z=0}^{z_{top}} \rho \dot{s}_{3\alpha} \Delta z}{\sum_{z=0}^{z_{top}} \rho \dot{s}_{3\alpha} \left(1 + \frac{1}{R_{EQ}}\right) \Delta z}$$

This fraction is calculated in the domain using laterally averaged values of  $\rho$  and  $\dot{s}_{3\alpha}$ . It is plotted as a function of time in Figure 6.2 to estimate when the  $3\alpha$  reaction dominates the nuclear flux contribution. As the figure shows, prior to the burst peak,  $F_{3\alpha}$  adequately accounts for most of the total nuclear flux. However, post-burst peak,  $F_{12,\alpha}$  dominates due to the diminishing of  $Y$  in the domain. Thus, in terms of energetics, the reactions involving  $^{12}_6C$  and  $^{16}_8O$  in Equations 6.3 and 6.4 are justifiably neglected before the peak of the burst, but they need to be included to more realistically account for the total nuclear flux after the burst peak. This has important consequences in the simulated light curves examined in the next section. Future work with the LMNA model should include the reactions in Equations 6.3 and 6.4 and more complete nuclear reaction networks, as proposed in Section 6.5.

## 6.2. 1D vs. 2D Flux Comparisons

In this section, detailed comparisons of the nuclear ( $F_{nuc}$ ), radiative ( $F_{rad}$ ), and advective ( $F_{adv}$ ) fluxes between the 1D and 2D models are presented. For these comparisons, the 1D model is evolved with the same initial conditions and vertical extent of the 2D model so that

the results can be directly compared. The Eddington value of the flux at the surface of a  $1.4 M_{\odot}$  neutron star of radius  $10^6$  cm is  $F_{Edd} = 2.5 \times 10^{25}$  erg s $^{-1}$  cm $^{-2}$ , assuming electron scattering, and is used as a reference value. Since the models which are calculated in this thesis do not extend up to the actual surface of the neutron star, the time evolution of the fluxes cannot be rigorously translated into simulated light curves without making certain assumptions about the regions between the upper boundary of the computational domain and the actual surface of the star. Nevertheless, many general features which distinguish the behavior of fluxes in the 1D and 2D models can be discerned and directly attributed to convective energy transfer mechanisms. Thus, the convective dynamics in the envelope of neutron stars which arise during a Type I X-ray burst may significantly affect what is actually observed, and simulated light curves from numerical calculations of this phenomenon need to properly account for convection.

**6.2.1. Nuclear Flux.** In this sub-section, the behavior of the nuclear flux  $F_{nuc} = \int_0^{z_{top}} \rho \dot{s}_{3\alpha} dz$  is examined to establish the total rate at which nuclear energy is released into the system per unit area as a function of time. In principle, the temporal behavior of  $F_{nuc}$  during an X-ray burst is directly related to the observed light curve, since the burst is powered by the thermonuclear event. The nuclear energy released during the event will be distributed in many ways, such as to heat up the star, to do work against gravity and expand the outer envelope, to drive hydrodynamical processes such as convection and turbulence, and to radiate away via diffusion. What is actually observed is the diffusive radiative flux  $F_{rad}$  at the surface of the star, and it is a fraction of the magnitude of  $F_{nuc}$ . Because convection provides an additional energy sink in 2D models, significant differences are expected to exist between the temporal behavior of  $F_{nuc}$  and  $F_{rad}$  in the 1D and 2D models.

In Figure 6.3, the log of  $F_{nuc}/F_{Edd}$  for both the 1D and 2D models are plotted with respect to time. As the figure shows, the 1D and 2D temporal evolution of  $F_{nuc}$  during the burst differs significantly. The total time required to reach burst peak from the beginning of the simulation is delayed 0.36 s for the 2D model (1.57 s vs. 1.21 s). Likewise, Table 6.1

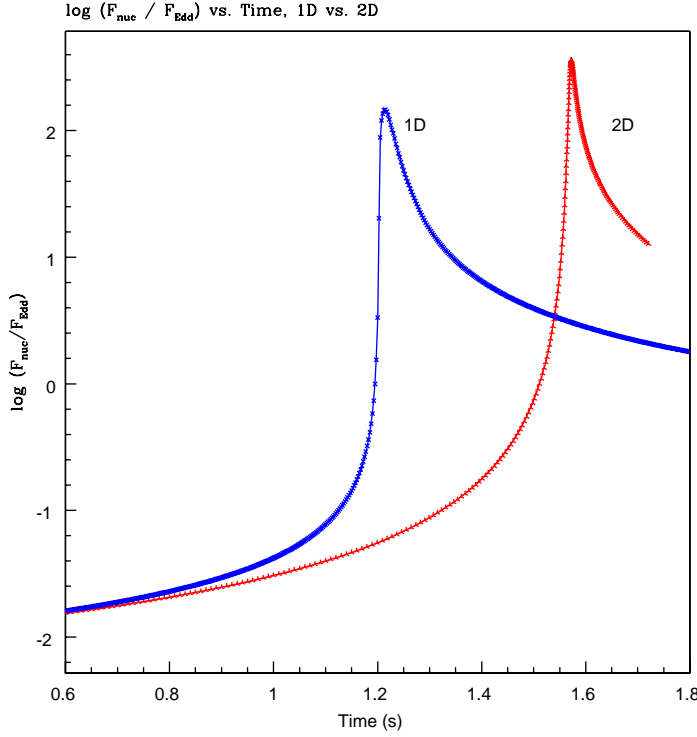


FIGURE 6.3. 1D, 2D Nuclear Flux Ratio vs. Time  
Log of  $F_{nuc}/F_{Edd}$ , 1D vs. 2D, vs. time (s).

Model	$t_{Edd}$	$t_{peak}$	$t_{e^{-1}peak}$	$\Delta t_{rise}$	$\Delta t_{fall}$
1D	1.180	1.210	1.242	0.030	0.032
2D	1.469	1.572	1.586	0.103	0.014

TABLE 6.1. 1D, 2D  $F_{nuc}$  Rise and Fall Times

$t_{Edd}$  = time to reach  $F_{Edd}$ ;  $t_{peak}$  = time to reach  $F_{peak}$ ;  $t_{e^{-1}peak}$  = time to reach  $e^{-1}F_{peak}$ ;  
 $\Delta t_{rise} = t_{peak} - t_{Edd}$ ;  $\Delta t_{fall} = t_{e^{-1}peak} - t_{peak}$ . All times are given in seconds.

shows that the time  $\Delta t_{rise}$  required for  $F_{nuc}$  to rise from the Eddington value ( $t_{Edd}$ ) to the peak value ( $t_{peak}$ ) is over three times greater in 2D than 1D. The delay in  $F_{nuc}$  rise time can be understood to be due to the additional mode of energy transfer provided by convection. Convective motions help to enhance thermal transport away from the regions in the domain where peak energy generation occurs, thus slightly moderating the nuclear runaway.

Another difference between the 1D and 2D results is the magnitude of the peak nuclear flux  $F_{peak}$ . The peak value in 2D ( $8.95 \times 10^{27}$  erg s $^{-1}$  cm $^{-2}$ ) is almost 2.5 times greater than

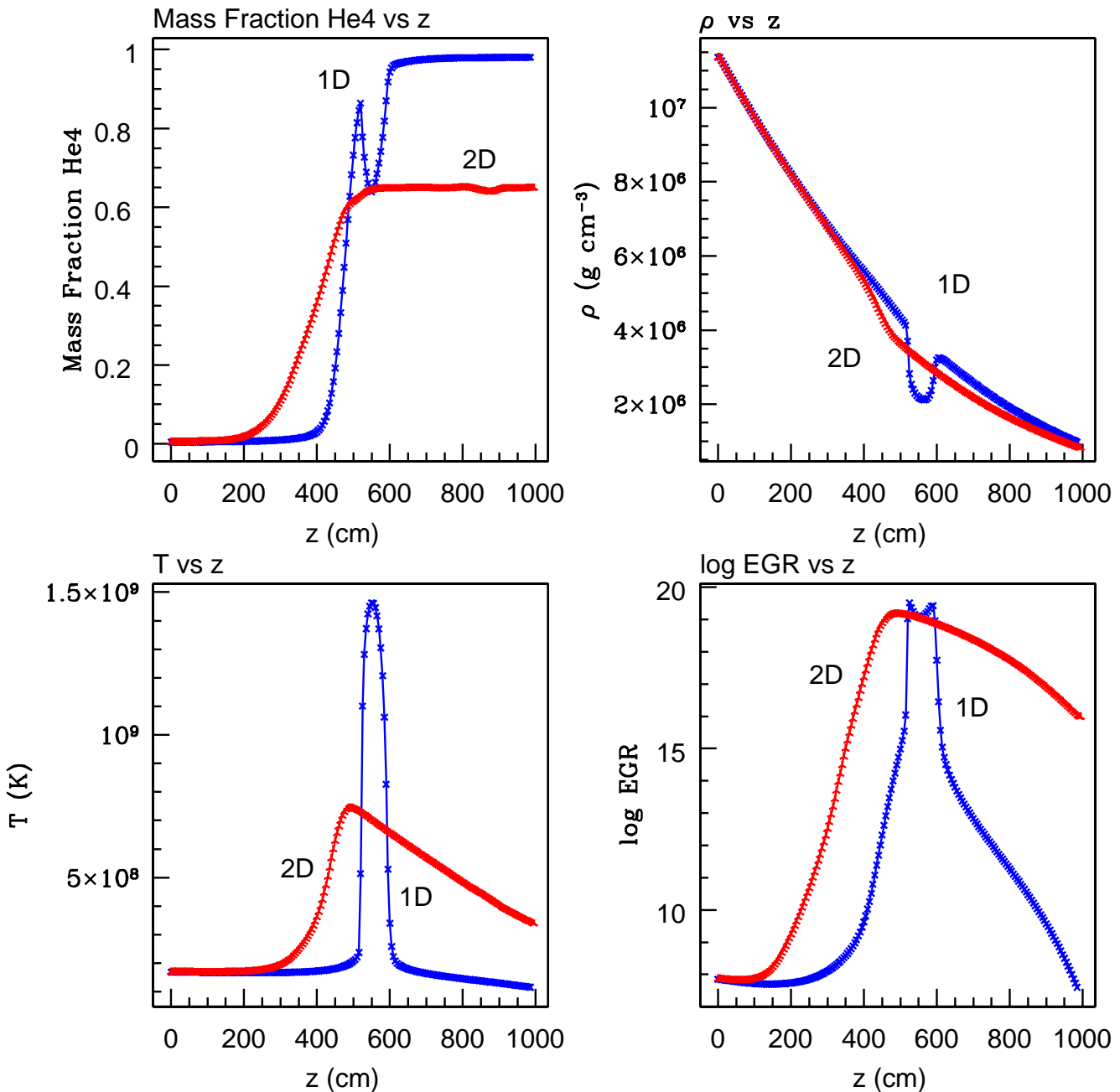


FIGURE 6.4. 1D, 2D Thermodynamic Quantities vs.  $z$   
 Mass fraction of  $He4$  (upper left),  $\rho$  (upper right),  $T$  (lower left), and  $\log EGR$  (lower right) as a function of height at burst peak for 1D ( $t = 1.210$  s, step = 242,000) and 2D ( $t = 1.571$  s, step = 440,000).  $5\text{ cm zone}^{-1}$  resolution.

in 1D ( $3.77 \times 10^{27}$  erg s $^{-1}$  cm $^{-2}$ ), a difference which can be explained by considering the dynamic effects of convection and the accompanying advection. For example, in Figure 6.4, the 1D and 2D vertical profiles of  $\rho$ ,  $T$ ,  $Y$ , and log EGR at the peak of the burst are directly compared (1D:  $t = 1.210$  s, step = 242,000; and 2D:  $t = 1.572$  s, step = 440,000). The vertical profile of temperature for the 2D model is noticeably broader than in 1D, a feature which can be attributed to the effect that convection plays in keeping the temperature profile adiabatic. Consequently, the temperature in the upper part of the 2D domain is several times greater compared to the same region in the 1D domain. Convection also directly effects the composition profile, since it thoroughly mixes fuel from upper regions, where  $Y$  is initially greater, to lower regions, where it is hotter. Consequently, by the time of burst peak, more fuel has burnt in 2D, as the upper-left panel in Figure 6.4 indicates. Likewise, the 2D model's gradients of  $Y$  and  $T$  over a region several hundred cm below the convective boundary are much less steep compared to 1D, an effect which is the result of advection in the 2D model. The net result of all these differences is that the EGR in a large part of the 2D domain exceeds 1D values by many orders of magnitude at burst peak. Moreover, the extreme drop observed in  $\rho$  where  $T$  peaks in 1D is completely avoided in 2D, due to the gentler slope in  $T$ . Thus, the greater  $F_{peak}$  in 2D compared to 1D can be understood to be the result of convective and advective effects which exclusively occur in the 2D model.

Finally, consistent with the picture that convective transport enhances the rate of cooling, Table 6.1 also shows that the time  $\Delta t_{fall}$  required for the  $F_{nuc}$  to diminish from  $F_{peak}$  to  $e^{-1}F_{peak}$  in 2D is less than half of what is needed in 1D. Taken together, these results indicate 2D hydrodynamics play important and significant roles in energy transport during the burst, which result in noticeable differences in the magnitude of peak  $F_{nuc}$ , and the rise and fall times of  $F_{nuc}$  when compared to 1D.

Since the results presented in Section 6.1 of this chapter suggest  $\dot{s}_{12,\alpha}$  should be included to properly account for the total EGR as  $Y$  diminishes post-burst peak, the actual rise and

fall times of  $F_{nuc}$  during an X-ray burst powered by helium burning may be different from what is presented here.

**6.2.2. Radiative and Advective Fluxes.** To obtain a realistic light curve from a numerical simulation, the domain which is modeled should include the actual surface of the star in order to be able to accurately calculate the radiative flux there. As explained in Chapter 4, the upper boundary of the current 2D model is 500 cm below the star's surface for a variety of reasons, including being able to avoid the small thermal diffusion time-step limitations of low-density regions which are not important for studying convective processes, the main topic of this thesis. Consequently, rigorously calculating a light curve from the current results is not possible. Nevertheless, in this sub-section, the 1D and 2D radiative flux  $F_{rad}$  and the 2D advective flux  $F_{adv}$  (which includes the convective flux) are analyzed as a function of space and time to more completely understand how they behave. Moreover, important differences exist between the 1D and 2D results, and, as before, these differences are directly attributable to convective processes in 2D.

The radiative flux  $F_{rad}$  is defined as:

$$(6.13) \quad F_{rad} = -\kappa \nabla T$$

The advective flux  $F_{adv}$  is defined as:

$$(6.14) \quad \frac{\partial F_{adv}}{\partial z} = w \left( \rho c_p \frac{\partial T}{\partial z} - \delta \frac{\partial P}{\partial z} \right)$$

$$(6.15) \quad F_{adv}(z') = \int_0^{z'} \frac{\partial F_{adv}}{\partial z} dz$$

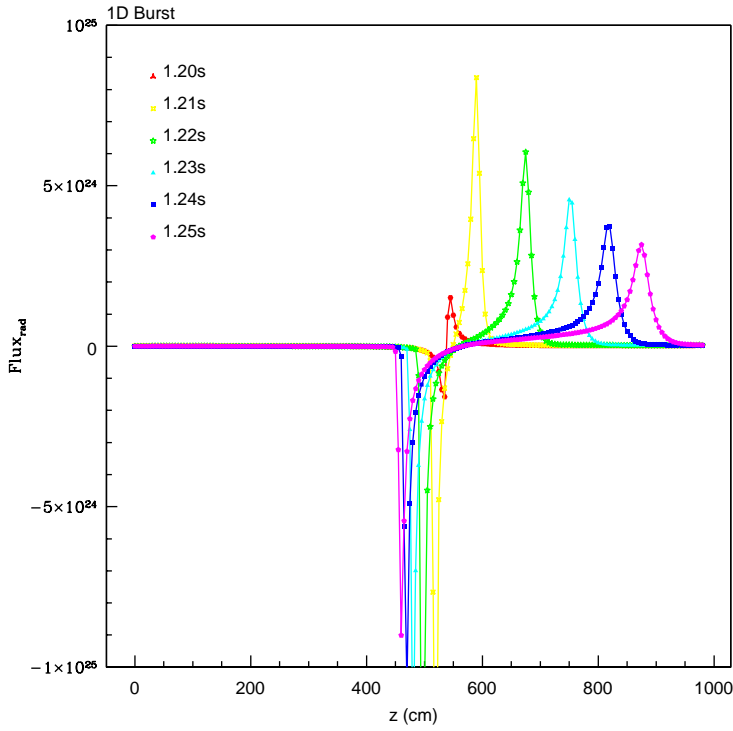


FIGURE 6.5. 1D  $F_{rad}$  vs.  $z$  for Several Times  
Log of  $F_{rad}/F_{Edd}$  vs.  $z$  (cm), 1D model, at several times.

In practice,  $\frac{\partial F_{adv}}{\partial z}$  is evaluated at every zone in the domain. Then, for each lateral position,  $F_{adv}(z')$  is determined by integrating up from the bottom of the domain to every vertical height  $z'$ . Finally, all values of  $F_{adv}(z')$  at every height are laterally averaged to obtain  $F_{adv}(z)$  as a function of height. To study  $F_{adv}$  and  $F_{rad}$  as a function of time, a specific height must be chosen. Heights of  $z = 700$ ,  $800$ , and  $900$  cm in the domain were examined. Heights above  $z = 900$  cm were avoided due to their proximity to the upper boundary at  $z = 1000$  cm. Likewise, heights below  $z = 700$  cm were avoided due to their proximity to the regionally hottest layer at  $z = 600$  cm. In 2D, the temporal behavior of  $F_{adv} + F_{rad}$  is independent of the heights examined, and  $z = 800$  cm is chosen because it is equidistant from the regionally hottest layer and the upper boundary. In 1D, the maximum value of  $F_{rad}$  depends on height, as suggested in Figure 6.5. Presumably, this is due to the upper boundary condition which inadequately accounts for temperature changes there. Ideally,

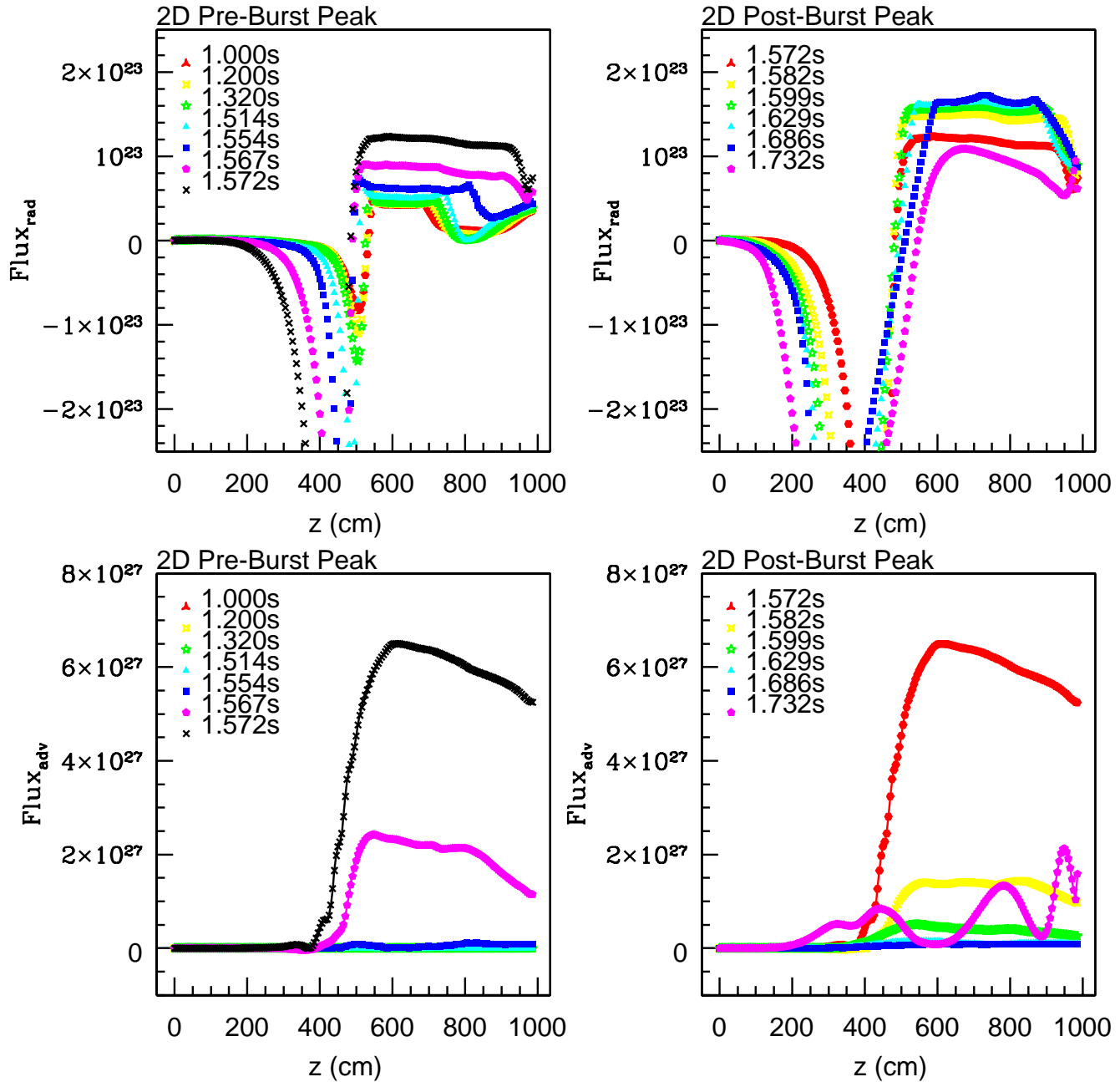


FIGURE 6.6. 2D  $F_{rad}$  and  $F_{adv}$  vs.  $z$  for Several Times  
 Log of  $F_{rad}/F_{Edd}$  (upper panels) and  $F_{adv}/F_{Edd}$  (lower panels) vs.  $z$  (cm), 2D model, at several times, pre-burst peak (right panels), post-burst peak (left panels).

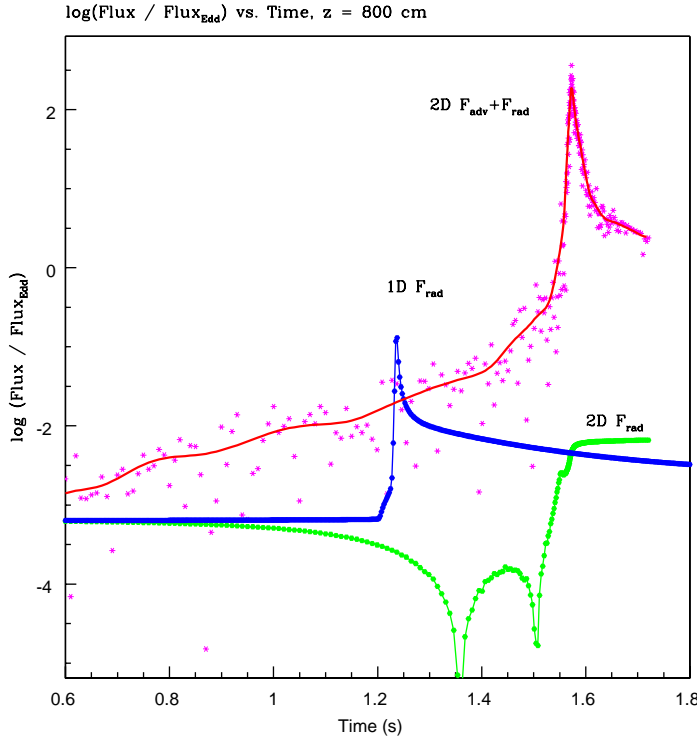


FIGURE 6.7. 1D, 2D  $F$  vs. Time  
Log of  $F_{rad}/F_{Edd}$  and  $F_{adv}/F_{Edd}$  vs time (s) for the 1D and 2D models.  
Fluxes are taken at  $z = 800$  cm.

the maximum value of  $F_{rad}$  sustains a constant value as it passes upward toward the star's surface. Nevertheless, the maximum value that  $F_{rad}$  attains in the 1D model never greatly exceeds  $0.1 F_{Edd}$ , and the height of analysis is chosen to be  $z = 800$  cm to be consistent with the analysis for the 2D model.

Figure 6.7 shows the 1D, 2D  $F_{rad}$  and 2D  $F_{adv}$  as functions of time at  $z = 800$  cm, expressed as the log of the fraction of  $F_{Edd}$ . The 1D  $F_{rad}$  shows a sharp rise, clear peak and exponential-like decay. The 2D  $F_{rad}$  suffers from more anomalous behavior between 1.2-1.5 seconds due to transient, dynamical processes occurring there during this time. As the burst ensues, the 2D  $F_{rad}$  likewise shows a sharp pre-burst peak rise, but plateaus after burst peak for the balance of the calculation. The spatial profiles of  $F_{rad}$  offer explanations for the difference in behavior. For the 1D model (Figure 6.5),  $F_{rad}$  passes through the domain as a well defined pulse. Thus, the 1D  $F_{rad}$  at a given point shows a distinct local maximum

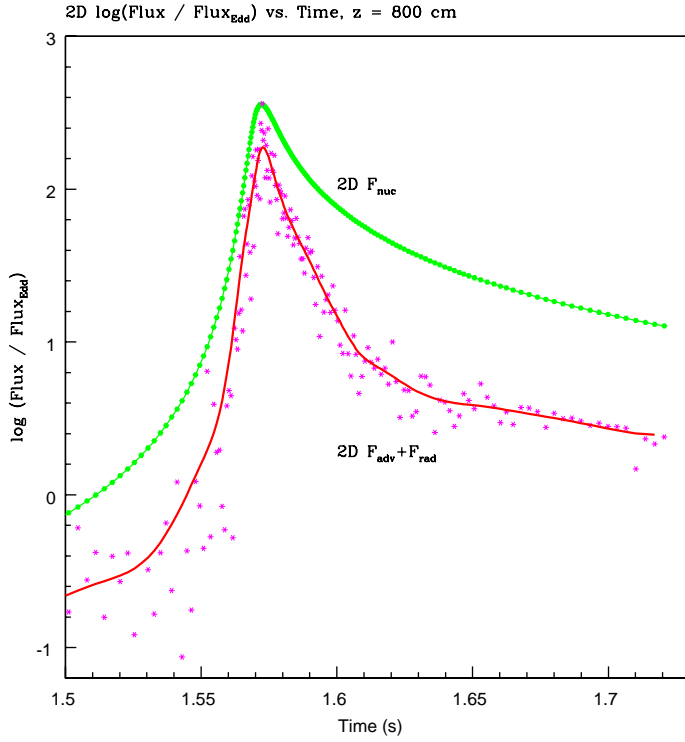


FIGURE 6.8. 2D  $F_{adv} + F_{rad}$  vs. Time

Log of  $(F_{adv} + F_{rad})/F_{Edd}$  vs. time (s) for the 2D model after  $t = 1.50$  s. Fluxes are measured at  $z = 800$  cm. The log of the 2D  $F_{nuc}/F_{Edd}$  is also plotted for reference.

in time. However, for the 2D model (upper left and upper-right panels in Figure 6.6), the  $F_{rad}$  profile is much more flat and table-top-like. While it takes time for the 2D  $F_{rad}$  to rise at a given vertical height, it remains roughly at that level after the convective layer boundary passes. This is the result of convection, since convective motions help to keep the temperature gradient adiabatic to zeroth order, which is approximately constant for the duration of the burst over the areas where convection is present. The value of  $F_{rad}$  may increase due to rising temperatures as the burst progresses, but it does so over the entire convective region uniformly. Thus,  $F_{rad}$  in 2D does not behave as a propagating pulse, but more as a lengthening plateau. The difference in the peak magnitude of the 1D and 2D  $F_{rad}$  is also understandable in terms of convective effects, since convection significantly moderates the temperature gradient, thus effectively diminishing  $F_{rad}$  in 2D.

As a function of time in 2D,  $F_{adv}$  nearly always dominates over  $F_{rad}$ . The actual behavior of  $F_{adv}$  in time is noisy, indicated by the scattered data points in Figures 6.7 and 6.8. However, the scatter is relatively well constrained about a distinct trend, and a smoothed fitting curve is overlayed against the individual data points. The lower-left and lower-right plots in Figure 6.6 show  $F_{adv}$  as a function of height for several times throughout the burst. At earlier times, it is relatively small, and varies between positive and negative depending on the height. However, approaching burst peak,  $F_{adv}$  becomes always positive in the upper part of the domain. Likewise, in Figure 6.7 before  $t = 1.55$  s at  $z = 800$  cm,  $F_{adv}$  oscillates between positive and negative values, but the magnitude of  $F_{adv}$  during this time is relatively small. For plotting purposes, the absolute value of  $F_{adv}$  is shown. After  $t = 1.55$  s,  $F_{adv}$  is always positive, and Figure 6.8 focuses on times later than  $t = 1.50$  s, which includes all of the burst rise and decay. Here,  $F_{2D} = F_{adv} + F_{rad}$  is plotted, and for reference, the 2D  $F_{nuc}$  is also plotted as well.

In 2D,  $F_{nuc}$  and  $F_{2D}$  peak at the same time. The rise time of  $F_{2D}$  from  $F_{Edd}$  to its peak value  $F_{peak}$  (from  $t = 1.511$  s to  $t = 1.572$  s) is  $\Delta t_{rise} = 0.06$  s. The burst fall time  $\Delta t_{fall}$  required for the  $F_{2D}$  to diminish from  $F_{peak}$  to  $e^{-1}F_{peak}$  (from  $t = 1.572$  s to  $t = 1.587$  s) is 0.015 s, while the decay time  $\Delta t_{decay}$  from  $F_{peak}$  to the time  $F_{2D}$  levels off slightly (at  $t = 1.65$  s) is around  $\Delta t_{decay} = 0.75$  s. Post-burst peak,  $F_{2D}$  always remains above pre-burst peak levels and gradually diminishes for the duration of the calculation. During the rapid rise of the burst between  $t = 1.55$  s and 1.57 s,  $F_{2D}$  accounts for nearly all of  $F_{nuc}$ , and at the burst peak,  $F_{2D}$  ( $= 360F_{Edd}$ ) nearly equals  $F_{nuc}$  ( $= 400F_{Edd}$ ). At other times during the burst,  $F_{2D}$  is only a small fraction of  $F_{nuc}$ .

Presumably, the behavior of  $F_{adv}$  will be directly related to the radiative flux at the surface of the star. However, translating these results into a light curve at the surface cannot be done rigorously. For example, the true surface of the star is not presently modeled and thus a surface flux can not be directly calculated. Another complication which arises is due to neglecting  $\dot{s}_{12,\alpha}$ , and the results presented in Section 6.1 of this chapter suggest it is

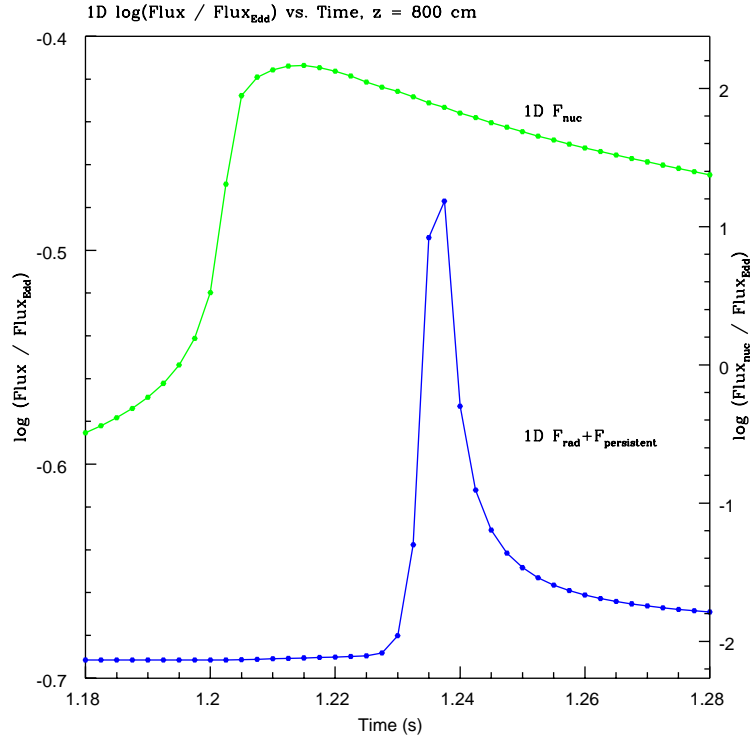


FIGURE 6.9. 1D Simulated Light Curve

Log of  $(F_{rad} + F_{persistent})/F_{Edd}$  for the 1D model.  $F_{rad}$  is measured at  $z = 800$  cm. The log of the 1D  $F_{nuc}/F_{Edd}$  is also plotted for reference, and its scale is the right axis.

required to properly model the burst at times after the current peak. Thus, the calculated rise and decay time for the burst may be modified when including more complete burning networks. Hence it is impossible to make an accurate prediction of an observable light curve from these results. What can be reasonably stated is that  $F_{adv}$  should reasonably diminish in the radiative regions at the stellar surface, and it will decrease more if the envelope expands. Also, the calculated burst rise time (admittedly subject to correction) reasonably represents the actual burst rise time, assuming the photon diffusion timescale for the radiative region at the actual surface is less.

Finally, a simulated light curve  $F_{1D} = F_{rad} + F_{persistent}$  for the 1D model is presented in Figure 6.9. (For reference, the 1D  $F_{nuc}$  is plotted on the same figure, and the right axis is its scale.) The persistent flux  $F_{persistent} = 0.203F_{Edd}$  is due to accretion (assumed to be spherical symmetric with a mass accretion rate of  $\dot{m} = \frac{5 \times 10^{-9}}{4\pi R_{NS}^2} M_\odot \text{ yr}^{-1} \text{cm}^{-2}$ ). The obvious delay in

Model	$t_1$	$t_{peak}$	$t_{e^{-1}peak}$	$\Delta t_{rise}$	$\Delta t_{fall}$	$\Delta t_{decay}$
1D	1.2275	1.2375	1.2420	0.010	0.0045	0.015
2D	1.5110	1.5720	1.5870	0.060	0.0150	0.750

TABLE 6.2. 1D, 2D  $F$  Rise, Fall, Decay Times

$t_1$  = time when  $F_{1D,sim} > F_{persistent}$  for 1D model;  $t_1$  = time to reach  $F_{Edd}$  for 2D model;  
 $t_{peak}$  = time to reach  $F_{peak}$ ;  $t_{e^{-1}peak}$  = time to reach  $e^{-1}F_{peak}$ ;  $\Delta t_{rise} = t_{peak} - t_1$ ;  
 $\Delta t_{fall} = t_{e^{-1}peak} - t_{peak}$ ;  $\Delta t_{decay}$  = time to level off from peak values. All times are given in seconds.

time ( $\sim 0.3$  s) between the time of the peak of  $F_{nuc}$  and  $F_{1D}$  represents the time it takes the burning front to travel from the hottest burning layer ( $z = 600$  cm) to the analysis height ( $z = 800$  cm). The burst rise time  $\Delta t_{rise}$  is measured from the time when  $F_{1D}$  increases from persistent levels to the peak value  $F_{peak}$  (from  $t = 1.2275$  s to  $t = 1.2375$  s), and  $\Delta t_{rise} = 0.01$  s. The burst decay is exponential, and  $\Delta t_{fall}$  required for the  $F_{1D}$  to diminish from  $F_{peak}$  to  $e^{-1}F_{peak}$  (from  $t = 1.2375$  s to  $t = 1.2420$  s) is 0.0045 s. The time it takes  $F_{1D}$  to level off (although never dropping below roughly 5% above the initial value of  $F_{persistent}$ ) is  $\Delta t_{decay} = 0.015$  s, and it gradually diminishes in magnitude over time until the end of the calculation.

Table 6.2 summarizes the rise, fall, and decay times of  $F_{1D}$  and  $F_{2D}$ .

The rise times of observed X-ray bursts generally range from 0.1 - 1.0 seconds, and the burst duration is generally between 1-10 seconds. Thus, the calculated rise time for the 1D model of 0.01 s is relatively short in comparison. The entire 1D burst lasts only about 0.3 s, and its peak flux is  $0.35F_{Edd}$ . The relatively short rise time and duration of the 1D burst may be accounted for by the relatively high accretion rate used. As a result, the hottest layer is close to the neutron star surface with the consequences that little fuel is available for burning, photon diffusion times are short, and the layer through which the burst rises is thin. Moreover,  $\dot{s}_{12,\alpha}$  is neglected in the current burner, and its inclusion should lengthen the duration and increase the magnitude of the burst.

While it may not be possible to calculate realistic light curves from the current results, significant differences in the temporal and spatial behavior of the 1D and 2D models' fluxes are clearly evident. These differences can be attributed to the effects of convective dynamics

which require more than one spatial dimension to model. The simulated light curve of the 1D model presented in this thesis is thus inherently incomplete, because it does not include the effects of convection. The present results reinforce the need to properly model the effects of convection in 1D models in order to produce more realistic calculated light curves of X-ray bursts and other astrophysical phenomena involving thermonuclear explosions.

### 6.3. Schwarzschild vs. Ledoux Criteria

As demonstrated in Chapter 4 on the main 2D results, the behavior of the lateral and temporal average of the actual gradient  $\nabla \equiv (\frac{d \ln T}{d \ln P})$  is very intriguing. At all EGR levels in the convective region, it is always between the adiabatic gradient,  $\nabla_{ad} \equiv (\frac{d \ln T}{d \ln P})_s$ , and the Ledoux gradient,  $\nabla_L \equiv \nabla_{ad} + \frac{c_1}{c_2} \nabla_\mu$ , where  $\nabla_\mu \equiv (\frac{d \ln \mu}{d \ln P})$ , and  $c_1 \equiv \left(\frac{\partial \ln \rho}{\partial \ln \mu}\right)_{P,T}$ ,  $c_2 \equiv -\left(\frac{\partial \ln \rho}{\partial \ln T}\right)_{P,\mu}$ . Toward the center of the convective region, the convective flows efficiently homogenize the composition, and so  $\nabla_{ad} \sim \nabla$ . Near the convective boundaries, however, convective motion significantly diminishes, and mixing becomes much less efficient. Composition gradients are therefore sustained, and  $\nabla$  deviates from the Schwarzschild criteria to favor the Ledoux criteria instead. Indeed, when examined locally and instantaneously, the spatial fluctuations in  $\nabla$  follow  $\nabla_\mu$  to a remarkable degree.

Whether the Schwarzschild or Ledoux criteria is satisfied in regions where composition gradients exist in massive stars is still an open question in astrophysics. Semiconvection, a relatively slow mixing caused by composition gradients, is poorly understood, and models which examine the Schwarzschild vs. Ledoux gradients yield conflicting results (Merryfield, 1995; Canuto, 2000). Moreover, Canuto (2000) demonstrates that the Schwarzschild criteria necessarily implies penetration (in his terms, “overshooting”). The Ledoux criteria also necessarily implies penetration if a certain relation for the mixing-length parameter is not satisfied, that is, if convection is non-local.

In the present results, convection develops naturally as a consequence of superadiabatic gradients arising from heat input into the system by nuclear burning in a bursting layer. No

model for convection is assumed; indeed, the results are not adequately represented by the predictions of local mixing-length theory. Throughout the burst, the average values of the actual gradient  $\nabla$  are best described as always between  $\nabla_{ad}$  and  $\nabla_L$ , while the instantaneous values are closer to  $\nabla_L$ . Moreover, some penetration occurs at the convective boundaries, where even on average,  $\nabla$  clearly deviates from  $\nabla_{ad}$  to conform better to  $\nabla_L$ . The current model includes all the key elements of convective and semiconvective processes, and the results suggest that deeper investigation is warranted.

## 6.4. Summary of Main Results

**6.4.1. Computational.** The LMNA as applied to strongly stratified environments with nuclear burning is successfully formulated, developed, and coded in two spatial dimensions, taking advantage of a parallel processing environment. The LMNA governing equations are solved as a split, explicit method, with a CFL factor of 0.50 for 2D simulations. The input physics include thermal diffusion,  $3\alpha$  nuclear burning (Fushiki and Lamb, 1987), strong gravity ( $g \sim 10^{14} \text{ cm s}^{-2}$ ), and a realistic equation of state (Timmes and Swesty, 2000). By design, acoustic (pressure-) waves are naturally excluded from the results, and to zeroth order, hydrostatic equilibrium always applies. The  $K$  function, a novel mathematical feature which is applied to reformulate the momentum and elliptic equations, is successfully implemented, and its inclusion in the LMNA model is required to successfully model a Type I X-ray burst powered by the  $3\alpha$  reaction ( $3_2^4He \rightarrow {}_6^{12}C$ ) on the surface of accreting neutron stars. The model is verified using several different spatial and temporal resolutions, as well as varying domain sizes; all verification studies demonstrate excellent qualitative and quantitative convergence of results.

**6.4.2. 2D Hydrodynamics of a Type I X-ray Burst.** The LMNA model is applied to investigate for the first time the 2D convective flows which develop during a Type I X-ray burst powered by the  $3\alpha$  reaction on a rectangular patch of the envelope of a neutron star. Starting from a pre-convective state, the domain is allowed to naturally develop regions of

superadiabaticity in a layer where higher temperatures lead to enhanced energy generation due to nuclear burning. Convective motions naturally begin to develop into cells which qualitatively resemble Benard-cells (Koschmieder, 1993), though of varying sizes, shapes, and orientations. The magnitudes of the instantaneous, convective velocities increase from order  $10^4$  to  $10^7 \text{ cm s}^{-1}$  as the burst progresses, however the maximum Mach number throughout the entire process is always less than 0.10. During the rise to the peak of the burst, the layer in the domain where the EGR has its maximum value stays at the same height of  $\sim 500 \text{ cm}$  above the base of the domain. After burst peak, a spreading temperature wave which is still increasing in magnitude as the EGR diminishes creates two outwardly advancing burning fronts which propagate at roughly  $10^3 \text{ cm s}^{-1}$ . Throughout the burst sequence, the upper and lower convective boundaries expand vertically as roughly uniform layers.

Compared to a calculation using the LMNA model in 1D mode, the burst peak in 2D is delayed by nearly half a second. Other significant differences between the 1D and 2D results include the rate at which the nuclear flux rises and falls; the spatial profiles of thermodynamic quantities such as  $T$ ,  $Y$ , and EGR; and the peak value of nuclear flux at burst peak. Significant differences between the behavior of the 1D and 2D models' radiative flux are also evident. All the differences can be attributed to convective dynamics, which provides an additional energy transport mechanism in 2D.

The instantaneous velocity field and the associated convective patterns evolve on a time-scale of a fraction of a convective time-scale ( $\sim 10^2\text{-}10^3 \mu\text{s}$ ), which is itself a fraction of the burning time-scale ( $\sim 10^4\text{-}10^5 \mu\text{s}$ ). Significant fluctuations in the fractional difference of temperature and composition from the lateral average, as well as fluctuations in the adiabaticity based on either the Schwarzschild or Ledoux criteria, also occur on sub-convective time-scales. In terms of the lateral and temporal average, however, the layer where convective motions develop is always slightly superadiabatic by the Schwarzschild criteria. At

the convective boundaries, the lateral and temporal average of the actual temperature gradient appears to better conform to the Ledoux criteria, reflecting the fact that significant compositional gradients are sustained there due to less efficient mixing.

A series of studies thoroughly examines how often and to what extent tracer particles penetrate through the upper and lower boundaries from both sides of the convective layer. Overall, the convective boundaries are found to be remarkably impenetrable from the inside of the convective region. Instances of temporary penetration occur more frequently at higher EGR levels, predominantly at the lower boundary, but tracer particles remain effectively trapped within the convective region. Tracer particles originally above the convective region can fall more easily into it, rather than rise up from below. Whether or not tracer particles do penetrate from above depends very sensitively on their initial positions above the convective boundary. Along a vertical slice, different heights in the domain consistently exhibit certain net directions of motions, for example, always downward in the regions above the convective region and in the upper part of the convective layer, resulting in an overall downward bias for top-penetration. Mixing from beneath the convective layer (dredge-up) is very limited.

Modal analysis reveals that near the convective boundaries, a gradual transition from gravity- to convective-modes exists. Thus, convective-modes are always present in regions where penetration occurs. Since they are also present when penetration does not occur, convective-modes are a necessary but not sufficient condition for particles to penetrate beyond the convective boundaries.

Finally, the current results suggest that the relationships between the convective flux, the temperature perturbation, the vertical velocity perturbation, and the gradient of the temperature perturbation are more complicated than what local mixing-length theory predicts.

## 6.5. Future Development and Applications

Presently, the LMNA code is a powerful computational tool and has been successfully applied to examining 2D numerical simulations of deflagrations during Type I X-ray bursts, a

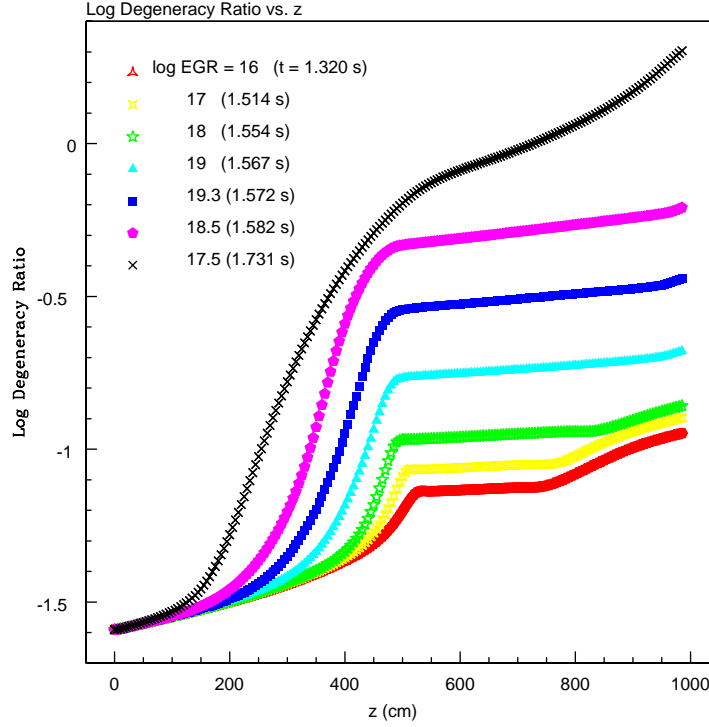


FIGURE 6.10. Log Degeneracy Ratio vs. z

Log of the degeneracy ratio as a function of  $z$  (cm) at several times throughout the burst sequence. The burst peak corresponds to  $\log EGR = 19.3$  ( $t = 1.572$  s).

problem which has thus far been intractable with other methodologies. However, it is limited in many respects, and continuing to develop the code will be a vital aspect of future work. More fully developed, it may be a useful tool to explore other astrophysical problems involving deflagrations in environments where gravity is relatively strong. In this final section, several ways to continue developing and applying the present LMNA model are presented.

**6.5.1. Computational.** Following are several ideas for future development of the LMNA code, which may significantly enhance and expand the present model.

*Time-Dependent Base State.* Currently, the LMNA model assumes a time-independent, hydrostatic background state. This assumption is justified when the level of the electron degeneracy in the gas is high, that is, when the Fermi energy for electrons is much greater than the thermal energy. In a highly degenerate state, a large increase in temperature does

not cause a corresponding increase in pressure. Thus, the pressure can be held constant in time to fair approximation. However, the assumption that the background pressure is independent of time can be easily relaxed in a more complete LMNA model, which will be better able to handle conditions when the degeneracy level decreases and expansion effects become important.

A calculation indicating the degree of degeneracy in the domain used in this thesis to model Type I X-ray bursts shows that the level of degeneracy decreases as the burst progresses, since the energy released during nuclear burning increases  $T$  and decreases  $\rho$  in the upper half of the domain during the evolution. The results of this calculation are plotted in Figure 6.10, where the degeneracy ratio is defined to be  $(T/\rho^{2/3})/D$ , where  $D = 1.3 \times 10^5 \text{ K cm}^2 \text{ g}^{-2/3}$ , which is the critical value of the quantity  $T/\rho^{2/3}$  for which the Fermi energy for electrons equals the thermal energy. (Although determining the level of degeneracy using this ratio strictly applies only to strongly degenerate conditions, it is used here only as an indication of the degeneracy level in the domain.) As the results show, while most of this region remains relatively degenerate during the entire rise to burst peak, the level of degeneracy significantly decreases in the upper third of the domain by the end of the calculation. Nevertheless, the degeneracy level in the convective layer by the time  $\log \text{EGR} = 18$  during rise to burst peak is comparable to the degeneracy level of the hottest patch ( $T_{\text{peak}} \sim 10^{10} \text{ K}$ ,  $\rho \sim 10^9 \text{ g cm}^{-3}$ ,  $\log \text{degeneracy ratio} = -1.11$ ) in a white dwarf star model which was studied using an alternative LMNA method by Almgren et al. (2006b). In this study, a LMNA model which allowed a time-dependent pressure base state captured the same density profile produced by a fully compressible model, but the profile of a LMNA model which used a time-independent base state deviated from those of the other models by roughly 10% in this region. (Granted, Almgren et al. neglected thermal diffusion, which would in principle decrease the peak temperature attained in their model, and thus lessen the discrepancy.)

These results suggest that expansion effects should be included in a more complete hydrodynamical model of a Type I X-ray burst by allowing the background pressure to change in time.

It is difficult to quantify the consequences of neglecting the time-dependency of the base state without actually performing the enhanced computation. Qualitatively, one can surmise that due to the decrease in density, the energy generation rate would decrease, since it depends upon the density. Thus, the burst rise time may increase. As the density decreases, the dynamical inertia should reasonably also decrease, but whether this translates into an increase in convective velocities is uncertain, since the EGR also decreases. Nevertheless, the current model's qualitative findings, such as the major convective cells filling up the entire vertical extent of the convective layer, are not likely to be affected by the change. Hopefully, the actual differences will be clearly shown in a future calculation using a LMNA model with a time-dependent base state.

*Second-order time accuracy.* Presently, the overall code is first order accurate in time. However, it can be readily made second-order accurate in time by incorporating a predictor-corrector step. A developmental version of the present code with this improvement did not yield significantly different results on limited test runs. Thus, to save on computational expense, the final models presented in this thesis were computed using the version of the code which is first-order accurate in time.

*Fully Three-Dimensional.* Currently, the LMNA model as presented in this thesis is limited to two spatial dimensions, the vertical ( $z$ ) and lateral ( $y$ ) directions. Extending the LMNA model into three dimensions is a very natural next-step, which will immediately yield more physically realistic results. Non-trivial differences between 2D and 3D results are well-documented in hydrodynamical computations both terrestrially (Davidson, 2004) and astrophysically (Khokhlov, 1994; Kercek et al., 1999).

*Sub-grid Turbulence.* Turbulent processes exist over many length-scales, and for the sake of practicality, the resolution of a computational domain is necessarily larger than the smallest turbulent scales which occur. To help remedy the situation, turbulence models attempt to account for unresolved scales (Mathiew and Scott, 2000; Davidson, 2004). Such models can be incorporated into the LMNA model to explore the effects of sub-grid turbulence on the resulting dynamics of astrophysical deflagrations.

*Rotation.* Rotational forces (such as the centripetal and Coriolis forces) may be included to model the effects of rotation. Indeed, observations show that neutron stars can rotate very rapidly, and rotational influences may play a significant role in how, when, and where ignition occurs. For instance, strong eddies due to Coriolis forces may confine a region of more highly concentrated fuel, resulting in enhanced localized burning. Or, centripetal forces may cause significant differences based on latitude, possibly affecting processes depending on whether they occur near the equator or the poles (Spitkovsky et al., 2002). Also, angular momentum conservation during a burster's rotational evolution may also account for the 1-2 Hz frequency changes which occurs during an X-ray burst (Cumming and Bildsten, 2000). Differential rotation may also affect elemental mixing (Fujimoto, 1988). In a white dwarf model, rotation was found to break a strong dipolar distribution of turbulent flows, a situation which would encourage a more substantial Type Ia supernova ignition (Kuhlen et al., 2005). Thus, including rotation would be an important addition to the LMNA model and allow for more realistic computational simulations of deflagrative processes such as Type I X-ray bursts.

*Alternative Coordinate Systems.* Currently, the code uses a straightforward Cartesian coordinate system in a plane-parallel approximation. This is sufficient to study the current problem of X-ray bursts on neutron stars over a limited region of a star. Other coordinate systems, such as cylindrical or spherical coordinates can be implemented, allowing for the calculation of problems which might involve greater portions of a star, or even an entire star.

For such problems, additional computational challenges such as the boundary conditions at the origin will need to be addressed.

**6.5.2. Astrophysics.** With the LMNA model, a number of interesting astrophysical problems which involve low Mach number flows in highly stratified environments can be computationally studied.

*X-ray bursts on Neutron Stars.* In this thesis, the LMNA model has been applied to simulate Type I X-ray bursts (Taam, 1980, 1985) on a rectangular patch on the surface of a neutron star. With FLASH, Type I X-ray bursts have previously been modeled as a helium detonation (Zingale et al., 2001), as well as a deflagration, albeit in a limited manner by imposing a temperature perturbation rather than using a realistic reaction network (Zingale et al., 2002). This thesis demonstrates that a  $3\alpha$  reaction powered X-ray burst may occur as a deflagration. Further computational study of this phenomenon can continue. For example, investigations in 3D may reveal important differences in dynamics compared to 2D. Three dimensions are also necessary to properly simulate turbulent dynamics using a sub-grid turbulent model, since turbulence is inherently a 3D phenomenon. More comprehensive parameter studies can also be performed, examining how the properties of the bursts depend upon the size, placement, and nature of initial perturbations. Also, different initial conditions involving composition gradients can be applied to examine the effects of baroclinic instabilities (Fujimoto, 1993). Another line of questioning involves what kinds of effects would result from including a more sophisticated nuclear reaction network, as recent 1D investigations suggest burst behavior is sensitive to the details of burning (Peng et al., 2003). Simulations of the hydrodynamics of classical nova on white dwarfs, to be discussed below, were also found to be significantly affected by a change in the nuclear reaction network (Starrfield et al., 2004).

*Classical Novae on White Dwarfs.* While classical nova on white dwarfs have previously been computationally demonstrated (Glasner et al., 1997; Kercek et al., 1999; Alexakis et al.,

2004), the calculations are limited in nature due to the computational expense. Encouragingly, the results of these calculations suggest that the flow speeds during the early phases of a classical nova are substantially subsonic, making the LMNA an appropriate model to routinely study this class of problems. Interesting questions involve the mechanism of elemental mixing and dredge-up, the sub-sonic stages before the ejection of matter, and accounting for the high luminosities observed initially in fast novae. Moreover, the same kinds of questions which pertain to X-ray bursts on neutron stars can be explored in the classical nova.

Classical novae are understood to be explosive thermonuclear events on white dwarf stars (Gallagher and Starrfield, 1978; Gehrz et al., 1998). Extensive spectroscopic analysis of novae ejecta reveal large amounts of metallic nuclei, such as C, N, O, Ne, Mg, and Al. Thus, novae help to enrich the interstellar medium, raising important implications in studying the pre-solar nebula, pre-solar grains, and meteoric stardust (Starrfield et al., 2000). On the white dwarf, mechanisms must exist which transfer heavier materials from its core to the surface, where they can be ejected during the initial phase of a nova explosion. Possible mixing mechanisms which have been suggested include (i) rotational shearing, (ii) convective diffusion, (iii) convective shearing, (iv) thermal convection (Livio and Truran, 1990).

Until recently, modeling convective processes under typical white dwarf conditions was limited to 1D approximations, such as the mixing-length theory (Spiegel, 1963). These calculations generally gave good agreement between observations and theory (Starrfield et al., 1985, 1986). However, unresolved issues include i) the mechanism of elemental mixing, ii) the amount of matter which is ejected during a nova, and iii) accounting for the high luminosities observed initially in fast novae. More detailed simulations of thermonuclear burning with hydrodynamics in multi-dimensions were recently conducted, but offered conflicting results. A 2D calculation (Glasner et al., 1997) suggested that the combustion process in a classical nova begins as a series of many local eruptions, scattered over the entire base of the hydrogen envelope. Convective motions set up by the outburst were found to effectively mix the C and O from the core with the hydrogen envelope, enriching the envelope by 15% to 30%,

agreeing well with observations of the ejecta. Also, Glasner et al. (2005) propose that the choice of outer boundary conditions significantly effects the results of recent 2D nova simulations and may help explain why runaway thermonuclear reactions on white dwarf models succeed in the study by Glasner et al. (1997) but not in Kercek et al. (1998). On the other hand, a 3D calculation (Kercek et al., 1999) did not find significant mixing under similar initial conditions. Compared to the 2D model, more small scale motions developed in 3D, thus decreasing larger convective motions which could mix elements between the core and the outer layers of the star. Notably, the authors of the 3D study acknowledge that computational limitations prevented them from exploring more parameter space which would have strengthened their conclusions.

With typical velocities far below the sound speed, simulations such as these would greatly benefit from the LMNA model. Parameters such as the mass and metalicity of the white dwarf core and accreted envelope can be explored, and multiple simulations run in much less time than current methods require. Furthermore, the results from these simulations can then be used as initial conditions in fully explicit calculations of models in which significant acoustic effects are expected, for instance, during the mass ejection phase.

*Type Ia Supernovae on White Dwarfs.* Type Ia supernovae, which are thought to be detonations on white dwarfs, are currently being computationally simulated using an alternative form of the low Mach number model (Bell et al., 2004a), which in its present formulation cannot model strongly stratified conditions. Thus far, these efforts have involved detailed comparisons of test problems between the LMNA, the anelastic approximation, and traditional hydrodynamic methods in a regime for which all are valid (Almgren et al., 2006a). Rayleigh-Taylor unstable flames have also been simulated in 2D and 3D (to a limited extent), and the turbulence which naturally arises shows a Kolmogorov-like power spectrum (Bell et al., 2004c; Zingale et al., 2005). Likewise, 2D Landau-Darrieus planar flame instabilities have been investigated during the late stages of a supernovae explosion, but their

effects were found to insignificantly contribute to the energetics of the supernova (Bell et al., 2004b).

FLASH has also been used to model in 3D an entire white dwarf star during the deflagration phase of Type Ia supernovae (Calder et al., 2004). In this study, a flame is ignited off-center and evolves into a bubble, composed of heavy elements, which eventually rises to the surface of the star at supersonic speeds. The authors note that while the model does not evolve into an explosive event, the results suggest a natural mechanism of transporting iron-group elements from the core to the surface, which may help explain observational features in certain supernovae (Filippenko, 1997).

The LMNA model as presented in this thesis is capable of modeling thermonuclear events in strongly stratified environments such as found on white dwarf stars, and is thus well suited to explore the sub-sonic, incipient stages of Type Ia supernovae. For instance, the nature of compositional mixing during the incipient stages can be examined, as it may influence the nature of the subsequent explosion. Detailed understanding of this phenomenon is vital to properly interpreting observations which have important cosmological implications. The LMNA model is ideally suited to simulate the initial stages of Type Ia supernova for the investigation of the initial dynamics leading up to the main explosive event.

*Convection and Turbulence Under Strong Gravity.* Convective and turbulent phenomena are inherently complex and highly non-linear processes (Chandrasekhar, 1949; Davidson, 2004). No comprehensive theory yet exists to properly describe them. Nevertheless, these processes occur at every size-scale in physical systems, and their effects cannot be neglected when trying to understand problems in which they appear. Potentially, the LMNA model is capable of numerically calculating the effects of convection and turbulence which arise due to combustive heating under strong gravitational fields. Indeed, the above three examples (X-ray bursts, classical novae, and Type Ia supernovae) all involve convective and turbulent processes. The LMNA can be utilized to quantify and numerically analyze these processes

which may help enhance our understanding of convection and turbulence under relatively extreme, astrophysical conditions.

In its current stage of development, the LMNA model enables preliminary examination of several interesting questions involving phenomena where nuclear burning, hydrodynamics, and strong gravity all play significant roles. More fully developed, the LMNA model will allow thorough investigations into a long line of interesting and important astrophysical questions.

## Bibliography

- (2006). HDF Web page. <http://hdf.ncsa.uiuc.edu/>.
- (2006). MPI Web page. <http://www-unix.mcs.anl.gov/mpi/mpich/>.
- Abbett, W., M. Beaver, B. Davids, D. Georgobiani, P. Rathbun, and R. Stein (1997). Solar convection: Comparison of numerical simulations and mixing-length theory. *Astrophysical Journal* 480, 395–399.
- Adams, J., P. Swarztrauber, and R. Sweet (1988). *FISHPAK, A Package of Fortran Subprograms for the solution of separable elliptic partial differential equations*. Boulder, Colorado: The National Center for Atmospheric Research.
- Alexakis, A., A. Calder, and A. Heger (2004). On heavy element enrichment in classical novae. *Astrophysical Journal* 602(2), 931–937.
- Almgren, A., J. Bell, C. Rendleman, and M. Zingale (2006a). Low Mach number modeling of Type Ia supernovae. I. Hydrodynamics. *Astrophysical Journal* 637(2), 922–936.
- Almgren, A., J. Bell, C. Rendleman, and M. Zingale (2006b). Low Mach number modeling of Type Ia supernovae. II. Energy evolution. *preprint*.
- Aoki, T., T. Dotani, K. Ebisawa, M. Itoh, F. Makino, F. Nagase, T. Takeshima, T. Mihara, and S. Kitamoto (1992). Discovery of two transient X-ray sources in the Vela-Puppis region - Pulsar GS 0834-430 and burster GS 0836-429. *Publications of the Astronomical Society of Japan* 44(6), 641–647.
- Balay, S., K. Buschelman, W. D. Gropp, D. Kaushik, M. G. Knepley, L. C. McInnes, B. F. Smith, and H. Zhang (2001). PETSc Web page. <http://www.mcs.anl.gov/petsc>.
- Balay, S., K. Buschelman, W. D. Gropp, D. Kaushik, M. G. Knepley, L. C. McInnes, B. F. Smith, and H. Zhang (2004). PETSc users manual. Technical Report ANL-95/11 - Revision

- 2.1.5, Argonne National Laboratory.
- Balay, S., V. Eijkhout, W. D. Gropp, L. C. McInnes, and B. F. Smith (1997). Efficient management of parallelism in object oriented numerical software libraries. In E. Arge, A. M. Bruaset, and H. P. Langtangen (Eds.), *Modern Software Tools in Scientific Computing*, pp. 163–202. Birkhäuser Press.
- Bannon, P. R. (1996). On the Anelastic Approximation for a compressible atmosphere. *Journal of Atmospheric Sciences* 53, 3618–3628.
- Bayliss, A., G. Leaf, and B. J. Matkowsky (1992). Pulsating and chaotic dynamics near the extinction limit. *Combustion Science and Technology* 84, 253–278.
- Bell, J., M. Day, C. Rendleman, S. Woosley, and M. Zingale (2004a). Adaptive low Mach number simulations of nuclear flame microphysics. *Journal of Computational Physics* 195(2), 677–694.
- Bell, J., M. Day, C. Rendleman, S. Woosley, and M. Zingale (2004b). Direct numerical simulations of Type Ia supernovae flames. I. The Landau-Darrieus instability. *Astrophysical Journal* 606(2), 1029–1038.
- Bell, J., M. Day, C. Rendleman, S. Woosley, and M. Zingale (2004c). Direct numerical simulations of Type Ia supernovae flames. II. The Rayleigh-Taylor instability. *Astrophysical Journal* 608(2), 883–906.
- Bildsten, L. (1993). Rings of fire: Nuclear burning as the origin of sub-Hertz noise and weak X-ray bursts in accreting neutron stars. *Astrophysical Journal* 418, L21–L24.
- Bildsten, L. (1995). Propagation of nuclear burning fronts on accreting neutron stars: X-ray bursts and sub-hertz noise. *Astrophysical Journal* 438, 852–875.
- Calder, A., T. Plewa, N. Vladimirova, D. Lamb, and J. Truran (2004). Type Ia supernovae: an asymmetric deflagration model. *astro-ph/0405162v1*.
- Canuto, V. (2000). Semiconvection and overshooting: Schwarzschild and Ledoux criteria revisited. *Astrophysical Journal* 534, L113–L115.

- Chan, K. L. and S. Sofia (1986). Turbulent compressible convection in a deep atmosphere. III. Tests on the validity and limitation of the numerical approach. *Astrophysical Journal* 307, 222–241.
- Chan, K. L. and S. Sofia (1987). Validity tests of the mixing-length theory of deep convection. *Science* 235, 465–467.
- Chandrasekhar, S. (1949). Turbulence, a physical theory of astrophysical interest. *Astrophysical Journal* 110, 329–339.
- Christy, R. F. (1966). A study of pulsation in RR Lyrae models. *Astrophysical Journal* 144, 108–179.
- Clark, G. W., F. K. Li, C. Canizares, S. Hayakawa, G. Jernigan, and W. H. G. Lewin (1977). Further observations of recurrent X-ray bursts from the globular cluster NGC 6624. *Monthly Notices of the Royal Astronomical Society* 179, 651–658.
- Colella, P. and P. R. Woodward (1984). The Piecewise Parabolic Method (PPM) for gas dynamical simulations. *Journal of Computational Physics* 54, 174–201.
- Cumming, A. and L. Bildsten (2000). Rotational evolution during Type I X-ray bursts. *Astrophysical Journal* 544, 453–474.
- Davidson, P. (2004). *Turbulence* (first ed.). New York, NY: Oxford University Press.
- Deupree, R. (2000). Two-dimensional hydrodynamic simulations of zero-age main-sequence convective cores. *Astrophysical Journal* 543, 395–405.
- D.H., P. and P. Woodward (2000). Three-dimensional simulations of turbulent compressible convection. *Astrophysical Journal Supplement* 127, 159–187.
- Duorah, K. and L. Duorah (1985). Nuclear reactions on accreting neutron star surface. *Astrophysics and Space Science* 116, 97–106.
- Filippenko, A. V. (1997). Optical spectra of supernovae. *Annual Review of Astronomy and Astrophysics* 35, 309–355.
- Fryxell, B., K. Olson, P. Ricker, F. X. Timmes, M. Zingale, D. Q. Lamb, P. MacNeice, R. Rosner, J. W. Truran, and H. Tufo (2000). FLASH: An adaptive mesh hydrodynamics code

- for modeling astrophysical thermonuclear flashes. *Astrophysical Journal Supplement* 131, 273–334.
- Fryxell, B. A. and S. E. Woosley (1982). Finite propagation time in multidimensional thermonuclear runaways. *Astrophysical Journal* 261, 332–336.
- Fujimoto, M. Y. (1988). Differential rotation and elemental mixing in accreting stars. *Astronomy and Astrophysics* 198, 163–172.
- Fujimoto, M. Y. (1993). The evolution of accreting stars with turbulent mixing. *Astrophysical Journal* 419, 768–775.
- Fushiki, I. and D. Q. Lamb (1987). S-Matrix calculation of the triple-alpha reaction. *Astrophysical Journal* 317, 368–388.
- Gallagher, J. and S. Starrfield (1978). Theory and observations of classical novae. *Review of Astronomy and Astrophysics* 16, 171–214.
- Gehrzi, R., J. Truran, R. Williams, and S. Starrfield (1998). Nucleosynthesis in classical novae and its contribution to the interstellar medium. *Publications of the Astronomical Society of the Pacific* 110, 3–26.
- Glasner, S., E. Livne, and J. Truran (1997). Reactive flows in nova outbursts. *Astrophysical Journal* 475, 754–762.
- Glasner, S., E. Livne, and J. Truran (2005). The sensitivity of multidimensional nova calculations to the outer boundary condition. *Astrophysical Journal* 625, 347–350.
- Glatzmaier, G. (1984). Numerical simulations of stellar convective dynamos. I. The model and method. *Journal of Computational Physics* 55, 461–484.
- Gottwald, M., F. Haberl, A. N. Parmar, and N. E. White (1986). The bursting behavior of the transient X-ray burst source EXO 0748-676 - a dependence between the X-ray burst properties and the strength of the persistent emission. *Astrophysical Journal* 308, 213–224.
- Guerriero, R., D. W. Fox, J. Kommer, W. H. G. Lewin, R. Rutledge, C. B. Moore, E. Morgan, J. van Paradijs, M. van der Klis, L. Bildsten, and T. Dotani (1999). The evolution of Rapid Burster outbursts. *Monthly Notices of the Royal Astronomical Society* 307, 179–189.

- Hanawa, T. and M. Y. Fujimoto (1984). Thermal response of neutron stars to shell flashes. *Publications of the Astronomical Society of Japan* 36, 199–214.
- Herwig, F., B. Freytag, R. Hueckstaedt, and F. Timmes (2006). Hydrodynamic simulations of He-shell flash convection. *astro-ph/0601164v1*.
- Hoffman, J., W. Lewin, H. Marshall, F. Primini, W. Wheaton, and L. Cominsky (1978). Other X-ray burst sources. *IAU Circular* 3190, 1.
- Iben, I. (1975). Thermal pulses; p-capture, alpha-capture, s-process nucleosynthesis; and convective mixing in a star of intermediate mass. *Astrophysical Journal* 196, 525–547.
- Kercek, A., A. Hillebrandt, and J. Truran (1998). Two-dimensional simulations of the thermonuclear runaway in an accreted atmosphere of a C+O white dwarf. *Astronomy and Astrophysics* 337, 379–392.
- Kercek, A., A. Hillebrandt, and J. Truran (1999). Three-dimensional simulations of classical novae. *Astronomy and Astrophysics* 345, 831–840.
- Khokhlov, A. (1994). Supernovae deflagrations in three dimensions. *Astrophysical Journal* 424, L115–L117.
- Kim, Y., P. Fox, P. Demarque, and S. Sofia (1996). Modeling convection in the outer layers of the sun: A comparison with predictions of the mixing-length approximation. *Astrophysical Journal* 461, 499–506.
- Kippenhahn, R. and A. Weigert (1990). *Stellar Structure and Evolution* (first ed.). Berlin, Germany: Springer-Verlag.
- Kong, A. K. H., L. Homer, E. Kuulkers, P. A. Charles, and A. P. Smale (2000). X-ray/optical bursts from GS1826-24. *Monthly Notices of the Royal Astronomical Society* 311, 405–413.
- Koschmieder, E. L. (1993). *Bénard Cells and Taylor Vortices*. Cambridge, U.K.: Cambridge University Press.
- Kuhlen, M., S. Woosley, and G. Glatzmaier (2002). 3D anelastic simulation of convection in massive stars. Volume 34, pp. 954. American Astronomical Society, 200th AAS Meeting.

- Kuhlen, M., S. Woosley, and G. Glatzmaier (2003). 3D anelastic simulations of convection in massive stars. In *3D Stellar Evolution*, Volume 293, pp. 147. ASP Conference Proceedings.
- Kuhlen, M., S. Woosley, and G. Glatzmaier (2005). Carbon ignition in type Ia supernovae: II. A three-dimensional numerical model. *astro-ph/0509367*.
- Kunz, R., M. Fey, M. Jaeger, and J. W. Hammer (2002). Astrophysical reaction rates of  $^{12}C(\alpha, \gamma)^{16}O$ . *Astrophysical Journal* 567, 643–650.
- Lamb, D. Q. (2000). Some startling discoveries about X-ray bursts. *Astrophysical Journal* 127, 395–408.
- Laney, C. B. (1998). *Computational Gasdynamics*. Cambridge, U.K.: Cambridge University Press.
- Lewin, W. H. G., J. van Paradijs, L. Cominsky, and S. Holzner (1980). X-ray observations of 4U/MXB 1735-44. *Monthly Notices of the Royal Astronomical Society* 193, 15–28.
- Lewin, W. H. G., J. van Paradijs, and R. Taam (1993). *Space Science Review* 62, 223–391.
- Lewin, W. H. G., J. van Paradijs, and R. E. Taam (1995). X-ray bursts. In W. H. G. Lewin, J. V. van Paradijs, and E. P. J. van Den Heuvel (Eds.), *X-Ray Binaries*, Cambridge, U.K., pp. 175–232. Cambridge University Press.
- Lin, D. J. (2000). Preliminary study of Type I X-ray bursts using FLASH. Unpublished study.
- Livio, M. and J. Truran (1990). Elemental mixing in classical nova systems. Nonlinear astrophysical fluid dynamics. Volume 617, pp. 126–137. Proceedings of the 5th Florida Workshop in Nonlinear Astronomy, New York Academy of Sciences.
- Makishima, K., K. Mitsuda, H. Inoue, K. Koyama, M. Matsuoka, T. Murakami, M. Oda, Y. Ogawara, T. Ohashi, N. Shibasaki, Y. Tanaka, F. J. Marshall, S. Hayakawa, H. Kunieda, F. Makino, F. Nagase, Y. Tawara, S. Miyamoto, H. Tsunemi, K. Tsuno, K. Yamashita, and I. Kondo (1983). Discovery of X-ray bursts from GX 3+1/4U 1744-26. *Astrophysical Journal* 267, 310–314.

- Marshall, F. E., R. Wijnands, and M. van der Klis (1998). SAX J1808.4-3658 = XTE J1808-369. *IAU Circular 6876*, 1.
- Mathiew, J. and J. Scott (2000). *An Introduction to Turbulent Flow* (first ed.). Cambridge, U.K.: Cambridge University Press.
- Matkowsky, B. and G. Sivashinsky (1979). An asymptotic derivation of two models in flame theory associated with the constant density approximation. *SIAM Journal of Applied Mathematics 37*, 686–699.
- McGrattan, K. B., H. Baum, R. Rehm, A. Hamins, G. Forney, J. Floyd, and S. Hostikka (2004). *Fire Dynamics Simulator* (NISTIR 1081 ed.). U.S. Department of Commerce: National Institute of Standards and Technology.
- Merryfield, W. (1995). Hydrodynamics of semiconvection. *Astrophysical Journal 444*, 318–337.
- Miller, M. C., F. K. Lamb, and D. Psaltis (1998). Sonic-point model of kilohertz quasi-periodic brightness oscillations in low-mass X-ray binaries. *Astrophysical Journal 508*, 791–830.
- Miralles, J., J. Pons, and V. Urpin (2000). Convective instability in proto-neutron stars. *Astrophysical Journal 543*, 1001–1006.
- Miralles, J., V. Urpin, and K. Van Riper (1997). Convection in the surface layers of neutron stars. *Astrophysical Journal 480*, 358–363.
- Muno, M. P., D. W. Fox, E. H. Morgan, and L. Bildsten (2000). Nearly coherent oscillations in Type-I X-ray bursts from KS 1731-260. *Astrophysical Journal 542*, 1016–1033.
- Nozakura, T., S. Ikeuchi, and M. Fujimoto (1984). Lateral propagation of the helium shell flash on an accreting neutron star. *Astrophysical Journal 286*, 221–231.
- Ogura, Y. and N. A. Phillips (1962). Scale analysis of deep and shallow convection in the atmosphere. *Journal of Atmospheric Science 19*, 173–179.
- Peng, F., E. Brown, F. Timmes, and J. Truran (2003). Unstable H/He burning on accreting neutron stars. pp. 2003HEAD, 7.1718P. American Astronomical Society HEAD Meeting

- 7, 17.8.
- Press, W. H., S. A. Teukolsky, W. T. Vellerling, and B. P. Flannery (1992). *Numerical Recipes in FORTRAN* (second ed.). Cambridge, U.K.: Cambridge University Press.
- Psaltis, D. and D. Chakrabarty (1999). The disk-magnetosphere interaction in the accretion-powered milisecond pulsar. *Astrophysical Journal* 521, 332–340.
- Smale, A. P. (1998). A Type I Burst with radius expansion observed from Cygnus X-2 with the Rossi X-Ray Timing Explorer. *Astrophysical Journal* 498, L141–L145.
- Spiegel, E. (1963). A generalization of the mixing-length theory of turbulent convection. *Astrophysical Journal* 138, 216–225.
- Spiegel, E. and G. Veronis (1959). On the Boussinesq approximation for a compressible fluid. *Astrophysical Journal* 131, 442–447.
- Spitkovsky, A., Y. Levin, and G. Ushomirsky (2002). Propagation of thermonuclear flames on rapidly rotating neutron stars: Extreme weather during Type-I X-ray bursts. *Astrophysical Journal* 566, 1018–1038.
- Spruit, H. C. and E. Knobloch (1984). Baroclinic instability in stars. *Astronomy and Astrophysics* 132(1), 89–96.
- Starrfield, S., W. Hix, C. Iliadis, F. Timmes, and W. Sparks (2004). The effects of improvements in the nuclear reaction rates on hydrodynamic simulations of the classical nova outburst. pp. 2005AAS, 207.7024S. American Astronomical Society Meeting 207, 70.24.
- Starrfield, S., W. Sparks, and J. Truran (1985). Recurrent novae as a consequence of the accretion of solar material onto a 1.38 solar mass white dwarf: Evidence for rotational modulation. *Astrophysical Journal* 291, 136–146.
- Starrfield, S., W. Sparks, and J. Truran (1986). Hydrodynamic models for novae with ejecta rich in oxygen, neon, and magnesium. *Astrophysical Journal* 303, L5–L9.
- Starrfield, S., J. Truran, and W. Sparks (2000). The nova outburst: Thermonuclear runaways on degenerate dwarfs. *New Astronomy Reviews* 44, 81–86.

- Steffen, M. and S. Jordan (2001). *Numerical simulation of stellar convection: Comparison with mixing-length theory*. Bristol, U.K.: Institute of Physics Publishing.
- Strohmayer, T. E. (2001). X-ray observations of neutron star binaries: Evidence for millisecond spins. In *Astrophysical sources for ground-based gravitational wave detectors*, pp. 2001AIPC..575..273S. American Institute of Physics.
- Strohmayer, T. E., W. Zhang, and J. H. Swank (1997). 363 Hz oscillations during the rising phase of bursts from 4U 1728-34: Evidence for rotational modulation. *Astrophysical Journal* 487, L77–L80.
- Strohmayer, T. E., W. Zhang, J. H. Swank, N. E. White, and I. Lapidus (1998). On the amplitude of burst oscillations in 4U 1636-54: Evidence for nuclear-powered pulsars. *Astrophysical Journal* 498, L135–L139.
- Taam, R. E. (1980). X-ray bursts from thermonuclear runaways on accreting neutron stars. *Astrophysical Journal* 241, 358–366.
- Taam, R. E. (1985). Nuclear processes at neutron star surfaces. *Annual Review of Nuclear and Particle Science* 35, 1–23.
- Taam, R. E., A. Baylis, and E. L. Sandquist (2000). Unpublished study.
- Tawara, Y., T. Hirano, T. Kii, M. Matsuoka, and T. Murakami (1984). Long X-ray burst from GX 17+2. *Publications of the Astronomical Society of Japan* 36(4), 861–867.
- Timmes, F. X. and F. D. Sweaty (2000). The accuracy, consistency, and speed of an electron-positron equation of state based on table interpolation of the Helmholtz free energy. *The Astrophysical Journal Supplement Series* 126, 501–516.
- Urpin, V. (2005). Instabilities, turbulence, and mixing in the ocean of accreting neutron stars. *Astronomy and Astrophysics* 438(2), 643–651.
- van der Klis, M., F. Jansen, J. van Paradijs, M. Lewin, W. H. G.; Sztajno, and J. Truemper (1987). Correlation between spectral state and quasi-periodic oscillation parameters in GX 5-1. *Astrophysical Journal* 313, L19–L23.

- van Paradijs, J., W. Penninx, W. H. G. Lewin, M. Sztajno, and J. Truemper (1988). The recurrence behaviour of X-ray bursts from 4U/MXB 1735-44. *Astronomy and Astrophysics* 192(1-2), 147–152.
- Weaver, T. A., G. B. Zimmerman, and S. E. Woosley (1978). Presupernova evolution of massive stars. *Astrophysical Journal* 225, 1021–1029.
- Wijnands, R., T. Strohmayer, and L. M. Frankco (2000). Discovery of nearly coherent oscillations with a frequency of 567 Hz during Type-I X-ray bursts of the x-ray transient and eclipsing binary X 1658-298. In *HEAD Meeting Number 32*, pp. Abstract 44.08. American Astronomical Society.
- Wijnands, R. and M. van der Klis (1998). A millisecond pulsar in an X-ray binary system. *Nature* 394, 344–346.
- Woosley, S. E. and T. A. Weaver (1985). pp. 115, 273. AIP Conference Proceedings.
- Zingale, M., F. Timmes, B. Fryxell, D. Lamb, K. Olson, A. Calder, L. Dursi, P. Ricker, R. Rosner, P. MacNeice, and H. Tufo (2001). Helium detonations on neutron stars. *Astrophysical Journal Supplement* 133(1), 195–220.
- Zingale, M., S. Woosley, A. Cumming, A. Calder, L. Dursi, F. B., P. Ricker, R. Rosner, and T. F.X. (2002). Investigations of pointwise ignition of helium deflagrations on neutron stars. pp. astro-ph/0211336. 3D Stellar Evolution Workshop.
- Zingale, M., S. Woosley, C. Rendleman, M. Day, and J. Bell (2005). Three-dimensional numerical simulations of Rayleigh-Taylor unstable flames in Type Ia supernovae. *Astrophysical Journal* 632, 1021–1034.

## APPENDIX A

**List of Symbols, Abbreviations, and Physical Constants****A.1. Definition of Symbols**

$t$	= time
$dt$	= time-step
$dt_{CFL}$	= Courant-Friedrichs-Lowy time-step
$x$	= a lateral direction (along with $y$ )
$y$	= a lateral direction (along with $x$ )
$z$	= the vertical direction (in line with gravity)
$dr$	= general spatial interval (in components, $dx$ , $dy$ , and $dz$ )
$i$	= index for the discretized $x$ direction
$j$	= index for the discretized $y$ direction
$k$	= index for the discretized $z$ direction
$\frac{D}{Dt}$	= the material derivative = $\frac{\partial}{\partial t} + \vec{v} \cdot \nabla$
$\vec{v}$	= velocity field
$u$	= $x$ component of velocity
$v$	= $y$ component of velocity
$w$	= $z$ component of velocity
$u'$	= $x$ component of perturbed velocity
$v'$	= $y$ component of perturbed velocity
$w'$	= $z$ component of perturbed velocity
$U$	= velocity correlation in $x$
$V$	= velocity correlation in $y$
$W$	= velocity correlation in $z$

$\rho$	= total density
$\rho_h$	= density of the hydrostatic base state
$\rho'$	= perturbed density
$P$	= total pressure
$P_h$	= pressure of the hydrostatic base state
$P'$	= perturbed pressure
$T$	= total temperature
$T_h$	= temperature of the hydrostatic base state
$T'$	= perturbed temperature
$e$	= specific internal energy
$F_{adv}$	= advective flux
$F_{nuc}$	= nuclear flux
$F_{rad}$	= radiative flux
$S$	= total entropy
$X$	= species mass abundance array
$X_l$	= mass fraction of the gas of element $l$
$Y$	= mass fraction of helium (He4)
$R$	= sum of the rate of all production and depletion of all species
$R_l$	= the rate of production and depletion of species $l$
$Q$	= rate of energy generation per unit volume
$\dot{s}$	= rate of energy generation per unit volume per unit mass = $\frac{Q}{\rho}$
$g$	= magnitude of the gravitational acceleration
$\vec{g}$	= gravitational acceleration = $-g\hat{k}$
$K$	= vertical density function = $\int^z \rho'(x, y, z') dz'$
$\phi$	= the potential-like function = $P' \pm gK$
$c_p$	= specific heat at constant pressure
$c_v$	= specific heat at constant volume

$\gamma$	= ratio of specific heats = $\left(\frac{d \ln P}{d \ln \rho}\right)_s = \frac{c_p}{c_v}$
$\delta$	= thermodynamic coefficient in energy equation = $-\left(\frac{\partial \ln \rho}{\partial \ln T}\right)_P$
$\kappa_o$	= radiative opacity
$\kappa(\rho, T, X_l)$	= radiative thermal conductivity = $\frac{4}{3} \frac{acT^3}{\kappa_o \rho}$
$\kappa_s$	= sub-grid scale eddy diffusivity
$\vec{f}$	= diffusive flux associated with sub-grid resolutions = $\nabla S$
$\mu$	= total mean molecular weight
$\mu_e$	= mean molecular weight per electron
$\mu_i$	= mean molecular weight per ion
$\alpha$	= degeneracy parameter = $-\eta = -\frac{\mu}{kT}$ , (where $\mu$ is the chemical potential)
$\dot{m}$	= local mass accretion rate per unit area
$H_P$	= pressure scale height
$\nabla$	= actual temperature gradient = $\left(\frac{d \ln T}{d \ln P}\right)_{actual}$
$\nabla_{ad}$	= adiabatic temperature gradient = $\left(\frac{d \ln T}{d \ln P}\right)_S$
$\nabla_L$	= Ledoux temperature gradient = $\nabla_{ad} + \frac{c_1}{c_2} \nabla_\mu$
$\nabla_\mu$	= actual composition gradient = $\left(\frac{d \ln \mu}{d \ln P}\right)_{actual}$
$c_1$	= Ledoux gradient coefficient 1 = $\left(\frac{\partial \ln \rho}{\partial \ln \mu}\right)_{P,T}$
$c_2$	= Ledoux gradient coefficient 2 = $-\left(\frac{\partial \ln \rho}{\partial \ln T}\right)_{P,\mu}$

## A.2. Abbreviations

AA	= anelastic approximation
BA	= Boussinesq approximation
CFL	= Courant-Friedrichs-Lowy (stability constraint on the time-step)
$d(T)$	= fractional difference in $T$ compared to the lateral average
$d(Y)$	= fractional difference in $Y$ compared to the lateral average
EGR	= energy generation rate = $\dot{s}$
HSE	= hydrostatic equilibrium

LMNA	= Low Mach Number Approximation
$M$	= Mach Number = local flow speed / local sound speed
$No - K$	= hydrodynamic model which does not use the $K$ formalism
SAd	= adiabatic-excess = $\Delta \nabla = \nabla - \nabla_{ad}$
SLed	= Ledoux-excess = $\Delta \nabla_L = \nabla - \nabla_L$

### A.3. Physical Constants

$m_p$	= proton mass = $1.6726231 \times 10^{-24}$ g
$M_u$	= the mass of 1 amu = $1.6605402 \times 10^{-24}$ g
$N_A$	= Avogadro's number = $\frac{1}{M_u} = 6.0221367 \times 10^{23}$ mole $^{-1}$
$k$	= Boltzmann constant = $1.380658 \times 10^{-16}$ erg K $^{-1}$
$\mathcal{R}$	= universal gas constant = $\mu(c_p - c_v) = 8.314510 \times 10^7$ erg mole $^{-1}$ K $^{-1}$
$a$	= radiation constant = $7.56591 \times 10^{-15}$ erg cm $^{-3}$ K $^{-4}$
$c$	= speed of light = $2.99792458 \times 10^{10}$ cm s $^{-1}$
$\sigma$	= Stefan-Boltzmann constant = $\frac{ac}{4} = 5.67051 \times 10^{-5}$ erg cm $^{-2}$ sec $^{-1}$ K $^{-4}$
$G$	= gravitational constant = $6.67259 \times 10^{-8}$ dyne cm $^2$ g $^{-2}$
$M_\odot$	= solar mass = $1.989 \times 10^{33}$ g
$M_{NS}$	= neutron star mass = $1.4 M_\odot$
$R_{NS}$	= neutron star radius = $1.0 \times 10^6$ cm
$g_{NS}$	= $g$ on the surface of a neutron star = $\frac{GM_{NS}}{R_{NS}^2} = 2 \times 10^{14}$ cm s $^{-2}$
$Q_{3\alpha}$	= energy release during the $3\alpha$ reaction = 7.274 MeV

## APPENDIX B

### The Numerical Procedure for the Low Mach Number Approximation

In this appendix, the numerical procedure for the Low Mach Number Approximation is detailed to supplement Chapter 2, which offers a more general discussion about the rationale for using the LMNA. To enhance readability, the expressions in this appendix are given in differential form. Appendix E explains how the differential expressions are numerically differenced. For generality, the equations in this appendix are expressed in 3D. The present LMNA model is limited to 2D, where the lateral dimension is  $y$  or  $j$ , and the vertical dimension is  $z$  or  $k$ . Appendix A defines all the symbols which are used.

At time  $t = n$  in zone  $i, j, k$ , the variables are:

$$\rho_{(i,j,k)}^{(n)}, e_{(i,j,k)}^{(n)}, P_{(i,j,k)}^{(n)}, T_{(i,j,k)}^{(n)}, X_{(i,j,k)}^{(n)}, \vec{v}_{(i,j,k)}^{(n)}$$

#### B.1. Composition $X_{(i,j,k)}^{(n+1)}$ and Total Reaction Rate $R_{(i,j,k)}^{(n+1)}$

The continuity equation for each species  $l$  in conservative form is:

$$(B.1) \quad \frac{\partial(\rho X_l)}{\partial t} + \nabla \cdot (\rho \vec{v} X_l) = \rho R_l$$

$R_l$  is the Lagrangian time derivative of species  $l$ :  $R_l \equiv \frac{DX_l}{Dt}$ .

Expand and use the continuity equation,  $\frac{\partial \rho}{\partial t} + \nabla \cdot (\rho \vec{v}) = 0$ , to find the non-conservative form of the composition equation:

$$(B.2) \quad \frac{\partial X_l}{\partial t} = -\vec{v} \cdot \nabla X_l + R_l$$

Operator split this step into two operations:

**B.1.1. Advect Composition:** First, advect by upwinding (Appendix E) to a half step,

$t = n + \frac{1}{2}$ , neglecting the burning rate  $R_l$ .

$$(B.3) \quad \begin{aligned} \frac{\partial X_l}{\partial t} &= -\vec{v} \cdot \nabla X_l \\ &= -\left(u \frac{\partial X_l}{\partial x} + v \frac{\partial X_l}{\partial y} + w \frac{\partial X_l}{\partial z}\right) \end{aligned}$$

Hence,

$$(B.4) \quad X_{l(i,j,k)}^{(n+\frac{1}{2})} = X_{l(i,j,k)}^{(n)} - \Delta t \left(u \frac{\partial X_l}{\partial x} + v \frac{\partial X_l}{\partial y} + w \frac{\partial X_l}{\partial z}\right)$$

**B.1.2. Burn.** Next, use  $X_{l(i,j,k)}^{(n+\frac{1}{2})}, \rho_{(i,j,k)}^{(n)}, T_{(i,j,k)}^{(n)}$  in the  $3\alpha$  burner to obtain the updated composition,  $X_{l(i,j,k)}^{(n+1)}$  and  $R_{l(i,j,k)}^{(n+1)}$ , where

$$(B.5) \quad R_l^{(n+1)} \left(X_l^{(n+\frac{1}{2})}, \rho^{(n)}, T^{(n)}\right) = \frac{X_{l(i,j,k)}^{(n+1)} - X_{l(i,j,k)}^{(n+\frac{1}{2})}}{\Delta t}$$

The combustive process is the  $3\alpha$  reaction ( $3\frac{4}{2}He \rightarrow \frac{12}{6}C$ ), where two species are considered,  $\frac{4}{2}He$  and  $\frac{12}{6}C$ .



The energy generation rate is obtained from the S-matrix calculations of Fushiki and Lamb (1987). In cgs units ( $\text{erg g}^{-1}\text{s}^{-1}$ ), the energy generation rate for this process is:

$$(B.8) \quad \dot{s}_{3\alpha} = 5.120 \times 10^{29} Y^3 \rho_6^2 G1(T_6, \rho_6) G2(T_6, \rho_6)$$

where  $T_6$  is the temperature in units of  $10^6 \text{K}$ ,  $\rho_6$  is the density in units of  $10^6 \text{g cm}^{-3}$ , and  $Y$  is the helium mass abundance. The functions  $G1$  and  $G2$  correspond to the reactions B.6 and B.7, and involve screening factors. See Fushiki and Lamb (1987) for details. For comparison, the classical energy generation rate for the  $3\alpha$  reaction in cgs units is:

$$(B.9) \quad (\dot{s}_{3\alpha})_{classical} = 5.120 \times 10^{29} Y^3 \frac{\rho_6^2}{T_6^3} e^{-\frac{4401.5}{T_6}}$$

The ash of the  $3\alpha$  reaction is  $^{12}_6C$ , and its concentration rises as helium burning progresses. Consequently, further  $\alpha$  captures may commence to form heavier nuclei:



The energy released in these reactions are not included in the current calculation. As demonstrated in Section 6.1 of Chapter 6, the energy generation rate is dominated by  $\dot{s}_{3\alpha}$  before the peak of the burst, but after burst peak, subsequent reactions involving  ${}^{12}_6C$  and  ${}^{16}_8O$  in Equations B.10 and B.11 need to be considered to account for the total energy generated during helium burning.

In general, any appropriate combustive process could be implemented for the burner, and future work with the LMNA model may involve using different nuclear reaction networks, as proposed in Chapter 6.

**B.2. Temperature  $T_{(i,j,k)}^{(n+1)}$** 

It can be shown that the conservative form of the equation of internal energy can be expressed in the following equivalent forms:

$$\begin{aligned}
 \rho \frac{De}{Dt} - \frac{P}{\rho} \frac{D\rho}{Dt} &= \frac{\partial(\rho e)}{\partial t} + \nabla \cdot [(\rho e + P) \vec{v}] - \vec{v} \cdot \nabla P \\
 &= \rho c_p \frac{DT}{Dt} - \delta \frac{DP}{Dt} \\
 (B.12) \quad &= \rho c_p \frac{\partial T}{\partial t} + \rho c_p \vec{v} \cdot \nabla T - \delta \frac{\partial P}{\partial t} - \delta \vec{v} \cdot \nabla P
 \end{aligned}$$

where  $\delta$  is defined as:

$$\begin{aligned}
 \delta &\equiv - \left( \frac{\partial \ln \rho}{\partial \ln T} \right)_P \\
 &= - \frac{T}{\rho} \left( \frac{\partial \rho}{\partial T} \right)_P \\
 (B.13) \quad &= \frac{T}{\rho} \frac{\left( \frac{\partial P}{\partial T} \right)_\rho}{\left( \frac{\partial P}{\partial \rho} \right)_T}
 \end{aligned}$$

where  $\left( \frac{\partial \rho}{\partial T} \right)_P = - \frac{\left( \frac{\partial P}{\partial T} \right)_\rho}{\left( \frac{\partial P}{\partial \rho} \right)_T}$  can be straightforwardly derived using the Maxwell relations of thermodynamic partial derivatives. Note that for an ideal gas,  $\delta = +1$ , but  $\delta$  must be explicitly evaluated using partial derivatives from the equation-of-state for a general gas.

In the LMNA, pressure is assumed to be constant only in time, and so  $\frac{\partial P}{\partial t}$  in the energy equation can be neglected. Then, the energy equation for the LMNA becomes:

$$(B.14) \quad \rho \frac{De}{Dt} - \frac{P}{\rho} \frac{D\rho}{Dt} = \rho c_p \frac{\partial T}{\partial t} + \rho c_p \vec{v} \cdot \nabla T - \delta \vec{v} \cdot \nabla P$$

Equate the right-hand-side to the source terms to find the temperature equation:

$$(B.15) \quad \rho c_p \frac{\partial T}{\partial t} + \rho c_p \vec{v} \cdot \nabla T - \delta \vec{v} \cdot \nabla P = Q + \nabla \cdot \kappa \nabla T$$

Hence,

$$(B.16) \quad \begin{aligned} \frac{\partial T}{\partial t} &= \frac{1}{c_p} \left( \frac{Q}{\rho} + \frac{1}{\rho} \nabla \cdot \kappa \nabla T - c_p \vec{v} \cdot \nabla T + \frac{\delta}{\rho} \vec{v} \cdot \nabla P \right) \\ &= -\vec{v} \cdot \nabla T + \frac{1}{c_p} \left( \dot{s} - \frac{\delta}{\rho} w \rho_h g + \frac{1}{\rho} \nabla \cdot \kappa \nabla T \right) \end{aligned}$$

where hydrostatic equilibrium  $\nabla P_h = -\rho_h g$  is used to simplify the pressure gradient term.

To update  $T$ , the temperature equation is operator split into separate steps. The advection term is upwinded, while the thermal diffusion term is calculated as two first-order central differences over one zone: i) to determine the negative of the thermal flux  $-F = \kappa \nabla T$  at the edges of a computational zone, and ii) to evaluate  $\nabla \cdot (-F)$  at the zone center (Appendix E).

For the thermal diffusion term,  $\kappa(\rho, T, X_l)$ , the radiative thermal conductivity, is found using the conductivity routine from FLASH (Fryxell et al., 2000). The expression for  $\kappa$  is:

$$(B.17) \quad \kappa = \frac{4}{3} \frac{acT^3}{\kappa_o \rho}$$

where  $\kappa_o(\rho, T, X_l)$  is the radiative opacity, calculated from analytical expressions as referenced in Iben (1975), Christy (1966), and Weaver (1978).

### B.3. Density $\rho_{(i,j,k)}^{(n+1)}$

Having updated  $X_{(i,j,k)}^{(n+1)}$  and  $T_{(i,j,k)}^{(n+1)}$ , and assuming  $P_{(i,j,k)}^{(n+1)} = P_{(i,j,k)}^{(n)}$  the equation of state (EOS)  $F(T, P_h, X_l)$  is used to update density. The internal energy  $e_{(i,j,k)}^{(n+1)}$  can be obtained in like fashion.

$$(B.18) \quad \begin{aligned} \rho_{(i,j,k)}^{(n+1)} &\Leftarrow F(T, P_h, X_l) \\ e_{(i,j,k)}^{(n+1)} &\Leftarrow F(T, P_h, X_l) \end{aligned}$$

The Helmholtz EOS (Timmes and Swesty, 2000) requires  $\rho$  and another thermodynamic quantity ( $T$ ,  $P$ , or  $e$ ) as inputs. Since  $\rho$  in this procedure is what is desired from the EOS, a Newton-Raphson convergence routine in the EOS is necessary to converge on the correct  $\rho$ . That is, given a desired temperature and pressure, find a density which is consistent. The pressure is used as the convergence variable in this routine.

Consider  $P$  as a function of  $\rho$  and  $T$ :

$$(B.19) \quad \begin{aligned} P(\rho, T) &= P_g + \left. \frac{\partial P}{\partial \rho} \right|_T d\rho \\ &= P_o \end{aligned}$$

where  $P_o$  is the desired pressure and  $P_g$  is the guessed value, in practice, that returned by the EOS.

Solving for  $d\rho$ :

$$(B.20) \quad d\rho = \frac{P_o - P_g}{\left. \frac{\partial P}{\partial \rho} \right|_T}$$

Then,

$$(B.21) \quad \rho_{new} = \rho_g + d\rho$$

The Newton-Raphson procedure is:

Coming into the procedure, we have an updated temperature and a desired pressure, which is the constant hydrostatic pressure  $P_o = P_h$ .

- (1) Give the EOS a guess for density  $\rho$  with the updated temperature. The initial guess is the value of density from the previous time step.
- (2) From the EOS is returned a pressure  $P_g$ .
- (3) Test whether the returned pressure is close to within a certain convergence factor of the desired pressure. That is, evaluate the error  $= \left| \frac{P_o - P_g}{P_o} \right|$ . If the error is less than the convergence factor, then  $\rho_g$  is the correct density. If the error is greater than the convergence factor, proceed to the next step.
- (4) Use the value  $P_g$  to find  $d\rho$ , using the thermodynamic partial derivative  $\frac{\partial P}{\partial T}|_\rho$  which is returned from the EOS.
- (5) Find a new density,  $\rho_{new}$ .
- (6) Go back to step 1 using this new density as the next guess for density.
- (7) Iterate these steps until the convergence criteria in Step 3 is met, or until a maximum number of iteration steps. If convergence is not achieved within a certain, maximum number of steps, stop the program and print an error message. If the error exceeds a critical value, stop the code.

## B.4. Elliptic Equation

From the momentum equation,

$$\begin{aligned}
 \rho \frac{D\vec{v}}{Dt} + \nabla P' &= \rho' \vec{g} \\
 (\nabla P' - \rho' \vec{g}) &= -\rho \frac{D\vec{v}}{Dt} \\
 \nabla(P' \pm gK) &= -\rho \frac{D\vec{v}}{Dt} \pm \left\{ \frac{\partial(gK)}{\partial x} \hat{i} + \frac{\partial(gK)}{\partial y} \hat{j} \right\} \\
 \nabla\phi &= -\rho \frac{D\vec{v}}{Dt} \pm \left\{ \frac{\partial(gK)}{\partial x} \hat{i} + \frac{\partial(gK)}{\partial y} \hat{j} \right\}
 \end{aligned} \tag{B.22}$$

where a potential-like term,  $\phi \equiv P' \pm gK$  is introduced, which includes the special density function,  $K \equiv \int^z \rho'(x, y, z') dz'$ . The right-hand-side of the equation is augmented accordingly with the lateral derivatives of  $K$ . Depending on the direction in which the integral is taken to evaluate  $K$ , the sign for its lateral derivatives is either positive or negative. The positive sign is taken when the integration begins from the bottom of the domain upward, and the negative sign, from the top of the domain downward. See Appendix C for more details about the  $K$  function.

Taking the divergence,

$$(B.23) \quad \begin{aligned} \nabla \cdot (\nabla \phi) &= -\nabla \cdot \left( \rho \frac{D\vec{v}}{Dt} \right) \pm \nabla \cdot \left\{ \frac{\partial(gK)}{\partial x} \hat{i} + \frac{\partial(gK)}{\partial y} \hat{j} \right\} \\ \nabla^2 \phi &= -\nabla \cdot \left( \rho \frac{D\vec{v}}{Dt} \right) \pm \left\{ \frac{\partial^2(gK)}{\partial x^2} + \frac{\partial^2(gK)}{\partial y^2} \right\} \end{aligned}$$

Using the definition of the material derivative  $\frac{D}{Dt} = \frac{\partial}{\partial t} + \vec{v} \cdot \nabla$  and the identity  $\frac{D\rho}{Dt} = -\rho \nabla \cdot \vec{v}$ , which is easily derived from the continuity equation,  $\rho \frac{D\vec{v}}{Dt}$  can be expressed as:

$$(B.24) \quad \begin{aligned} \rho \frac{D\vec{v}}{Dt} &= \frac{D(\rho\vec{v})}{Dt} - \vec{v} \frac{D\rho}{Dt} \\ &= \frac{\partial(\rho\vec{v})}{\partial t} + \vec{v} \cdot \nabla(\rho\vec{v}) + \vec{v} \rho \nabla \cdot \vec{v} \\ &= \frac{\partial(\rho\vec{v})}{\partial t} + \nabla \cdot (\rho\vec{v}\vec{v}) \end{aligned}$$

By considering its parts and then taking the divergence, a relatively simple and symmetric expression is obtained for  $\nabla \cdot \{\nabla \cdot (\rho\vec{v}\vec{v})\}$ :

$$\begin{aligned}
\nabla \cdot \{\nabla \cdot (\rho \vec{v} \vec{v})\} &= \frac{\partial^2(\rho u^2)}{\partial x^2} + \frac{\partial^2(\rho v^2)}{\partial y^2} + \frac{\partial^2(\rho w^2)}{\partial z^2} \\
&\quad + \frac{\partial}{\partial x} \frac{\partial(\rho uv)}{\partial y} + \frac{\partial}{\partial x} \frac{\partial(\rho uw)}{\partial z} \\
&\quad + \frac{\partial}{\partial y} \frac{\partial(\rho vu)}{\partial x} + \frac{\partial}{\partial y} \frac{\partial(\rho vw)}{\partial z} \\
&\quad + \frac{\partial}{\partial z} \frac{\partial(\rho wu)}{\partial x} + \frac{\partial}{\partial z} \frac{\partial(\rho ww)}{\partial y} \\
(B.25) \qquad \qquad \qquad &= C.T.
\end{aligned}$$

where  $C.T.$  stands for “convective terms.”

Thus, using the continuity equation,  $\nabla \cdot (\rho \frac{D\vec{v}}{Dt})$  can be expressed as:

$$\begin{aligned}
\nabla \cdot \left( \rho \frac{D\vec{v}}{Dt} \right) &= \nabla \cdot \left\{ \frac{\partial(\rho \vec{v})}{\partial t} + \nabla \cdot (\rho \vec{v} \vec{v}) \right\} \\
&= \nabla \cdot \frac{\partial(\rho \vec{v})}{\partial t} + \nabla \cdot \{\nabla \cdot (\rho \vec{v} \vec{v})\} \\
&= \frac{\partial \nabla \cdot (\rho \vec{v})}{\partial t} + \nabla \cdot \{\nabla \cdot (\rho \vec{v} \vec{v})\} \\
(B.26) \qquad \qquad \qquad &= -\frac{\partial^2 \rho}{\partial t^2} + C.T.
\end{aligned}$$

Putting all the pieces together, the Laplacian of  $\phi$  becomes:

$$(B.27) \qquad \nabla^2 \phi = -\nabla \cdot \left( \rho \frac{D\vec{v}}{Dt} \right) \pm \left\{ \frac{\partial^2(gK)}{\partial x^2} + \frac{\partial^2(gK)}{\partial y^2} \right\}$$

$$(B.28) \qquad = \frac{\partial^2 \rho}{\partial t^2} - C.T. \pm \left\{ \frac{\partial^2(gK)}{\partial x^2} + \frac{\partial^2(gK)}{\partial y^2} \right\}$$

This is the elliptic equation for  $\phi$  which is solved using FISHPAK, a package of FORTRAN subprograms for the solution of separable, elliptic partial differential equations (Adams et al., 1988).

The terms on the right-hand-side of the elliptic equation (Equation B.27) are evaluated as follows: (Appendix E explains the methods used in numerical differencing.)

- 1) using the continuity equation, the time derivative of  $\frac{\partial^2 \rho}{\partial t^2}$  is expressed as:

$$(B.29) \quad \frac{\partial^2 \rho}{\partial t^2} = \frac{1}{\Delta t} \left[ \left( \frac{\partial \rho}{\partial t} \right)^{n+1} + \nabla \cdot (\rho \vec{v})^n \right]$$

where at time-level  $n+1$ ,  $\frac{\partial \rho}{\partial t}^{n+1}$  is calculated analytically (see Appendix D), and at time-level  $n$ ,  $\nabla \cdot (\rho \vec{v})^n$  is centrally differenced over two zones;

- 2) each second-order convective term is calculated as two first-order derivatives: i) up-winding is used first to obtain the terms in  $\nabla \cdot (\rho \vec{v} \vec{v})$ , and ii) these terms are then centrally differenced over one zone to obtain the final expressions in  $\nabla \cdot \{ \nabla \cdot (\rho \vec{v} \vec{v}) \}$ ;
- 3) the second-order lateral derivatives of  $gK$  are centrally differenced.

Test runs have been performed to show that using numerical versus analytical forms of  $\frac{\partial \rho}{\partial t}$  does not significantly change the results. While the analytical form is more computationally expensive, since it requires multiple calls to the EOS, it is used in the computations in this report, primarily because the analytical expression involves another instance where the low Mach number approximation ( $\frac{\partial P}{\partial t} = 0$ ) can be explicitly included. See Appendix D for details regarding analytically evaluating  $\frac{\partial \rho}{\partial t}$ .

**B.4.1. Modification to impose lateral homogeneity.** To reduce round-off errors in the solutions from the elliptic solver in the 2D calculations, a numerical procedure is used to modify the right-hand-side of the elliptic equation. Its implementation helps to sustain lateral homogeneity of the results when the domain is completely laterally homogeneous, such as in the test case when no perturbation is applied. Without this procedure, an initially laterally homogeneous domain would break lateral symmetry due to the inherent round-off errors of the elliptic solver, consequently developing asymmetric dynamical motions. Even when a perturbation is applied, the procedure is still included in the calculation to help minimize potential artifacts resulting from the same kind of round-off errors of the elliptic solver.

Let the elliptic equation be written as

$$(B.30) \quad A\phi = b$$

where  $A$  is a matrix,  $\phi$  is the desired solution vector, and  $b$  is the right-hand-side of the elliptic equation, a vector over the 2D grid. Considering  $b$ , it is clear that

$$(B.31) \quad b = (b - bm) + bm$$

where  $bm$  is the lateral mean of  $b$  for every vertical row of zones. By definition,  $bm$  is completely laterally homogeneous. Proceed to solve the system of equations twice:

$$(B.32) \quad \begin{aligned} A\phi_1 &= (b - bm) \\ A\phi_2 &= bm \end{aligned}$$

While  $\phi_2$  will always be laterally homogeneous to the accuracy of the computer, it can be redefined to be completely laterally homogeneous to ensure strict lateral homogeneity. Then, the desired  $\phi$  is determined by simply summing the two solutions:

$$(B.33) \quad \phi = \phi_1 + \phi_2$$

Note that this procedure ensures that lateral homogeneity will be preserved to machine accuracy when the domain is completely laterally homogeneous. Moreover, even when lateral inhomogeneities are present, using this procedure will help minimize round-off errors and potential artifacts due to the inherent limitations of the elliptic solver.

**B.5. Velocity**  $\vec{v}_{(i,j,k)}^{(n+1)}$ 

From the momentum equation,

$$\begin{aligned}
 \nabla\phi &= -\rho \frac{D\vec{v}}{Dt} \pm \left\{ \frac{\partial(gK)}{\partial x} \hat{i} + \frac{\partial(gK)}{\partial y} \hat{j} \right\} \\
 \rho \frac{D\vec{v}}{Dt} &= -\nabla\phi \pm \left\{ \frac{\partial(gK)}{\partial x} \hat{i} + \frac{\partial(gK)}{\partial y} \hat{j} \right\} \\
 \frac{\partial(\rho\vec{v})}{\partial t} + \nabla \cdot (\rho\vec{v}\vec{v}) &= -\nabla\phi \pm \left\{ \frac{\partial(gK)}{\partial x} \hat{i} + \frac{\partial(gK)}{\partial y} \hat{j} \right\} \\
 (B.34) \quad \frac{\partial(\rho\vec{v})}{\partial t} &= -\nabla \cdot (\rho\vec{v}\vec{v}) - \nabla\phi \pm \left\{ \frac{\partial(gK)}{\partial x} \hat{i} + \frac{\partial(gK)}{\partial y} \hat{j} \right\}
 \end{aligned}$$

Solving each component updates the velocity:

**B.5.1. x component: u.**

$$(B.35) \quad \frac{\partial(\rho u)}{\partial t} = - \left\{ \frac{\partial(\rho uu)}{\partial x} + \frac{\partial(\rho uv)}{\partial y} + \frac{\partial(\rho uw)}{\partial z} \right\} - \frac{\partial\phi}{\partial x} \pm \frac{\partial(gK)}{\partial x}$$

**B.5.2. y component: v.**

$$(B.36) \quad \frac{\partial(\rho v)}{\partial t} = - \left\{ \frac{\partial(\rho vu)}{\partial x} + \frac{\partial(\rho vv)}{\partial y} + \frac{\partial(\rho vw)}{\partial z} \right\} - \frac{\partial\phi}{\partial y} \pm \frac{\partial(gK)}{\partial y}$$

**B.5.3. z component: w.**

$$(B.37) \quad \frac{\partial(\rho w)}{\partial t} = - \left\{ \frac{\partial(\rhowu)}{\partial x} + \frac{\partial(\rho wv)}{\partial y} + \frac{\partial(\rho ww)}{\partial z} \right\} - \frac{\partial\phi}{\partial z}$$

Upwinding (Appendix E) is used for spatial differencing of convective terms, which are first calculated in Section B.4 above.

Because the domain utilizes a staggered-grid system, the velocity components are determined and stored at zone edges. To determine a zone's central values of the velocity components, the appropriate component's values at the zone edges are spatially averaged.

### B.6. Pressure Perturbation $P'^{(n+1)}_{(i,j,k)}$

While unnecessary for the procedure, the pressure perturbation  $P'$  can be found by definition ( $\phi = P' \pm gK$ ):

$$(B.38) \quad P'^{(n+1)}_{(i,j,k)} = \phi^{(n+1)}_{(i,j,k)} \mp gK^{(n+1)}_{(i,j,k)}$$

### B.7. Check Criteria of Validity

The order of  $\frac{P'}{P_h}$ ,  $\frac{\rho'}{\rho_h}$ , and  $\frac{T'}{T_h}$  is checked to satisfy the LMNA validity constraints. (See Appendix F for details.)

### B.8. Time-Step Complete

All quantities are updated to  $t = n + 1$  :

$$\rho^{(n+1)}_{(i,j,k)}, e^{(n+1)}_{(i,j,k)}, P'^{(n+1)}_{(i,j,k)}, T^{(n+1)}_{(i,j,k)}, X^{(n+1)}_{(i,j,k)}, \vec{v}^{(n+1)}_{(i,j,k)}$$

Iterate the procedure for the desired number of time-steps.

### B.9. Final Comment

As explained in Sub-section 2.5.3 in Chapter 2, an alternative and apparently equivalent procedure would be to evolve the density using the continuity equation and use the EOS to obtain a consistent temperature and internal energy. In fact, this was attempted during the earlier development phase of the LMNA procedure. However, because the conditions on the surface of a neutron star are semi-degenerate, experimental tests revealed that small errors in density, which naturally arose due to truncation and other numerical errors, quickly translated into large errors in temperature, ultimately leading to unrealistic and unstable results. Consequently, the current procedure of using the energy equation to solve for temperature, and then the EOS to determine the consistent density, was implemented and found to be computationally stable and more accurate. Thus, the degenerate conditions of the system

being studied requires the direct evolution of temperature and the indirect determination of a consistent density, not the other way around.

## APPENDIX C

### The $K$ Function

This Appendix explains the rationale for the  $K$  function, detailing the way it is calculated, its different forms, and its appropriate sign in the elliptic equation.

From the momentum equation (Equation B.22, see Appendix B),

$$(C.1) \quad \nabla\phi = -\rho \frac{D\vec{v}}{Dt} \pm \left\{ \frac{\partial(gK)}{\partial x} \hat{i} + \frac{\partial(gK)}{\partial y} \hat{j} \right\}$$

#### C.1. $K_{bottom-up}$

Choosing the positive root, the  $\phi$  function is defined to be:

$$(C.2) \quad \phi \equiv P' + gK_{bottom-up}$$

and the  $K$  function is defined to be:

$$(C.3) \quad K_{bottom-up} \equiv \int_0^{z'} \rho' dz$$

In this example,  $K$  is numerically summed from the “*bottom – up*,” that is, from the bottom of the domain ( $z = 0$ ) to the zone of interest ( $z = z'$ ).

$$(C.4) \quad K_{(i,j,k)} = \sum_{z=0}^{z'} \rho'_{(i,j,k)} \Delta z$$

The  $K$  function is introduced as an important mathematical device to absorb the sum  $P' + gK$  into one function  $\phi$ . Without the  $K$  function, two terms of relatively large magnitude  $\frac{\partial P'}{\partial z}$  and  $\rho'g$  need to be summed. Numerical errors may result and accumulate over many steps. This introduces a possible source of artificial motions. The new variable  $\phi$  should help to minimize these errors in the vertical direction. In exchange, lateral derivatives of  $K$  are introduced. However, because  $K$  is a summed quantity in the vertical direction, lateral differences in the  $K$  function may not be as severe compared to differences between  $\frac{\partial P'}{\partial z}$  and  $\rho'g$ .

In the vertical direction,  $\frac{\partial \phi}{\partial z} = \frac{\partial P'}{\partial z} + \rho'g$  is the vertical component of the force. So,  $\rho'g$  is recovered when the derivative of  $K$  is taken with respect to  $z$ .

$$\begin{aligned} \frac{\partial(gK)}{\partial z} &= \frac{\partial}{\partial z} \left\{ g \int \rho' dz \right\} \\ (C.5) \quad &= \rho'g \end{aligned}$$

Also taking the numerical derivative of  $gK$  yields the same answer,  $\rho'g$ .

$$\begin{aligned} \frac{1}{\Delta z} (gK_{(i,j,k)}) &= g \frac{1}{\Delta z} [K_{upper(i,j,k)} - K_{lower(i,j,k)}] \\ &= g \frac{1}{\Delta z} \left[ \sum_{z=0}^{z'} (\rho'_{upper(i,j,k)} \Delta z) - \sum_{z=0}^{z'} (\rho'_{lower(i,j,k)} \Delta z) \right] \\ &= \rho'_{(i,j,k)} g \frac{\Delta z}{\Delta z} \\ (C.6) \quad &= \rho'_{(i,j,k)} g \end{aligned}$$

since  $\Delta z$  is the same for all zones in a uniformly spaced domain, and *upper* and *lower* refer to the upper and lower faces of the zone at  $i, j, k$ .

Thus, both numerically and analytically, the desired answer  $\rho'g$  is obtained. While the derivative of  $K$  with respect to the vertical component  $z$  is never needed in the current

method, the derivatives with respect to the lateral components  $x$  and  $y$  are needed. So, for instance in the  $x$  direction,

$$(C.7) \quad \begin{aligned} \frac{1}{\Delta x}(gK_{(i,j,k)}) &= g \frac{1}{\Delta x} [K_{left(i,j,k)} - K_{right(i,j,k)}] \\ &= g \frac{1}{\Delta x} \left[ \sum_{z=0}^{z'} \rho'_{left(i,j,k)} \Delta z - \sum_{z=0}^{z'} \rho'_{right(i,j,k)} \Delta z \right] \end{aligned}$$

where *left* and *right* refer to the values of  $K$  at the left and right faces of the zone  $i, j, k$ . This is used in the momentum equation (Equation B.22, see Appendix B). On a staggered grid where the velocity is treated at zone edges, the above differencing can be taken with zone-centered quantities of  $K$ , thus yielding the appropriate edge values of  $\frac{1}{\Delta x}(gK)$ .

For the right-hand-side of the elliptic equation (where *C.T.* are the convective terms as defined in Equation B.25; see Appendix B),

$$(C.8) \quad \nabla^2 \phi = \frac{\partial^2 \rho}{\partial t^2} - C.T. \pm \left\{ \frac{\partial^2(gK)}{\partial x^2} + \frac{\partial^2(gK)}{\partial y^2} \right\}$$

where the second derivatives of  $K$  with respect to  $x$  and  $y$  are needed. Since  $\rho'$  is stored in the center of the zone, central differencing can be used to evaluate the second derivative:

$$(C.9) \quad \frac{\partial^2 K}{\partial x^2} = \frac{1}{(\Delta x)^2} [K_{(i+1,j,k)} - 2K_{(i,j,k)} + K_{(i-1,j,k)}]$$

$$(C.10) \quad \frac{\partial^2 K}{\partial y^2} = \frac{1}{(\Delta y)^2} [K_{(i,j+1,k)} - 2K_{(i,j,k)} + K_{(i,j-1,k)}]$$

## C.2. *K<sub>top-down</sub>*

As an alternative to the *bottom-up* method of calculating the  $K$  function, the *top-down* method can also be used, integrating from the top-most zone,  $z_{top}$  to the zone of interest,  $z'$ :

$$\begin{aligned}
 K_{top-down} &= \int_{z_{top}}^{z'} \rho'(-dz) \\
 (C.11) \quad &= \int_{z'}^{z_{top}} \rho' dz
 \end{aligned}$$

Evaluated from the *top – down*,  $K$  must be *subtracted* from  $P'$  to form  $\phi$ . That is,

$$(C.12) \quad \phi \equiv P' - gK_{top-down}$$

The minus sign is critically needed to recover the vertical component of the force when the vertical derivative of  $\phi$  is taken. That is,

$$\begin{aligned}
 \frac{\partial \phi}{\partial z} &= \frac{\partial P'}{\partial z} - \frac{\partial}{\partial z}(gK_{top-down}) \\
 &= \frac{\partial P'}{\partial z} - g \frac{\partial}{\partial z} \left( \int_z^{z_{top}} \rho' dz \right) \\
 (C.13) \quad &= \frac{\partial P'}{\partial z} + \rho' g
 \end{aligned}$$

where the counteracting minus sign arises when taking the derivative at the lower limit of the integral.

Thus, when using  $K_{bottom-up}$ , the proper sign to use in the elliptic and momentum equations is *positive*, whereas for  $K_{top-down}$ , the proper sign is *negative*. All terms involving  $K$  in the momentum and elliptic equations must be likewise consistent.

### C.3. Taylor's Rule

In practice, the  $K$  integral is evaluated as a discrete summation using Taylor's rule. That is, the value of  $K$  at zone  $k$  is determined by summing all the values of  $\rho' dz$  of the zones in the same column below (in the case of the *bottom – up* formalism) or above (*top – down*) it.

$$\begin{aligned}
K_{bottom-up} &\equiv \int_0^k \rho' dz \\
(C.14) \quad &= \left\{ \frac{1}{2}\rho'(0) + \sum_{z=1}^{k-1} \rho'(z) + \frac{1}{2}\rho'(k) \right\} \Delta z
\end{aligned}$$

$$\begin{aligned}
K_{top-down} &\equiv \int_{k_{top}}^k \rho'(-dz) \\
(C.15) \quad &= \left\{ \frac{1}{2}\rho'(k_{top}) + \sum_{z=k_{top}-1}^{k+1} \rho'(z) + \frac{1}{2}\rho'(k) \right\} \Delta z
\end{aligned}$$

#### C.4. Boundary Conditions on $\phi$

By definition, the integral of zero interval is zero, so the value of  $K$  for the first zone being calculated is identically zero. Thus, at the upper (for the *top-down* formalism) or lower (for the *bottom-up* formalism) boundary, the Dirichlet condition  $\phi = P' \pm gK = 0$  can be made, where  $P' = 0$  is set at the appropriate boundary, depending on the formalism used.

For example in the *top-down* formalism, the Dirichlet condition  $\phi = P' - gK_{top-down} = 0$  at the upper boundary is equivalent to two boundary conditions at the top:  $P' = 0$  and  $gK_{top-down} = 0$ . The former is justified, because  $P'$  acts as a potential term and its value can be arbitrarily set as a constant. (Only  $\nabla P'$  is physically important in the evolution.) The latter is justified, because  $K$  is defined as an integral of perturbed densities as a function of height, but since the integral of zero interval is zero, the value of  $K$  for the first zone being calculated is identically zero. Thus, at the upper boundary  $K$  is also identically zero. Hence, the Dirichlet condition  $\phi = 0$  is fully justified at the top.

At the bottom boundary, the Neumann condition ( $\frac{\delta\phi}{\delta z} = 0$ ) is used in the elliptic solver. Note that this implementation of the Neumann condition is equivalent to imposing hydrostatic equilibrium at the lower boundary, implying no net vertical force exists there. Thus,

stetting the vertical component of velocity to be zero at the lower boundary for all time is valid, since the initial value there is zero.

## APPENDIX D

### The Analytical Determination of $\frac{\partial \rho}{\partial t}$

The analytical expression for  $\frac{\partial \rho}{\partial t}$  is derived by taking the time derivative of the internal energy  $e(\rho, T, X_l)$ :

$$\begin{aligned}
 \frac{de}{dt} &= \left. \frac{\partial e}{\partial T} \right|_{\rho, X_l} \frac{dT}{dt} + \left. \frac{\partial e}{\partial \rho} \right|_{T, X_l} \frac{d\rho}{dt} + \left. \frac{\partial e}{\partial X_l} \right|_{\rho, T} \frac{dX_l}{dt} \\
 (D.1) \quad &= G(\rho^n, T^n, X_l^n)
 \end{aligned}$$

where  $G(\rho^n, T^n, X_l^n)$  is a term which depends only on the values of  $\rho, T, X_l$  at time step n.

Also,

$$\begin{aligned}
 \frac{dP}{dt} &= \frac{\partial P}{\partial t} + \vec{v} \cdot \nabla P \\
 (D.2) \quad &= \left. \frac{\partial P}{\partial \rho} \right|_{T, X_l} \frac{d\rho}{dt} + \left. \frac{\partial P}{\partial T} \right|_{\rho, X_l} \frac{dT}{dt} + \left. \frac{\partial P}{\partial X_l} \right|_{\rho, T} \frac{dX_l}{dt}
 \end{aligned}$$

which yields an expression for  $\frac{dT}{dt}$  when the constraint that the Eulerian time derivative of pressure is zero ( $\frac{\partial P}{\partial t} = 0$ ) is applied:

$$(D.3) \quad \frac{\partial T}{\partial t} = \frac{\vec{v} \cdot \nabla P - \left( \left. \frac{\partial P}{\partial \rho} \right|_{T, X_l} \frac{d\rho}{dt} + \left. \frac{\partial P}{\partial X_l} \right|_{\rho, T} \frac{dX_l}{dt} \right)}{\left. \frac{\partial P}{\partial T} \right|_{\rho, X_l}}$$

Substituting the above expression for  $\frac{dT}{dt}$  into the expression for  $\frac{de}{dt}$  yields an expression for  $\frac{d\rho}{dt}$ :

$$(D.4) \quad \frac{d\rho}{dt} = C_1^{-1} \left( \frac{de}{dt} + C_2 \frac{dX_l}{dt} - C_3(\vec{v} \cdot \nabla P) \right)$$

where:

$$(D.5) \quad C_1 = \frac{\partial e}{\partial \rho} \Big|_{T,X_l} - \left( \frac{\frac{\partial e}{\partial T} \Big|_{\rho,X_l} \frac{\partial P}{\partial \rho} \Big|_{T,X_l}}{\frac{\partial P}{\partial T} \Big|_{\rho,X_l}} \right)$$

$$(D.6) \quad C_2 = \left( \frac{\frac{\partial e}{\partial T} \Big|_{\rho,X_l} \frac{\partial P}{\partial X_l} \Big|_{\rho,T}}{\frac{\partial P}{\partial T} \Big|_{\rho,X_l}} \right) - \frac{\partial e}{\partial X_l} \Big|_{\rho,T}$$

$$(D.7) \quad C_3 = \frac{\frac{\partial e}{\partial T} \Big|_{\rho,X_l}}{\frac{\partial P}{\partial T} \Big|_{\rho,X_l}}$$

Next, an expression for  $\frac{de}{dt}$  is determined. Consider the total derivative form of the energy equation:

$$(D.8) \quad \rho \frac{de}{dt} - \frac{P}{\rho} \frac{d\rho}{dt} = Q + \nabla \cdot \kappa \nabla T$$

Thus,

$$(D.9) \quad \frac{de}{dt} = \frac{1}{\rho} \left( Q + \nabla \cdot \kappa \nabla T + \frac{P}{\rho} \frac{d\rho}{dt} \right)$$

Using  $\frac{de}{dt}$  in the expression for  $\frac{d\rho}{dt}$  above yields:

$$(D.10) \quad \frac{d\rho}{dt} = \frac{\left[ \frac{1}{\rho} (Q + \nabla \cdot \kappa \nabla T) + C_2 \frac{dX_l}{dt} - C_3(\vec{v} \cdot \nabla P) \right]}{\left( C_1 - \frac{P}{\rho^2} \right)} - \vec{v} \cdot \nabla \rho$$

where  $C_1$ ,  $C_2$ , and  $C_3$  are defined above.

The term  $\frac{Q}{\rho}$  is the energy generation rate, with units erg g<sup>-1</sup> s<sup>-1</sup>.

The term  $\nabla \cdot \kappa \nabla T$  represents the contribution due to thermal diffusion, with a diffusion constant  $\kappa(\rho, T, X_l)$ . (See Section B.2 in Appendix B for the definition of  $\kappa$ .)

The hydrostatic pressure gradient is  $\nabla P_h = -\rho_h g \hat{k}$ . Hence,  $\vec{v} \cdot \nabla P = -w \rho_h g$ .

Finally,

$$(D.11) \quad \frac{d\rho}{dt} = \frac{\left[ \frac{1}{\rho} (Q + \nabla \cdot \kappa \nabla T) + C_2 \frac{dX_l}{dt} + C_3 w \rho_h g \right]}{\left( C_1 - \frac{P}{\rho^2} \right)} - \vec{v} \cdot \nabla P$$

All the thermodynamic partial derivatives except those which are taken with respect to composition  $\left( \frac{\partial P}{\partial X_l}, \frac{\partial e}{\partial X_l} \right)$  are obtained from the Helmholtz equation of state via interpolation from a table. However,  $\frac{\partial P}{\partial X_l}$  and  $\frac{\partial e}{\partial X_l}$  are numerically evaluated, changing the composition a little by a factor of 1.e-6 and obtaining the resulting  $P$  and  $e$  from the EOS.

Also, note that

$$(D.12) \quad \frac{dX_l}{dt} = R_l$$

where  $R_l$  is the Lagrangian rate of burning from the burner.

## APPENDIX E

### Methods of Discretizing Differentials

In this appendix, the methods used in the LMNA model to discretize differential expressions into difference expressions are presented. Refer to Appendix B for the detailed examination of the differential equations solved in the LMNA model. The expressions in this appendix are given in 3D for generality. The present LMNA model is limited to 2D, where the lateral dimension is  $y$  (or  $j$ ), and the vertical dimension is  $z$  (or  $k$ ).

#### E.1. Temporal Derivatives

The form of temporal differencing used in the LMNA model is the forward-Euler method.

$$(E.1) \quad \left( \frac{\partial u}{\partial t} \right)^{(n)}_{(i,j,k)} = \frac{u^{(n+1)}_{(i,j,k)} - u^{(n)}_{(i,j,k)}}{\Delta t}$$

#### E.2. Spatial Derivatives

The LMNA model uses a staggered-grid system, where thermodynamic quantities (such as  $T$ ,  $X_l$ ,  $\rho$ ,  $K$ , and  $\phi$ ) are defined at zone centers, and the dynamical quantities (the components of the velocity  $u$ ,  $v$ ,  $w$ ) are defined at zone edges. Advective and first-order convective terms are upwinded, while all other spatial derivatives are centrally differenced over one or two zones.

**E.2.1. Upwinding Advection Terms.** Composition and temperature are advected in the LMNA procedure by upwinding. Let  $A$  represent the quantity to be differenced with respect to the spatial coordinate  $r$ . For example, to advect  $A$  at time level  $n$ ,

$$\begin{aligned}
 \frac{\partial A}{\partial t} &= -\vec{v} \cdot \nabla A \\
 (E.2) \quad &= - \left( u_c \frac{\partial A}{\partial x} + v_c \frac{\partial A}{\partial y} + w_c \frac{\partial A}{\partial z} \right)
 \end{aligned}$$

Let  $c = u_c, v_c$ , and  $w_c$ , which are the zone-centered values of the velocity components and may be either positive or negative. Then, for each spatial coordinate  $r$ ,

$$\begin{aligned}
 c \left( \frac{\partial A}{\partial r} \right)_{(i,j,k)}^{(n)} &= c \left( \frac{A_{(i+1,j,k)}^{(n)} - A_{(i,j,k)}^{(n)}}{\Delta r} \right), \text{ for } c < 0 \\
 (E.3) \quad &= c \left( \frac{A_{(i,j,k)}^{(n)} - A_{(i-1,j,k)}^{(n)}}{\Delta r} \right), \text{ for } c > 0
 \end{aligned}$$

where in this expression, the meaning of the index  $i$  is generalized to represent the specific coordinate which  $r$  represents, and the two other coordinates are held fixed.

Because  $A$  represents a value at a given computational zone's center, consistency requires that the components of velocity for the purpose of upwinding should also be zone-centered values. Since the computational domain consists of a staggered grid, where  $\vec{v}$  is calculated at zone-edges, the zone-centered values of the velocity components are determined by taking the simple average of the appropriate values at a given zone's edges. Specifically,

$$(E.4) \quad u_{c(i,j,k)} = \frac{u_{(i+\frac{1}{2},j,k)} + u_{(i-\frac{1}{2},j,k)}}{2}$$

$$(E.5) \quad v_{c(i,j,k)} = \frac{v_{(i,j+\frac{1}{2},k)} + v_{(i,j-\frac{1}{2},k)}}{2}$$

$$(E.6) \quad w_{c(i,j,k)} = \frac{w_{(i,j,k+\frac{1}{2})} + w_{(i,j,k-\frac{1}{2})}}{2}$$

For clarity, the edges are notated in this appendix as half-integer steps, for example,  $i + \frac{1}{2}$  and  $i - \frac{1}{2}$  for the front and back edge of the computational domain in the  $i$  direction. In the LMNA code itself, the indexing scheme follows the staggered-grid system which is presented in Figure 2.1 in Chapter 2. That is, the edge  $i - \frac{1}{2}$  here corresponds to index  $i$  in the code, and likewise,  $i + \frac{1}{2}$  here corresponds to index  $i + 1$  in the code.

**E.2.2. Upwinding Convective Terms.** As explained in Section B.4 of Appendix B, each second-order convective term is calculated as two first-order derivatives: i) upwinding is used first to obtain the terms in  $\nabla \cdot (\rho \vec{v} \vec{v})$  at zone edges, and ii) these terms are then centrally differenced over one zone to obtain the final expressions in  $\nabla \cdot \{\nabla \cdot (\rho \vec{v} \vec{v})\}$  which are needed at zone centers.

The terms in  $\nabla \cdot (\rho \vec{v} \vec{v})$  have the form

$$(E.7) \quad \frac{\partial(\rho u_a u_b)}{\partial r_a}$$

where  $u_a$  represents a generalized component of velocity,  $r$  represents a generalized dimension, and  $a$  and  $b$  are dummy indices which can equal 1, 2, or 3, corresponding to the specific dimensions,  $x$ ,  $y$ , or  $z$ . Each term is first expanded using the product rule:

$$(E.8) \quad \frac{\partial(\rho u_a u_b)}{\partial r_a} = \rho u_a \frac{\partial(u_b)}{\partial r_a} + u_b \frac{\partial(\rho u_a)}{\partial r_a}$$

The two terms on the right-hand-side of this expression are then upwinded over *one-half* of a computational zone, such that the terms may be determined at the computational cell's appropriate *edges*. The upwinding scheme is then:

$$\begin{aligned}
 c \left( \frac{\partial A}{\partial r} \right)_{(i+\frac{1}{2},j,k)} &= c \left( \frac{A_{(i+1,j,k)} - A_{(i+\frac{1}{2},j,k)}}{(\Delta r/2)} \right), \text{ for } c < 0 \\
 (E.9) \quad &= c \left( \frac{A_{(i+\frac{1}{2},j,k)} - A_{(i,j,k)}}{(\Delta r/2)} \right), \text{ for } c > 0
 \end{aligned}$$

where  $c$  and  $A$  represent either  $\rho u_a$  or  $u_b$ , depending on which term is being evaluated in Equation E.8.

Great care is taken to calculate the appropriate input values  $\rho u_a$  and  $u_b$  at the correct locations in the cell. Careful consideration of how these terms will be next differenced to find the final terms in  $\nabla \cdot \{\nabla \cdot (\rho \vec{v} \vec{v})\}$  ensures their proper evaluation. For example, “pure” convective terms (where  $a = b$ , such as  $\frac{\partial(\rho uu)}{\partial x}$ ,  $\frac{\partial(\rho vv)}{\partial y}$ , and  $\frac{\partial(\rho ww)}{\partial z}$ ) can be evaluated relatively straightforwardly, since these terms are next differenced with respect to the same coordinate direction to yield  $\frac{\partial^2(\rho uu)}{\partial x^2}$ ,  $\frac{\partial^2(\rho vv)}{\partial y^2}$ , and  $\frac{\partial^2(\rho ww)}{\partial z^2}$ . Thus, for example,

$$(E.10) \quad \left( \frac{\partial^2(\rho uu)}{\partial x^2} \right)_{(i,j,k)} = \frac{T_{(i+\frac{1}{2},j,k)} - T_{(i-\frac{1}{2},j,k)}}{\Delta x}$$

where

$$(E.11) \quad T_{(i+\frac{1}{2},j,k)} = \frac{\partial \left( (\rho u)_{(i+\frac{1}{2},j,k)} u_{(i+\frac{1}{2},j,k)} \right)}{\partial x}$$

which is upwinded according to the prescription given in Equations E.8 and E.9.

More complicated are the “mixed” convective terms (where  $a \neq b$ , such as  $\frac{\partial(\rho vu)}{\partial x}$ ,  $\frac{\partial(\rho uw)}{\partial x}$ ,  $\frac{\partial(\rho vw)}{\partial y}$ ,  $\frac{\partial(\rho uw)}{\partial y}$ ,  $\frac{\partial(\rho uw)}{\partial z}$ , and  $\frac{\partial(\rho vw)}{\partial z}$ ), which must be more carefully evaluated. (Refer to Equation B.25 in Appendix B).

As a specific example, consider the proper evaluation of  $\frac{\partial(\rho vw)}{\partial z}$ . Because it will next be differenced with respect to the  $y$  direction to yield  $\frac{\partial}{\partial y} \frac{\partial(\rho vw)}{\partial z}$ , the  $\frac{\partial(\rho vw)}{\partial z}$  term must be evaluated at the lateral  $y$  edges of the zone. Hence, for proper upwinding,  $\rho v$  and  $w$  must ultimately be evaluated at each of the computational zone’s four corners (for example,

$w_{(i,j-\frac{1}{2},k-\frac{1}{2})}$ ,  $w_{(i,j-\frac{1}{2},k+\frac{1}{2})}$ ,  $w_{(i,j+\frac{1}{2},k-\frac{1}{2})}$ , and  $w_{(i,j+\frac{1}{2},k+\frac{1}{2})}$ ), as well as the center of the lateral  $y$  edges ( $w_{(i,j-\frac{1}{2},k)}$  and  $w_{(i,j+\frac{1}{2},k)}$ ). Since  $w$  is stored at the vertical  $z$  edges, simple averaging over two or four values is required to obtain  $w$  at the precise locations needed. After  $\rho v$  and  $w$  are properly calculated in this manner, the prescriptions described by Equations E.10 and E.11 are used to determine the final convective expressions for  $\frac{\partial}{\partial y} \frac{\partial(\rho v w)}{\partial z}$ . The same careful consideration is made for all  $\nabla \cdot (\rho \vec{v} \vec{v})$  convective terms.

Once determined, the terms in  $\nabla \cdot (\rho \vec{v} \vec{v})$  are centrally differenced over one zone to obtain the final expressions in  $\nabla \cdot \{\nabla \cdot (\rho \vec{v} \vec{v})\}$ , for example, as described in Equation E.10. Moreover, because the terms in  $\nabla \cdot (\rho \vec{v} \vec{v})$  are evaluated at time level  $n$ , they are appropriately used in the momentum equation to update the velocity to time level  $n+1$  (Section B.5 in Appendix B).

**E.2.3. Central Differencing.** Let  $A$  represent the quantity to be differenced with respect to the spatial coordinate  $r$  at time-level  $n$ . In the following expressions, the meaning of the index  $i$  is generalized to represent the specific coordinate which  $r$  represents, and the two other coordinates are held fixed.

E.2.3.1. *First-order central differencing over one zone.*

$$(E.12) \quad \left( \frac{\partial A}{\partial r} \right)_{(i,j,k)}^{(n)} = \frac{A_{(i+1,j,k)}^{(n)} - A_{(i,j,k)}^{(n)}}{\Delta r}$$

The first-order convective terms in  $\nabla \cdot (\rho \vec{v} \vec{v})$  are centrally differenced in this manner to calculate  $\nabla \cdot \{\nabla \cdot (\rho \vec{v} \vec{v})\}$ .

Also, the thermal diffusion term  $\nabla \cdot \kappa T$  is calculated as two first-order central differences over one zone: i) to determine the negative of the thermal flux  $-F = \kappa \nabla T$  at the edges of a computational zone, and ii) to evaluate  $\nabla \cdot (-F)$  at the zone center. For example, in the  $r$  direction,

$$(E.13) \quad -F_{(i+\frac{1}{2},j,k)} = \kappa_{(i+\frac{1}{2},j,k)} \left( \frac{T_{(i+1,j,k)} - T_{(i,j,k)}}{\Delta r} \right)$$

$$(E.14) \quad \left( \frac{\partial(-F)}{\partial r} \right)_{(i,j,k)} = \left( \frac{-F_{(i+\frac{1}{2},j,k)} - (-F_{(i-\frac{1}{2},j,k)})}{\Delta r} \right)$$

where  $\kappa$  is the radiative thermal conductivity (which is calculated at zone centers based on  $\rho_{(i,j,k)}$ ,  $X_{l(i,j,k)}$ , and  $T_{(i,j,k)}$ ) and is simply averaged to find edge values. (See Section B.2 in Appendix B for the definition of  $\kappa$ .)

#### E.2.3.2. First-order central differencing over two zones.

$$(E.15) \quad \left( \frac{\partial A}{\partial r} \right)_{(i,j,k)}^{(n)} = \frac{A_{(i+1,j,k)}^{(n)} - A_{(i-1,j,k)}^{(n)}}{2\Delta r}$$

Evaluating  $\nabla \cdot (\rho \vec{v})^n$  in the elliptic equation is the only instance where this kind of differencing is used.

#### E.2.3.3. Second-order central differencing.

$$(E.16) \quad \left( \frac{\partial^2 A}{\partial r^2} \right)_{(i,j,k)}^{(n)} = \frac{A_{(i+1,j,k)}^{(n)} - 2A_{(i,j,k)}^{(n)} + A_{(i-1,j,k)}^{(n)}}{(\Delta r)^2}$$

Second-order central differencing of this kind is required for the expressions involving  $K$  on the right-hand-side of the elliptic equation:  $\frac{\partial^2(gK)}{\partial x^2}$  and  $\frac{\partial^2(gK)}{\partial y^2}$ .

## APPENDIX F

# The Low Mach Number Approximation vs. the Anelastic Approximation

Both the Anelastic Approximation (AA) and the Low Mach Number Approximation (LMNA) are routinely used in terrestrial studies to approximate the fully compressible Euler equations. Important differences distinguish the two methods, and they are valid approximations in different physical regimes. In this Appendix, the criteria of validity of both approximations will be presented. Table F.1 at the end of this Appendix summarizes the key characteristics of each approximation.

### F.1. Preliminary Definitions

Let  $A(\mathbf{r}, t)$  represent a thermodynamic state variable, such as density, entropy, temperature, or pressure. Each state variable is expressed as a sum of a dominant term  $A_0$  and a perturbation  $A'$ . In general,  $A_0$  and  $A'$  can be functions of both space and time. That is, most generally,

$$(F.1) \quad A(\mathbf{r}, t) = A_0(\mathbf{r}, t) + A'(\mathbf{r}, t)$$

In some versions of the AA,  $A_0(\mathbf{r}, t)$  is a spherically symmetric mean of the state variable. In other versions of the AA,  $A_0(\mathbf{r}, t)$  is a hydrostatic base state, in which case, it would be a function only of the vertical coordinate,  $A_0(z)$ . That is, for the AA,  $A(\mathbf{r}, t) = A_0(\mathbf{r}, t) + A'(\mathbf{r}, t)$ , or  $A(\mathbf{r}, t) = A_0(z) + A'(\mathbf{r}, t)$ .

In the LMNA,  $A_0$  is a hydrostatic base state, and thus is independent of time, dependent only on the vertical coordinate  $A_0(z)$ . Thus, for the LMNA,  $A(\mathbf{r}, t) = A_0(z) + A'(\mathbf{r}, t)$ .

Next, define the ratio  $\xi$  as:

$$(F.2) \quad \xi \equiv \frac{A'(\mathbf{r}, t)}{A_0(\mathbf{r}, t)}$$

## F.2. The Anelastic Approximation

In the AA,  $\xi$  is of the order  $M^2$  for *all* thermodynamic state variables. That is, the perturbed quantities are all assumed to be very small for subsonic flows, and they are all of the same order  $M^2$ . Physically, when convective motions are subsonic, the stratification of the fluid is only slightly superadiabatic. Thus, it is reasonable to assume the resulting departures of the thermodynamic state variables from  $A_0$  should also be small. For subsonic flows, pressure and density perturbations are smoothed out on an acoustic time scale, which is much smaller than the convective time scale. Thus, by assuming  $\frac{\partial \rho'}{\partial t} = 0$  in the continuity equation, the effects of acoustic waves are filtered out of the domain. This approximation instantaneously equilibrates acoustic density and pressure perturbations, since density and pressure are directly related for isentropic processes. Thus, the system is allowed to evolve on a convective rather than an acoustic time scale. Time dependent changes in density due to convective motion can still be evolved on the convective time scale. Thus, two criteria for validity for the AA are: i) convective fluid velocities are subsonic ( $M \ll 1$ ); and, ii)  $\xi$  for all state variables are of order  $M^2$ .

## F.3. The Low Mach Number Approximation

In the LMNA,  $\xi$  is of order  $M^2$  for pressure *only*. The  $\xi$  for the other thermodynamic state variables are assumed to be of order  $M^0$  (or 1). When these conditions are met, the pressure perturbation  $P'$  can be neglected in the equations of energy and state. In the LMNA, potentially large pressure changes due to acoustic effects are completely neglected. The actual filtering of the acoustic waves occurs by assuming pressure is constant in the equation of state, that is, by setting  $P' = 0$  in this equation. Also,  $P'$  is neglected in the

Characteristic	LMNA	AA
Order of $\xi$ for $P$	$M^2$	$M^2$
Order of $\xi$ for $\rho, T$	$M^0$	$M^2$
Order of Flow Speeds	$M \ll 1$	$M \ll 1$
Acoustic Filtering	$P'$ is omitted from the energy equation and equation of state	$\frac{\partial \rho'}{\partial t}$ is omitted from the continuity equation
Physically Appropriate Regimes	burning fronts, combustion with large $\rho$ and $T$ gradients	subsonic convective motion without combustion, entropy gradient slightly superadiabatic
Physically Inappropriate Regimes	$\xi$ for $P$ is of the same order as $\xi$ for $\rho$ and $T$	$\xi$ for $\rho$ and $T > M$

TABLE F.1. LMNA vs AA

energy equation, since this term is of order  $M^2$ . Any small pressure perturbations which arise will drive mass motion, which is governed by the equation of motion. Thus,  $P'$  is not neglected in the momentum equation. Unlike the AA, the LMNA allows for potentially large density perturbations, and thus,  $\frac{\partial \rho'}{\partial t}$  is *not* assumed to be zero in the continuity equation. Large gradients in density and temperature are expected across a burning front, so the LMNA is well-suited for studying problems involving combustion.

#### F.4. Summary

In summary, while the LMNA shares with the AA the criteria that flows must be subsonic ( $M \ll 1$ ), the AA assumes  $\xi$  for all perturbed thermodynamic state quantities are of the same order  $M^2$ , while the LMNA assumes  $\xi$  for only pressure is of the order  $M^2$ , and for the other variables, order  $M^0$ . In both approximations, it is assumed that acoustic waves do not significantly affect the dynamics of the flow fields. This is a fair assumption for very subsonic flows, since in these systems, inertial, gravitational, rotational, and thermal effects should dominate acoustic ones.

Table F.1 summarizes the essential qualities of the two approximation methods.

## APPENDIX G

### Computing Environment Specifications

In this Appendix, important specifications of the computing environment used to perform the calculations in this thesis are presented. While the preliminary coding and initial test runs were conducted on the supercomputing facilities at NCSA (University of Illinois, Urbana-Champaign) and the ASCI/Alliances Center for Astrophysical Thermonuclear Flashes (University of Chicago), the bulk of the code development, testing, and final calculations were completed using Northwestern University's Department of Applied Mathematics' Linux cluster *Hydra* ([hydra.esam.northwestern.edu](http://hydra.esam.northwestern.edu)), administered by Jesse Becker.

The key hardware and software specifications of *Hydra* are detailed in Tables G.1 and G.2.

Hardware Component	Specification
CPU architecture	Xeon
CPU speed per node	2.66 GHz, dual processor
BUS speed	400 MHz
RAM per node	2 Gbytes
Hard drive per node	40 Gbytes
Head node storage	400 Gbyte RAID5 array
Total Number of nodes	32
Internal network Ethernet switches	24-port Gigabit

TABLE G.1. *Hydra* Hardware Specifications

Software Component	Version number
GCC	3.2.3
Intel compiler (C and FORTRAN)	8.1
MPICH (Argonne implementation)	1.2.6
LAM (alternate MPI implementation)	7.1.1
Sun Gridengine (Queueing system)	6
ROCKS (cluster management)	3.3

TABLE G.2. *Hydra* Software Specifications